Commissioning Scenarios and Tests for the LHC Collimation system

Thèse de Doctorat

N° 4271

par

Chiara Bracco

Physicien diplômé de l'Universitá degli Studi di Milano, Italie.

Président du jury: **Prof. Robert Schaller**
Directeur de thèse: **Prof. Leonid Rivkin**
Expert Interne: **Prof. Aurelio Bay**
Expert Externe: **Dr. Ralph Assmann**
Expert Externe: **Dr. Steve Peggs**

Lausanne 2008

Abstract

The physics reach of the LHC requires unprecedented luminosity and beam intensity in proton-proton collisions. The maximum intensity in the LHC is directly coupled to the maximum peak beam loss rate and the cleaning efficiency from the collimation system. A sophisticated LHC collimation system is implemented in two cleaning insertions and in the experimental areas. In a first phase 88 collimators are installed, being controlled by 344 stepping motors in total. The work of this PhD analyzes the achievable cleaning efficiency with realistic imperfections, defines the required collimator settings and establishes available tolerances for collimator setup and transient optics changes. An optimal setup strategy can optimize cleaning efficiency, ensure passive protection, maximize tolerances, minimize the required beam time for setup of the system and support the expected evolution in LHC beam intensity. Such an optimized strategy is described.

Key words: LHC, collimation, cleaning efficiency, machine protection, commissioning.

Résumé

Les performances prévues dans le cahier des charges du LHC exigent une luminosité et une intensité des faisceaux sans précédent pour un collisionneur proton-proton. L'intensité maximum dans le LHC est directement liée au maximum du taux de pertes de particules ainsi qu'à l'efficacité du système de collimation. Ce système sophistiqué de collimation (ou de "nettoyage") est mis en œuvre dans deux insertions dédiées et dans les zones proches des expériences. 88 collimateurs sont installés et contrôlés par 344 moteurs pas à pas. Le travail de cette thèse de doctorat analyse l'efficacité de la collimation qu'on peut obtenir en tenant compte d'imperfections réalistes, définit les positions nécessaires des collimateurs et établit les tolérances acceptables à la fois pour les positions des collimateurs et pour les changements transitoires d'optique. Une stratégie optimale de positionnement des collimateurs permet de maximiser l'efficacité du nettoyage, de fournir une protection passive, de maximiser les tolérances, de réduire le temps de faisceau nécessaire pour le positionnement du système et de rendre possible l'augmentation prévue de l'intensité du faisceau dans le LHC. Une telle stratégie d'optimisation est décrite dans cette thèse.

Mot-clé: LHC, collimation, efficacité de nettoyage, protection de la machine, commissioning.

Contents

List of Figures

List of Tables

Chapter 1

Introduction

On September the 10th 2008 the first proton beams were circulating in the Large Hadron Collider (LHC) at CERN, 14 years after the approval of the project.

The LHC is designed to accelerate two counterrotating beams of $3.2 \cdot 10^{14}$ protons and $4.1 \cdot 10^{10}$ heavy ions up to $7\,\mathrm{TeV}$ and $574\,\mathrm{TeV}$ respectively. More than 5000 superconducting magnets (including correctors) are installed along the $27\,\mathrm{km}$ machine circumference and are kept at temperatures between $1.8\,\mathrm{K}$ and $4.5\,\mathrm{K}$ to guide and focus the circulating beams.

Each proton beam of the LHC stores an energy of up to $360\,\mathrm{MJ}$. This stored energy corresponds to about $86\,\mathrm{kg}$ of TNT explosive and could melt $500\,\mathrm{kg}$ of copper. The superconducting magnets would quench after an energy deposition of $5\,\mathrm{mJ\,s^{-1}\,cm^{-3}}$, a tiny fraction of the stored energy. A 0.001% fraction of the stored energy can damage metal if deposited instantaneously. A sophisticated system of collimators is therefore needed to handle the LHC beams in the superconducting magnets by providing beam cleaning and passive machine protection.

The LHC collimation system is constructed and installed in several phases. This phased implementation relies on the fact that difficulties and performance goals for the LHC are distributed in time, following the natural evolution of the machine performance.

The phase 1 LHC collimation system consists of 88 collimators for the two beams (7 times more collimators than in TEVATRON) which are set to different openings to implement a multi-stage cleaning and protection system. Two insertions in the LHC ring are dedicated to momentum and betatron cleaning. The remaining collimators protect the most sensitive parts of the machine (injection, extraction and interaction regions).

The LHC system is the first collimation system that must be active during the full machine cycle, from injection up to physics and extraction.

LHC collimators consist of two parallel, fully movable jaws of special materials. The two jaws define a gap for free passage of the beam core. The particles in the beam tails (or halo) are intercepted and cleaned by the jaw material. In total one needs to set up more than 340 independent degrees of freedom in order to commission

this system.

Robustness was defined as the priority for phase 1 collimators closest to the beam. Primary and secondary collimators must withstand an energy deposition of 2 MJ (0.6% of total stored energy corresponding to 0.5 kg of TNT) in case of expected failures.

The collimation system is characterized by a cleaning efficiency. This term defines the fraction of particles that hit a primary collimator and are stopped in the cleaning insertion. For the 7 TeV protons the cleaning efficiency must be above 99.99% in order to prevent quenches in the superconducting magnets for the specified LHC beam loss rates. It is noted that this imposes a strong challenge (stop a 7 TeV proton in collimators distributed over a 200 m cleaning insertion). The small beam size in the LHC and the required cleaning efficiency imposes small gaps of down to 2.5 mm over 1 m long jaws. Setup and beam tolerances are challenging and can be as small as 30 μm, the width of a human hair.

The commissioning of the sophisticated LHC collimation system imposes that important questions are addressed: 1)What is the best order and method to set up collimators such that required cleaning efficiency is achieved? 2)What setup accuracy is needed for different intensities? 3)How must the collimators be set during the energy ramp and other parts of the cycle? 4)How must unavoidable collimator and machine imperfections be handled? 5)Can the system be set up in stages of increasing number of collimators?

This PhD work addresses these questions which will have a crucial impact on the performance and luminosity of the LHC during its commissioning to nominal beam intensity.

An optimized strategy for the commissioning of the collimation system is developed, based on simulations and experimental tests in the SPS proton accelerator. Special emphasis is put on intensity reach, imperfections and available tolerance budgets.

Chapter 2

The Large Hadron Collider

Particle colliders accelerate and store high energy charged beams that are collided inside high energy physics experiments. The higher the energy of the colliding beams and the higher the event rate, the wider is the spectrum of the generated particles. It is the hope that new high energy colliders like the Large Hadron Collider (LHC) allow the discovery of new particles and forces.

The LHC [1] is a circular accelerator with a 26.659 km circumference situated at the border between Switzerland and France at an average depth of 100 m underground. It is formed by eight arcs hosting 23 FODO cells [2] and eight straight sections (IRs) where the experimental regions and the utility insertions are located (see Fig. 2.1).

Two counter rotating proton or Lead ion beams (Beam 1 clockwise, Beam 2 counterclockwise), will be injected into the machine in IR2 (Beam 1) and IR8 (Beam 2) and accelerated up to the nominal top energy (see Table 2.1 and 2.2) by the RF cavities located in IR4. The two beams will then be brought into collision at the four interaction points (IPs) where the main experiments are placed: ATLAS (IP1), ALICE (IP2), CMS (IP5) and LHCb (IP8). In normal conditions the beams will collide for several hours (Physics) and at the end of this period or in case of a failure detection, the beams will be aborted by the dump system located in IR6.

2.1 The LHC experiments

The LHC will provide proton-proton and heavy ion collisions with a centre-of-mass energy of 14 TeV and 1.15 PeV respectively. The event rate at the experiments is described by the luminosity ($\mathcal{L}$) that for a Gaussian beam is given by [3]:

$$\mathcal{L} = \frac{N_b^2 n_b f_{rev} \gamma}{4\pi\varepsilon_n \beta_z *} F,$$
(2.1)

where N_b and n_b are number of particles per bunch and number of bunches per beam respectively and f_{rev} is the revolution frequency. The luminosity $\mathcal{L}$ varies in
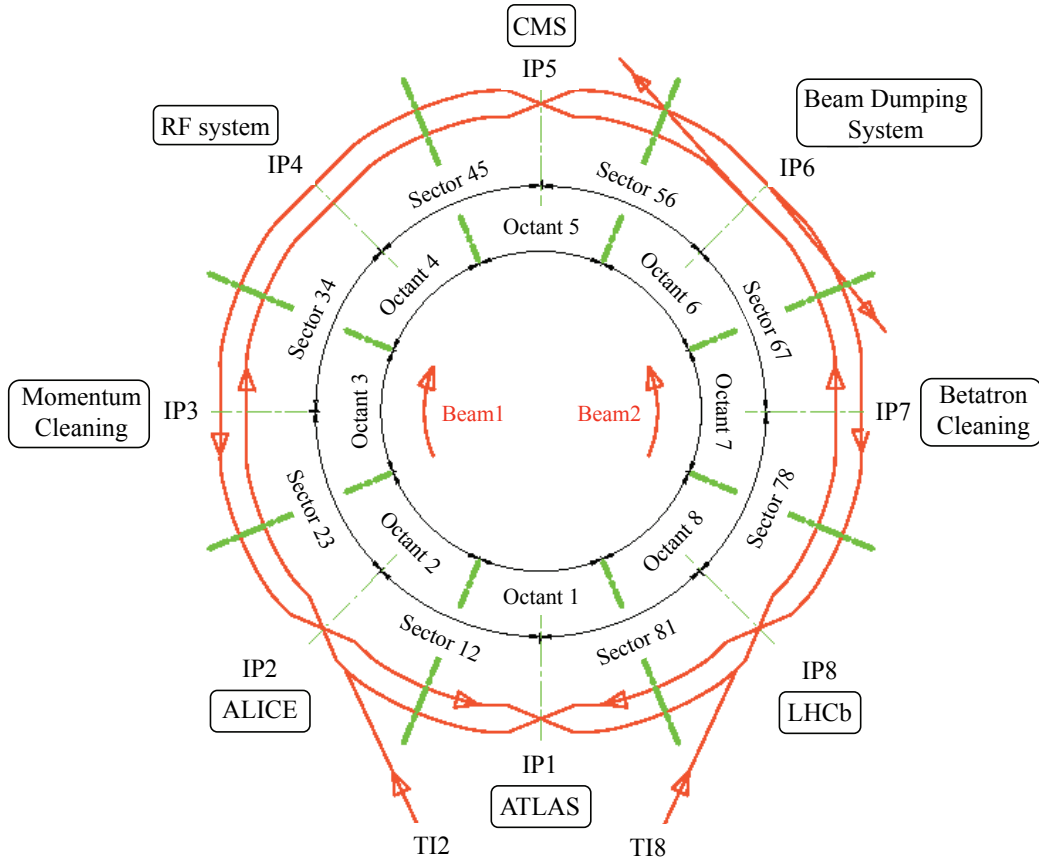
Figure 2.1: Basic layout of the Large Hadron Collider (LHC). Beam 1 circulates clockwise and Beam 2 counterclockwise. Collisions take place in the four interaction regions where experiments are located: ATLAS (IP1), ALICE (IP2), CMS (IP5) and LHCb (IP8).

inverse proportion to the transverse normalized emittance ε_n and the β-function at the IPs (β_z^*) (see 3.1.1). A geometric correction factor F is necessary to take into account the luminosity reduction induced by the crossing angle that is imposed to the colliding bunches in order to avoid parasitic collisions. Table 2.1 lists the beam parameters for nominal machine operation with protons. The LHC is designed to reach a peak luminosity of 10^{34} cm^{-2}s^{-1} in ATLAS [4] and CMS [5]; these are multi-purpose detectors dedicated to investigation of the broadest range of Physics possible and to the Higgs Boson discovery. LHCb [6] is a low luminosity ($\mathcal{L} = 10^{32}$ cm^{-2}s^{-1} for $\beta_z^* = 50$ m) specialized detector with the main aim of explaining the asymmetry between matter and antimatter in the universe by studying the "beauty quark" Physics. Two further experiments TOTEM [7] and LHCf [8], installed upstream and downstream of the high luminosity IPs (IP5 and IP1 respectively), have been devised to detect particles coming out from the experiments with small deviation angles in

Table 2.1: Nominal beam parameters for LHC operation with protons [1].

Protons	Injection	Collision
Energy [GeV]	450	7000
Relativistic γ	479.6	7461
Number of particles per bunch	$1.15 \cdot 10^{11}$	
Number of bunches per beam	2808	
Stored energy per beam [MJ]	23.3	362
Bunch spacing [ns]	25	
Transverse normalized emittance [μm rad]	3.75	
Longitudinal emittance (4σ) [eV s]	1	2.5
Revolution frequency [kHz]	11.245	
$\beta_z{}^*$ at IP1 and IP5 [m]	11	0.55
$\beta_z{}^*$ at IP2 [m]	10	10
$\beta_z{}^*$ at IP8 [m]	10	1$\leftrightarrow$50
Geometric factor at IP1 and IP5	−	0.836
Peak Luminosity in IP1 and IP5 [cm^{-2}s^{-1}]	−	10^{34}

order to measure the elastic scattering cross section. Finally, ALICE [9] is dedicated
to the studies of the "quark-gluon" plasma generated by Lead ion collisions. The
nominal beam parameters for ion operation are summarized in Table 2.2.

Table 2.2: Nominal beam parameters for LHC operation with Lead ions [1]. The
$\beta_z{}^*$ values at the omitted IPs are the same as in table 2.1

Lead ions	Injection	Collision
Energy [GeV]	36900	574000
Energy per nucleon [GeV]	177.4	2759
Relativistic γ	190.5	2963.5
Number of particles per bunch	$7 \cdot 10^7$	
Number of bunches per beam	592	
Stored energy per beam [MJ]	0.245	3.81
Bunch spacing [ns]	100	
Transverse normalized emittance [μm rad]	1.5	
Longitudinal emittance (4σ) [eV s]	0.7	2.5
Revolution frequency [kHz]	11.245	
$\beta_z{}^*$ at IP2 [m]	10	0.5
Geometric factor at IP2	−	1
Peak Luminosity in IP2 [cm^{-2}s^{-1}]	−	10^{27}

2.2   The LHC superconducting magnets

The high beam energy of the LHC can be reached thanks to the use of superconducting magnets for bending and focusing the beams. In the LHC tunnel 1232 main dipoles (MB), 386 main quadrupoles (MQ) plus more than 4000 correctors are operated at cryogenic temperatures of $1.8\,$K and $4.5\,$K. A picture of superconducting magnets in the LHC is shown in Fig. 2.2.

Figure 2.2: Superconducting dipoles in the LHC tunnel.

The superconducting magnets are sensitive against heating from the beam or other sources. They loose their super-conductivity (quench) after an energy deposition per second of $5\,\mathrm{mJ\,cm^{-3}}$ (corresponding to $5\,\mathrm{mW\,cm^{-3}}$) when run at the nominal field for the $7\,$TeV optics (i.e. $8.33\,$T for the MB) and in case of continuous heating [10]. In addition quenches are also provoked by transient heating. The energy required for inducing a quench depends in this case on the loss duration δt: about $30\,\mathrm{mJ\,cm^{-3}}$ are expected to cause a quench at $7\,$TeV if $\delta t \geq 8\,$ms. more details on the quench limit are given in chapter 4.

2.3   The LHC cleaning insertions

The stored energy per beam in the LHC at top energy corresponds to $362\,$MJ for protons and $3.81\,$MJ for ions. The LHC, when operated with protons, exceeds the stored energy handled at TEVATRON (Fermilab, USA) and HERA (Desy, Germany) by 2 orders of magnitude (see Fig. 2.3). The stored energy is about 10 orders of magnitude above the quench limit of the superconducting magnets. Even small
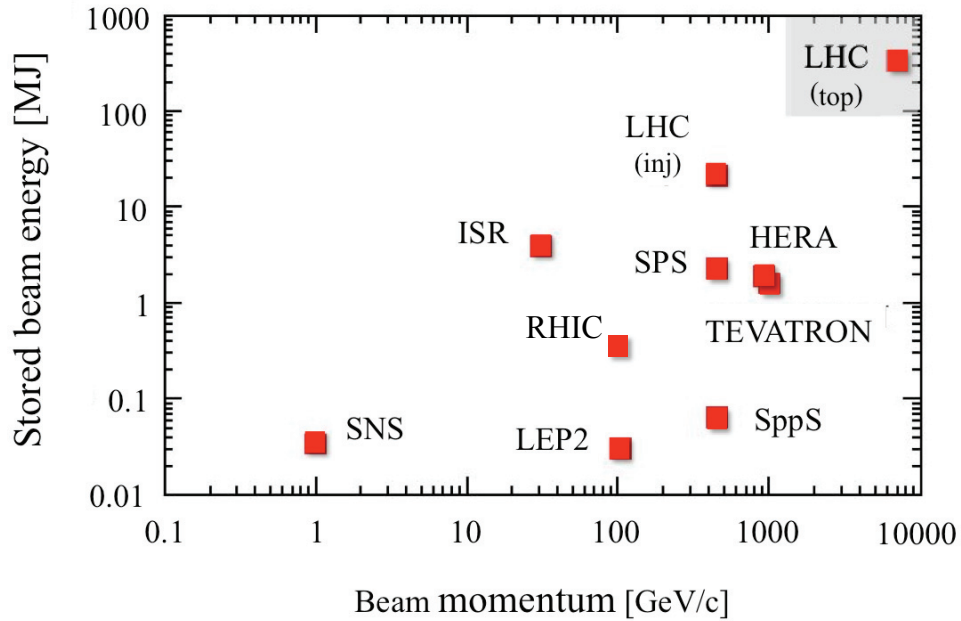
Figure 2.3: Stored beam energy for different proton storage rings [11].

fractional losses of beam can induce quenches. It is then evident that a powerful cleaning system against beam induced losses is needed to avoid quenches of the superconducting magnets. For this reason two machine insertions are dedicated to beam cleaning: momentum cleaning in IR3 and betatron cleaning in IR7. These are insertions without superconducting magnets, where several collimators are installed to intercept and scatter the beam halo particles before they are lost in the superconducting aperture of the machine. A large fraction of the electromagnetic showers, that are generated by interactions of the halo particles with the collimator jaws, is swept away by bending magnets located downstream of the collimators, the so called dogleg magnets [1]. The energy deposition is then concentrated in the cleaning regions where the room-temperature magnets are tolerant to energy deposition. The cleaning insertions are described in detail in chapter 4.

2.4 LHC layout and optics

For the studies presented in this report the version V6.500 of the optics has been used for defining the LHC sequence and the strength of the magnets. The design tune and chromaticity values for this optics are listed in Table 2.3 (see chapter 3 for definitions).

Table 2.3: Nominal horizontal and vertical tunes and chromaticities for the nominal LHC optics at injection and collision energy.

	450 GeV	7 TeV
Q_x	64.28	64.31
Q_y	59.31	59.32
ξ_x	2.00	2.00
ξ_y	2.00	2.00

2.4.1 Nominal optics

The main differences between injection and collision optics in the LHC are the beam crossing and separation schemes and the $\beta_z{}^*$ values at the IPs. The closed orbit between the two beams differs from zero in the four straight insertions dedicated to the experiments. This is done with the purpose of avoiding unwanted parasitic interactions when bringing the beams into collision at the interaction points . At injection energy, this separation is achieved by activating the separation of the beams in the plane that is orthogonal to the one where the collisions take place (see Table 2.4, Fig. 2.4 and Fig. 2.5). A vertical crossing is used for IP1 and IP2 (Fig. 2.4) and a horizontal crossing for IP5 and IP8 (Fig. 2.5). Initially, a 17 m injection $\beta_z{}^*$ was envisaged for IP1 and IP5 and several studies in this report refer to this optics. Recently, an 11 m option for $\beta_z{}^*$ was adopted, when the possibility of performing collisions at injection energy was investigated (see 2.4.2). No significant differences in the loss patterns around the LHC ring were expected and observed in simulations due to this change.

   Table 2.4 shows three different options for machine nominal optics at top energy.

1. The "lowb.coll_all" and the "lowb.all" optics are completely equivalent from the point of view of the collision schemes and they foresee beam impacts at the four IPs.

2. "Lowb.all" is intended mainly for the operation of the machine with heavy ions and has not been used for the studies in this thesis.

3. Finally, collisions are allowed only at the high luminosity interaction points (IP1 and IP5) in the "lowb.coll" case. The spectrometers of Alice and LHCb are switched off. This optics has the same $\beta_z{}^*$ values as the "lowb.coll_all" file.

Table 2.4: Crossing and separation schemes plus $\beta_z{}^*$ values for injection and several collision optics (V6.500).

injection optics					
	Crossing	**Separation**	**Spectrometer**	β^* [m]
				old	**new**
IP1	ON	ON	–	17	11
IP2	ON	ON	OFF	10	10
IP5	ON	ON	–	17	11
IP8	ON	ON	OFF	10	10

lowb.coll_all optics				
	Crossing	**Separation**	**Spectrometer**	β^* [m]
IP1	ON	OFF	–	0.55
IP2	ON	OFF	ON	10
IP5	ON	OFF	–	0.55
IP8	ON	OFF	ON	10

lowb.coll optics				
	Crossing	**Separation**	**Spectrometer**	β^* [m]
IP1	ON	OFF	–	0.55
IP2	ON	ON	OFF	10
IP5	ON	OFF	–	0.55
IP8	ON	ON	OFF	10

lowb.all optics				
	Crossing	**Separation**	**Spectrometer**	β^* [m]
IP1	ON	OFF	–	0.55
IP2	ON	OFF	ON	0.50
IP5	ON	OFF	–	0.55
IP8	ON	OFF	ON	1.00
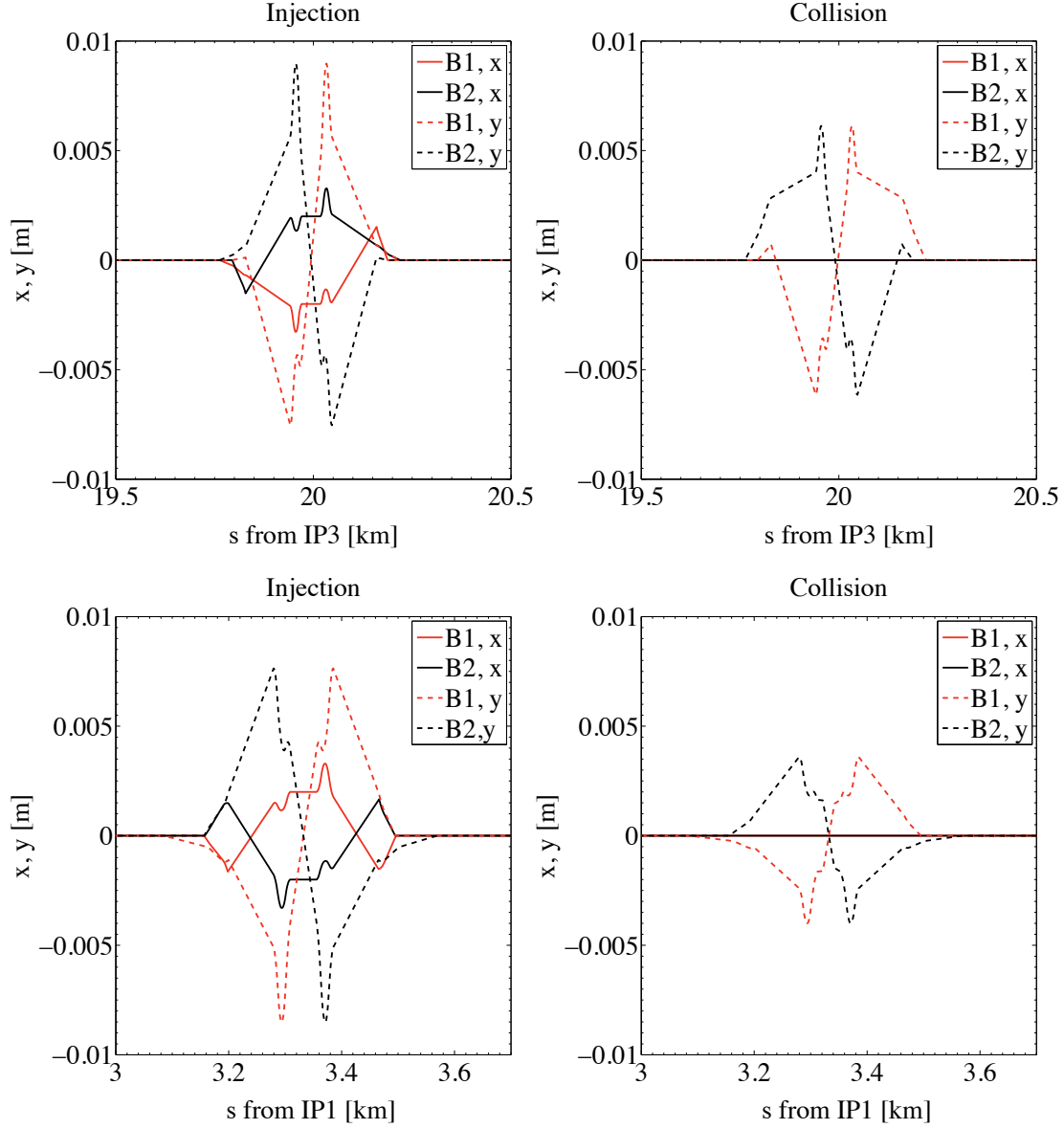
Figure 2.4: Horizontal and vertical orbits of the two beams (Beam 1 red line, Beam 2 black line) at IP1 (top) and IP2 (bottom) for injection (left) and the "lowb.coll_all" collision (right) optics. The s coordinate is following the Beam 1 direction.
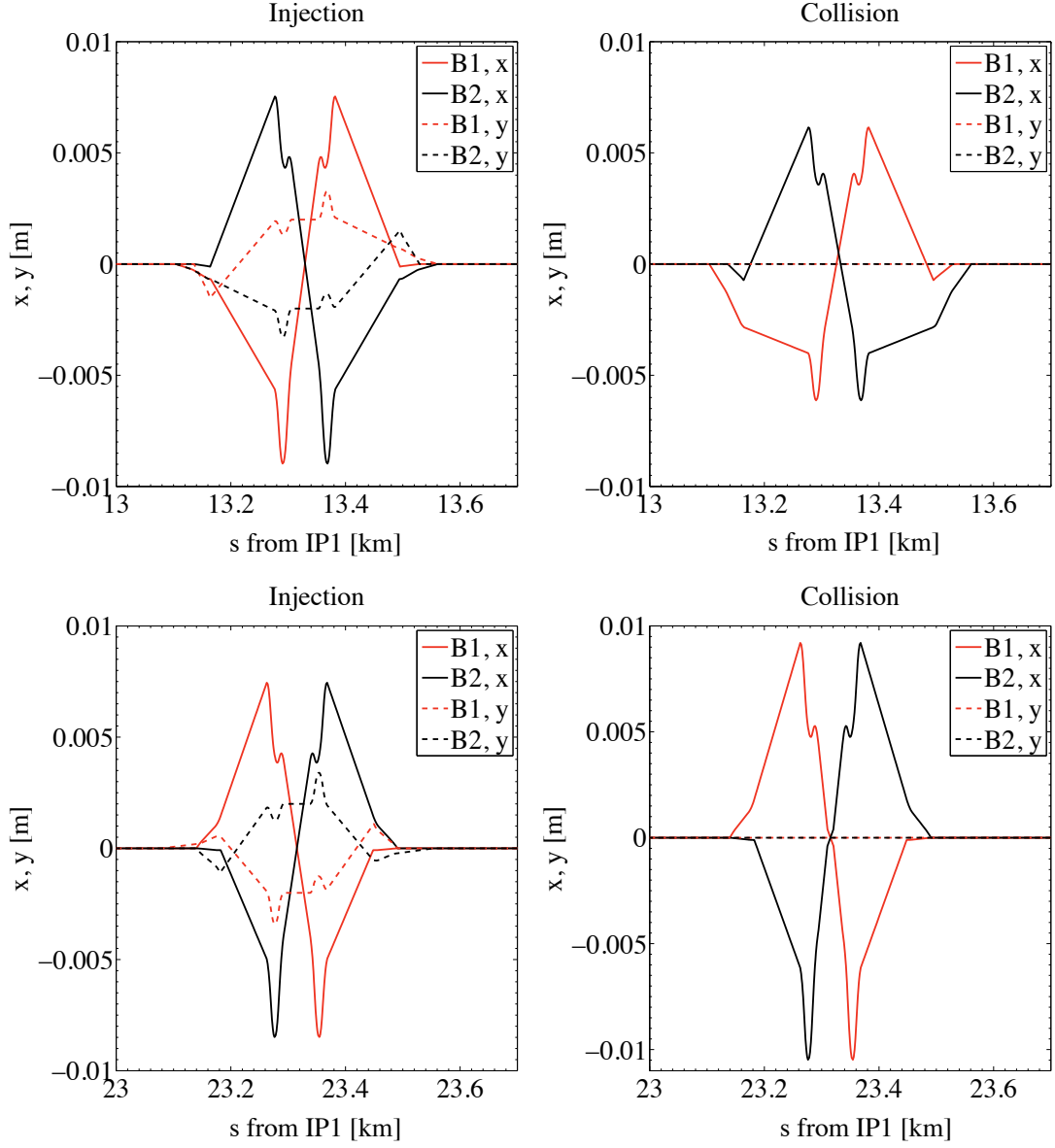
Figure 2.5: Horizontal and vertical orbit for the two beams (Beam 1 red line, Beam 2 black line) at IP5 (top) and IP8 (bottom) for injection (left) and the "lowb.coll_all" collision (right) optics. The s coordinate is following the Beam 1 direction.

2.4.2   Special optics

This PhD work is mainly centred on studying different scenarios for the commissioning of the LHC collimation system. With this scope special optics other than the nominal ones have been analyzed and they are listed in Table 2.5.

Table 2.5: Crossing schemes plus β_z* values for several special optics (V6.500).

Collision at 450 GeV				
	Crossing	**Separation**	**Spectrometer**	β* [m]
IP1	OFF	OFF	−	11
IP2	OFF	OFF	OFF	10
IP5	OFF	OFF	−	11
IP8	OFF	OFF	OFF	10
Energy ramp (from 450 GeV upto 7 TeV)				
	Crossing	**Separation**	**Spectrometer**	β* [m]
IP1	ON	ON	−	11
IP2	ON	ON	OFF	10
IP5	ON	ON	−	11
IP8	ON	ON	OFF	10
Early collision optics (7 TeV)				
	Crossing	**Separation**	**Spectrometer**	β* [m]
IP1	ON	OFF	−	2
IP2	ON	OFF	ON	10
IP5	ON	OFF	−	2
IP8	ON	OFF	ON	2

a) "450 GeV collision optics": the option of bringing the two beams into collision at 450 GeV was considered in view of a possible commissioning of the machine in 2007 at low intensity (43 bunches of $4\cdot10^{10}$ protons each). This should have been an engineering run with the scope of testing the full hardware and calibrating the experiments and the acquisition devices more than performing any Physics studies. Anyway a pre-squeeze of the β_z* from 17 m down to 11 m (IP1 and IP5) was planned and, due to the low intensity, head-on collisions with no crossing angle would have been performed. The beam commissioning, however, was delayed and the 2007 run at 450 GeV was cancelled. The nominal injection optics was since then modified and β_z*=11 m became the standard value for IP1 and IP5. This allows to reduce the number of steps for achieving the nominal squeezed optics and leaves the opportunity open for easily performing collisions at 450 GeV during beam commissioning.

b)"Ramp": After injection the two beams must be accelerated up to 7 TeV and this is one of the most delicate stages of the machine commissioning. Detailed studies were devoted to the definition of the best collimation settings as a function of the beam energy. For this analysis the nominal injection crossing scheme with the new injection $\beta_z{}^*$ values were kept during the full ramp.

c)"Early collision": This optics has the nominal crossing and separation schemes foreseen for the "lowb.coll_all" and the "lowb.coll" files but with $\beta_z{}^*$ values of 2 m in IP1, IP5 and IP8 and of 10 m in IP2. A low intensity machine operation is foreseen for this scenario.

Chapter 3

Theory of Beam Loss and Collimation

Beams in circular accelerators are constituted by bunches of particles that can be described as a statistical distribution of points (typically a Gaussian). The motion of each particle in the horizontal and vertical planes are presented according to basic principles of linear beam dynamics. The transverse oscillation frequencies are much higher than the typical phase oscillation frequency and this allows to treat the longitudinal degree of freedom independently. Particles in the core of the bunch perform stable oscillations but several processes can kick these particles into the tails of the distribution, determining the population of the so called primary halo. Halo particles with high oscillation amplitudes become unstable and are lost at the mechanical aperture of the machine. Moreover, accident scenarios can induce fast losses of a large fraction of the beam particles. A multistage collimation system allows to intercept the halo particles providing halo cleaning and passive protection to the machine.

3.1   Basic linear beam dynamics

3.1.1   Transverse motion

The beam particles in a circular accelerator are guided by dipolar bending magnets, which curve the beam and make it follow the ideal orbit, and by quadrupoles which focus the beam. These magnetic fields are linear and the motion of one particle in the x-y transversal plane [2] is given by the equation:

$$z(s) = \sqrt{\varepsilon_z \beta_z(s)} \cdot \sin\left(\phi_z(s) + \phi_{z0}\right) + D_z(s)\delta_p \qquad (3.1)$$

where z is used from now for either x or y, s is the longitudinal coordinate (see Fig. 3.1), $\delta_p = \Delta p / p$ is the momentum offset and D_z is the dispersion.
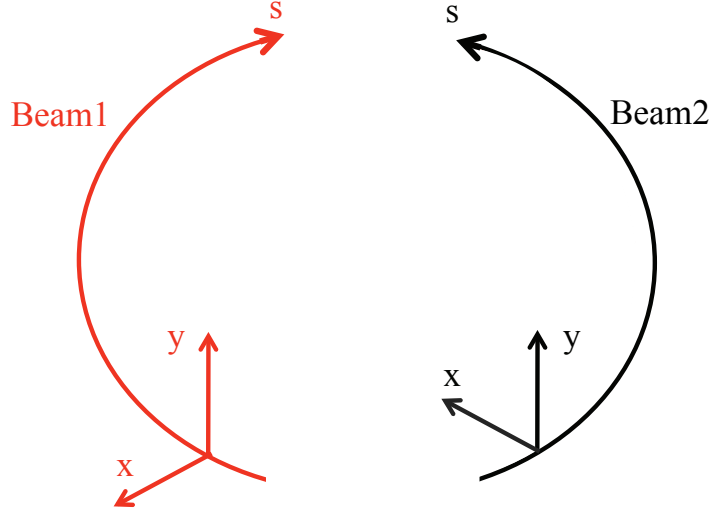
Figure 3.1: Reference frame for Beam 1 and Beam 2 in the LHC. The positive x-axis points outwards with respect to the ring for Beam 1 and inwards for Beam 2.

The first term on the right of eq. 3.1 represents the betatron oscillation function in the selected plane. The optical function β_z gives the amplitude modulation of this oscillation. ϕ_z and ϕ_{z0} are respectively the phase advance and the initial phase of the betatron oscillation and ϕ_z can be defined as:

$$\phi_z(s) = \int_0^s \frac{ds}{\beta_z(s)}. \tag{3.2}$$

The number of betatron oscillations per revolution is calculated dividing the phase advance over one turn by 2π; this quantity is called the machine tune Q_z. The tune must be an irrational number in order to avoid resonances which would amplify any existing perturbation and would induce a growth of the particle oscillation amplitude.

The particle trajectory in the phase space $z - z'$ (with $z'(s) = \frac{dz(s)}{ds}$) is represented by an ellipse of the form:

$$\varepsilon_z = \gamma_z(s)z^2(s) + 2\alpha_z(s)z(s)z'(s) + \beta_z(s)z'^2(s) \tag{3.3}$$

where

$$\alpha_z(s) = -\frac{1}{2}\frac{d\beta_z(s)}{ds} \tag{3.4}$$

and

$$\gamma_z(s) = \frac{1 + \alpha_z^2(s)}{\beta_z(s)}. \tag{3.5}$$

β_z, α_z and γ_z are called the "Twiss parameters" and they define the machine optics. The shape of the ellipse changes at the different s locations while the area $(\pi\varepsilon_z)$ does not change if the energy of the particle is kept constant and stochastic effects are neglected.

A beam is constituted by many particles which can be represented as a statistical distribution of points in the transversal phase space. It is then possible to define a "root mean square emittance" $\varepsilon_{rms,z} = \sqrt{<z^2><z'^2> - <zz'>^2}$ that allows to introduce the "betatronic beam size" σ_z and "divergence" $\sigma_{z'}$ as:

$$\sigma_z(s) = \sqrt{\varepsilon_{rms,z}\beta_z(s)} \tag{3.6}$$

and

$$\sigma_{z'}(s) = \sqrt{\varepsilon_{rms,z}\gamma_z(s)}. \tag{3.7}$$

Generally the beam particles in $z - z'$ are well approximated by a Gaussian distribution; particles within $3\sigma_z$ represent the beam core while the tails of the distribution above $3\sigma_z$ are populated by the beam halo particles. It is also possible to define a quantity called normalized emittance $\varepsilon_{n,z}$ that does not vary with the energy and reads:

$$\varepsilon_{n,z} = \gamma\beta_{rel}\varepsilon_{rms,z} \tag{3.8}$$

with the relativistic factors of $\beta_{rel} = \frac{v}{c}$ (v: particle velocity, c: speed of light in vacuum) and $\gamma = (1 - \beta_{rel}^2)^{-\frac{1}{2}}$.

The second term on the right side of eq. 3.1 is the dispersive orbit and is the product of the periodical dispersion function D_z and the particle momentum offset δ_p. This term vanishes for an on-momentum particle and in the region of the machine with zero dispersion. Off-momentum particles see a quadrupole strength different from the nominal one. This induces a tune spread defined as:

$$\Delta Q_z = \xi_z \frac{\Delta p}{p}. \tag{3.9}$$

The term ξ_z is called chromaticity.

The "beam size" can be defined taking into account this contribution as:

$$\sigma_z^{beam}(s) = \sqrt{\varepsilon_{rms,z}\beta_z(s) + (D_z(s)\sigma_p)^2} \tag{3.10}$$

where σ_p is the rms momentum spread of the beam particles.

3.1.2 Longitudinal motion

The particles in synchrotrons are accelerated by radio frequency (RF) cavities. The electric field inside the cavities varies sinusoidally with angular frequency ω_{RF} and particles must be placed in the accelerating part of the RF period. For this reason

the beam is bunched and ω_{RF} is an integer multiple of the revolution frequency ω_r. A particle with charge q at each passage across a cavity gains an energy

$$\Delta E = q\hat{V} \sin \varphi(t) \tag{3.11}$$

where $\hat{V}$ is the peak accelerating potential of the cavity and φ is the phase of the particle with respect to the RF phase [2]. Particles circulating in the machine are also subject to dissipative phenomena (as for example synchrotron radiation) which contribute to momentum deviation $\Delta p = \Delta E/c$. The length of the orbit L varies as a consequence of the momentum deviation according to:

$$\frac{\Delta L}{L} = \alpha_c \frac{\Delta p}{p} \tag{3.12}$$

where α_c is the "momentum compaction" factor. The ideal particle always crosses the cavity with the same phase φ_s that corresponds to the nominal energy gain and is called "synchronous phase". The other particles of the bunch reach the RF cavity with a small advance/delay with respect to the nominal one and get a different energy gain. The principle determining the longitudinal stability of the bunch is called "phase focusing" [12] and depends for a given particle on the relation:

$$\frac{\Delta T}{T} = \left(\alpha_c - \frac{1}{\gamma^2} \right) \frac{\Delta p}{p} \tag{3.13}$$

with T being the revolution period. Two different regimes are defined by eq. 3.13 if the transition energy $\gamma_{tr} = \sqrt{\frac{1}{\alpha_c}}$ is introduced:

- below transition when $\gamma < \gamma_{tr}$

- above transition when $\gamma > \gamma_{tr}$.

Below transition the stability of the bunch requires $0 < \varphi_s < \pi/2$, which corresponds to the rising part of the sinusoid defined in eq. 3.11 (see Fig. 3.2). In this case more energetic particles reach the cavity earlier than the synchronous one ($\varphi(t) < \varphi_s$) and gain less energy. This implies that these particles will be closer to φ_s at the following passage. On the other hand less energetic particles approach φ_s due to the higher acceleration they get by crossing the RF cavity at $\varphi(t) > \varphi_s$. Analogous arguments allow to establish that the longitudinal stability condition above transition is satisfied if $\pi/2 < \varphi_s < \pi$. Particles with small longitudinal amplitude hence follow bounded trajectories and perform "synchrotron oscillations" around the ideal particle. Their equation of motion is:

$$\ddot{\varphi} + \frac{\Omega_s^2}{\cos \varphi_s} (\sin \varphi - \sin \varphi_s) = 0 \tag{3.14}$$
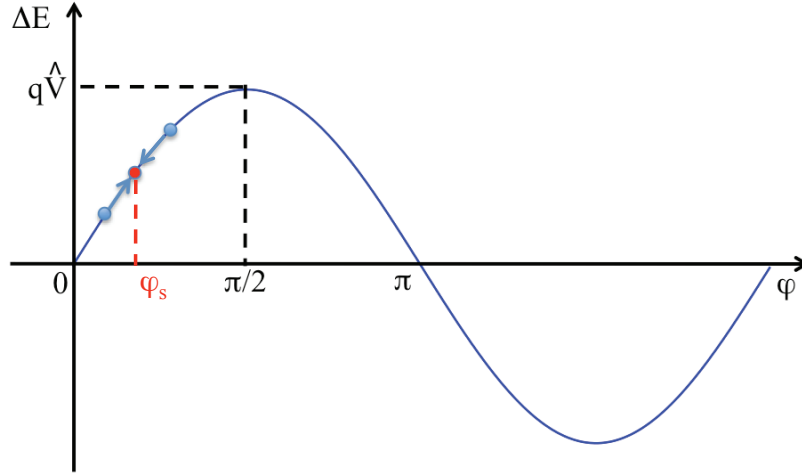
Figure 3.2: Example of phase focusing for particles (blue dots) close to the synchronous one (red dot) in case of operation below transition.

where Ω_s is a constant. This motion is intrinsically non-linear and determines the existence of a trajectory defined as "separatrix" that delimits the region of longitudinal stability: in case of acceleration, particles outside this region lose energy turn by turn and are finally lost. The area in the ΔE-φ phase space enclosed in the separatrix is the "RF bucket" (see Fig. 3.3) while the space occupied by the bunch delimits the "longitudinal emittance" defined as:

$$\varepsilon_s = \pi \sigma_t \sigma_{E_b} E_0. \tag{3.15}$$

σ_t is the bunch length in seconds, σ_{E_b} is the rms energy spread of the bunch particles and E_0 is the nominal energy. The half-height of the RF bucket ΔE_b defines the "energy acceptance" of the machine and reads:

$$\Delta E_b = k'' \cdot \sqrt{1 - \left(\frac{\pi}{2} - \varphi_s\right) \cdot \tan \varphi_s} \tag{3.16}$$

with k'' being a constant. In the LHC, for a 400 MHz RF system, $\Delta E_b = 9.68 \cdot 10^{-4} \, \Delta p/p$ at injection energy of 450 GeV and $\Delta E_b = 3.53 \cdot 10^{-4} \, \Delta p/p$ at 7 TeV [13].

3.2   Aperture and beam stability

The machine aperture is one of the most important parameters for a circular accelerator since it plays a crucial role in beam stability and beam intensity lifetime (see 3.3.1). As an effect of several processes, described in section 3.3, some beam particles drift towards the walls of the machine where they are lost. The loss locations
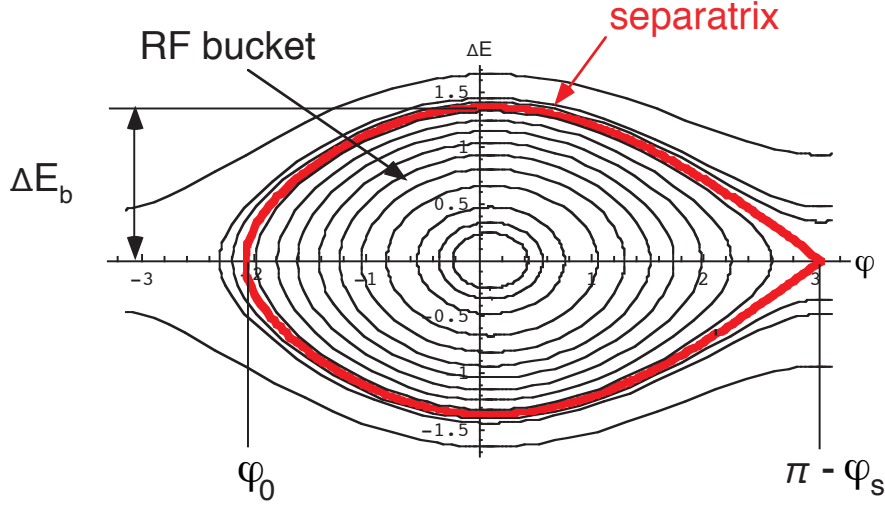
Figure 3.3: Example of trajectories in the longitudinal phase space for accelerated particles. The centre of the RF bucket coincides with the synchronous phase φ_s and the red line defines the separatrix delimiting the region of longitudinal stability. ΔE_b is the half height of the bucket [14].

and the time particles take before being lost depend on the mechanical aperture of the machine and on lattice and beam parameters as described in the following.

3.2.1   Geometrical aperture and beam acceptance

The geometrical aperture A_{geom} of an accelerator is given by the physical space delimited by the vacuum chamber and by the different elements installed along the full length (L_m) of the machine: i.e. beam screens, collimators, diagnostic equipments, etc. In order to avoid losses, the geometric aperture A_{geom} at each location must be bigger than the maximum oscillation amplitude of the beam particles. The maximum emittance that can be accepted by the machine is called "beam acceptance" and is related to the geometrical aperture A_{geom}^z in the considered plane z according to the formula:

$$\varepsilon_z^{max} = min_{s\in[0,L_m]}\left[\frac{(A_{geom}^z(s)- \mid D_z(s)(\Delta E_b) \mid)^2}{\beta_z(s)}\right]. \tag{3.17}$$

Ideally, the vertical plane is dispersion free and the particles follow a pure betatron oscillation. In this case the acceptance depends only on the ratio between the minimum geometrical aperture and the maximum β-function.

3.2.2 Dynamic Aperture

Non-linear magnetic field components are due to unavoidable multipole field errors, to sextupoles, which are used for machine chromaticity correction, and to higher order correctors. The non linear fields act on all the beam particles and their effect increases with the amplitude of the betatron oscillations. Particles with an amplitude bigger than the so called "dynamic aperture" (A_{dyn}) become unstable due to non linearities and are lost after a certain number of turns. This process is called diffusion. Beam core particles are stable and ideally have a constant amplitude $A < A_{geom}$. In reality several processes, described in the next section, transport some particles out of the core. These particles form the primary beam halo which slowly diffuses towards A_{dyn}. Studies for the LHC demonstrated that the particle diffusion speed away from the core of the beam is of the order of 5.3 nm/turn at around $6\sigma_z$ [15].

For an ideal machine we have $A_{dyn} > A_{geom}$ but this is not the case for a non-linear machine like the LHC. Tracking simulations and analytical models allowed to define $A_{dyn} = 12\sigma_z$ at injection energy and $10\sigma_z$ at 7 TeV [16]. For these studies the dynamic aperture was defined as the radius of the maximum area, in the transverse plane, that shows a stable behavior after 10^5 turns (~ 10 s in the LHC).

3.2.3 LHC available aperture

The target aperture for the LHC corresponds to a horizontal and vertical acceptance of $8.4\sigma_z$ (pure betatron) [17]. A model was used to calculate the effective LHC available transverse aperture around the ring. This was done by taking into account the mechanical and optical tolerances listed in Table 3.1 and using the LHC optics version V6.5. Results show that at injection energy (450 GeV) the main aper-

Table 3.1: Mechanical and optics tolerances used to calculate the LHC transverse aperture [18].

Tolerance	Design value
Magnet manufacturing errors	≤1.6 mm
Transverse magnet alignment	≤1.6 mm
Allowance for separation/crossing schemes	≤1.5 mm
Allowance for spurious dispersion	27% of arc (normal.)
Allowance for beam energy offset	0.05%
Allowance for closed orbit (radial), injection	≤4.0 mm
Allowance for closed orbit (radial), collision	≤3.0 mm
Allowance for beta-beat ($\Delta\beta/\beta$)	21%

ture limitations come from the arcs with their superconducting dipole (MB) and

quadrupole (MQ) magnets. At top energy (7 TeV) the arc aperture is no longer crit-

Table 3.2: Minimum horizontal $A_x^{aperture}$ and vertical $A_y^{aperture}$ available aperture at injection and collision optics for warm and cold magnets [18].

		Injection		Collision	
		Warm	**Cold**	**Warm**	**Cold**
Beam 1	$A_x^{aperture}[\sigma]$	6.78	7.88	28.10	8.90
	$A_y^{aperture}[\sigma]$	7.68	7.79	8.34	8.43
Beam 2	$A_x^{aperture}[\sigma]$	6.68	7.70	27.6	8.13
	$A_y^{aperture}[\sigma]$	7.65	7.60	8.69	8.75

ical due to the adiabatic damping of the beam emittance during acceleration. On the other hand, the achievement of the design luminosity requires the squeeze of $\beta_z{}^*$ to 0.55 m in IP1 and IP5. This is obtained by changing the IP optics with dedicated superconducting magnets, called "triplets", where β_z grows up to about 4500 m. The triplets in IR1 and IR5 constitute the aperture bottlenecks for the collision optics. Minimum horizontal and vertical available apertures at injection and collision optics for warm and cold magnets are listed in Table 3.2.

3.3 Beam halo population and beam loss mechanisms

The beam halo particles can be lost at the mechanical aperture of the machine after a certain number of turns. Moreover, the halo is continuously repopulated by particles of the beam which are transported out from the core due to several processes. Some of these processes are induced by normal machine operation (i.e. beam-beam, tune shift, orbit and chromaticity change, etc.) and unavoidable beam dynamics instabilities; in this case we speak about "regular beam losses". When on the other hand accidental beam instabilities and sudden fast increases of beam losses are caused by machine failures or operational errors we refer to "irregular beam losses".

3.3.1 Regular beam losses

The beam intensity N versus time t can be described as:

$$N(t) = N(0) \exp\left(-\frac{t}{\tau}\right).$$ (3.18)

Here, τ is the exponential beam lifetime and gives the time needed to reduce the initial beam population $N(0)$ to a fraction $1/e$. Processes causing regular beam losses are introduced in the following.

3.3.1.1 Intrabeam scattering (IBS)

The IBS process refers to multiple small-angle Coulomb scatterings of particles belonging to the same bunch. A continuous exchange of energy between the interacting particles induces the coupling of horizontal, vertical and longitudinal emittances [19]. The evolution of the bunch depends on the initial energy: below transition (see 3.1.2) the motion is bounded and the increase of beam size in one direction is compensated by a decrease in the other two dimensions. Above transition no equilibrium condition exists and the bunch emittance increases continuously in all directions. This is the case for the LHC that works above transition already at injection energy (γ_{tr}=55.68). Growth times τ_{trans} and τ_{long} for the transverse and longitudinal emittances at injection and collision energy are listed in Table 3.3. These values have been computed using the Bjorken-Mtingwa theory implemented in the "MAD-X" optics code [20]. According to this theory the IBS growth rate in longitudinal and transverse planes can be defined for a Gaussian beam as [21]:

$$\frac{1}{\tau_{long}} = \frac{1}{\sigma_p}\frac{d\sigma_p}{dt} \qquad\qquad \frac{1}{\tau_{trans}} = \frac{1}{\varepsilon_z^{1/2}}\frac{d\varepsilon_z^{1/2}}{dt}. \qquad (3.19)$$

Table 3.3: Typical transverse and longitudinal emittance growth times induced by the intrabeam scattering process in the LHC at injection and collision energy [1].

	τ_{trans}[hours]	τ_{long}[hours]
450 GeV	38	30
7 TeV	80	61

If the energy transfer from the transverse to the longitudinal plane is big enough to remove particles from the longitudinal dynamic aperture we speak of the **Touschek effect**. The bunch population N_b decreases in time t according to [22]:

$$N_b(t) = N_b(0)\frac{1}{1 + \alpha N_b(0)t} \qquad (3.20)$$

while the number of RF uncaptured particles increases as:

$$N_{coast}(t) = N_b(0)\frac{\alpha N_b(0)t}{1 + \alpha N_b(0)t} \qquad (3.21)$$

creating the so called "coasting beam". The Touschek lifetime can then be defined as $\tau_{Touschek} = \frac{1}{\alpha N_b(0)}$ where α is a constant value which depends on the shape of the beam. Values for the LHC are listed in Table 3.4 and refer to a round beam.

Table 3.4: Typical values for $\tau_{Touschek}$ for the LHC at injection and collision energy. These values are calculated for a round beam [22].

	$\tau_{Touschek}$ [hours]
450 GeV	4830.9
7 TeV	12077.3

3.3.1.2   Scattering with residual gas molecules

Elastic and inelastic interactions can occur between the circulating protons and the nuclei of the gas molecules left in the vacuum chamber. This process creates losses of primary and secondary (in case of inelastic interaction) particles and emittance growth. Amount and location of the losses depend on the local density n_g of the residual gas, that must be low enough to limit the heat load induced by such losses. Hydrogen is expected to be the dominant residual gas in the LHC and a density of H_2 molecules of $1.2 \cdot 10^{15} \, \mathrm{m}^{-3}$ is required for a beam lifetime of 100 hours and a maximum heat load of $0.1 \, \mathrm{W \cdot m^{-1}}$ [1]. The relation between beam lifetime due to beam-gas interactions τ_g and n_g is given by [23]:

$$\frac{1}{\tau_g} = c \sum_i \sigma_i n_i \tag{3.22}$$

where the sum is evaluated over the different species of gas present in the vacuum chamber and σ gives the total cross section for the different interactions.

3.3.1.3   Beam-beam effects

In case of head on collisions, elastically scattered particles can populate the beam halo provoking a transversal emittance growth. Moreover, proton-proton collisions are the main cause for the decay of the luminosity that varies in time as [1]:

$$\mathcal{L}(t) = \frac{\mathcal{L}(0)}{1 + \frac{t}{\tau_0}} \tag{3.23}$$

where the initial decay time τ_0 is given by:

$$\tau_0 = \frac{N(0)}{\mathcal{L}(0)\sigma_{tot}k}. \tag{3.24}$$

Here σ_{tot}=10^{-25} cm^{-2} is the total cross section at 7 TeV, taking into account both elastic and inelastic interactions, and k is the number of interaction points. The high luminosity IPs (IP1 and IP5) give the biggest contribution to the luminosity degradation and $\tau_0 = 44.85$ hours can be calculated using the parameters reported in Table 2.1. The time needed to reduce the initial luminosity to a fraction $1/e$ defines the luminosity lifetime which for the LHC corresponds to 29 hours (only beam-beam contribution). Long range electromagnetic interactions between the two beams in the four interaction regions can also induce emittance growth, beam lifetime limitation and instabilities. These are non linear interactions, inducing a tune spread both in the x and y planes that can lead to resonance-related losses of particles. Moreover, long range beam-beam interactions reduce the dynamic aperture.

3.3.1.4   Synchrotron radiation

Synchrotron radiation is an electromagnetic radiation emitted by ultrarelativistic particles when bent by electromagnetic fields. The synchrotron radiation is emitted forward tangentially to the particle trajectory and a fraction of the particle energy is lost in the same direction. The amount of energy lost per turn is [24]:

$$U_0 = \frac{e^2 \beta^3 \gamma^4}{3\varepsilon_0 \rho}, \tag{3.25}$$

where e is the electron charge, ε_0 is the vacuum dielectric constant and ρ is the bending radius. In the LHC at 7 TeV one finds U_0=6.7 keV (ρ=2803.95 m) that corresponds to a total power irradiated per beam of 3.9 kW. Synchrotron radiation stays negligible at injection with U_0=0.11 eV and an irradiated power of 66 mW per beam [1]. The RF cavities have to compensate this energy loss but the acceleration is purely longitudinal: the transverse components of the momentum are not increased after the passage through the cavities and the motion in the x-y plane is adiabatically damped. The emittance damping time τ_ε due to synchrotron radiation for a circular proton machine can be expressed as [25]:

$$\tau_{\varepsilon_j} = \frac{16644}{J_j E\, B^2} \cdot \frac{C}{2\pi\rho} \tag{3.26}$$

where the energy is in units of TeV and the magnetic field is in T. C is the machine circumference. The term J_j is the "Damping partition number" [26] for the three space coordinates and is $J_x \approx 1$, J_y=1 and $J_s \approx 2$. Transverse and longitudinal damping time for the LHC at top energy are $\tau_{\varepsilon_{x,y}}$=26 hours and τ_{ε_s}=12.9 hours [1].

Synchrotron radiation damping can partially compensate the emittance growth induced by other phenomena. The general assumption for the LHC is that this process just cancels the beam blow up caused by beam beam interactions and RF noise. The remaining loss mechanisms (IBS, scattering with residual gas, beam-beam collisions) reduce the assumed luminosity lifetime defined in 3.3.1.3 to about 15 hours.

3.3.1.5   Operational losses

The experience shows that accelerator operation induces losses due to unavoidable machine optimization. For example, tune optimization, orbit correction, chromaticity changes etc. will occasionally induce transient lifetime reduction during optimization. Such losses are considered as regular.

3.3.2   Irregular beam losses

In case of equipment failures or operational errors a fast increase of the intensity loss rate can occur.

3.3.2.1   Fast losses from injection errors

During injection the beam is transferred from the "Super Proton Synchrotron" (SPS) to the LHC. Transverse and longitudinal matching between the end of the transfer line and the injection point is required. A transverse mismatch of the beam (different Twiss parameters) can cause a significant increase in the emittance. Parts of the beam can be lost in a few turns. In addition, particles injected outside of the RF bucket (longitudinal mismatch) are lost at the high dispersion regions when the energy ramp starts.

Fast transient losses can also be induced by misfiring or power failure of the injection kicker magnets [27]. In this case, the design orbit changes both for the injected and circulating particles. The full injected batch (288 bunches) can be instantaneously deflected on any downstream aperture limit. Protection elements and collimators are designed to safely abort fast losses from injection errors.

3.3.2.2   Fast losses from unsynchronised beam abort

The LHC beam dumping system is formed by 15 extraction kicker magnets MKD which deflect horizontally the beam towards a set of 15 steel septum magnets MSD [29] before it is dumped onto special graphite absorber blocks TED. Dilution kickers paint the beam on the TED block in order to reduce energy density. The filling pattern in the LHC is constituted by batches of 72 consecutive bunches, with two bunches separated by 25 ns. The abort gap is defined as the unfilled space between the first and the last injected batch and corresponds to $3\,\mu$s. All the MKDs must be triggered simultaneously and with the correct phase with respect to the beam abort gap. The accelerator components located downstream of the extraction region can be exposed to beam losses in case of an asynchronous beam dump. Such an event is assumed to happen with a rate of one per year. Several failure scenarios can induce abnormal beam dumps:

- All 15 MKDs are triggered at the same time but they are not synchronized with respect to the abort gap. The beam enters in the extraction region when

the kicker voltage is still rising and part of it is swept across the machine aperture.

- One of the MKDs fires spontaneously and induces a re-triggering of the remaining modules. This is the worst case in term of beam load on the downstream components. For the LHC the re-triggering time is $1.2\,\mu$s at injection and $0.7\,\mu$s at collision energy.

In addition, un-captured particles can populate the abort gap and be lost downstream of the dump insertion, even in case of normal operation of the extraction kickers.

3.3.2.3   Losses from other failures

Injection and extraction errors are fast "single turn" processes and the only solution to avoid damage is to protect sensitive regions of the machine with special absorbers and collimators. Errors and malfunctions of various other equipments can produce slower losses (from few turns up to seconds) [30]. Examples are: quenches of a superconducting magnet, problems with the RF system, vacuum leaks, wrong movement of movable components (collimators, experimental detectors, trip of a power converter for superconducting or warm magnets etc.). In this case a dedicated detection system (Beam Loss Monitors BLM) allows to monitor beam losses around the ring and to trigger a beam abort when losses surpass a certain threshold. About 4000 BLMs are installed along the LHC ring and close to elements which are good candidates for losses (collimators, machine aperture bottlenecks). The majority of the detectors ($\sim$3500) of the BLM system consist of ionization chambers, whereas secondary emission monitors SEM are foreseen for regions with very high loss rate [31], like the collimators.

3.4   Interaction of protons with jaw material

Halo particles intercepted by the material of collimator jaws undergo different kinds of interactions:

1. Particles can lose part of their energy by **ionization** and **excitation** [32] of the atoms of the material they are passing through. The average lost energy rate per unit length $-\frac{dE}{dx}$ is called "stopping power" and is defined, in units of MeV·g^{-1}·cm^2, by the Bethe-Bloch equation:

$$-\frac{dE}{dx} = Kz^2\frac{Z}{A}\frac{1}{\beta_{rel}^2}\left[\frac{1}{2}ln\frac{2m_ec^2\beta_{rel}^2\gamma^2T_{max}}{I^2} - \beta_{rel}^2 - \frac{\delta}{2}\right]. \qquad (3.27)$$

Here K is a constant, Z and A are atomic number and atomic mass of the target material, m_e is the electron mass while z, β_{rel} and γ are respectively

charge, velocity and relativistic factor of the incident particle. I is the mean excitation energy[1] , T_{max} is the maximum kinetic energy that an electron can gain in one single collision and finally δ is a correction term depending on the density of the material [32]. Stopping powers for several materials implemented in the used tracking code (see Chapter 5) are presented in Table 3.5 [33]. These values refer to injection energy. Small changes are expected for the 7 TeV case, due to the slow relativistic rise of the $-\frac{dE}{dx}$ curves at high energy.

Table 3.5: Stopping power for several materials implemented in the tracking code. The unit of the stopping power is determined by taking into account the correction factor δ.

Material	dE/dx [GeV/m]
Beryllium	0.55
Graphite	0.68
Alluminium	0.81
Copper	2.69
Tungsten	5.79
Lead	3.40

2. **Multiple Coulomb Scattering (MCS)** with nuclei of the material atoms. The particle experiences numerous small deviations (see Fig. 3.4) and the r.m.s
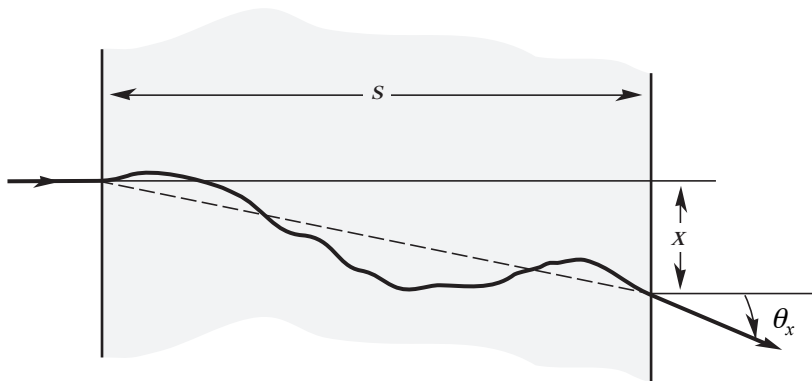
Figure 3.4: Example trajectory of one particle experiencing Multiple Coulomb Scattering while crossing a block of material of thickness s. The particle exits from the block with a deflection angle θ_x.

---

[1]"I is taken as (10±1 eV)·Z for elements heavier than Oxygen" [33]

deflection angle θ_x, after having crossed a thickness of material s, is given by (Molière's theory [34]):

$$\theta_x(s) = \frac{13.6\,MeV}{\beta_{rel}cp}z\sqrt{\frac{s}{X_0}}\left[1 + 0.038\ln(\frac{s}{X_0})\right].\qquad(3.28)$$

Here, p is the momentum of the incident particle while X_0 is the radiation length of the material and is defined as "the main distance over which a high-energy electron loses $1/e$ of its energy by bremsstrahlung, and $7/9$ of the mean free path for pair production by a high-energy photon" [32]. In Table 3.6 values of X_0 are listed for several materials [33].

Table 3.6: Radiation length for several materials implemented in the tracking code.

Material	X_0 [cm]
Beryllium	35.28
Graphite	18.80
Alluminium	8.90
Copper	1.43
Tungsten	0.35
Lead	0.56

3. **Rutherford Scattering (RS)**: The particle acquires a large deflection angle as a consequence of an interaction with a nucleus. Defining the momentum transfer $t = p \cdot \theta$, we have that the Rutherford scattering process becomes dominant for $t \geq t_{cut}$=0.998·10^{-3} GeV^2. The differential cross section for this process is [33]:

$$\frac{d\sigma_{RS}}{dt} = 4\pi\alpha^2(\hbar c)\frac{Z^2}{t^2}\exp(-0.856 \cdot 10^3 \cdot t \cdot R^2)\qquad(3.29)$$

where $\alpha \approx 1/137$ is the fine-structure constant and $R \approx 1.2 \cdot 10^{-15} \cdot A^{1/3}$ is the radius of the nucleus.

4. **Proton-nucleon pn interactions**: Here we refer both to proton-proton and proton-neutron interactions. The relative cross-sections at injection and collision energy for elastic σ_{pn}^{el} and inelastic σ_{pn}^{inel} interactions are listed in Table 3.7 [35]. A special case is represented by **single diffractive scattering SD** [36] (σ_{pn}^{SD}): This is a quasi-elastic process where momentum transfer during collision implies a high mass excitation state for one of the interacting particles. Particles experiencing SD scattering have a non-zero probability to

Table 3.7: Cross-sections for point like interactions between a proton and a nucleon.

Energy [TeV]	σ_{pn}^{el} [mbarn]	σ_{pn}^{inel} [mbarn]	σ_{pn}^{SD} [mbarn]
0.45	7	33	3.15
7	7.98	38.9	4.9

escape from the collimator jaw and to contribute to the population of the off-momentum halo, even if particles were on-momentum originally.

5. **Proton-nucleus pN interactions**: The total cross-section σ_{pN}^{tot} for this kind of interaction scales with the atomic mass as $A^{0.77}$ [37] and is given by the sum of the elastic and inelastic contributions (σ_{pN}^{el}, σ_{pN}^{inel}). Elastic and SD scattering due to the interaction of the halo proton with the outer nucleons must be added. These are obtained by multiplying σ_{pp}^{el} and σ_{pp}^{SD} with $n_{eff}(A) = 1.6 \cdot A^{1/3}$ [38]. Cross section values used in the tracking code are listed in Table 3.8 [14, 33]. These values are valid in the range between 20 and 240 GeV but only minor changes are expected for higher energies [37].

Table 3.8: Cross-sections for pN interactions and Rutherford scattering for several materials included in the tracking code.

Material	σ_{pN}^{tot} [barn]	σ_{pN}^{inel} [barn]	σ_{RS} [mbarn]
Beryllium	0.268	0.199	0.035
Graphite	0.331	0.231	0.076
Alluminium	0.634	0.421	0.34
Copper	1.232	0.782	1.53
Tungsten	2.767	1.65	7.68
Lead	2.960	1.77	9.07

3.5 Theory of multistage betatron and momentum collimation

Collimators consist of blocks of material, called jaws, which are placed between the beam and the mechanical aperture of the machine to intercept halo particles. The distance between the beam axis and the surface of the jaws defines the collimator half-gap. Primary collimators are the closest elements to the beam and they have

to intercept the primary halo particles without interfering with the motion of the core particles. Protons scattered by the primary jaws form the secondary halo and must be intercepted before they reach the cold aperture of the machine. For this reason secondary collimators are installed downstream of the primaries, creating a so called "two-stage cleaning system". The half-gap of the secondary jaws (n_2 in σ_z units) must be larger than the half-gap of the primary (n_1 in σ_z units) so that only protons which experienced an interaction with the primaries are caught. The mutual retraction must be fixed, taking into account a safety margin for machine errors (closed orbit, beta-beat), to avoid that a secondary collimator starts intercepting the primary halo, as no further protection behind is "a priori" foreseen. The tertiary halo, populated by protons outgoing from the secondary collimators, can be lost in the machine cold aperture and must be minimized in order to avoid quenches of superconducting magnets. Further absorbers and protection elements can be implemented in the most sensitive regions of the machine.

A multistage collimation system is needed both for betatron and momentum halo cleaning; principles and optimization of these processes are presented here.

3.5.1   Betatron cleaning

The betatron cleaning system allows to limit the transverse extension of the beam halo by "cleaning" particles with large betatron oscillation amplitude. Studies are performed for a linear uncoupled optics. The normalized coordinates Z and Z' are used, where:

$$
\begin{pmatrix} Z \\ Z' \end{pmatrix} = \frac{1}{\sigma_z} \begin{pmatrix} 1 & 0 \\ \alpha_z & \beta_z \end{pmatrix} \begin{pmatrix} z \\ z' \end{pmatrix}.
$$

In addition, the aperture of the collimators is assumed to be small enough that the halo particles drift slowly towards the jaws. Particles which, at the phase location of the primary collimator, have $Z = n1$ and $Z'=0$ hit the collimator as shown in Fig. 3.5. In case of a slow diffusion, the impact parameter, defined as the transverse offset between the jaw surface and the impact point, is much smaller than n_1 and can be neglected. Escaping particles receive a deflection k, due to the effect of the elastic interactions inside the jaw.

3.5.1.1   One-Dimensional collimation

As a first approximation only the scattering in the same plane of the analyzed halo is considered. The kick can be positive or negative (case a and b in Fig. 3.5) and can have different size. The scattered particles are distributed along the lines defined by $Z = n1$ and either $Z'>0$ (positive kicks) or $Z'<0$ (negative kicks). Two secondary jaws are necessary to intercept scattered particles: one located at a phase advance μ_1 to catch positively kicked particles, and one at μ_2 for negatively kicked ones (see Fig. 3.6).
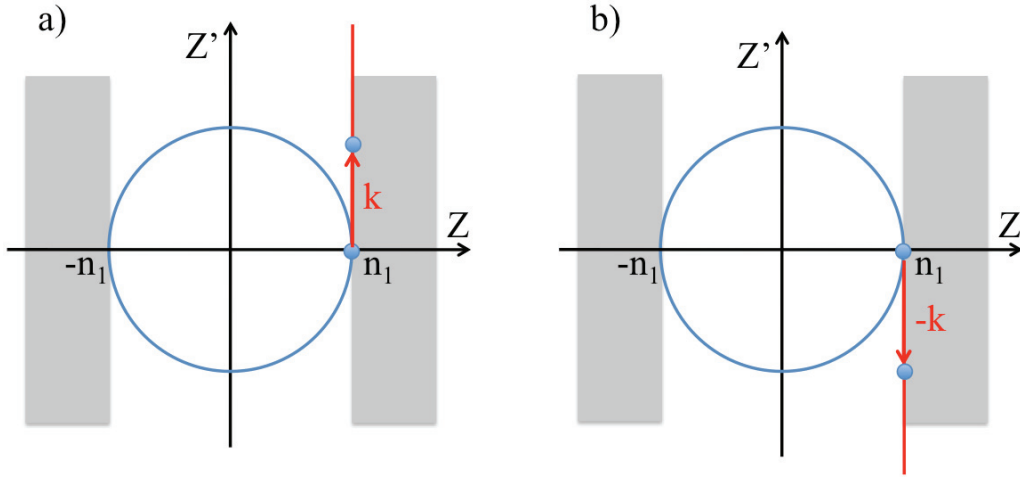
Figure 3.5: A particle hitting a primary collimator, set with an opening of $n_1 \sigma_z$, is plotted in the transverse normalized phase space. The particle can receive a positive (a) or negative (b) kick k in the same plane of its motion. The red lines represent particles receiving different kicks.
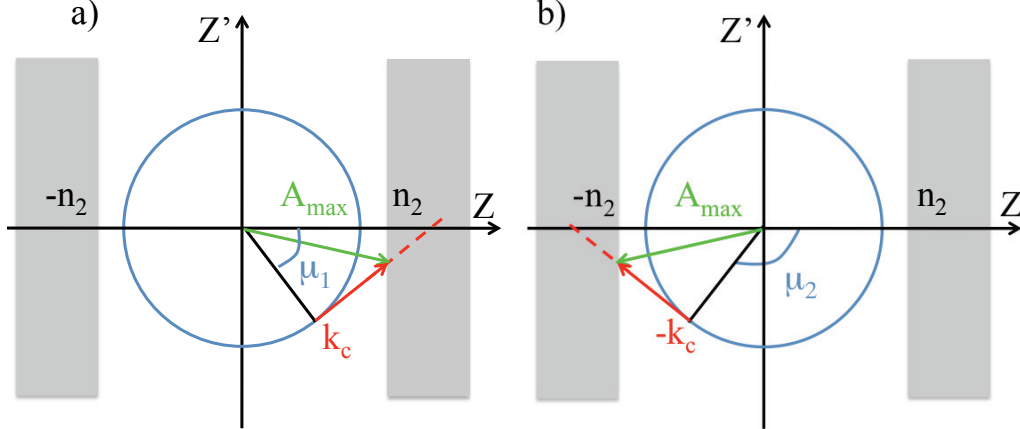
Figure 3.6: Two secondary collimator jaws, located at a phase advance μ_1 and μ_2 with respect to the primary, are necessary to catch particles which received positive (a) and negative (b) kicks. Critical kick and maximum amplitudes defining escaping particles are indicated.

The collimator jaws intercept only particles having excursions $Z > n_2$ at μ_1 and $Z < -n_2$ at μ_2 (see Fig. 3.6), determining the existence of a critical kick k_c [39] defined as:

$$k_c = \frac{n_2 - n_1 \cos \mu}{\sin \mu}. \tag{3.30}$$

Secondary halo particles with $k <\mid k_c \mid$ are not captured by the collimators. k_c must be minimized in order to reduce as much as possible the maximum amplitude $A_{max} = \sqrt{n_1^2 + k_c^2}$ of the escaping particles. This can be done by optimizing the phase advance μ, since n_1 and n_2 are fixed. Optimal values for μ and k_c can be derived:

$$\mu_{opt} = \cos^{-1}\left(\frac{n_1}{n_2}\right) \tag{3.31}$$

$$k_{c,opt} = \sqrt{n_2^2 - n_1^2}. \tag{3.32}$$

Here, $\mu_1 = \mu_{opt}$ and $\mu_2 = \pi - \mu_{opt}$ guarantee that only particles with $A_{max} <\mid n_2 \mid$ do not interact with the secondary jaws. The minimum deflection $\delta z'$ required from a primary collimator such that the deflected particle is intercepted by a secondary collimator can be defined from eq. 3.32 (transforming back to real space coordinates):

$$\delta z' \approx \frac{\sigma_z}{\beta_z}\sqrt{n_2^2 - n_1^2}. \tag{3.33}$$

Analogous considerations can be applied to particles impacting on a primary jaw set at $-n_1$. In this case an efficient cleaning requires one secondary jaw at $\pi - \mu_{opt}$ for positive kicks and one at μ_{opt} for negative kicks. Even if in principle only one primary jaw per plane is needed, the LHC collimators use two jaws, centered with respect to the closed orbit, in order to insure a more stable cleaning and machine protection. Calculated values of μ_{opt} and $\delta z'$ for the LHC are listed in Table 3.9 (see Table 4.5 for n_1 and n_2 values at injection and top energy).

Table 3.9: Values for μ_{opt} and $\delta z'$ for the LHC at injection and top energy.

	μ_{opt}[deg]	$\delta z'[\mu$rad]
Injection	30	23
Top energy	30	6

3.5.1.2 Two-Dimensional collimation

A full decoupling between horizontal and vertical halo is unrealistic and skew primary collimators are necessary to catch particles having large horizontal and vertical excursion at the same time. Moreover, particles interacting with a collimator jaw are scattered isotropically in the transverse plane and further secondary collimators have to be installed at defined phase advances and azimuthal orientations (see Fig. 3.7).
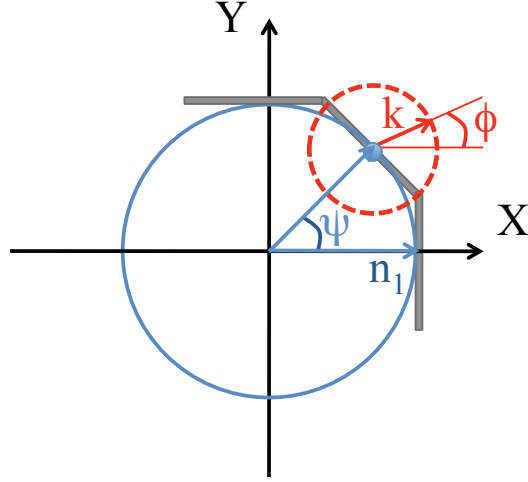
Figure 3.7: Impact on a skew primary collimator at coordinates (n_1, ψ). The scattering in the X'-Y' plane is expressed with polar coordinate (k, ϕ) and is superimposed to the X-Y plane (normalized coordinates). Impacting particles can be scattered isotropically to any ϕ with different kicks k.

Theoretical and numerical optimization studies allowed to estimate a total number of four secondary jaws per each primary jaw. Table 3.10 lists the optimum phase location (μ_x and μ_y) and the jaw orientation (ψ_{sec}) of the required secondary collimators [40]. The same definition of μ_{opt} as for the 1D case is still valid. Scattering in the planes parallel and orthogonal to the primary jaws were considered as extreme cases.

3.5.2   Momentum cleaning

The momentum cleaning system catches the "longitudinal" losses induced by off-momentum particles. While a pure betatron cleaning is achievable in regions of the machine with dispersion close to zero, off-momentum particles have generally a non negligible betatron component as well. Momentum cleaning is needed only in the horizontal plane since the horizontal dispersion is much larger than the vertical one. Normalized coordinates are used:

$$\begin{pmatrix} \chi \\ \chi' \end{pmatrix} = \frac{1}{\sigma_x} \begin{pmatrix} 1 & 0 \\ \alpha_x & \beta_x \end{pmatrix} \begin{pmatrix} D_x \\ D'_x \end{pmatrix}.$$

The trajectory of an off-momentum particle impacting on a primary horizontal jaw is shown in Fig. 3.8. The momentum collimators should not intercept particles which are in the RF-bucket and have stable betatron oscillation below the cut of the betatron collimators. This is avoided by placing the momentum primary collimator

Table 3.10: Optimal secondary collimator jaw phase locations and orientations evaluated for horizontal, skew and vertical primary jaws in case of parallel and orthogonal scattering [40]. Here, μ_{opt} was evaluated for the 1D case and is defined in eq 3.31.

	ψ	ϕ	μ_x	μ_y	ψ_{sec}
Horizontal	0	0	μ_{opt}	$-$	0
	0	π	$\pi - \mu_{opt}$	$-$	0
	0	$\pi/2$	π	$3\pi/2$	μ_{opt}
	0	$-\pi/2$	π	$3\pi/2$	$-\mu_{opt}$
Skew	$\pi/4$	$\pi/4$	μ_{opt}	μ_{opt}	$\pi/4$
	$\pi/4$	$5\pi/4$	$\pi - \mu_{opt}$	$\pi - \mu_{opt}$	$\pi/4$
	$\pi/4$	$3\pi/4$	$\pi - \mu_{opt}$	$\pi + \mu_{opt}$	$\pi/4$
	$\pi/4$	$-\pi/4$	$\pi + \mu_{opt}$	$\pi - \mu_{opt}$	$\pi/4$
Vertical	$\pi/2$	$\pi/2$	$-$	μ_{opt}	$\pi/2$
	$\pi/2$	$-\pi/2$	$-$	$\pi - \mu_{opt}$	$\pi/2$
	$\pi/2$	π	$\pi/2$	π	$\pi/2 - \mu_{opt}$
	$\pi/2$	0	$\pi/2$	π	$\pi/2 + \mu_{opt}$
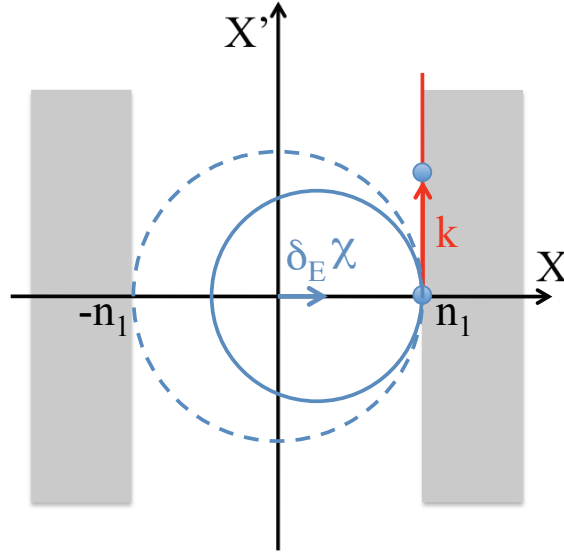
Figure 3.8: The trajectory of an off-momentum particle impacting on a primary horizontal jaw is shown in the normalized phase space. The centre of the circular trajectory is shifted due to the effect of the normalized dispersion χ and of the particle energy offset δ_E.

at a place of the maximum dispersion. A two-stage cleaning system must be implemented also for momentum cleaning and four secondary collimators are needed.

The critical kick does not depend on the energy offset when:

$$\chi' = 0, \tag{3.34}$$

or, in real space coordinates,

$$D'_z = -\frac{\alpha_z}{\beta_z} D_z \tag{3.35}$$

at the location of the primary collimator [39]. In this case the optimum phase advance of the secondary collimators with respect to the primary collimator is the same for all off-momentum particles. The conditions defined for the pure betatron cleaning are applicable also in this case.

Chapter 4

The LHC Collimation System

Collimators in proton machines were historically used to reduce the radiation background at the experiments. The high energy and intensity reached in the LHC and the use of superconducting technologies require a sophisticated collimation system for beam cleaning and machine protection. Two straight sections of the LHC ring are dedicated to momentum (IR3) and betatron (IR7) cleaning. Moreover, additional protection devices are installed upstream of the most sensitive components of the machine. Different materials, length and settings have been chosen for various collimator types, depending on their function. Several implementation phases are foreseen to follow the increase in machine performance. The cleaning insertions and the main characteristics of the LHC collimators are presented in this Chapter.

4.1 Design goals of the LHC collimation system

The energy stored in the LHC at $7\,\mathrm{TeV}$ would be sufficient to melt $500\,\mathrm{kg}$ of Copper. Such a high power must be controlled in a superconducting environment so that tight limitations are imposed on the amount of beam that can be lost. About 10^{-9} of the total beam power can induce the quench of a superconducting magnet. A sophisticated system of collimators has been designed for the LHC to provide:

1. Beam cleaning, to intercept efficiently the unavoidable particle losses due to the continuous population of the beam halo.

2. Passive machine protection, to protect the accelerator against losses following equipment failures or wrong operation of the machine.

3. Minimization of collimation-related background at the experiments to ensure a clean data acquisition.

The parameters characterizing the LHC and its collimation system extend the present state of the art by more than two orders of magnitude [41, 42] (see Fig. 2.3).

4.1.1 Quench limit of the LHC superconducting magnets

Superconducting magnets can stand a limited amount of local heating before quenching. The maximum allowed loss rate depends on the energy of the particles and on the timescale of the loss process.

4.1.1.1 Transient losses

In case of transient losses the number of protons n_q inducing a quench is given by [10]:

$$n_q = \frac{\Delta Q_c}{\epsilon} \tag{4.1}$$

where ΔQ_c is the amount of heat per unit volume necessary to increase the temperature of the superconducting coils of the magnet to the transition temperature T_c. ϵ is the energy per proton and per unit volume deposited in the coil. Three different regimes can be identified:

1. The duration of the losses δt is much shorter than the time τ_{metal} needed to reach a thermal equilibrium inside the coil cable ($\tau_{metal} = 6$ ms at 450 GeV and $\tau_{metal} = 3$ ms at 7 TeV) and the heat is concentrated around the impact point.

2. Losses are slow enough ($\delta t \geq \tau_{metal}$) that the heat can diffuse in the cable but is not transferred to the surrounding cryogenic liquid helium.

3. The loss duration allows reaching an equilibrium temperature between the helium and the cable ($\delta t \geq \tau_{He}$ where, $\tau_{He} = 44$ ms at 450 GeV and $\tau_{He} = 8$ ms at 7 TeV).

Details on these studies are extensively explained in [10] and Table 4.1 summarizes the values of n_q calculated for the different regimes.

Table 4.1: Number of protons inducing the quench of a superconducting magnet for transient losses at different time scales.

Energy [TeV]	Time	Quench limit for local losses [protons]
0.45	$\delta t < 6$ ms	$1.0 \cdot 10^9$
	$\delta t \geq 6$ ms	$2.7 \cdot 10^9$
	$\delta t \geq 44$ ms	$2.5 \cdot 10^{10}$
7.00	$\delta t < 3$ ms	$4.7 \cdot 10^5$
	$\delta t \geq 3$ ms	$8.5 \cdot 10^5$
	$\delta t \geq 8$ ms	$3.4 \cdot 10^7$

4.1.1.2 Continuous losses

In case of continuous losses the heat deposited on the coils should be constantly evacuated in order to keep the temperature below T_c. In reality superconducting cables are covered by an insulating layer that limits the heat exchange with the superfluid helium. Studies performed in Saclay provided measurements of the power deposition required for causing the quench of a magnet in a regime of slow continuous losses [10]. The maximum allowed proton loss rate on the LHC superconducting magnets R_q was then evaluated for different energies (see Table 4.2) [43].

Table 4.2: Maximum allowed proton loss rate R_q and local loss rate $\tilde{R}_q$ for continuous slow losses on the LHC superconducting magnets as a function of the energy.

Energy [TeV]	R_q [p s^{-1}]	$\tilde{R}_q$ [p s^{-1}m^{-1}]
0.45	$7.0 \cdot 10^8$	$7.0 \cdot 10^8$
1	$1.6 \cdot 10^8$	$1.9 \cdot 10^8$
1.5	$8.2 \cdot 10^7$	$9.7 \cdot 10^7$
2	$5.1 \cdot 10^7$	$6.1 \cdot 10^7$
2.5	$3.6 \cdot 10^7$	$4.2 \cdot 10^7$
3	$2.7 \cdot 10^7$	$3.1 \cdot 10^7$
3.5	$2.1 \cdot 10^7$	$2.4 \cdot 10^7$
4	$1.6 \cdot 10^7$	$1.9 \cdot 10^7$
4.5	$1.3 \cdot 10^7$	$1.6 \cdot 10^7$
5	$1.1 \cdot 10^7$	$1.4 \cdot 10^7$
5.5	$9.1 \cdot 10^6$	$1.2 \cdot 10^7$
6	$7.6 \cdot 10^6$	$1 \cdot 10^7$
6.5	$6.4 \cdot 10^6$	$8.8 \cdot 10^6$
7	$5.4 \cdot 10^6$	$7.8 \cdot 10^6$

The energy of the impacting protons is dissipated over a certain length that can be approximated with the effective length of the secondary particle showers L_{eff}. The local proton loss rate $\tilde{R}_q$ inducing a quench can then be defined as:

$$\tilde{R}_q = \frac{R_q}{L_{eff}}. \tag{4.2}$$

"Monte-Carlo" programs permitted to compute L_{eff}=1 m at 450 GeV and L_{eff}=0.7 m at 7 TeV [10]. A linear variation of L_{eff} was assumed to evaluate in this thesis for the first time $\tilde{R}_q$ as a function of the beam energy. The results are reported in Table 4.2 and in Fig. 4.1. A numerical fit of the data shows that the variation of $\tilde{R}_q$ with the energy is well approximated by the equation:

$$\tilde{R}_q = 1.7 \cdot 10^8 E^{-\frac{3}{2}} \tag{4.3}$$

where the energy is in units of TeV.
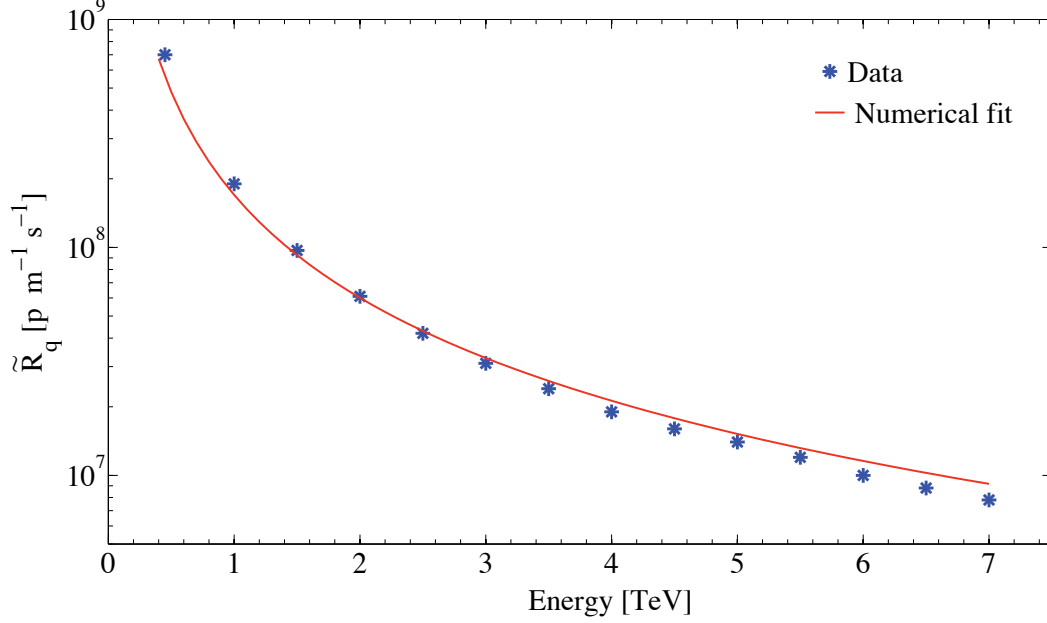
Figure 4.1: Maximum allowed proton loss rate $\tilde{R}_q$ for local slow continuous losses as a function of the energy. The red line shows that $\tilde{R}_q$ varies with the energy approximately like $E^{-3/2}$.

4.1.2   Cleaning inefficiency

Particles escaping from primary and secondary collimators can be lost in the cold aperture of the machine. The performance of the collimation system is described by the "global cleaning inefficiency" η_c that measures the leakage rate and is defined, for a certain aperture A_c, as [44]:

$$\eta_c(A_c) = \frac{N_p(A > A_c)}{N_{abs}}. \tag{4.4}$$

Here $N_p(A > A_c)$ is the number of particles leaving the cleaning insertion with a normalized amplitude $A > A_c$. N_{abs} gives the total number of particles which experienced inelastic interactions in a collimator jaw. For the LHC $A_c=10\,\sigma$ is considered as a typical case (aperture of the absorbers see 4.3.2). Inefficiency η_c should be smaller than 10^{-3} when operating the machine at top energy, corresponding to 99.9% efficiency. Another important aspect for the evaluation of the cleaning

performance is the distribution of losses along the machine. A local concentration of losses could induce quenches of the superconducting magnets even if the global cleaning efficiency satisfies the design requirements. On this basis the local cleaning inefficiency $\tilde{\eta}_c$ was introduced [44] and reads:

$$\tilde{\eta}_c = \frac{\eta_c}{L_{dil}}, \tag{4.5}$$

where L_{dil} is the dilution length of the losses. A dilution length L_{dil} of $50\,\mathrm{m}$ was assumed for early efficiency studies. The development of powerful tracking tools [45] and detailed machine aperture models [18] allowed to localize losses with a high resolution (up to $10\,\mathrm{cm}$) (see section 5.3). Local loss spikes were revealed permitting to identify the critical loss regions of the machine.

4.1.3 Maximum beam load at the collimators

The LHC collimation system has to protect the machine both during normal operation and in case of accident. Therefore, collimators must set the tightest aperture restrictions in the machine. They receive the highest radiation dose and are the first objects hit by the beam in case of failure. The total transverse energy density ρ_E is defined as:

$$\rho_E = \frac{E\,N_{tot}}{2\pi\sigma_x\sigma_y} \tag{4.6}$$

and is $1\,\mathrm{GJ\,mm^{-2}}$ at the location of the primary collimators (rms transverse beam size: $\sigma_x\approx\sigma_y\approx240\,\mu\mathrm{m}$) for nominal beam intensity ($N_{tot}{=}3.22{\cdot}10^{14}$ p) at $E{=}7\,\mathrm{TeV}$. Any possible hardware solution for the collimators can only stand a small fraction of the LHC beam. An accurate estimation of the beam load at the collimators, in case of regular and abnormal beam losses, was required to finalize the hardware design.

4.1.3.1 Normal losses

The LHC collimators should withstand losses necessary to run the machine close to the quench limit of the superconducting magnets. The maximum allowed proton loss rate R_{loss} at the collimators is given by the quench limit $\tilde{R}_q$ and the local cleaning inefficiency $\tilde{\eta}_c$ [46]:

$$R_{loss} = \frac{\tilde{R}_q}{\tilde{\eta}_c}. \tag{4.7}$$

It is correlated to the beam lifetime through:

$$\tau \approx \frac{N_{tot}}{R_{loss}}. \tag{4.8}$$

Based on operational experience at LEP, RHIC, TEVATRON and HERA, a minimum LHC beam lifetime of 0.1 h at 450 GeV and 0.2 h at 7 TeV was specified [11] for a period ΔT=10 s. The loss rate can reach a peak during the first second of the acceleration ramp when the expected beam lifetime drops to 20 s and about 5% of N_{tot} can be lost (uncaptured beam). A minimum lifetime τ of 1 h is specified for continuous losses both at injection and collision energy [11]. The loss rate R_{loss} and the maximum power deposition P_{loss} in the collimators were calculated from eq. 4.8 for the beam lifetimes and loss durations just introduced. Results are summarized in Table 4.3.

Table 4.3: Specified minimum beam lifetimes, loss durations, maximum proton loss rates and power deposition in the LHC collimators in case of normal losses [11].

	ΔT [s]	τ [s]	R_{loss} [p s^{-1}]	P_{loss} [kW]
Injection	continuous	1.0	$0.8 \cdot 10^{11}$	6
	10	0.1	$8.6 \cdot 10^{11}$	63
Ramp	≈ 1	0.006	$1.6 \cdot 10^{13}$	1200
Top energy	continuous	1.0	$0.8 \cdot 10^{11}$	97
	10	0.2	$4.3 \cdot 10^{11}$	487

4.1.3.2   Abnormal losses

The dump system is too slow (2-3 LHC turns) to provide protection in case of a fast increase of the loss rate (over one LHC turn), induced by injection and extraction failures. For this reason, robustness is one of the main design features of the LHC collimators which must withstand high instantaneous energy deposition without damage. The specified beam loads over one turn for the various error scenarios described in 3.3.2 are reported in Table 4.4 [1]. These values refer to the nominal LHC beam parameters. For the asynchronous beam dump scenario it was assumed that protons between $5\sigma_x$ and $10\sigma_x$ can impact on a collimator. An average β_x of 410 m at the extraction kickers was considered [47].

4.1.4   Performance reach from cleaning efficiency

An estimate of the maximum allowed beam intensity I_{max} (expressed in number of protons) at the quench limit is obtained in case of slow continuous losses by combining eq. 4.7 and eq. 4.8, and reads [46]:

$$I_{max} = \frac{\tau \cdot \tilde{R}_q}{\tilde{\eta}_c}. \tag{4.9}$$

Table 4.4: Beam load deposited in collimators for injection and extraction failure scenarios [1].

	Beam energy [TeV]	Deposited intensity [p]	Deposited energy [kJ]	Duration [ns]
Injection error	0.45	$2.9 \cdot 10^{13}$	2073	6250
Asynchronous dump (all MKDs)	0.45	$6.8 \cdot 10^{11}$	49	150
	7	$4.8 \cdot 10^{11}$	538	100
Asynchronous dump (one MKD)	0.45	$10.2 \cdot 10^{11}$	74	225
	7	$9.1 \cdot 10^{11}$	1021	200

The higher the local cleaning inefficiency, the lower is the number of particles which can circulate in the ring without inducing quenches, for a given beam lifetime. The "equivalent quench limit" $\tilde{\eta}_q$ can be calculated from eq. 4.9 as:

$$\tilde{\eta}_q = \frac{\tau \tilde{R}_q}{I_{nom}}. \tag{4.10}$$

Thus we get, for the nominal beam intensity ($I_{nom} \equiv N_{tot}$), the minimum beam lifetimes from Table 4.3 and the maximum allowed local loss rates from Table 4.2:

- $\tilde{\eta}_q = 7.8 \cdot 10^{-4} \, \mathrm{m}^{-1}$ at injection.

- $\tilde{\eta}_q = 1.7 \cdot 10^{-5} \, \mathrm{m}^{-1}$ at top energy.

Local losses on superconducting magnets must always be compared to $\tilde{\eta}_q$ in order to estimate I_{max}. For the collimation studies presented in this report I_{max} is derived from eq. 4.9 and eq. 4.10 as:

$$I_{max} = \left(\frac{\tilde{\eta}_q}{\tilde{\eta}_{max}^{cold}} \right) I_{nom} \tag{4.11}$$

where $\tilde{\eta}_{max}^{cold}$ is with the maximum of local losses on any cold element (see section 5.3). The same quench limit values are used for all superconducting magnet types without distinction, corresponding to an energy deposition of $5 \, \mathrm{mW \, cm}^{-3}$. This is a conservative assumption for operation of the magnets at the nominal temperature of $1.9 \, \mathrm{K}$ while a factor of two lower values can be expected for the MQM and MQY quadrupole magnets if the temperature rises up to $4.5 \, \mathrm{K}$ [48].

4.1.5 Performance reach from collimator induced impedance

The LHC collimator jaws are movable (see 4.3.1) in order to follow size and position of the beam. The smallest jaw openings are about $8 \, \mathrm{mm}$ at injection and $2.5 \, \mathrm{mm}$ at top energy. The presence of the collimator jaws close to the beam has consequences:

1. The transverse geometric and electrical discontinuity of the vacuum tank cross section can create electromagnetic trapped modes.

2. Coherent tune shifts are induced by the "resistive-wall impedance" of the collimator jaws [49].

Collimator related impedance can lead to an important reduction in the stable beam intensity I_{max} since the effect directly depends on the beam intensity. The problem of trapped modes is addressed by tapering the ends of the jaws (see Fig. 4.4), and by adding RF fingers (see Fig. 4.5). RF fingers provide electrical contact to the vacuum tank and pipes. The real part of the impedance (resistive contribution) can be reduced by increasing collimator gaps (accepting lower cleaning efficiency see section 6.1.5.3) or by using low resistivity materials. Also, a transverse feedback system can be used to damp coupled bunch instabilities [50]. In addition two families of magnetic octupoles are installed in the LHC to provide "Landau damping" of the coherent beam oscillation modes [51]. This increases the stability of the beam.

4.2   Phased implementation

The LHC collimators ideally should satisfy all the requirements introduced so far in order to allow reaching nominal and ultimate machine performance. One crucial point of the collimator hardware design concerns the choice of the jaw materials. A suitable material should be characterized by:

- Good absorption rate for cleaning efficiency.

- High robustness to withstand normal and abnormal operation without damage.

- Low electrical resistivity to reduce the impedance.

However, the constraints are conflicting. Robustness against damages imposes the usage of a low Z (atomic number) material to reduce the power deposition in the jaw. On the other hand, maximum cleaning efficiency would require a high Z material. Metallic materials could reduce the impedance from the collimators but they would hardly survive in case of an accident. A phased approach was adopted to address the various issues [52].

4.2.1   Phase 1

The initial phase 1 collimation system is the central part of the overall system. A detailed description is given in section 4.3. It is a multi-stage system composed by primary, secondary collimators and absorbers, located in dedicated cleaning insertions of the LHC ring. In addition, protection elements shield the most sensitive parts of the machine.

Maximum robustness and flexibility were defined as the priority for phase 1 even if this implies initially lower cleaning efficiency and higher impedance. On this basis, a low Z material was chosen for primary and secondary collimators which then are highly resistant to beam impact. The phase 1 system will be used, for the whole lifetime of the LHC, from injection up to the end of the energy ramp for any beam intensity. The loss rate and the risk of damaging the collimators is higher during these phases of operation. Phase 1 collimators will also be used initially for cleaning at high energies and reduced intensities.

4.2.2   Phase 2

A complementary set of secondary collimators will be installed behind existing secondary collimators in a second phase. The phase 2 collimators should use low impedance material jaws with a higher cleaning efficiency (for example higher Z). A higher atomic number results in a bigger energy deposition which would make phase 2 collimators less robust in case of beam impact. This is the reason why these collimators will be used only in stable conditions at top energy.

CERN is working on the phase 2 project in collaboration with several US laboratories like "Stanford Linear Accelerator Center" (SLAC), "Fermi National Accelerator Laboratory" (FNAL) and "Brookhaven National Laboratory" (BNL). A cylindrical Copper jaw prototype has been designed at SLAC that, in the eventuality of a damage, could rotate showing a fresh intact surface to the beam [53]. In case of an accident, the metallic phase 2 jaws could experience significant plastic deformation (hundreds of μm) and also surface melting and/or vaporization.

CERN experts are working on alternative designs and are investigating, in collaboration with the material science department of the "Ecole Polytechnique Fédérale de Lausanne" (EPFL), advanced materials combining good characteristics of efficiency, robustness, electrical and thermal properties.

4.2.3   Further implementation phases

A further strengthening of the collimation system is necessary when approaching nominal and/or ultimate (10^{35} cm^{-2} s^{-1}) luminosity. Two additional collimators TCLP will be installed per beam downstream of IP1 and IP5. These collimators absorb the high luminosity collision debris, once LHC exceeds about 30% of the nominal design luminosity (phase 3).

The number of collimators in the cleaning insertions was reduced by 16 with respect to the ideal system. This was done to reduce cost and work load for phase 1. It also limits the collimation-induced impedance budget while a 30% loss in cleaning inefficiency is predicted. In case of problems with cleaning efficiency during operation, these collimators could be added (phase 4) to the existing system.

4.3   Phase 1 collimation system

The phase 1 collimation system consists of 88 collimators which are installed along the ring plus 14 collimators in the transfer lines. Fig. 4.2 shows a not in scale scheme of the ring collimator distribution. The main devices are primary (TCP), secondary (TCSG) and absorbing (TCLA) collimators. They are located in two dedicated cleaning insertions in the LHC ring: the momentum cleaning in IR3 and the betatron cleaning insertion in IR7. The remaining ring collimators protect the most sensitive parts of the machine like injection (TCLI and TDI installed in IR2 for Beam 1 and IR8 for Beam 2) and extraction regions (TCDQA plus a TCSG in IR6). In addition, tertiary collimators (TCT) are installed upstream of the interaction regions to protect the triplet magnets. Absorbers (TCL) are located downstream of the IPs to catch debris from physics collisions coming from the experiments. A list of all the ring collimators and of their main parameters is given in Appendix A.

4.3.1   Collimator hardware design

LHC collimators use two movable jaws which must be centered and aligned with respect to the beam envelope. In addition the jaw openings must be varied according to the changes of the beam dimensions as a function of the energy. Four stepping motors, one at each end of the jaws, are used for aperture and angular adjustments while a fifth motor shifts transversally the full collimator tank. A rack and pinion system limits the maximum jaw tilt to less than 3 mrad and preloaded return springs can induce some auto-retraction of the jaws in case of motor failure (see Fig. 4.3 [54]). The jaws contain blocks of different materials, depending on the collimator type, and are water cooled through a heat exchanger formed by copper-nickel pipes. A GlidCop support bar presses the cooling pipes against the jaw material by means of clamping springs. Glidcop plates are used to assemble all components together (see Fig. 4.3 and 4.4). The clamping system allows to enhance the thermal contact between jaw and heat exchanger without creating mechanical constraints between materials having different thermal expansion coefficients. The length of the jaws is not the same for all the collimator types but is always constituted by a flat part, determining the jaw active length, and by a 10 cm tapering at both ends to avoid geometrical impedance effects (see Fig. 4.4). All the jaws are 80 mm wide and 25 mm deep along the active length.

Two collimator jaws are put in a vacuum tank and the whole apparatus is mounted on dedicated supports installed in the LHC tunnel [55]. A fast plug in system has been designed in order to reduce as much as possible the installation time, especially in view of a future operation in a radioactive environment [56]. A remote control for robotic mounting and dismounting of highly activated collimators is also under development.

Fig. 4.5 shows the open tank of a secondary collimator. The front view shows the RF fingers.
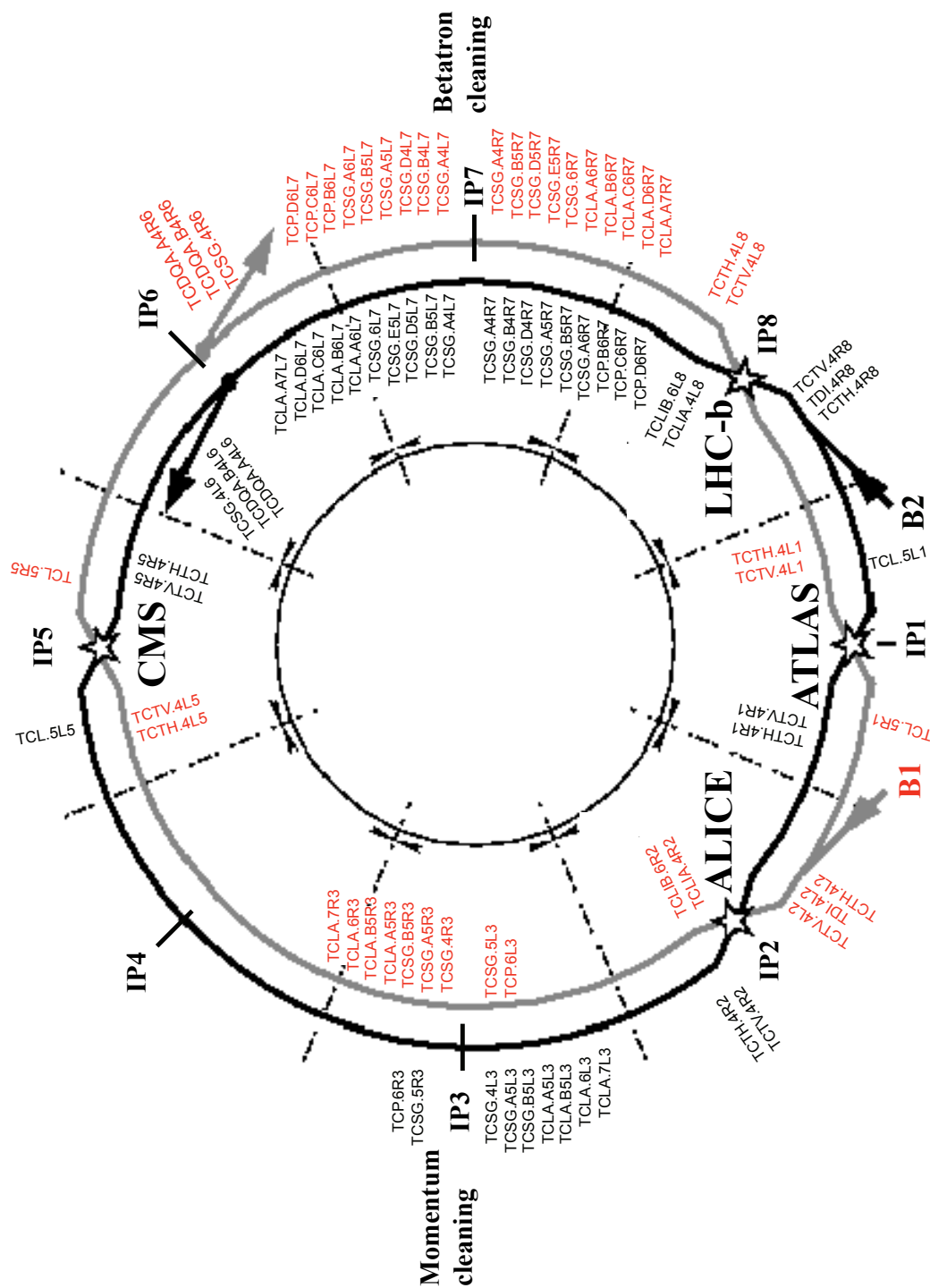
Figure 4.2: Layout of the phase 1 collimation system for the two beams (not in scale).
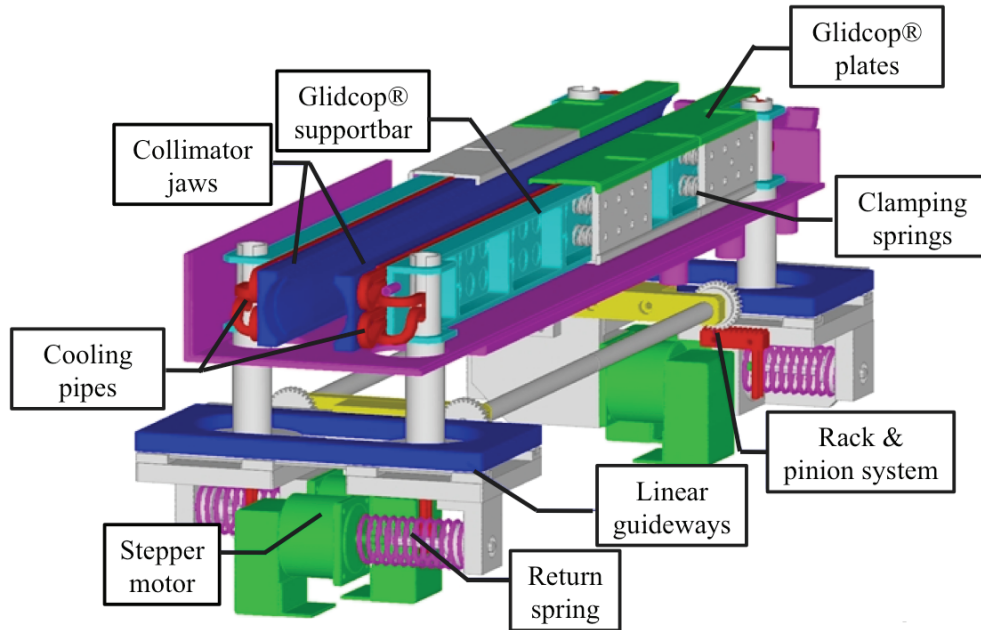
Figure 4.3: Scheme of the LHC collimator: the two jaws are water cooled and a clamping system insures a good thermal contact with the cooling pipes. Stepping motors allow to adjust opening and angle of the collimator jaws.
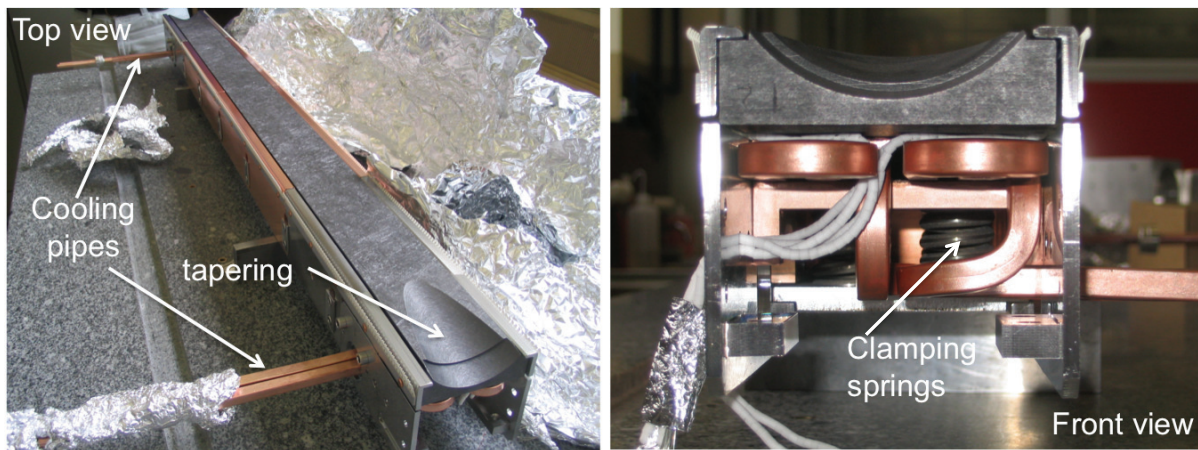
Figure 4.4: Top and front view of a secondary collimator jaw assembly. The CFC jaw measures in total 120 cm: 100 cm of active length plus 10 cm of tapering at each end (top view). Thermal contact with the cooling pipe is enhanced by a system of springs located behind the GlidCop support bar (front view).
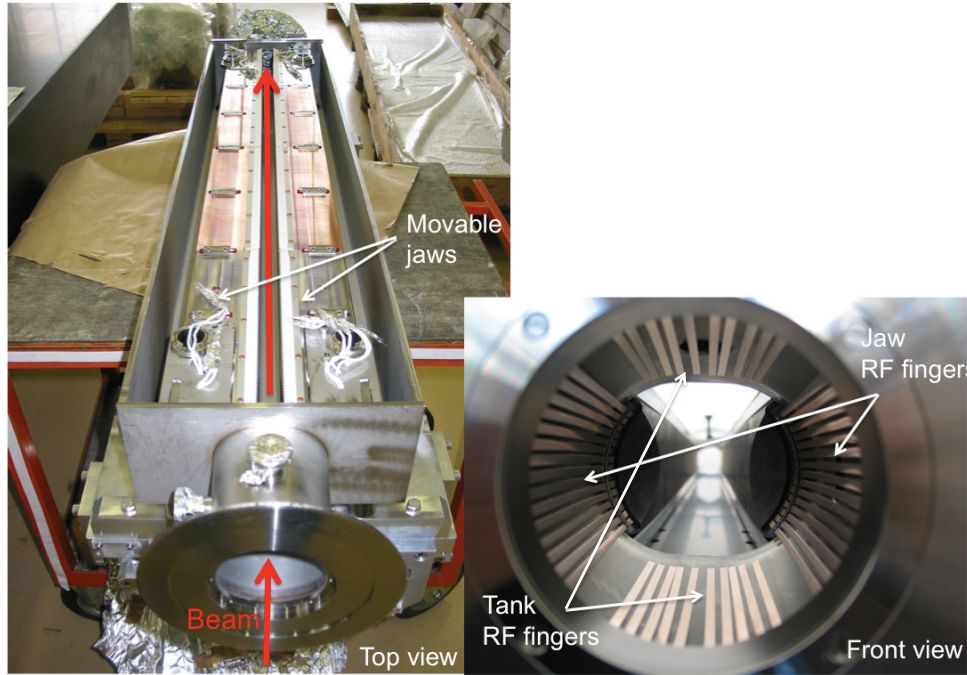
Figure 4.5: Two jaws are enclosed in a vacuum tank and can be centered with respect to the beam closed orbit. The front view shows the RF fingers.

4.3.2 Cleaning insertions

Conflicting optics requirements make it necessary to use separate insertions for betatron and momentum collimation [57]. The two insertions were designed both on the basis of the theoretical conditions presented in section 3.5 and empirical optimizations. The layout consists of primary (TCP) and secondary (TCSG) collimators plus absorbers (TCLA). TCPs and TCSGs have to scatter the beam halo particles in order to constrain their losses in the beam cleaning insertions. These are two sided collimators with fiber-reinforced graphite (CFC) jaws. This low Z material limits the energy absorption in the jaws and makes these devices extremely robust. Secondary collimators are 1 m long at the flattop. An active length of 60 cm was chosen for the primary collimators in order to have the best compromise between cleaning efficiency and robustness [58]. The TCLA active absorbers are located downstream of the secondary collimators and have to intercept the tertiary halo particles and the showers produced by inelastic interactions of the protons inside the TCP and the TCSG jaws. The TCLAs are also two-sided but use a high Z material (copper jaws with a tungsten inlay) for the 1 m long flattop of jaws: they have to absorb as much energy as possible.

4.3.2.1 Betatron cleaning insertion

The layout of the betatron cleaning insertion is sketched in Fig. 4.6. It includes three primary collimators (one vertical, one horizontal and one skew TCP), eleven secondary collimators (two horizontal, one vertical and eight skew TCSGs) and five active absorbers (three horizontal and two vertical TCLAs). For details see Appendix A. The angle that defines the azimuthal position of the skew collimator jaws is shown in Fig. 4.7. We introduce $\sigma = \sigma_z$ for the x and y plane, and $\sigma = \sqrt{\sigma_x^2 \cos^2 \psi + \sigma_y^2 \sin^2 \psi}$ for the skew plane, to be used in the following.
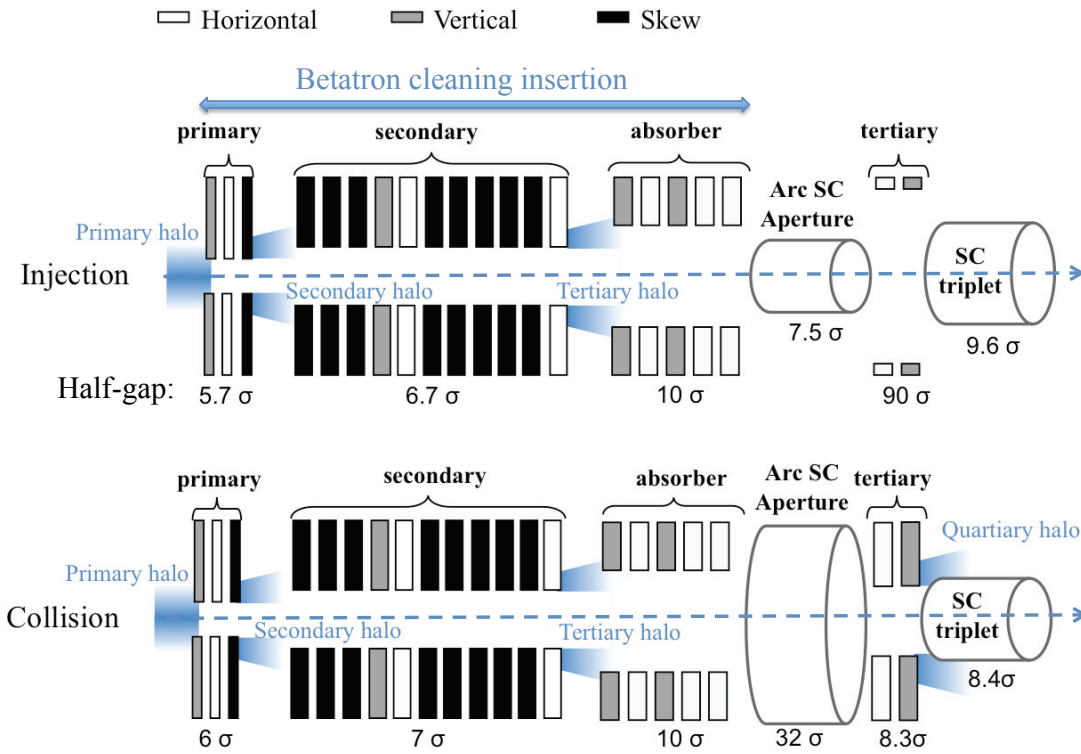
Figure 4.6: A three-stage cleaning system is set up for the protection of the arc cold aperture at injection (top). At collision the machine bottleneck is given by the superconducting triplets. Tertiary collimators are closed defining a four-stage cleaning system (bottom).

The long straight sections of the LHC provide a phase advance in the two transverse planes ($\Delta\mu_z$) of about 200 degrees. This is not sufficient to fulfill the ideal phase conditions presented in Table 3.10. Numerical simulations allowed to define the number of collimators, their relative phase advance and azimuthal positions in order to achieve the best coverage in the available transverse phase space. Collimators were placed in a low dispersion region. High β_z locations were preferred for obtaining larger gap openings and for reducing impedance (one example is shown in
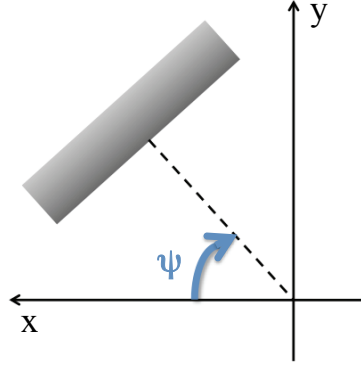
Figure 4.7: The azimuthal angle ψ for skew collimators is defined by starting from the positive x-axis and rotating clockwise in the x-y plane.

Fig. 4.8).
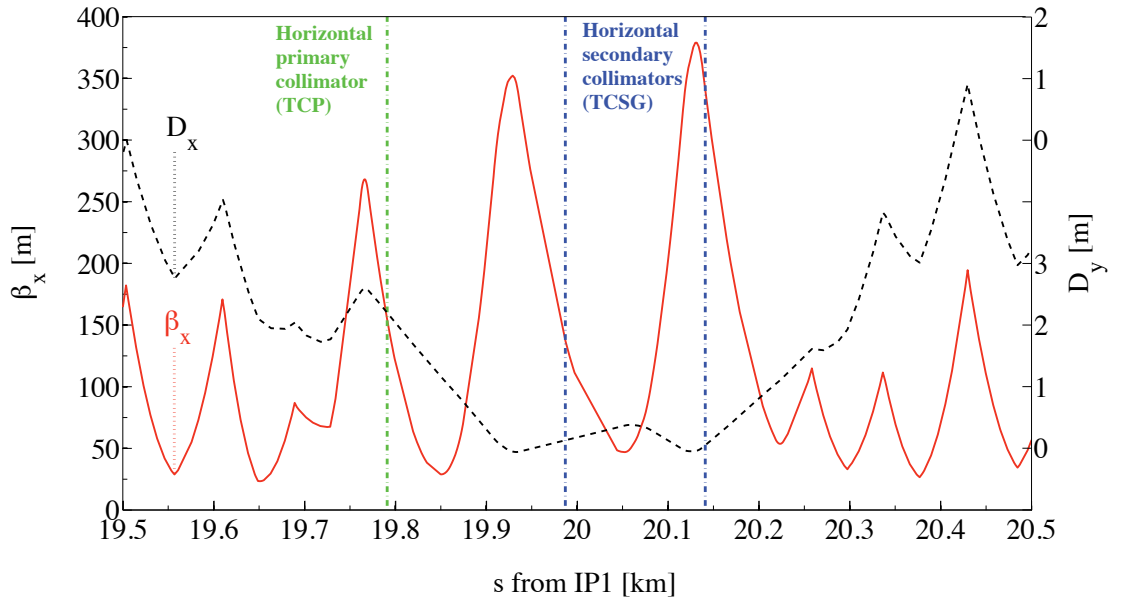
Figure 4.8: Horizontal β-function (β_x) and dispersion (D_x) in the betatron cleaning insertion for the Beam 1 injection optics. The longitudinal positions of the horizontal primary (green line) and secondary (blue lines) collimators are shown.

The opening of the collimator jaws depends on the machine available aperture a_{ring}. A strict setting hierarchy is fundamental to guarantee the performance and the protection required during the different operational stages. The protection elements must always be set to an aperture $a_{prot} < a_{ring}$. For secondary collimators the

condition $a_{sec} < a_{prot}$ must always be satisfied. The primary collimators (TCP) must be the closest element to the beam and $a_{prim} < a_{sec}$ has to be valid. The standard betatron collimator settings were defined, according to these rules, for the nominal injection and collision parameters and are shown in Table 4.5 and in Fig. 4.6.

Table 4.5: Nominal betatron collimator settings at injection and collision energy.

Location	Collimator type	Half-gap [σ]	
		Injection	Collision
IR7	TCP	5.7	6
	TCSG	6.7	7
	TCLA	10	10

At injection the tightest aperture limitation is in the arcs ($a_{ring} \approx 7.5\sigma$) and the protection elements (see 4.3.3.1) are set to 6.8σ. The half-gap of the secondary collimators (TCSG) is 6.7σ. Therefore a 1σ retraction is kept between primary and secondary collimators. A three-stage cleaning system is then completed, by setting the active absorbers to 10σ, for protecting the arc cold aperture. At collision, the aperture of the triplets in the high luminosity insertions ($a_{ring} \approx 8.4\sigma$ in IR1 and IR5 for $\beta_z^* = 0.55\,\mathrm{m}$) imposes to close the tertiary collimators (TCT see 4.3.3.3) to 8.3σ. These collimators intercept particles of the tertiary halo escaping from the cleaning insertions and reduce the losses on the downstream magnets. Primary and secondary collimators are set to 6σ and 7σ respectively and the TCLA to 10σ. The TCTs strengthen the betatron system by introducing a fourth stage of cleaning.

4.3.2.2 Momentum cleaning insertion

The LHC momentum cleaning insertion is optimized for horizontal collimation. This system consists of one horizontal primary, four secondary (all horizontal within $\pm 10\,\mathrm{deg}$ azimuthal angles) and four absorbing (three horizontal and one vertical) collimators. For details see Appendix A.

Table 4.6: Nominal momentum collimator settings at injection and collision energy.

Location	Collimator type	Half-gap [σ]	
		Injection	Collision
IR3	TCP	8	15
	TCSG	9.3	18
	TCLA	10	20
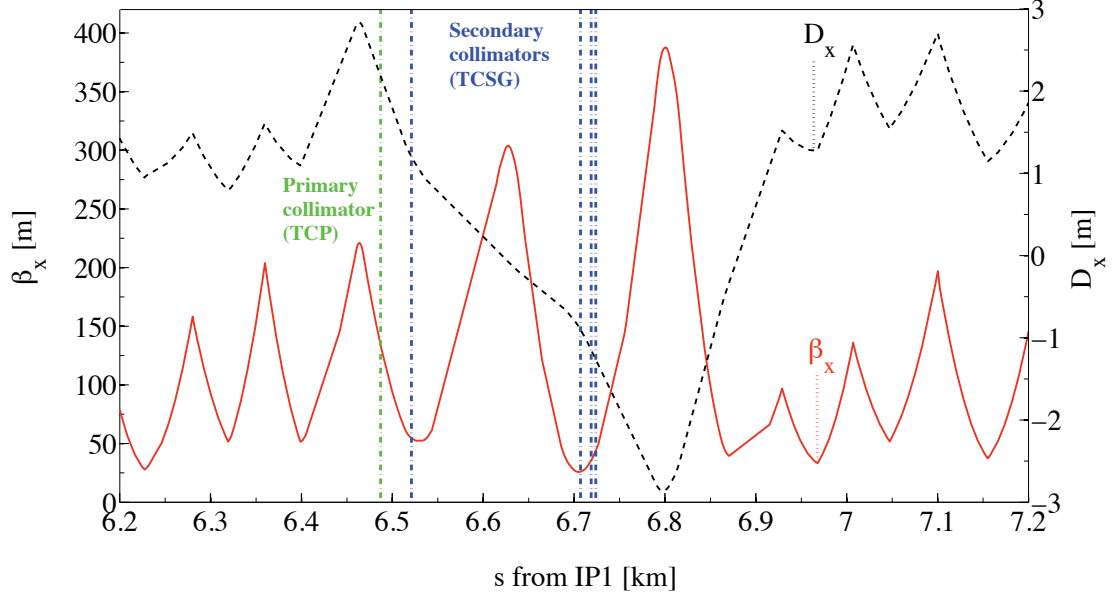
Figure 4.9: Horizontal β-function (β_x) and dispersion (D_x) in the momentum cleaning insertion for Beam 1 injection optics. The longitudinal position of the horizontal primary (green line) and secondary (blue lines) collimators is shown.

The momentum collimators must intercept off-energy protons which, for example, are lost at the beginning of the energy ramp. Their openings were defined in order to intercept particles with $\Delta p/p <$-10^{-3}. The nominal settings are listed in Table 4.6.

The horizontal dispersion D_x in IR3 (see Fig. 4.9) is high by design and, at the location of the primary collimator, eq. 3.35 is valid (for the MAD-X optics version V6.500: α_x=1.72, β_x=131.18 m, D_x=2.14 m, D'_x=-0.03). The specifications (as given in Table 3.10) for the horizontal case can then be applied to this system with a limited redesign. The horizontal (μ_x) and vertical (μ_y) phase advances along the momentum cleaning insertion with respect to the primary collimator location are shown in Fig. 4.10. The effective positions of the secondary collimators (blue dashed lines) show a good agreement with the optimum phases predicted by the theory (red circles).

4.3.3   Protection elements

Special protection devices shield the most sensitive parts of the LHC.

4.3.3.1   Injection regions

The injection beam stopper (TDI) is used for injection setup and machine protection in case of failure of the injection kickers. The TDI is a vertical collimator and consists
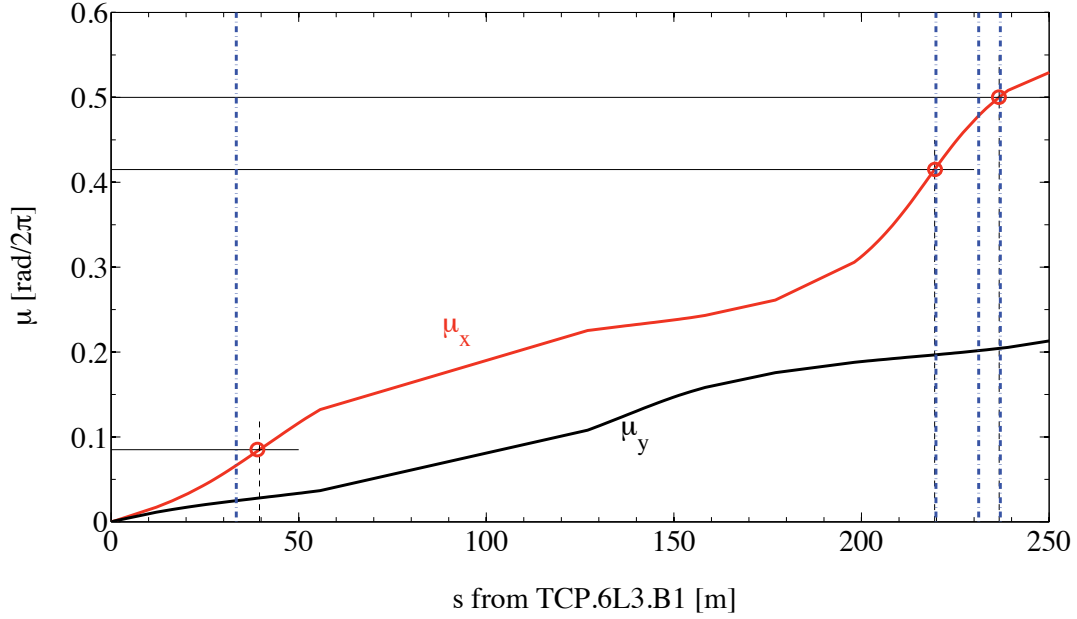
Figure 4.10: Phase advances along the momentum cleaning insertion with respect to the primary collimator location [57]. Red circles indicate the optimum phase advances for the secondary jaws according to theory (see Table 3.10). Blue dashed lines define the effective positions of the secondary collimators. Note, that theory requires four secondary jaws for one primary collimator. One of the secondary collimators account for two of these jaws such that only three locations for secondary collimators are retained. The installed system has one additional collimator.

of two 4.2 m long carbon-carbon composite jaws. The upper jaw should intercept bunches not sufficiently deflected by the injection kickers, while the lower jaw should catch miskicked circulating beam.

Two supplementary injection protection collimators (TCLI) are installed downstream of IP2 (Beam 1) and IP8 (Beam 2). The TCLI are vertical two-sided collimators. Two different designs are required for these collimators:

- TCLIA: These are "two beams in one tank" design collimators located in the machine regions with common beam pipes for Beam 1 and Beam 2.

- TCLIB: Classical "one beam in one tank" design, identical to the TCSG type.

The injection protection collimators must be retracted before the beginning of the energy ramp. Their half-gaps at injection are listed in Table 4.7 and are defined according to the requirement that $a_{prot} < a_{ring}$.

Table 4.7: Nominal settings of the injection protection devices. These elements are fully retracted at top energy.

Location	Collimator type	Half-gap $[\sigma]$
IR2-IR8	TDI	6.8
	TCLIA/B	6.8

4.3.3.2   Extraction region

The power load on the superconducting magnets downstream of the extraction region (IR6) has been presented in Table 4.4 for the case of asynchronous beam dump. Two identical, single-sided mobile diluter elements (TCDQA) are installed in IR6 and have to absorb the beam swept over the machine aperture in order to avoid damage. Each TCDQA is constituted by one horizontal, 3 m long CFC jaw located at the extraction side (positive x coordinate; see Fig. 3.1). One horizontal TCSG collimator is placed immediately after the TCDQAs to provide further protection to the downstream elements. Table 4.8 contains the nominal settings at injection and collision energies.

Table 4.8: Nominal settings of the extraction protection elements at injection and collision energies.

Location	Collimator type	Half-gap $[\sigma]$	
		Injection	Collision
IR6	TCDQA	8	8
	TCSG	7	7.5

4.3.3.3   Experimental insertions

At top energy the beam has to be squeezed in order to reach the nominal $\beta_z{}^*$ values at the interaction points. The squeeze implies that the β-function at the triplet magnets increases and this induces a reduction of the available aperture in these regions (see Fig. 4.11).

Horizontal (TCTH) and vertical (TCTV) tertiary collimators are installed upstream of the triplet magnets to provide protection during squeeze and collision. They are two-sided collimators formed by 1 m copper jaws with a tungsten inlay. Tertiary vertical collimators in IR1 and IR5 have the classical one-beam design (TCTVA identical to the TCLA type), while the TCTV in IR2 and IR8 have a "two beams in one tank" design (TCTVB). The TCTs have to be closed following the
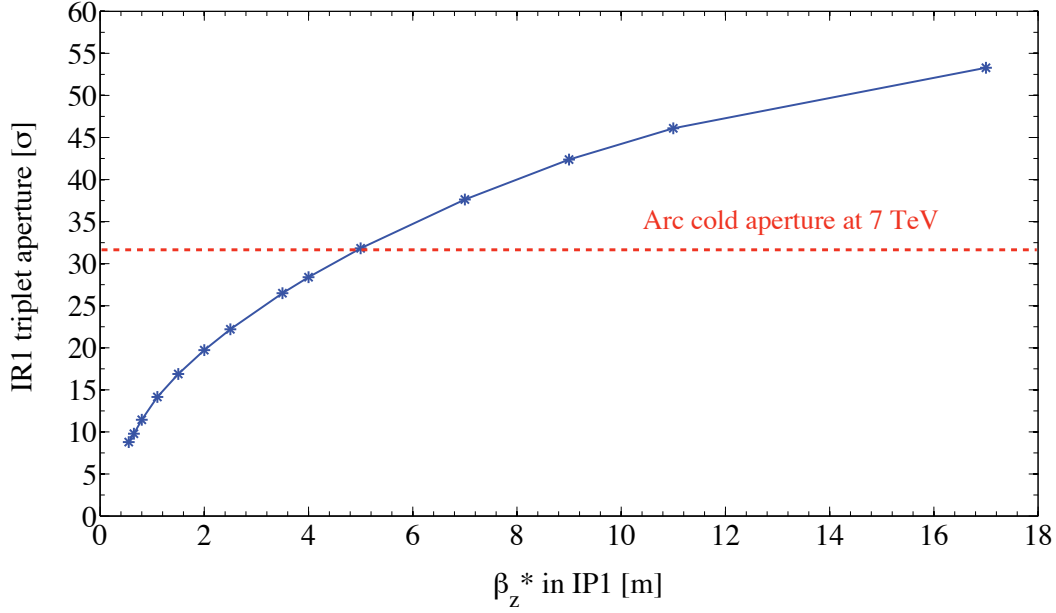
Figure 4.11: Aperture at the triplet magnets as a function of the $\beta_z{}^*$ values. This case refers to the squeeze of Beam 1 in IP1 from [59].

squeeze of the beam and, in particular, when the triplet aperture becomes smaller than the arc aperture (for example, in IR1 when $\beta_z{}^*<5$ m as seen in Fig. 4.11). Collimation studies that are presented in this PhD work, were performed by setting the collimators in all the experimental regions according to the gap requirements of the high luminosity insertions, namely to 8.3σ for a $\beta_z{}^*$ of 0.55 m (see Table 4.9 "simulated"). This is a performance optimized setting that allows to distribute the load of the quartiary halo over all the TCTs. More relaxed gaps can be applied to the TCTs in IR2 and IR8, for reducing the halo-related background in ALICE and LHCb (see Table 4.9 "Triplet protection"). This would lead to an increase in the halo load on the TCTs in IR1 and IR5.

The arc cold aperture at injection shields the triplet aperture so that, ideally, the tertiary collimators could be kept completely retracted. This setting was used for the studies presented here (TCTs out, see Table 4.9 "simulated"). Only few losses were seen in the experimental straight sections. During operation, however, the TCTs might be closed to the apertures listed in Table 4.9 ("triplet protection") to insure a safer machine protection.

Finally, special absorbers (TCL) located downstream of the high luminosity IPs use two pure copper jaws (1 m flattop) to catch the physic debris coming out from the interaction points during collisions (see settings in Table 4.9).

Table 4.9: Settings of tertiary collimators in the experimental regions at collision (β_z*=0.55 m in IP1 and IP5, β_z*=10 m in IP2 and IP8) and injection energies (β_z*=11 m in IP1 and IP5, β_z*=10 m in IP2 and IP8). The values required for triplet protection and used for simulations are listed. It is noted that the triplets at injection are protected by the smaller aperture in the preceding arc. Using TCTs for protection at injection is therefore a safety measure but not required (see also text).

	Location	Collimator type	Half-gap [σ]	
			Triplet protection	Simulated
Collision	IR1-5	TCTH/V	8.3	8.3
	IR2	TCTH/V	45	8.3
	IR8	TCTH/V	30	8.3
Injection	IR1-5	TCTH/V	9.5	out
	IR2-8	TCTH/V	9.2	out

Table 4.10: Nominal settings of the absorbers for physics debris located downstream of the high luminosity experimental regions. These elements are completely retracted when collisions do not take place.

Location	Collimator type	Half-gap [σ]
IR1-5	TCL	10

4.3.4   Phase 1 limitations

The impedance budget of the LHC is dominated by the contribution of the CFC collimators installed along the ring. At collision energy, their small half-gaps and the high resistivity of the jaw material ($10^{-5}\,\Omega$m) can cause instability if the beam intensity is higher than 40% of the nominal one [60]. This estimate takes into account the beam stabilization provided by the octupoles through "Landau damping".

The values calculated for the equivalent quench limit $\tilde{\eta}_q$ in 4.1.4 show that a 99.998% cleaning efficiency (for the conservative case of L_{dil}=1 m) is necessary for a safe machine operation. Studies performed during this PhD and presented in the following demonstrate that the design cleaning efficiency of the full phase 1 collimation system at top energy is 99.995%, in case of a perfect machine. This implies that some magnets could quench if I_{max}>$0.37I_{nom}$ (see section 6.1.2). The basic limitation comes from concentration of losses above the quench limit in the dispersion suppressor just downstream of the betatron cleaning insertion. These losses are due to particles which experience "single diffractive scattering" (see section 3.4 and

6.1.2) in the primary collimator jaws and escape from the cleaning insertion without interacting with any secondary collimator. The cleaning efficiency is expected to worsen by up to a factor of 11 in the real machine due to unavoidable imperfections (see section 6.2).

4.3.5   Beyond phase 1 limitations

Different possibilities for the upgrade of the collimation system are under investigation, in order to improve the cleaning efficiency and to reduce the collimator induced impedance. The implementation of phase 2 collimators should reduce the impedance of the machine from the high resistivity of CFC secondary phase 1 jaws. On the other hand the new collimators will not solve the efficiency problem linked to the single diffractive scattering at the TCPs. Possible solutions to the problem are being studied:

- Higher efficiency TCPs.

- Magnetic collimators.

- Cryogenic collimators [61].

- Electron lens [62].

- Crystals [63].

Between all listed options, performance studies are presently concentrating on the possibility of adding 2 additional "cryogenic" collimators for each beam in the IR7 dispersion suppressor at the location of the loss peaks.

4.4   Installation stages

For the commissioning of the LHC different stages with increasing beam intensity are planned [64]. A number of sub-systems of collimators have been defined which have specific tasks in order to meet the current LHC requirements. Collimators are installed in phases, compatible with the LHC commissioning and operational schedule. This phased approach relies on the fact that difficulties and performance goals for the LHC are distributed in time, following the natural evolution of the machine. The installation stages are as follows:

- **2008:** The beam intensity will be $<1\%$ of I_{nom} and a reduced number of collimators, with respect to the nominal phase 1 system, will insure the suitable cleaning and machine protection. The momentum cleaning insertion is complete while in the betatron cleaning insertion only six (out of the eleven foreseen) secondary collimators are installed. Optimization studies allowed to

identify the best collimator locations for the start up of the machine. The TCTVB and TCLIA in IR2 and IR8 are missing, as well as the TCLs in IR1 and IR5.

- **2009:** During the first shut down the delayed collimators will be installed in order to complete the nominal phase 1 system.

- **2011/12:** Momentum and betatron cleaning insertions will be complemented with the phase 2 secondary collimators and other improvements.

Chapter 5

Simulation Setup of Cleaning Efficiency Studies

In order to study the performance of the LHC collimation system for different optics and collimator settings a collimation version of the Single Particle Tracking code "SixTrack" has been developed [45]. This tool together with a detailed aperture model [18] of the full machine allows assessing the efficiency of the collimation system and mapping the regions of the ring which are exposed to proton losses. The "SixTrack" output provides input for energy deposition studies of secondary particle showers, generated by the interaction of the proton beams with the collimator jaws. In this section, the simulation setup for obtaining detailed loss maps is presented.

5.1 LHC optics files for SixTrack

The first step for running simulations with "SixTrack" [65] consists in the definition of the machine optics. This is done through the program "MAD-X" [20] specifying the following parameters:

- Magnetic strength and sequence of the machine elements (including collimators) for the tracked beam (Beam 1 or Beam 2).

- Beam energy.

- Type of tracked particles.

- Crossing and separation schemes at the interaction points.

Moreover, specific matching routines are used to set the horizontal (Q_x) and vertical (Q_y) tunes and the chromaticities (ξ_x and ξ_y) to the design values listed in Table 2.3.

The collimation "SixTrack" code requires the use of the thin lens approximation. In this formalism each element is represented by a marker located at the centre of the

drift space replacing the element itself. A conversion module included in the "MAD-X" program creates a so called "fc.2" output file, containing the geometry and the magnetic strength of the LHC elements for the analyzed optics. This file, renamed as "fort.2" [65], is the model of the lattice used by "SixTrack" for the element-by-element tracking.

5.2   "SixTrack" for collimation studies

The version of the "SixTrack" code modified for collimation studies [45, 66, 67] allows to track each particle of an initial distribution along the machine for many hundred turns. It performs an element-by-element, fully chromatic and coupled tracking, it can handle magnet non-linearities up to the 20th order and it can apply linear and non-linear error models. Moreover, dedicated subroutines are implemented to take into account the interaction of the halo particles with the collimator jaws ("K2" code [68]). A six-dimensional coordinate vector is defined for every particle at each element of the lattice. This code and its interface with a detailed aperture model [18] are the main tools used for the efficiency studies of the LHC collimation system that are presented in this report.

5.2.1   Scattering routine

The "K2" scattering routine [68] is implemented in the tracking code used for collimation studies, in order to simulate the interaction of each incident particle with the collimator jaw materials (see section 3.4 for a description of interactions). This routine is based on the Monte Carlo method. Interaction processes (MCS, ionization, elastic or inelastic point like interactions etc.) are randomly applied to the particle depending on the initial coordinates and a weighting of the different point-like interactions (according to the relative cross-sections) is applied. In this way the program calculates the distance between two consecutive interactions and evaluates if and where the particle leaves the jaw. Inelastic interactions cause the creation of secondary particles, which are not taken into account in the tracking studies for accelerator physics. Instead, the original proton is considered as "absorbed" by the collimators, saving its coordinate for transfer to the FLUKA code. Particles experiencing elastic interactions, including MCS and SD, exit from the jaw with modified 6D coordinates. Details on scattering routines and definition of cross-sections can be found in [33, 67].

5.2.2   Input files for tracking

Apart from the "fort.2" file (defining the lattice of the machine without magnetic field errors), two further input files are needed to run the collimation version of

"SixTrack". These files contain all the details about the collimator geometry (collimator "database") and the tracking parameters ("fort.3" [65, 66]). The "database" file includes for each collimator the following information:

- Collimator name.

- Half gap in σ units.

- Jaw material. The scattering routine of "SixTrack" allows to treat graphite, copper, tungsten, aluminum, beryllium and lead.

- Jaw active length [m].

- Azimuthal angle [rad] of collimator jaws.

- Transverse collimator gap offset [m].

- Design horizontal and vertical β-function [m] at the collimator location.

In the "fort.3" file it is possible to define the number of particles to be tracked, their initial distribution and the number of turns. Typically, each simulation uses about $5 \cdot 10^6$ halo particles which are followed over 200 turns. The different options for the initial distribution are:

1. Flat distribution in the selected plane between $A_x \pm \delta A_x$ (horizontal) or $A_y \pm \delta A_y$ (vertical). $A_{x,y}$ is the normalized amplitude of the particles, which are generated in a range of $\pm \delta A_{x,y}$ around this value (see Fig. 5.1 left). The amplitude in the other plane is zero.

2. Same as in 1, plus a Gaussian distribution cut at 3σ in the other plane (see Fig. 5.1 right).

3. Same as in 2, plus a longitudinal component defined through an rms bunch length (nominally 11.24 cm at 450 GeV, 7.55 cm at 7 TeV [1]) and rms energy spread (nominally $3.06 \cdot 10^{-4} \Delta E/E$ at 450 GeV, $1.13 \cdot 10^{-4} \Delta E/E$ at 7 TeV [1]). See Fig. 5.2.

4. An arbitrary six-dimensional external distribution.

5. A radial transverse distribution of radius A_r. This correspond to a flat distribution both in horizontal and vertical plane between $A_x \pm \delta A_x$ and $A_y \pm \delta A_y$ where: $A_x = A_y = \frac{A_r}{\sqrt{2}}$.

The values for $A_{x,y,r}$, $\delta A_{x,y,r}$ (in σ units) and the distribution type are indicated in the "fort.3" file and define the size of the beam halo in the selected plane. The halo has to be defined precisely in order to generate impacts of the halo particles at the betatron primary collimators. Its amplitude must be larger than the collimator setting (5.7σ
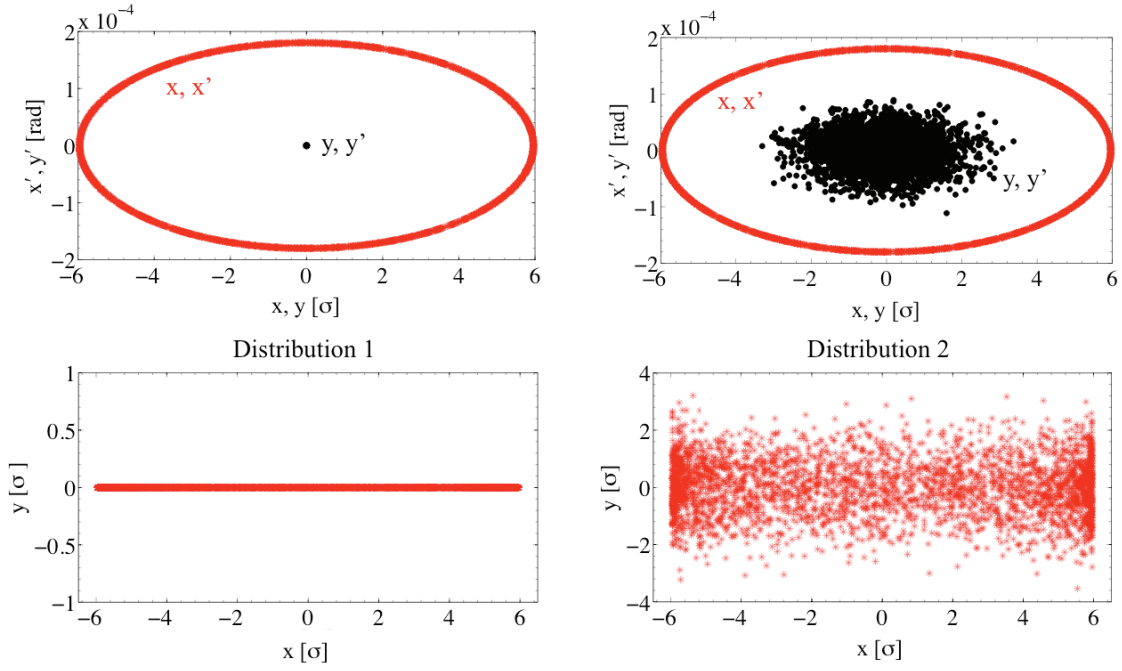
Figure 5.1: Particle distribution in the $x - x'$ and $y - y'$ phase space (top) and in the $x - y$ space (bottom) for a horizontal halo of type 1 (left) and type 2 (right) .
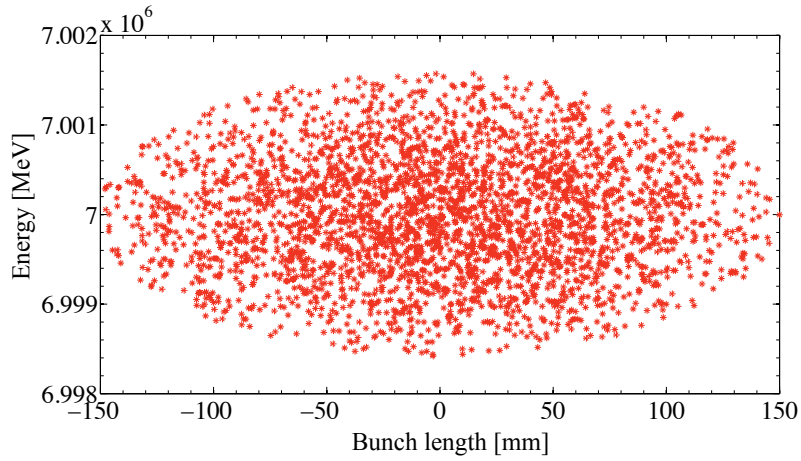
Figure 5.2: Gaussian distribution of the halo particles, cut at 2σ, in the longitudinal plane (type 3).

at $450\,\mathrm{GeV}$ and 6σ at $7\,\mathrm{TeV}$, see section 5.4). Moreover the impact parameter b (see 3.5.1) can be controlled by defining the amplitude A and the spread δA around it. Studies on diffusion processes of the LHC beam [15] showed an expected impact
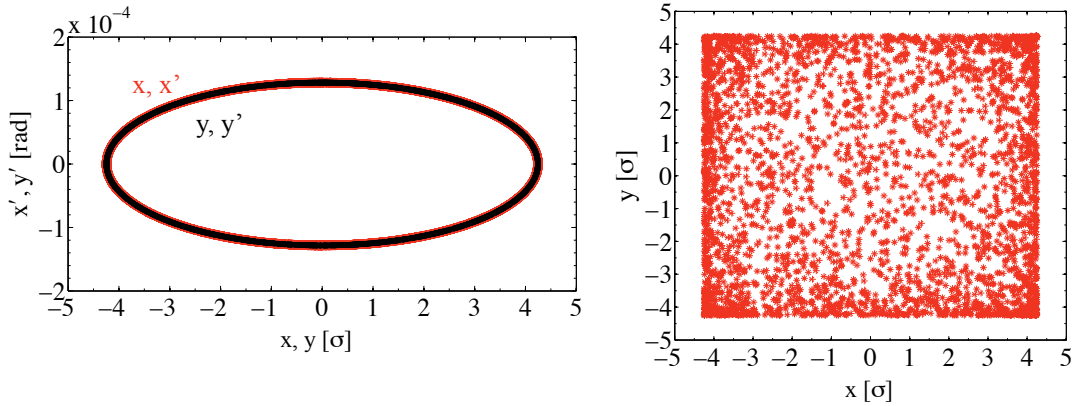
Figure 5.3: Particle distribution in the $x - x'$, $y - y'$ phase space (left) and in the $x - y$ space (right) for a radial halo of type 5.

parameter smaller than $1\,\mu\text{m}$ at the primary collimators [46]. This was used as target value for all studies reported in this PhD work.

The "fort.3" input file allows to define the aperture of the collimators by families, as classified in the file itself, or by reading the half gap of each collimator from the "database". Also, a logical flag allows choosing either to use the β-function values calculated for the specified optics at the location of the collimators or to read the design values listed in the "database" file. These two last options are needed to simulate special settings for single collimators and error scenarios.

Specialized subroutines are implemented in "SixTrack" to treat collimator imperfections. A systematic deformation can be applied to the collimator jaws. The bending is approximated by a polynomial function of 5th order maximum whose coefficients are specified in the "fort.3" file. The original flat jaw is sliced in a number of equal parts (indicated in "fort.3") and the ends of each slice are projected on the polynomial curve. The slices represent the deformed jaw as depicted in Fig. 5.4. The code allows to apply a different deformation to left and right jaws (different polynomial coefficients).
Finally, the "fort.3" permits to specify symmetric or antisymmetric jaw tilts and offsets, plus random tilts, offsets and gap errors for the jaws of whatever family of two sided collimators.

5.2.3 Simulation output files

Every particle interacting with a collimator is tracked until it experiences an inelastic scattering with a jaw. It is then considered absorbed for "SixTrack". All the trajectories of halo particles are saved in the "tracks2.dat" file that contains the co-
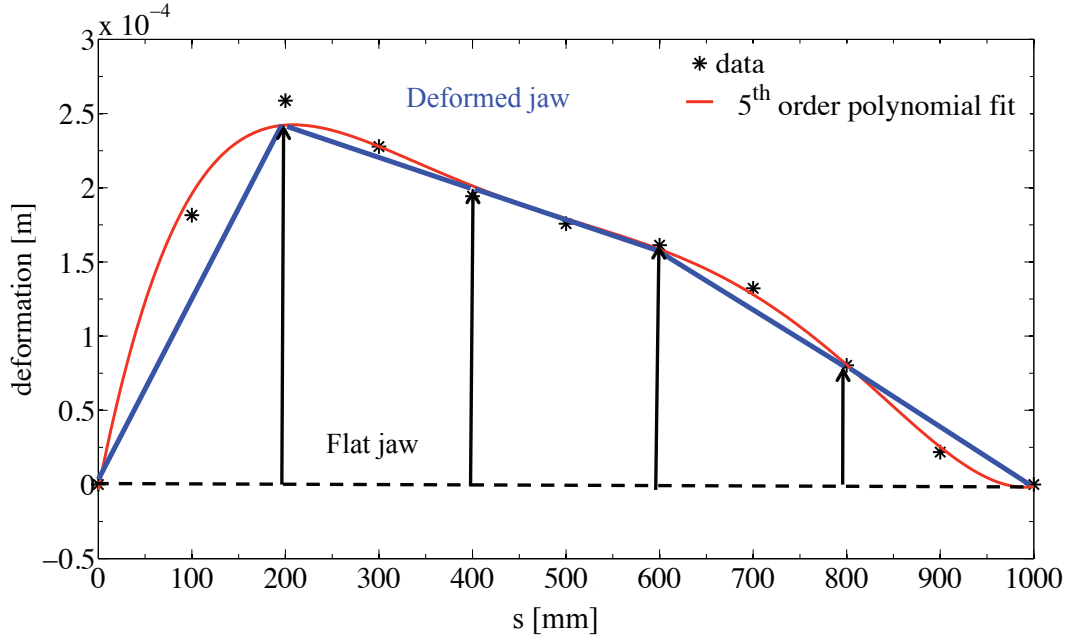
Figure 5.4: Example of a jaw with non-zero flatness. The 5th order polynomial has been defined by fitting real flatness measurements (TCSG prototype after the 2004 robustness test [69]).

ordinates of each particle in the six-dimensional phase space $(x, x', y, y', s, \Delta E/E)$. Particle coordinates are saved at the location of each element for all the tracked turns. Similarly, the transverse coordinates of the inelastic interactions along the jaw lengths are stored in the "FLUKA.dat" file, as input for energy deposition studies. This file overestimates the number of absorptions, since "SixTrack" does not perform any aperture check and carries on tracking particles which in reality would be lost in the mechanical aperture of the machine. The same overestimate is found in the "coll_summary.dat" file that summarizes for each collimator the number of impacts and absorptions and the impact parameter b averaged over the total number of impacting particles. The overestimates are corrected later on.

A further estimate of b can be deduced by the "FirstImpacts.dat" file that lists the incoming and outgoing transverse and longitudinal coordinates of particles, interacting for the first time with a collimator as a function of the turn number. This file allows to estimate the effect of non linear magnets (mainly sextupoles) on b already at the first turn and then to verify if the amplitude of the initial distribution (generated at the IP1) on the primary collimator matches with the expected value (see 5.4). Finally the "collgaps.dat" file includes all the information related to the collimator geometry and main optics parameters at the collimators, while the "efficiency.dat" file contains the global cleaning efficiency data as defined in eq. 4.5 for

each simulated plane.

5.3   Maps of particle losses

In order to identify the particles which are lost in the mechanical aperture of the
LHC ring and to localize these losses, a detailed aperture model of the full machine,
not including collimators and protection elements, is available [18]. The "Beam-
LossPattern" program [66] compares trajectories derived from the "tracks2.dat" file,
through element-by-element interpolation with the aperture model. It permits to
identify loss locations with an arbitrary resolution Δs. In Fig. 5.5 an example of a
particle trajectory in the LHC aperture model is shown. Two equivalent files, dif-
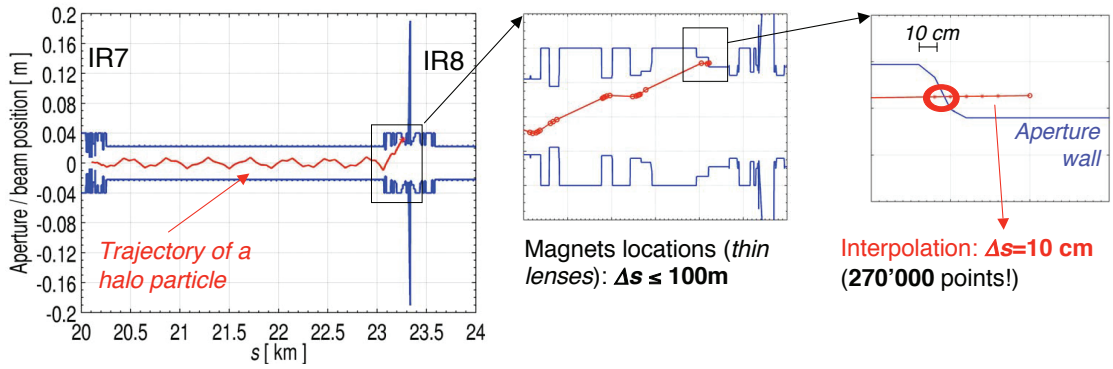
Figure 5.5: Example of a trajectory of a particle lost in an LHC interaction re-
gion [18].

fering only in the resolution used for the interpolation, are generated as output: the
"LP_PartLost.dat" (1 m resolution) and the "LPI_PartLost.dat" (10 cm resolution)
files. These files store the 6D phase space coordinates of every particle that hits an
aperture limit as well as information to which halo they belong to. An auxiliary
program ("CleanInelastic") uses this output to clean up the "FLUKA.dat" file from
the fake absorptions due to particles formerly lost in the machine aperture. The re-
sulting new "impacts_real.dat" file is the main input for energy deposition (FLUKA)
and background studies. FLUKA calculates the showers of particles generated by
the inelastic interaction of the primary protons with the different collimator jaw
materials. For this PhD no FLUKA studies were performed by myself, though lots
of input files were provided to various experts.

The simulation tools allow to draw detailed loss maps for different optics and
collimator settings. One example is shown in Fig. 5.6. This graph refers to the old
injection optics (see Table 2.4) for a Beam1 horizontal halo (distribution number 1
in 5.2.2) and the full phase 1 collimation system at nominal settings. Here, the local
cleaning inefficiency $\tilde{\eta}_c$ is defined as:

$$\tilde{\eta}_c = \frac{N_{lost}^{\Delta s}}{\Delta s \cdot N_{abs}}. \tag{5.1}$$

This is analyzed along the length of the machine with a Δs=10 cm resolution. $N_{lost}^{\Delta s}$ is the number of particles lost within Δs while N_{abs} is the number of particles absorbed by the full collimation system. The blue bars in Fig. 5.6 represent proton losses on the superconducting magnets, while the red bars indicate losses on the room-temperature magnets.

   The gray peaks show the particles which are absorbed by the collimators. In this case, Δs in the definition of $\tilde{\eta}_c$ is substituted by the jaw active length. This is the reason why $\tilde{\eta}_c$ for the 0.6 m primary collimators can be bigger than 1. Furthermore, the expected quench limit for the specified peak beam loss is indicated in order to provide a visual reference for the target value in collimation inefficiency. Losses in superconducting magnets (blue lines) must be below the quench limit for preventing that the superconducting magnets quench during a peak beam loss.
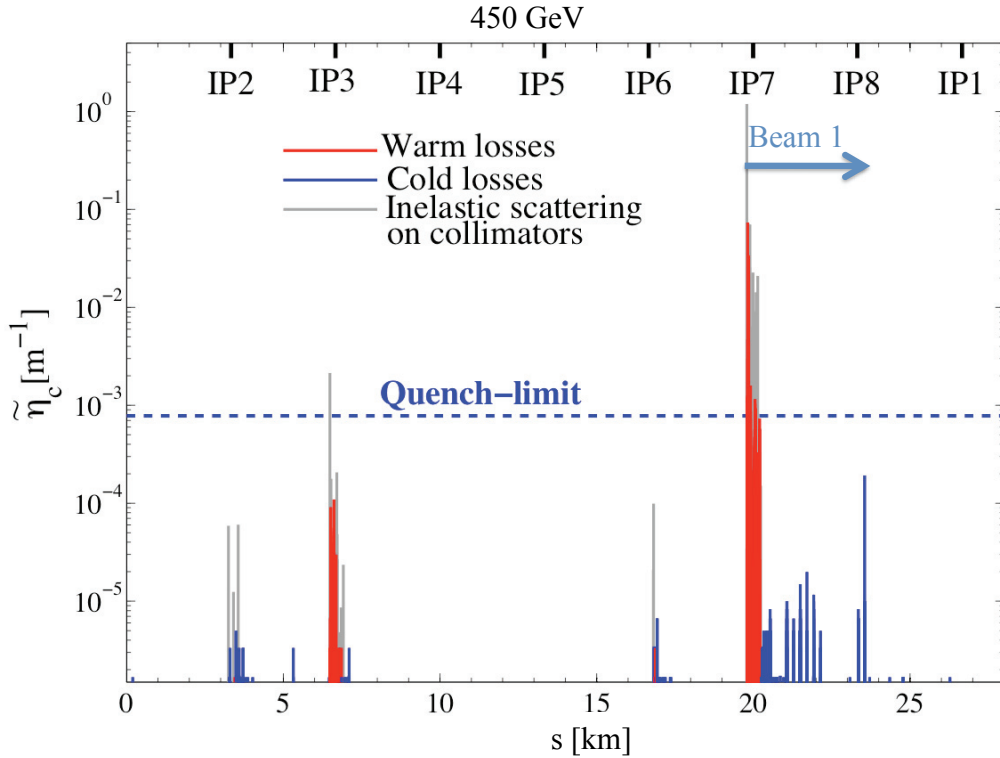
Figure 5.6: Example of loss map with a 10 cm resolution for the horizontal halo of beam 1 (distribution type 1) at injection energy and for the nominal phase 1 collimator settings.

5.4 Impact parameter and efficiency

The collimation studies presented in this report focus on simulations of betatron halos, because the tightest requirements apply here. The halos are generated at IP1 by defining a particle distribution with such an amplitude as to interact with the primary collimators installed in the betatron cleaning insertion of IR7. The amplitude of this distribution is calculated on the basis of the the TCP half-gaps and the target impact parameter. The primary collimators have an half opening of

Table 5.1: Starting beam size and spread for on momentum particle distribution that gives a $1\,\mu$m impact parameter at the horizontal primary collimator in IR7 (for optics V6.500).

	$A_{x,y} \pm \delta A_{x,y}$ at 450 GeV	$A_{x,y} \pm \delta A_{x,y}$ at 7 TeV
Beam 1	5.630±0.0015	5.958±0.0015
Beam 2	5.666±0.0015	5.975±0.0015

$5.7\,\sigma$ at injection and $6\,\sigma$ at top energy. In order to have a $1\,\mu$m impact parameter, the initial distribution should be generated around $5.701\,\sigma$ at injection and $6.004\,\sigma$ at top energy. In reality, some smear induced by non-linear magnets must be taken
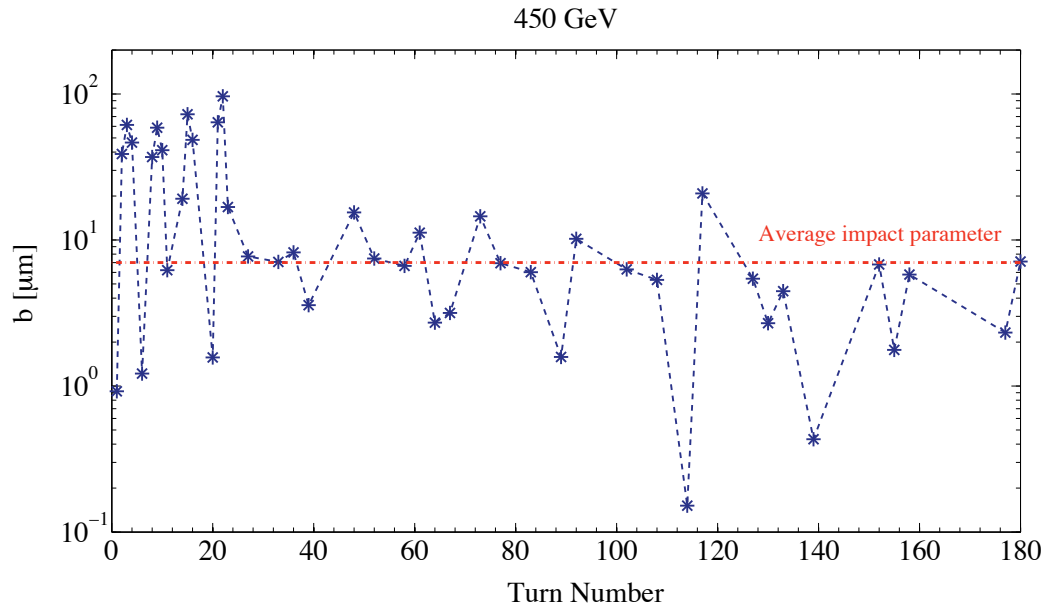
Figure 5.7: Impact parameter b as a function of the number of turns for the $b = 1\,\mu$m at first turn case, injection energy and Beam 1 horizontal halo. Only the particles interacting for the first time with the collimator are considered.

into account. Size and spread of the distributions that give, at the first turn, the desired impact parameter at the TCPs are listed in Table 5.1 for the two beams at injection and collision energy. An average increase, from IP1 to IR7, of the order of $50\,\mu$m at $450\,$GeV and of $10\,\mu$m at $7\,$TeV is found.

This smearing is amplified by multi turn effects with an increase of b by up to a factor of 100. In Fig. 5.7 the variation of b as function of the number of turns is presented for the injection energy case (Beam 1 horizontal halo). The impact parameter is evaluated averaging over all the particles impacting for the first time with the collimator at the selected turn. The plot shows that b is modulated by the phase advance between consecutive turns and that it reaches its maximum after 22 turns. The value of b averaged over 200 turns is $7\,\mu$m.

Dedicated studies were performed to estimate the influence of the impact parameter on the global and local cleaning inefficiency. For this purpose a scan over b was done for the two beams at injection and collision energy. Results are presented here for Beam 1 at $450\,$GeV. Using the $17\,$m β_z^* optics, several values of b from $0.1\,\mu$m up to $250\,\mu$m were considered and the relative inefficiency curves are shown in Fig. 5.8.
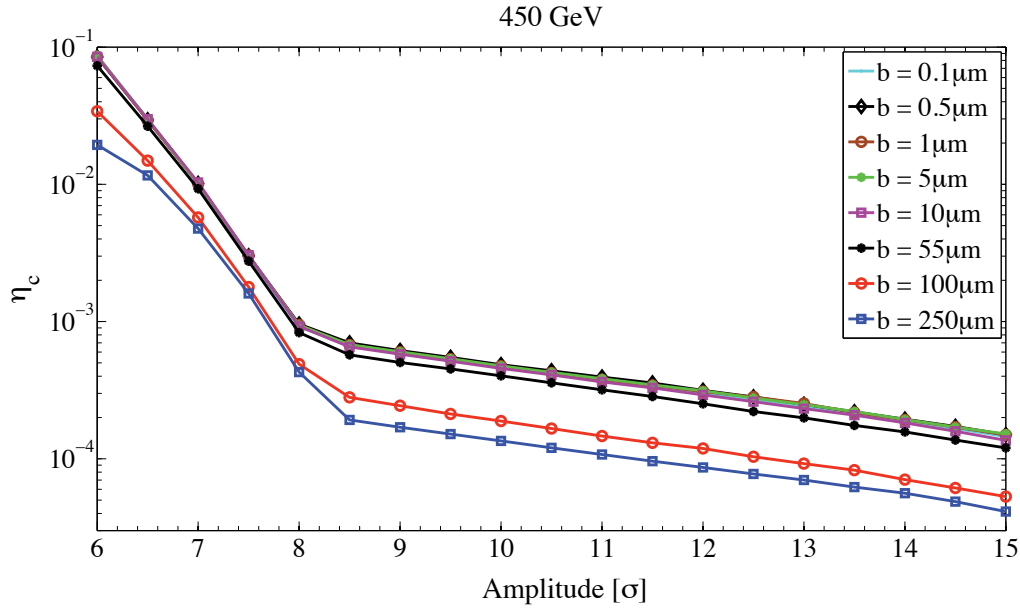
Figure 5.8: Inefficiency curves for impact parameters at first turn varying from $0.1\,\mu$m up to $250\,\mu$m. The statistical error is within the marker width.

Globally, the inefficiency of the LHC collimation system does not change for b spanning from $0.1\,\mu$m up to $10\,\mu$m while it starts decreasing for $b = 55\,\mu$m (becoming better). For higher impact parameters there is an average gain of a factor of two. This is due to the fact that the impact parameter averaged over the full number of

turns varies slightly (from 6.7μm up to $8.8\,\mu$m) for b up to $10\,\mu$m and starts then increasing significantly for higher b (up to $275\,\mu$m for an initial b of $250\,\mu$m). For $b{>}55\,\mu$m the probability of having particles absorbed at the primary collimators is higher, as well as the chance for the out-going particles to interact with one of the downstream collimators. Looking at the local cleaning inefficiency and in particular at the highest peak corresponding to losses on a superconducting magnet ($\tilde{\eta}_{cold}^{max}$), equivalent results are found (see Fig. 5.9).

It is concluded, that performance estimates can be artificially better when impact parameters become too high. Sextupoles for chromaticity corrections were used for all studies performed during this work. The impact parameter was checked to be small enough, that error in cleaning efficiency are below about 10%.
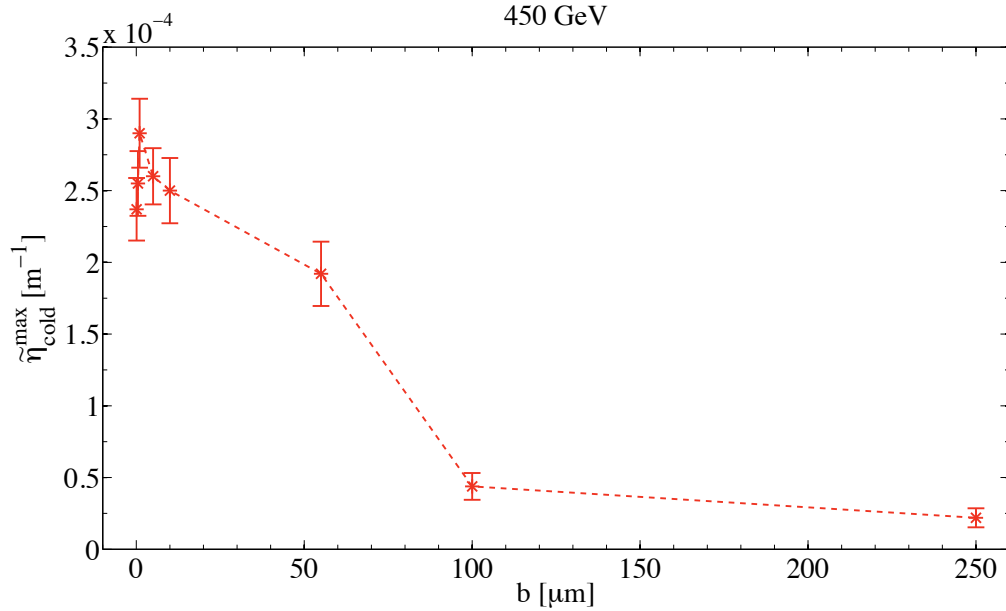
Figure 5.9: Local cleaning inefficiency corresponding to the highest peak of losses on a superconducting magnet for b at first turn varying from $0.1\,\mu$m upto $250\,\mu$m. Error bars indicate the statistical error.

Chapter 6

Simulations for LHC Collimation Commissioning

This chapter contains the main results of a large number of simulations performed for several optics schemes and possible settings of collimators during the LHC beam commissioning. The degradation of the cleaning efficiency as a function of machine and collimator imperfections is evaluated for the first time with multiple errors.

6.1 Efficiency of the LHC collimation system after ideal beam based setup

The performance of the LHC collimation system is evaluated by deriving detailed loss maps through the use of "SixTrack" and a realistic machine aperture model as described in section 5.3. The horizontal, vertical and skew (radial distribution) halos are simulated separately. Ideally, for each optics and collimator settings, all the halos should be analyzed, for both beams, in order to identify the one imposing the tightest limitation in beam intensity for safe machine operation. This has been done for the ideal machine and nominal collimator layout of the full phase 1 system (see section 4.3).

6.1.1 Perfect machine at injection energy

In Table 6.1 the values of local cleaning inefficiency $\tilde{\eta}_{max}^{cold}$ are listed for all the mentioned halos at injection energy. The error on $\tilde{\eta}_{max}^{cold}$ is purely statistical and is given by:

$$\sigma_{\tilde{\eta}_{cold}^{max}} = \frac{\sigma_{N_{lost}^{\Delta s}}}{\Delta s \cdot N_{abs}} \tag{6.1}$$

where

$$\sigma_{N_{lost}^{\Delta s}} = \sqrt{N_{lost}^{\Delta s}}. \tag{6.2}$$

Throughout this work a longitudinal aperture binning of $\Delta s = 10\,\text{cm}$ was used.

Table 6.1: $\tilde{\eta}_{max}^{cold}$ for the nominal machine, horizontal, vertical and skew halo, Beam 1 and Beam 2, injection optics ($17\,\text{m}\ \beta_z^*$). The error on $\tilde{\eta}_{max}^{cold}$ is purely statistical. $6.4 \cdot 10^6$ particles were tracked over 200 turns. The number of absorbed protons is listed for each case.

	Beam 1		Beam 2	
	$\tilde{\eta}_{max}^{cold}$ $[10^{-5}\text{m}^{-1}]$	tot. abs.	$\tilde{\eta}_{max}^{cold}$ $[10^{-5}\text{m}^{-1}]$	tot. abs.
horizontal	19.2 ± 1.8	6,033,061	5.6 ± 1.0	6,062,911
vertical	3.5 ± 0.7	6,344,013	10.1 ± 1.3	6,351,093
skew	0.6 ± 0.3	6,388,541	0.5 ± 0.3	6,179,590

Fig. 6.1 shows the loss map for the Beam 1 horizontal halo at 450 GeV, that is the worst injection case. Losses on superconducting magnets appear downstream of
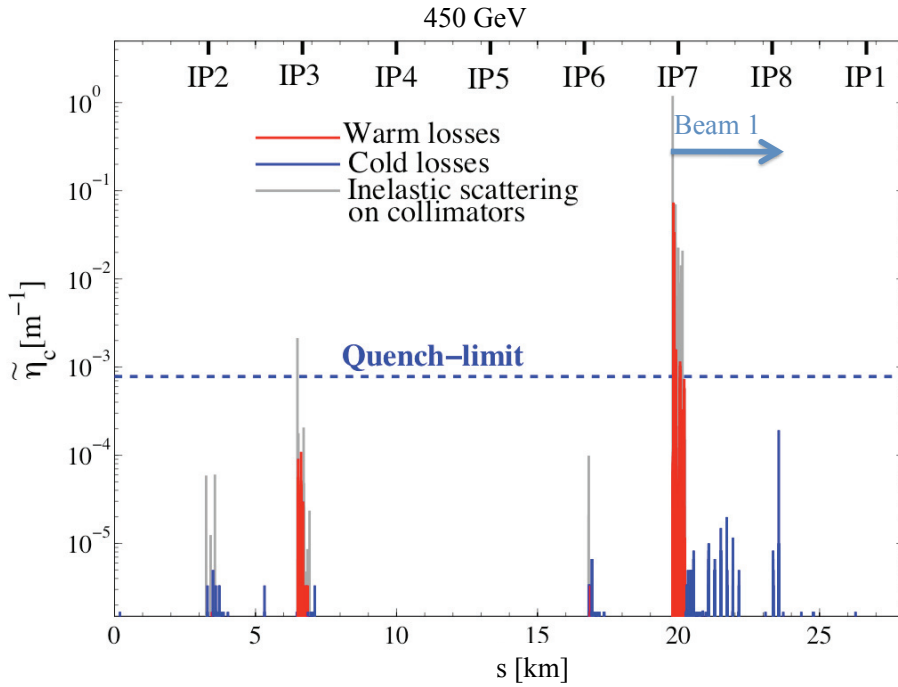
Figure 6.1: Loss map for the horizontal halo of Beam 1 at injection energy and for the nominal phase 1 collimator settings.

the injection protection collimators in IR2, of the cleaning insertions in IR3 and IR7

and of the protection collimators located in IR6. The highest peak is downstream of IP8 where the β_x function has a maximum (asymmetric optics see Fig. 6.2); $\tilde{\eta}_{max}^{cold}$ is anyhow well below the quench limit ($\tilde{\eta}_q = 7.8 \cdot 10^{-4} \, \mathrm{m}^{-1}$).
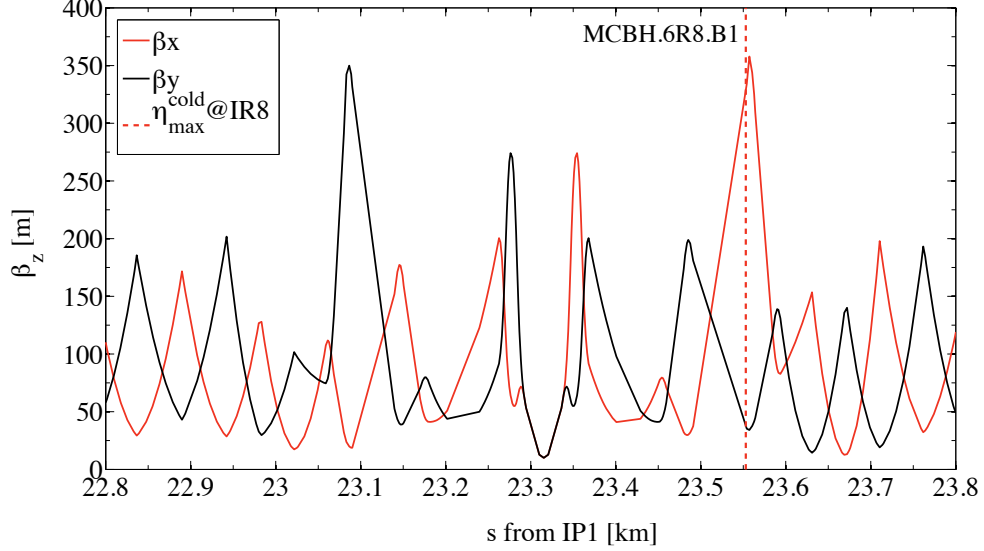
Figure 6.2: β_x and β_y functions around IP8. The location of $\tilde{\eta}_{max}^{cold}$ the Beam 1 horizontal halo at injection energy is shown. The optics around IP8 is asymmetric and the β-function reaches its maximum downstream of the interaction point.

Even if not shown here, considering the same beam, similar loss patterns are found for the other halos, with the exception that for the vertical one the dominant cold peak is in IR2. Beam 2 and Beam 1 loss maps present systematic differences due to the asymmetry of the machine [14]. Beam 2 is injected in IR8 and the collimators for protection against injection failures are hence located in this insertion. $\tilde{\eta}_{max}^{cold}$ is found just downstream of these elements for the vertical and skew halo, while it is in IR6 for the horizontal one.

6.1.2 Perfect machine at collision energy

At collision energy the Beam 1 vertical halo is the most critical one (see Table 6.2 and Fig. 6.3).

The absolute number of particles lost on the machine aperture is smaller than at injection, and the losses are mainly all concentrated in the region just downstream of the betatron cleaning insertion. However, these losses exceed the quench limit ($\tilde{\eta}_q = 1.7 \cdot 10^{-5} \, \mathrm{m}^{-1}$) introducing an important limitation on the maximum allowed beam intensity I_{max} to 37% of its nominal value (see section 4.1.4) [14]. Again only the loss map referring to the worst performance is shown but the remaining

Table 6.2: $\tilde{\eta}_{max}^{cold}$ for the nominal machine, horizontal, vertical and skew halo, Beam 1 and Beam 2, nominal collision optics (see Table 2.4 "lowb.coll_all" case). $5.76 \cdot 10^6$ particles were tracked over 200 turns for the horizontal and vertical halos and over 400 turns for the skew halo. The number of absorbed protons is listed for each case.

	Beam 1		Beam 2	
	$\tilde{\eta}_{max}^{cold}$ $[10^{-5}\mathrm{m}^{-1}]$	tot. abs.	$\tilde{\eta}_{max}^{cold}$ $[10^{-5}\mathrm{m}^{-1}]$	tot. abs.
coll.hor.	3.2 ± 0.7	5,685,752	2.6 ± 0.7	5,747,982
coll.vert.	4.6 ± 0.9	5,621,437	2.6 ± 0.7	5,716,251
coll.skew	1.7 ± 1.0	1,739,076	3.4 ± 1.5	1,455,572
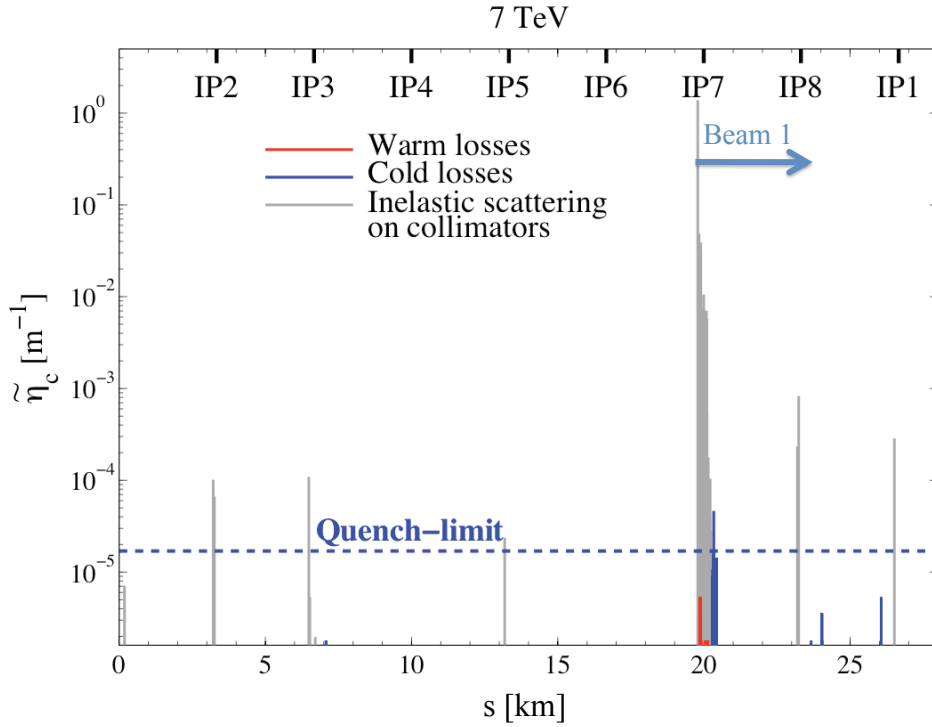
Figure 6.3: Loss map for the Beam 1 vertical halo at collision energy and optics "lowb.coll_all" (see Table 2.4).

Beam 1 halos have similar behaviors. For Beam 2 the losses gather downstream of IR7 (counterclockwise) with some particles lost in sector 6-7. Losses in superconducting magnets are dominated (about 94%) by particles experiencing single diffractive scattering in the primary collimators (see top Fig. 6.4). These particles are interacting only with the TCPs and lose part of their energy during this interaction. When such off-momentum particles exit from the zero dispersion region of

IR7, they deviate from the nominal betatron orbit and they have a high probability of being immediately lost in the dispersion suppressor region (see bottom Fig. 6.4).

Starting from the loss maps at 7 TeV, several FLUKA simulations were performed to evaluate the energy deposition on the most critical cold regions downstream of the cleaning insertions. The worst case of thermal load was found for the horizontal beam halo and corresponds to $3.7\,\text{mW}\cdot\text{cm}^{-3}$ on the MQ11 quadrupole of IR7 [70]. This estimate is valid both for Beam 1 and Beam 2. A comparable energy deposition of $3.1\,\text{mW}\cdot\text{cm}^{-3}$ was also found on the MQY.4L6.B2 magnet (IR6) for Beam 2 [71]. The main source of radiation in IR6 are the electromagnetic showers originating from the TCSG installed downstream of the TCDQAs in the dump region. The local cleaning inefficiency at the TCSG.4R6.B2 collimator, that corresponds to the defined energy deposition on the downstream elements, is $\tilde{\eta}_{TCSG}^{IR6}=1.53\cdot10^{-4}\,\text{m}^{-1}$.

FLUKA simulations predict an energy deposition on the superconducting magnets which is a factor of 1.4 lower than the quench limit. Tracking simulations, on the other hand, predict losses above the quench limit by up to a factor of 2.7. A conservative assumption that particles deposit their full energy over 10 cm is made for these studies (see section 6.1.1). This is done in order to leave some margin for imperfections and uncertainties on the considered quench threshold (see section 6.2.5). Using a $1\,\text{m}\ \Delta s$ in eq. 5.1 would reduce the local cleaning inefficiency on average by a factor of 5 and make it consistent with the FLUKA results.

The number of skew halo particles absorbed by the collimation system, for the two beams at collision energy, is very low. Tracking the same number of particles $(5.76\cdot10^6)$, it was found that mostly all of them are absorbed after 200 turns in the horizontal and vertical cases, while 70% of the skew halo particles keep circulating in the machine without interacting with any collimator even after 400 turns. Fig. 6.5 shows the number of absorptions at the collimators (top) and of losses on the machine aperture (bottom) for Beam 2 halos over the first 120 turns.

The studies performed and presented in this work, concern mainly horizontal and/or vertical halo. The choice to study both of them for the two beams or to concentrate only on particular cases depends on the different demands of the analyzed scenarios. The complete exam, presented here, for the nominal optics and collimator settings provides a useful tool to estimate, for each scenario, the cleaning efficiency of the collimation system.
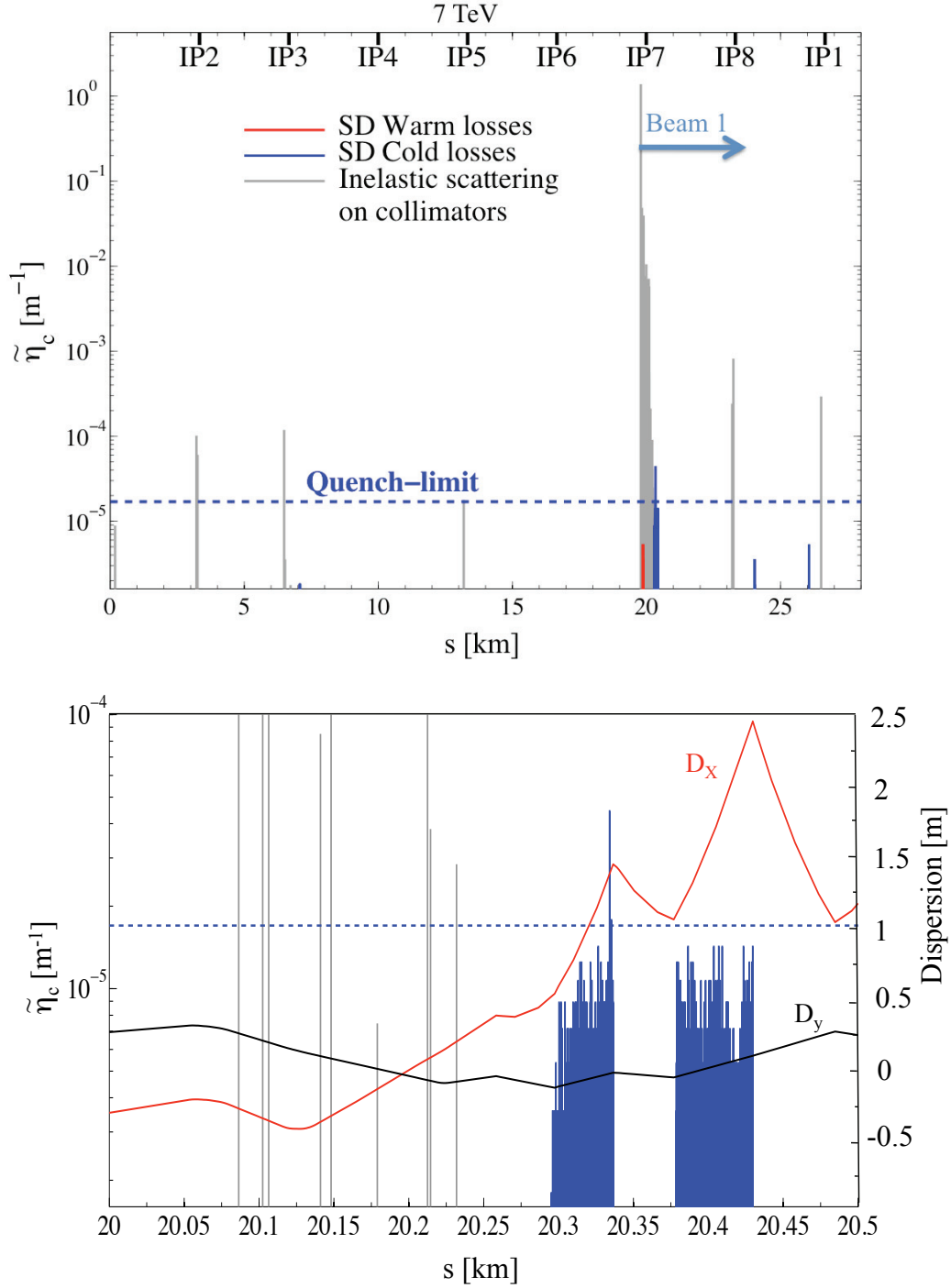
Figure 6.4: Same case as in Fig. 6.3 but just for losses of particles which experienced single diffractive (SD) scattering at the primary collimators (top). Zoom over the region of the dispersion suppressor downstream of IR7 (bottom). Horizontal and vertical dispersion are shown.
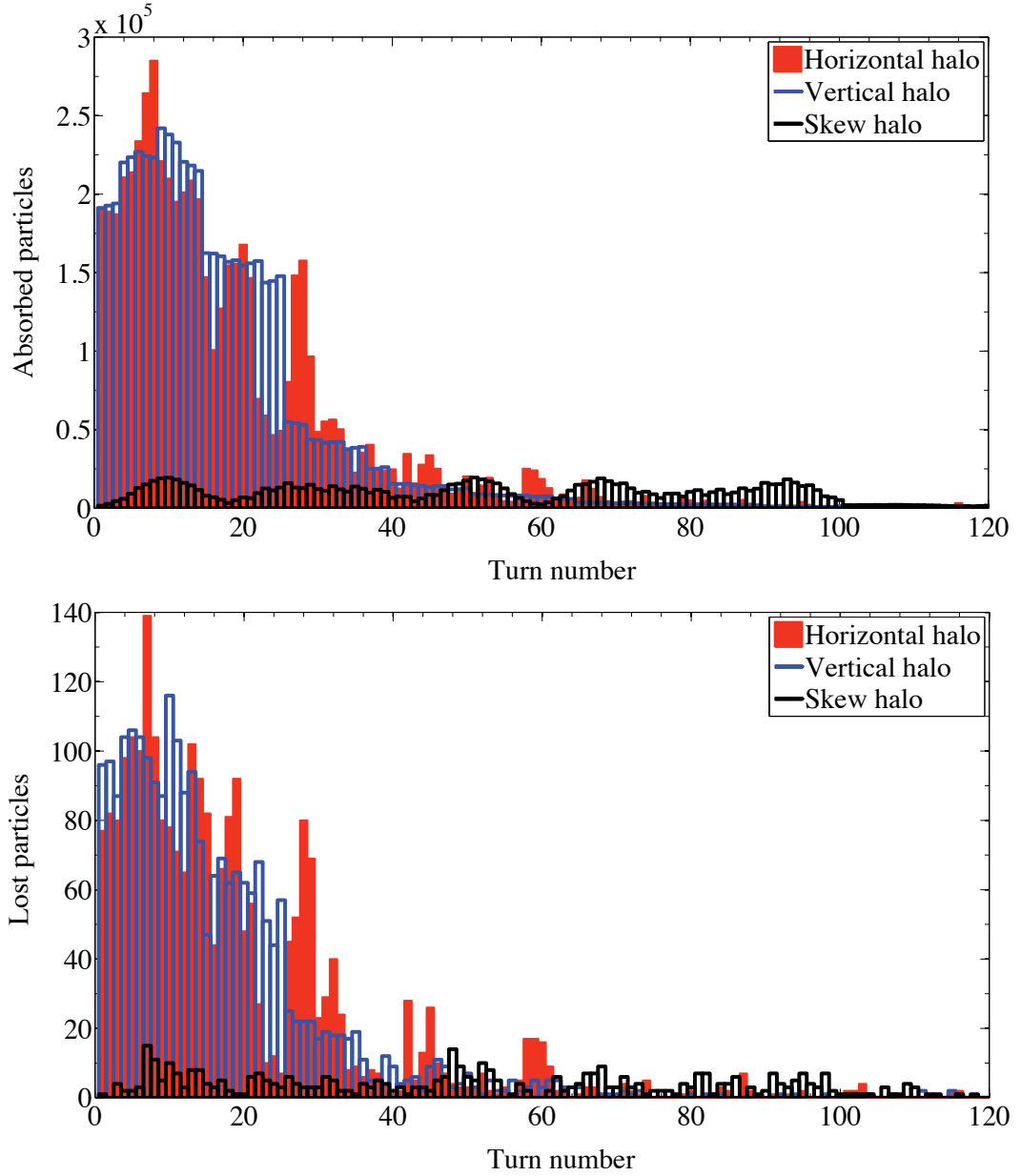
Figure 6.5: Number of particles absorbed at the collimators (top) and lost in the machine aperture (bottom) for horizontal (red), vertical (blue) and skew (black) halos over the first 120 turns.

6.1.3 Beam loss maps during collimator beam based alignment

The beam based alignment procedure (see section 7.2.3) requires that each collimator jaw touches directly the beam halo, acting temporarily as a primary collimator. The multi-stage cleaning hierarchy is violated. The alignment procedure must therefore be carried out at low beam intensity. Several scenarios have been analyzed for Beam 1, in order to quantify the maximum usable number of particles. In the first scheme the last IR7 secondary collimator (TCSG.6R7.B1) was set to act as a primary collimator (see Table 6.3). All the other collimators were kept at their nominal

Table 6.3: $\tilde{\eta}_{max}^{cold}$ is listed for the different configurations used to simulate the beam based alignment of the TCSGs, TCLAs and TCTs. The loss factor in cleaning efficiency with respect to the nominal settings is shown. For all these cases the rest of the system stays at the nominal settings (see sections 4.3.2 and 4.3.3).

Injection	Collimator@5.7σ	$\tilde{\eta}_{max}^{cold}$ [10^{-2}m^{-1}]	Loss factor
TCP@6σ	TCSG.6R7.B1	1.63 ± 0.02	84.9
	TCLA.A7R7.B1	2.20 ± 0.02	114.6
Collision	Collimator@6σ	$\tilde{\eta}_{max}^{cold}$ [10^{-4}m^{-1}]	Loss factor
TCP@6.3σ	TCSG.6R7.B1	1.51 ± 0.41	4.8
	TCLA.A7R7.B1	2.76 ± 0.22	8.7
	TCTH.4R2.B1	2.59 ± 0.22	8.2
	TCTV.4R2.B1	6.40 ± 0.34	13.8
	TCTH.4R5.B1	7.24 ± 0.45	22.8
	TCTV.4R5.B1	1.41 ± 0.16	3.1

settings except the primary collimator (TCP.C6L7.B1) which was retracted by 0.3σ. The horizontal halo was tracked and the results at injection energy are shown in Fig. 6.6. The comparison with the loss map for the nominal settings (Fig. 6.1) reveals both the presence of new loss locations and the increase in the number of particles lost in the usual positions. In particular $\tilde{\eta}_{max}^{cold}$ is still in IR8 but is 84.9 times higher and I_{max} is reduced to 5% of I_{nom}. Moreover the number of particles absorbed at the TCLAs increase in average by a factor of 50. The results for the same settings but at collision energy are illustrated in Fig. 6.7. In this case the load on the warm magnets in IR7 is slightly reduced, few new cold loss locations appear and $\tilde{\eta}_{max}^{cold}$ is enlarged by a factor of 4.8. In addition the number of particles absorbed at the TCTs increases by a factor of 9.7 in IR1, 25.2 in IR2 and 20.1 in IR8 while IR5 stays mostly unchanged.

Even tighter conditions are found if the alignment of the last IR7 absorber (TCLA.A7R7.B1, horizontal) is simulated. $I_{max} = 3.5\%$ of I_{nom} is found for the injection energy case using a setting of collimators completely analogous to the pre-
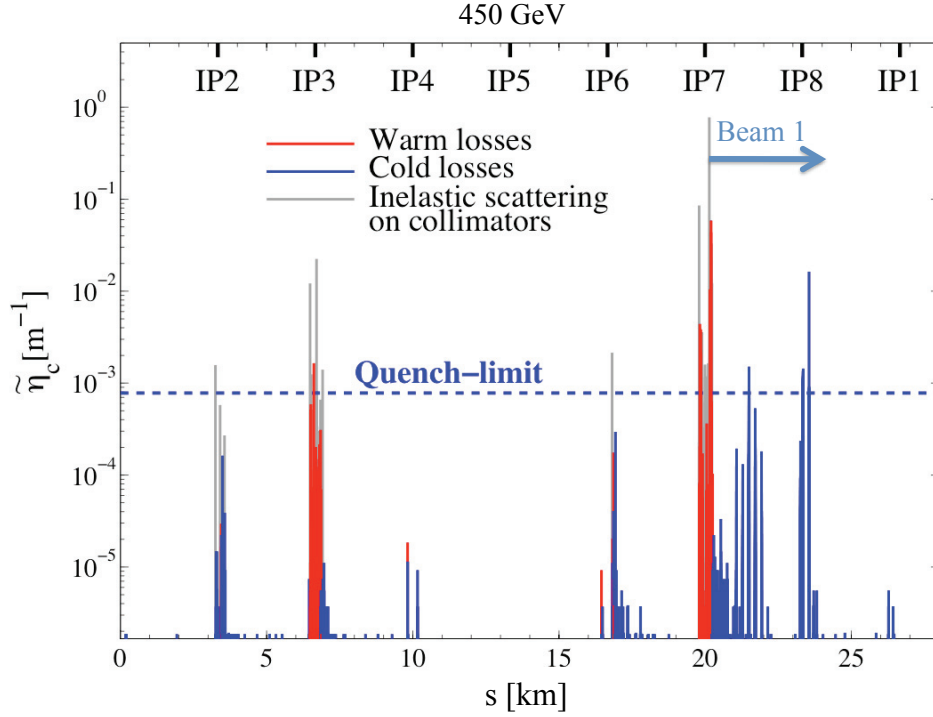
Figure 6.6: Loss map for the $17\,\mathrm{m}$ β_z^* injection optics and the Beam 1 horizontal halo. The TCP.C6L7.B1 collimator is set at $6\,\sigma$ while the last secondary collimator (TCSG.6R7.B1) has an half gap of $5.7\,\sigma$. The rest of the collimation system is set at the nominal openings.

vious one, but this time with the TCLA set as a primary. A strong increase in the absorbed particles is recorded, at $7\,\mathrm{TeV}$, at the tertiary collimators in IR8 (about 3 orders of magnitude more than the nominal settings) and at the TCSG in IR6 (2 orders of magnitude) imposing a reduction of I_{max} to $<2\%$ of I_{nom}.

Finally, the TCTs must be aligned for the low-beta collision optics. Horizontal and vertical halos were simulated when setting the TCTH and TCTV half gaps at $6\,\sigma$ in IR2 and IR5 in order to analyze two different crossing schemes (vertical and horizontal) and β_z^* values ($10\,\mathrm{m}$ and $0.55\,\mathrm{m}$). Table 6.3 contains the $\tilde{\eta}_{max}^{cold}$ for all the cited cases and $I_{max} = 2\%$ of I_{nom} can be calculated for the alignment of tertiary collimators. The high peaks (up to $7 \cdot 10^{-1}\ \mathrm{m}^{-1}$) appearing at the considered TCTs, impose to use a further reduced intensity for the setup of the full system in order to avoid damage. For reference, the loss maps for various collimator types during setup are shown in Appendix B.

Ideally the beam based alignment of the full system should be performed with 1-5 nominal bunches (1.15×10^{11} p per bunch) at regular intervals given by the machine stability.
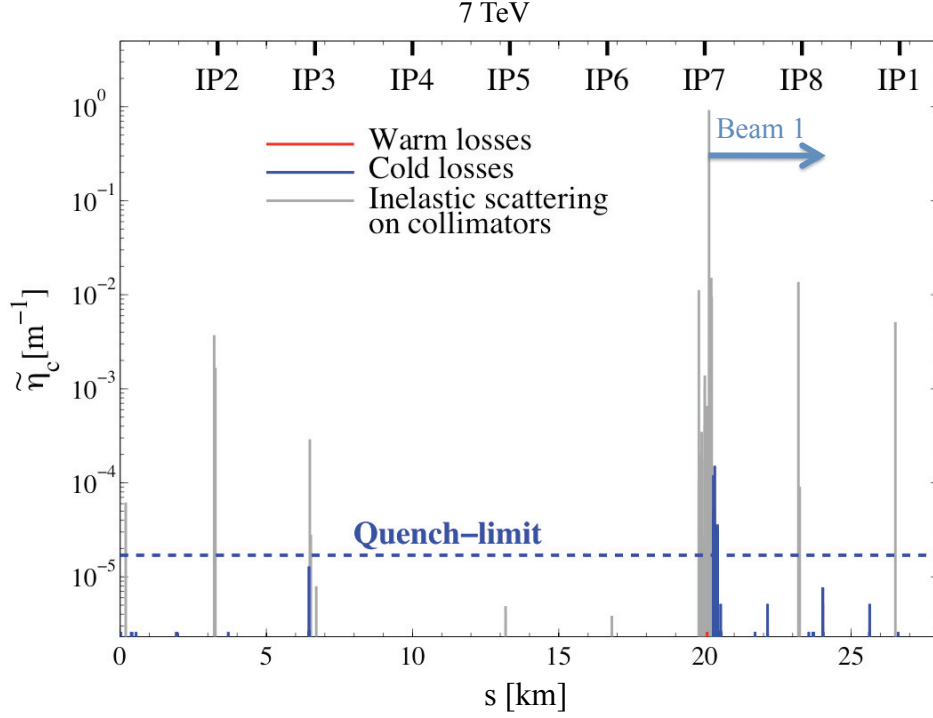
Figure 6.7: Loss map for the low-beta optics and the Beam 1 horizontal halo. The TCP.C6L7.B1 collimator is set at $6.3\,\sigma$ while the last secondary collimator (TCSG.6R7.B1) has an half gap of $6\,\sigma$. The rest of the collimation system is set at the nominal openings.

6.1.4   Tolerance budget for collimation

The tolerance budget T_b in setting primary and secondary collimators for an optimized cleaning efficiency is defined as [72]:

$$T_b = n_2 - n_1 - 0.4\sigma \tag{6.3}$$

where n_2 and n_1 are respectively the half gap of the TCSGs and of the TCPs. According to this formula, at injection energy a setup accuracy of $400\,\mu$m still allows $300\,\mu$m closed orbit transient change with 10% dynamic beta-beat ($0.3\,\sigma$). At collision only $150\,\mu$m, out of the $250\,\mu$m corresponding to the nominal 1σ retraction, are left as a margin for beam instabilities. It is then evident that only a stringent control and reproducibility of the beam conditions can ensure safe and efficient operation of the LHC. The tolerance budget is evaluated in more detail in chapter 8.

6.1.5   Performance reach of minimal collimation systems

Efficiency studies for various implementations of the LHC collimation system have been performed, taking into account the evolution in optics and beam intensity

according to the LHC commissioning schedule [64]. At low intensity the number of collimators needed, their openings and setup tolerances are less demanding than during nominal operation. For this reason different minimal and relaxed settings were studied in order to define the optimal procedure for the setup of the system.

6.1.5.1 Collimator commissioning scenarios at 450 GeV

Several studies with reduced complements of collimators, at their nominal openings, were carried out at injection energy. Fig. 6.8 shows the performance improvement
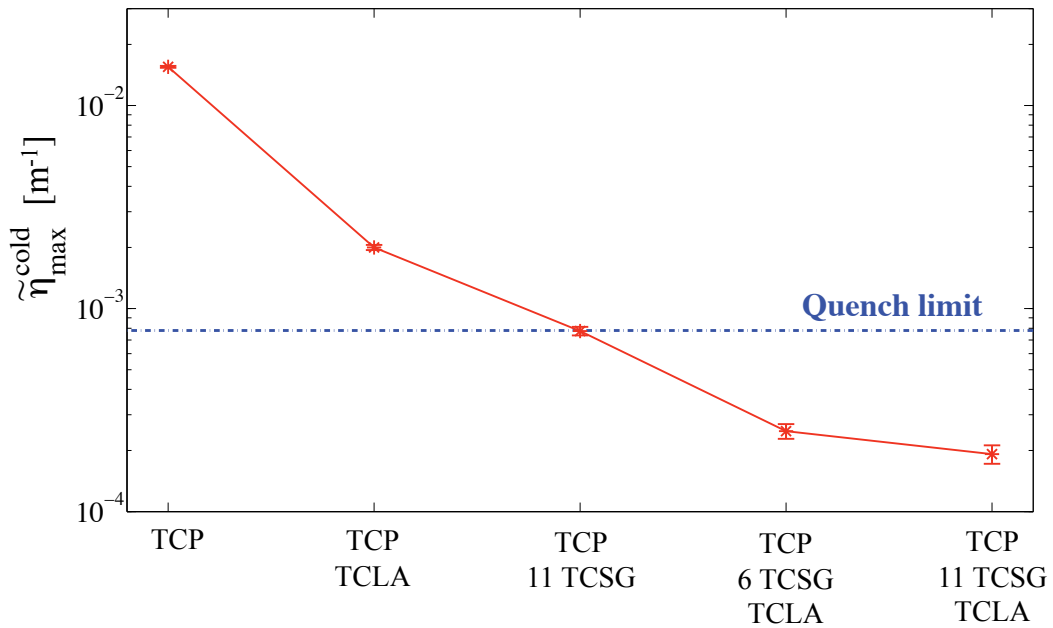
Figure 6.8: $\tilde{\eta}^{cold}_{lmax}$ for different collimator layouts at injection energy (Beam 1 horizontal halo). Collimators are set to the nominal openings, protection elements in injection and dumping regions are included.

when shifting from a single stage to a multistage cleaning system. When the TCLAs are added to the TCPs the local cleaning inefficiency is lowered by a factor of 7.8. If the two-stage system is formed by primary and secondary collimators the performance is improved by a factor of 20 and the operation of the 450 GeV machine with nominal intensity is possible. A further gain of a factor 3.5 is obtained by implementing this configuration with the TCLAs (nominal phase 1 system). For the 2008 start up only six out of the eleven foreseen secondary collimators are installed in the betatron cleaning insertion of IR7 (see Table 6.4). Such a reduced system implies a decrease in the local cleaning efficiency with respect to the nominal phase 1 layout by 30%. All these results are valid both during injection (TDI and TCLI at 6.8 σ)

Table 6.4: List of collimators installed in the LHC ring for the 2008 run. Collimators used to perform simulations for the 450 GeV collision optics are indicated in the last column.

Beam 1	Beam 2	450 GeV complement
TCP.6L3.B1	TCP.6R3.B2	X
TCSG.5L3.B1	TCSG.5R3.B2	X
TCSG.4R3.B1	TCSG.4L3.B2	X
TCSG.A5R3.B1	TCSG.A5L3.B2	X
TCSG.B5R3.B1	TCSG.B5L3.B2	X
TCLA.A5R3.B1	TCLA.A5L3.B2	
TCLA.B5R3.B1	TCLA.B5L3.B2	
TCLA.6R3.B1	TCLA.6L3.B2	
TCLA.7R3.B1	TCLA.7L3.B2	
TCSG.4R6.B1	TCSG.4L6.B2	X
TCDQA.A4R6.B1	TCDQA.A4L6.B2	X
TCDQA.B4R6.B1	TCDQA.B4L6.B2	X
TCP.B6L7.B1	TCP.B6R7.B2	X
TCP.C6L7.B1	TCP.C6R7.B2	X
TCP.D6L7.B1	TCP.D6R7.B2	X
TCSG.A6L7.B1	TCSG.A6R7.B2	X
TCSG.A5L7.B1	TCSG.A5R7.B2	X
TCSG.B4L7.B1	TCSG.B4R7.B2	
TCSG.A4L7.B1	TCSG.A4R7.B2	X
TCSG.A4R7.B1	TCSG.A4L7.B2	X
TCSG.6R7.B1	TCSG.6L7.B2	X
TCLA.A6R7.B1	TCLA.A6L7.B2	
TCLA.B6R7.B1	TCLA.B6L7.B2	
TCLA.C6R7.B1	TCLA.C6L7.B2	
TCLA.D6R7.B1	TCLA.D6L7.B2	
TCLA.A7R7.B1	TCLA.A7L7.B2	
TCTH.4L1.B1	TCTH.4R1.B2	
TCTVA.4L1.B1	TCTVA.4R1.B2	
TCTH.4L2.B1	TCTH.4R2.B2	
TCTH.4L5.B1	TCTH.4R5.B2	
TCTVA.4L5.B1	TCTVA.4R5.B2	
TCTH.4L8.B1	TCTH.4R8.B2	X
TDI.4L2.B1	TDI.4R8.B2	X
TCLIB.6R2.B1	TCLIB.6L8.B2	

and during the flat bottom (injection protection collimators retracted), preceding the energy ramp. These scenarios include the presence of the protection elements in the dump region of IR6.

A commissioning run with collisions at $450\,\mathrm{GeV}$ was initially planned for 2007 (see section 2.4.2). According to the production and installation schedule, only 18 collimators per beam (see Table 6.4) would have been installed at that time in the LHC ring. Dedicated simulations were performed to establish the maximum intensity reach of the machine with such a reduced system for the horizontal and vertical halo of the two beams. The resulting $\tilde{\eta}_{max}^{cold}$ for the "Collision at $450\,\mathrm{GeV}$" optics (see Table 2.5) are listed in Table 6.5: no intensity limitation was found considering that only 43 bunches (4×10^{10} protons per bunch) were foreseen for this run. The updated settings for 2008 beam commissioning include the installation of all TCLAs, TCTH and TCTV in IR1 and IR5 and the TCTH and TCLIB in IR2 and IR8 (see Table 6.4). This system will be able to ensure safe operation of the ideal machine at $450\,\mathrm{GeV}$ with nominal intensity, also in case of collisions.

Table 6.5: $\tilde{\eta}_{max}^{cold}$ for the "Collision at $450\,\mathrm{GeV}$" optics with a reduced system of 18 collimators per beam which are set at the nominal injection settings.

Halo	$\tilde{\eta}_{max}^{cold}$ $[10^{-4}\mathrm{m}^{-1}]$
B1 horizontal	9.69 ± 0.40
B2 horizontal	9.41 ± 0.40
B1 vertical	2.32 ± 0.20
B2 vertical	1.38 ± 0.15

6.1.5.2   Collimator commissioning scenarios at high energy (7 TeV)

Before reaching the nominal luminosity, intermediate steps with higher $\beta_z{}^*$ values and lower beam intensities are foreseen. This section shows results of several possible collimation scenarios for the early collision optics [73] (see section 2.4.2). The full phase 1 layout was used for the cleaning insertions, whereas the TCTVBs in IR2 and IR8 and the TCLPs downstream of IP1 and IP5 were not included because they are not installed. Simulations for Beam 1 and Beam 2 horizontal halos were carried out for this optics and the collimation settings listed in Table 6.6.

The cleaning insertions are reduced to a one stage system in scenario 1, a two-stage system with the absorbers acting as secondaries in scenario 2, and a canonical three-stage system in scenario 3. This last scenario presents more relaxed tolerances than the nominal one, placing the TCSGs at 9.5σ instead of 7σ and the TCLAs at 11σ instead of 10σ. The TCTs in the experimental regions are put at $17\,\sigma$.

Similarly to the $450\,\mathrm{GeV}$ case, all the analyzed scenarios exhibit an increase in the number of protons lost in the IR7 dispersion suppressor magnets, when compared to

Table 6.6: Collimator half gaps, in σ units, for different commissioning scenarios and the early collision optics. The TCTs installed at the experimental regions are placed at $17\,\sigma$.

	Half gaps [σ]							
	IR3			IR7			IR6	
scenario	TCP	TCSG	TCLA	TCP	TCSG	TCLA	TCSG	TCDQA
1	15	out	out	10	out	out	13.5	14
2	15	out	20	6	out	10	8	8.5
3	15	18	20	6	9.5	11	10	10.5
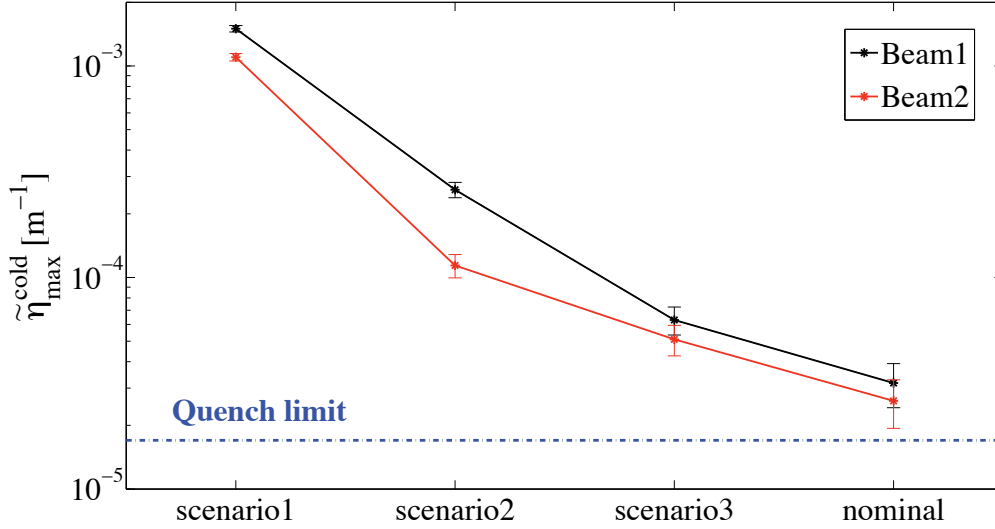
Figure 6.9: $\tilde{\eta}_{max}^{cold}$ for the nominal full phase 1 collimation system at 7 TeV and for the scenarios listed in Table 6.6. The maximum loss peak in superconducting magnets was found for the two beams in the dispersion suppressor downstream of the betatron cleaning insertion.

the nominal settings. The local cleaning inefficiency is increased by up to a factor of 46.8 for Beam 1 (scenario 1: $I_{max} = 1.3\%$ of I_{nom}) and a factor of 42.1 for Beam 2 (scenario 1: $I_{max} = 2\%$ of I_{nom}), see Fig. 6.9 for a summary.

The operation with secondary collimators completely retracted or set at larger openings requires to relax the half-gaps of the protection elements in the extraction region in order not to overload them. In scenario 1 and scenario 2, the IR6 collimators act as secondary collimators and absorb many more particles than in the case when they are in the shadow of the IR7 TCSGs. This effect is particularly evident for

Beam 2 since the dump region comes directly after the betatron cleaning insertion: $\tilde{\eta}_{TCSG}^{IR6}$ increases up to a factor of 143.9 (Beam 2 scenario 1, see Fig. 6.10).
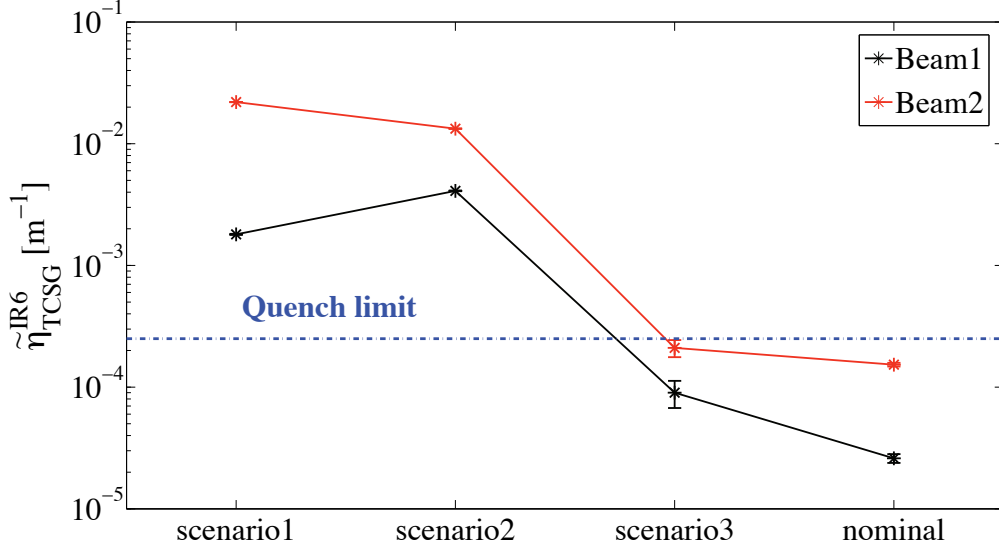
Figure 6.10: $\tilde{\eta}_{TCSG}^{IR6}$ for the nominal full phase 1 collimation system at 7 TeV and for the commissioning scenarios listed in Table 6.6.

According to what was stated in section 6.1, the nominal collimator setup produces a thermal load of 3.1 mW·cm^{-3} (for $\tilde{\eta}_{TCSG}^{IR6} = 1.53 \cdot 10^{-4}$ m^{-1}) on the superconducting magnets of the dump region. A linear scaling of the energy deposition with the beam load on the TCSG in IR6, allows to calculate $\tilde{\eta}_{TCSG}^{IR6} = 2.50 \cdot 10^{-4}$ m^{-1} as the value that induces the quench of the downstream magnets (corresponding to 5 mW·cm^{-3}). The limitation in terms of beam intensity for the scenarios presented here comes then from the number of absorptions of Beam 2 halo particles at the IR6 collimators (scenario 1: $I_{max} = 1\%$ of I_{nom}). In order to reduce the load on these elements different options were analyzed for scenario 2, by relaxing the opening of IR6 collimators (see Table 6.7). In Fig. 6.11 the maximum beam intensity for the ideal machine (Beam 2 horizontal halo) is plotted as a function of the described collimator settings in IR7 and IR6. When the TCSGs are completely retracted (scenarios 2, 2.2 and 2.3) the maximum intensity reach is approximately 3% of I_{nom}. I_{max} increases to 33% of I_{nom} as soon as the TCSGs are closed. Losses in the IR7 dispersion suppressor become the limiting factor when the IR6 collimators are in the shadow of the TCSGs (scenario 3.3 and nominal).

The machine operation with 156 bunches ($\approx 5\%$ of I_{nom}), as foreseen for the early collision optics, allows to keep the secondary collimators at relaxed settings, provided that the protection elements do not get excessive losses.

Table 6.7: Collimator half gaps, in σ units, for different options of scenario 2. The half gaps of the momentum cleaning insertion collimators do not change.

scenario	Half gaps [σ]				
	IR7			IR6	
	TCP	TCSG	TCLA	TCSG	TCDQA
2.2	6	out	10	9	9.5
2.3	6	out	11	9.5	10
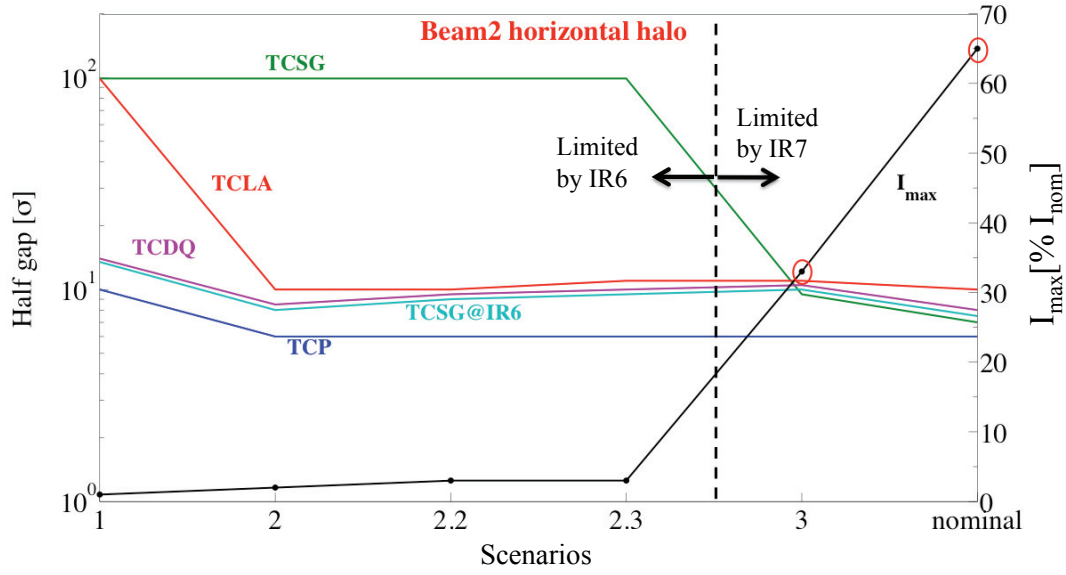
Figure 6.11: I_{max} at 7 TeV as a function of IR6 and IR7 collimator settings. The red circles refer to scenarios where the beam intensity is limited by losses in the IR7 dispersion suppressor.

The 2008 commissioning run foresees collisions at 5 TeV, results for this case are presented in section 6.1.6.

6.1.5.3   Trade off between efficiency and collimator-induced impedance

Setting the LHC collimators to larger gaps allows an easier machine operation and makes the system less sensitive to setup errors and beam instabilities. Moreover, increased half-gaps would reduce the collimator-induced impedance and improve limitation in maximum allowed beam intensity from impedance driven instabilities. At top energy, these instabilities can partially be damped by using Landau octupoles which create a tune spread, determining a stability area as shown in Fig. 6.12 [60].

Red and blue lines in the plot represent the stability limit for maximum Landau octupole current with negative and positive anharmonicity. The horizontal and vertical axes give the real and imaginary parts of the coherent tune shift.
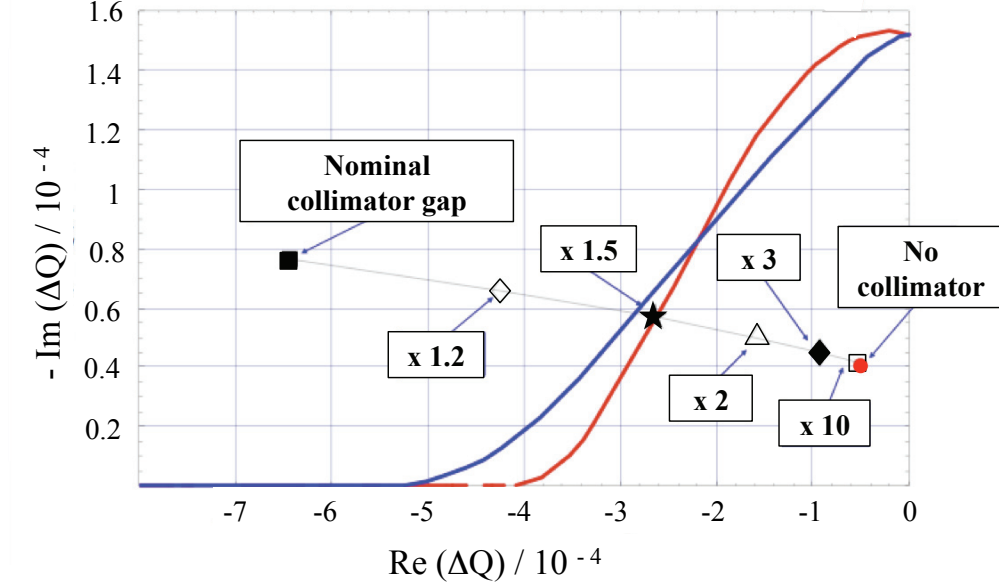
Figure 6.12: Stability limits at top energy as a function of the collimator openings: nominal collimator gap (black squares), no collimators (red circle), and intermediate situations where the collimator gap is increased by 20%, 50%, a factor of 2, 3 and 10 [60].

The points in Fig. 6.12 show the variation of machine impedance (that is proportional to the complex tune shift) as a function of the collimator openings. The nominal collimator settings for the collision optics bring the working point out of the stability region and I_{max} is limited to about 40% of I_{nom}. An increase in the collimator gaps by about 50% would be necessary to stabilize the nominal intensity beam (black star). For example: TCPs set at 9σ, TCSGs at 10.5σ and TCLAs at 15σ in IR7. It is seen that larger collimator gaps are beneficial for the machine impedance. On the other hand, larger gaps worsen the cleaning efficiency of the LHC collimation system, as shown in Fig. 6.13. The local cleaning inefficiency $\tilde{\eta}_{max}^{cold}$ is shown for different optics and collimator settings at 7 TeV (Beam 1 vertical halo):

- Scenario A: nominal collision optics and collimator settings (smallest gaps).

- Scenario B: nominal collision optics, all the collimator openings are relaxed by 3σ with respect to scenario A (LHC upgrade studies [74] compatible with 50% gap increase).

- Scenario C: 7 TeV unsqueezed optics, all the collimator openings are relaxed by $5\,\sigma$ with respect to scenario B.

- Scenario D: 7 TeV unsqueezed optics and constant collimator settings in mm (energy ramp commissioning studies, see section 6.1.6.1 and the 7 TeV case of Table 6.8).
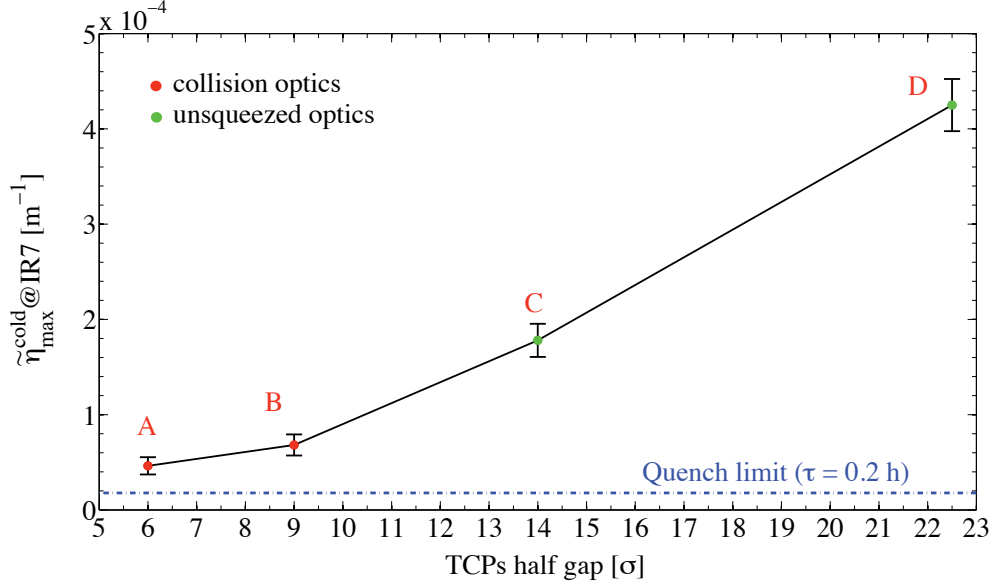
Figure 6.13: $\tilde{\eta}_{max}^{cold}$ at IR7 as a function of different settings and optics at 7 TeV. As indication of collimation gaps, the setting of the primary betatron collimators is given on the horizontal axis.

Losses in the dispersion suppressor downstream of IR7 are dominated by the single diffractive scattering events at the primary collimators (see section 6.1.2). At high energy these off-momentum particles are lost where the dispersion increases. The closer the collimators are to the machine cold aperture and the bigger the retraction is between the TCPs and the TCSGs, the higher are these losses. Scenario B could be used to alleviate impedance induced intensity limitations but with the price of a 30% worsening in cleaning efficiency. The maximum allowed intensity I_{max} would be reduced to 25% of I_{nom}, for the perfect machine and nothing would be gained from impedance reduction.

6.1.6 Performance of collimation during the energy ramp

The change in collimator settings from the 450 GeV "flat-bottom" to the 7 TeV "flat-top" part of the LHC cycle (Fig. 6.14) must be defined for the commissioning of the acceleration ramp.
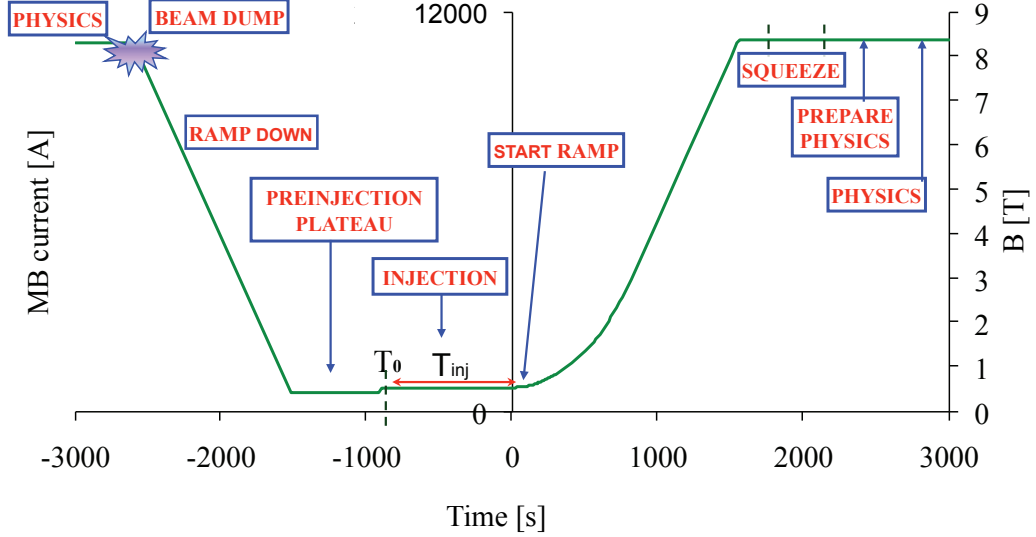
Figure 6.14: Current in the main dipoles MB and magnetic field B versus time. Beam is injected after each dump and accelerated up to 7 TeV (B=8.3 T). Squeeze of the optics and physics follow after reaching the top energy plateau [75].

For this purpose the cleaning performance of the complete phase 1 system was studied for several setups at different energies [76] (Beam 1 only). A beam life time τ of 0.1 hours was assumed to calculate the equivalent quench limit $\tilde{\eta}_q$ as a function of the energy (see Table 4.2 and eq. 4.10). A temporarily reduced life time is expected during parts of the ramp. The results presented in the following do not include losses of particles that are not captured by the RF bucket at the start of the ramp.

6.1.6.1 Constant collimator settings during ramp

The optics and the available aperture of the machine do not change during the acceleration and before the β_z squeeze at the IPs. Moreover, the accelerated beam is adiabatically damped and collimation gaps increase in terms of σ. One possible scenario is to close the collimators only after the end of the ramp before the change in the IR optics. Table 6.8 lists the half gaps of the collimator families at different energies in σ units. The normalized openings change as an effect of the decrease in beam size with energy, while the physical apertures (in mm) stay constant. T_b (see eq. 6.3) increases with energy and at 7 TeV is equal to $3.6\,\sigma$ (0.9 mm). On the other hand, the cleaning efficiency gets worse: losses downstream of the betatron cleaning insertion are two orders of magnitude higher at top energy than at 450 GeV both for vertical ($\tilde{\eta}_{max}^{cold} = 4.25 \cdot 10^{-4}\,\mathrm{m}^{-1}$) and horizontal ($\tilde{\eta}_{max}^{cold} = 4.05 \cdot 10^{-4}\,\mathrm{m}^{-1}$) betatron

Table 6.8: Collimator settings as a function of the beam energy: the collimators are kept at the same opening in mm as at $450\,\mathrm{GeV}$. Normalized openings change as an effect of the decrease in betatronic beam size with energy. The average betatronic σ at the primary collimator is shown.

Constant collimator settings (in mm)									
Energy	**σ**	**Half gap [σ]**							
[TeV]	**TCPs**	**IR3**			**IR6**		**IR7**		
	[μm]	TCP	TCSG	TCLA	TCSG	TCDQA	TCP	TCSG	TCLA
0.45	969	8	9.3	10	7	8	5.7	6.7	10
1	644	12	14	15	10.6	12	8.6	10.1	15
2	460	16	19	20	14	16	11.4	13.4	20
3	372	20.8	24.2	26	18.2	20.8	14.8	17.4	26
4	322	24	28	30	21	24	17	20	30
5	288	26.4	30.7	33	23	26.4	18.8	22.1	33
6	263	29.2	34	36.5	25.6	29.2	20.8	24.5	36.5
7	244	31.6	36.7	39.4	27.6	31.6	22.5	26.5	39.4

halo (see Fig. 6.15 and Fig. 6.16). I_{max} is reduced to 2% of I_{nom}. This limitation is also driven by the reduced quench limit $\tilde{\eta}_q$ from $7.8\cdot10^{-4}\,\mathrm{m}^{-1}$ to $8.7\cdot10^{-6}\,\mathrm{m}^{-1}$ (see section 4.1.1.2). This is an effect of increased magnet currents and higher stored beam energy. Vertical halo particles, which are lost at the cold aperture of the machine, mainly experience single diffractive scattering at the TCPs (see Fig 6.15 bottom), whereas this is not the case for losses at IR8 due to horizontal halo particles (see red circled region in Fig 6.16 bottom).

Looking at the behavior of losses in the IR7 dispersion suppressor, we find comparable results for the two halos with a slightly worse efficiency at top energy for the vertical plane (see Fig. 6.17 blue lines). $\tilde{\eta}_{max}^{cold}$ at IR7 increases with the acceleration: at low energy the particles are strongly deflected and are mainly lost in the warm magnets located in the betatron cleaning insertion. At higher energy more and more of the off-momentum particles are lost in the dispersion suppressor as explained in section 6.1.5.3.

The two planes differ in terms of the local cleaning inefficiency at IR8 (see Fig. 6.17 red lines). The maximum allowed beam intensity for the horizontal halo up to $4\,\mathrm{TeV}$, is determined by the losses on the MCBCH.6R8.B1 magnet. These losses are induced by the high value of β_x at this location (see Fig 6.2) and they decrease during acceleration. The vertical halo is instead dominated by losses in the dispersion suppressor of IR7 for energies $>1.5\,\mathrm{TeV}$. The actual phase 1 collimation system cannot provide any cure for the losses due to single diffractive scattering events in the dispersion suppressor region downstream of the betatron cleaning insertion.
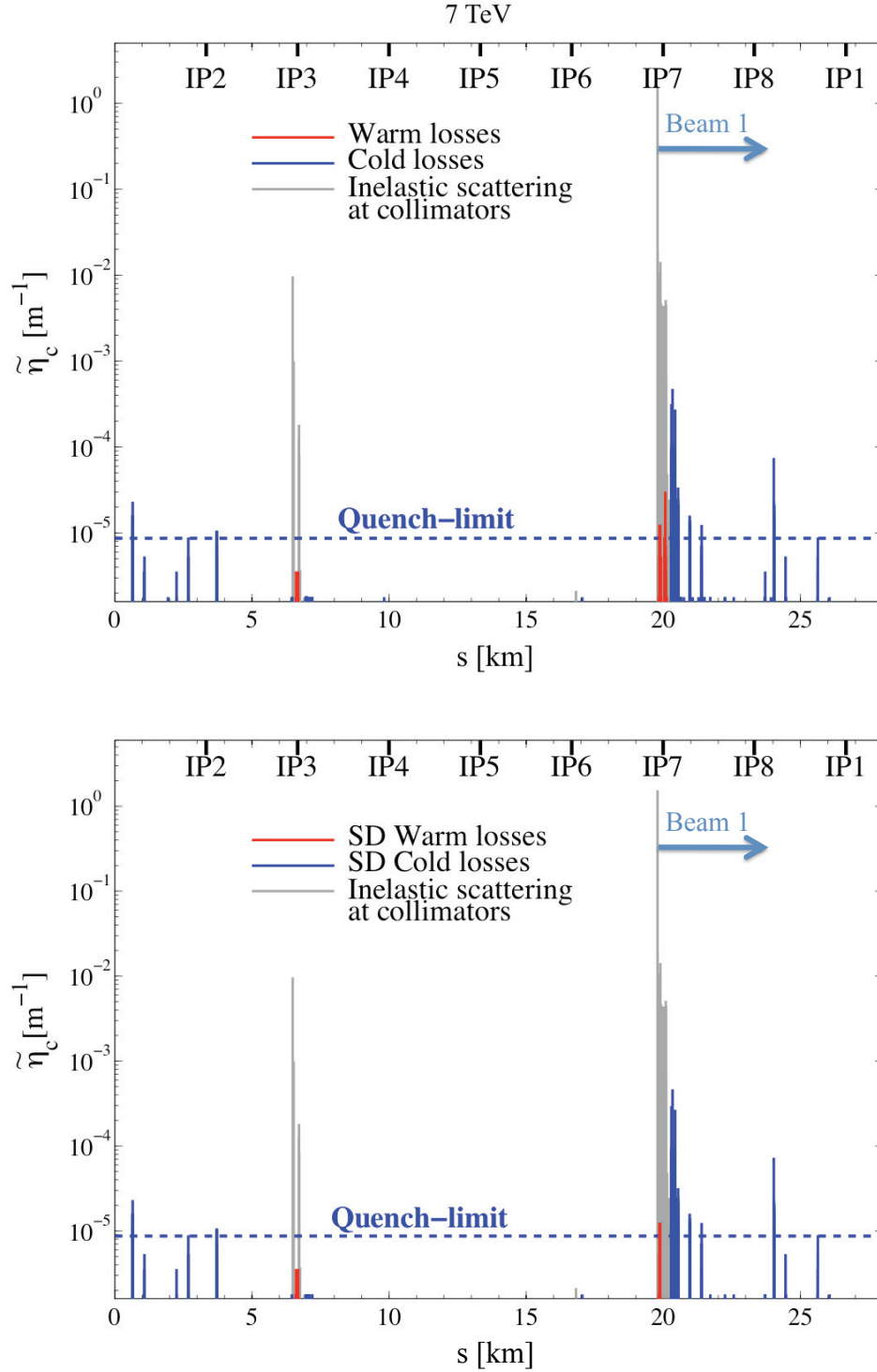
Figure 6.15: Loss map for the Beam 1 vertical halo at top energy. The collimators are kept at the same settings as during the flat-bottom. The graph on the bottom shows only losses of particles which experienced single diffractive scattering (SD) at the TCPs while the top shows all particles.
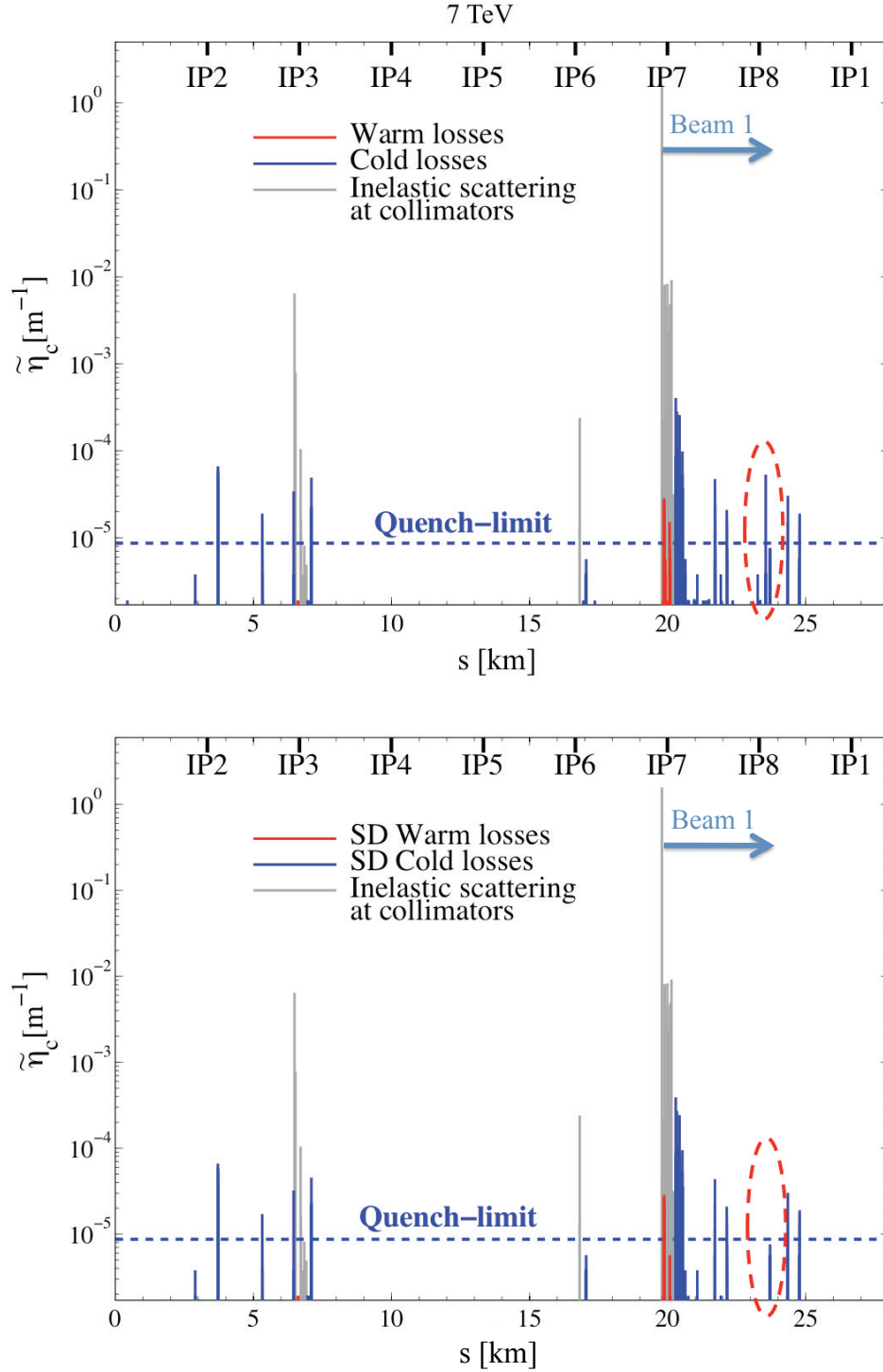
Figure 6.16: Loss map for the Beam 1 horizontal halo at top energy. The collimators are kept at the same settings as during the flat-bottom. The plot on the bottom shows only losses of particles which experienced single diffractive scattering (SD) at the TCPs while the top graph includes all particles. The red circle highlights that some cold peaks in IR8 are not due to SD.
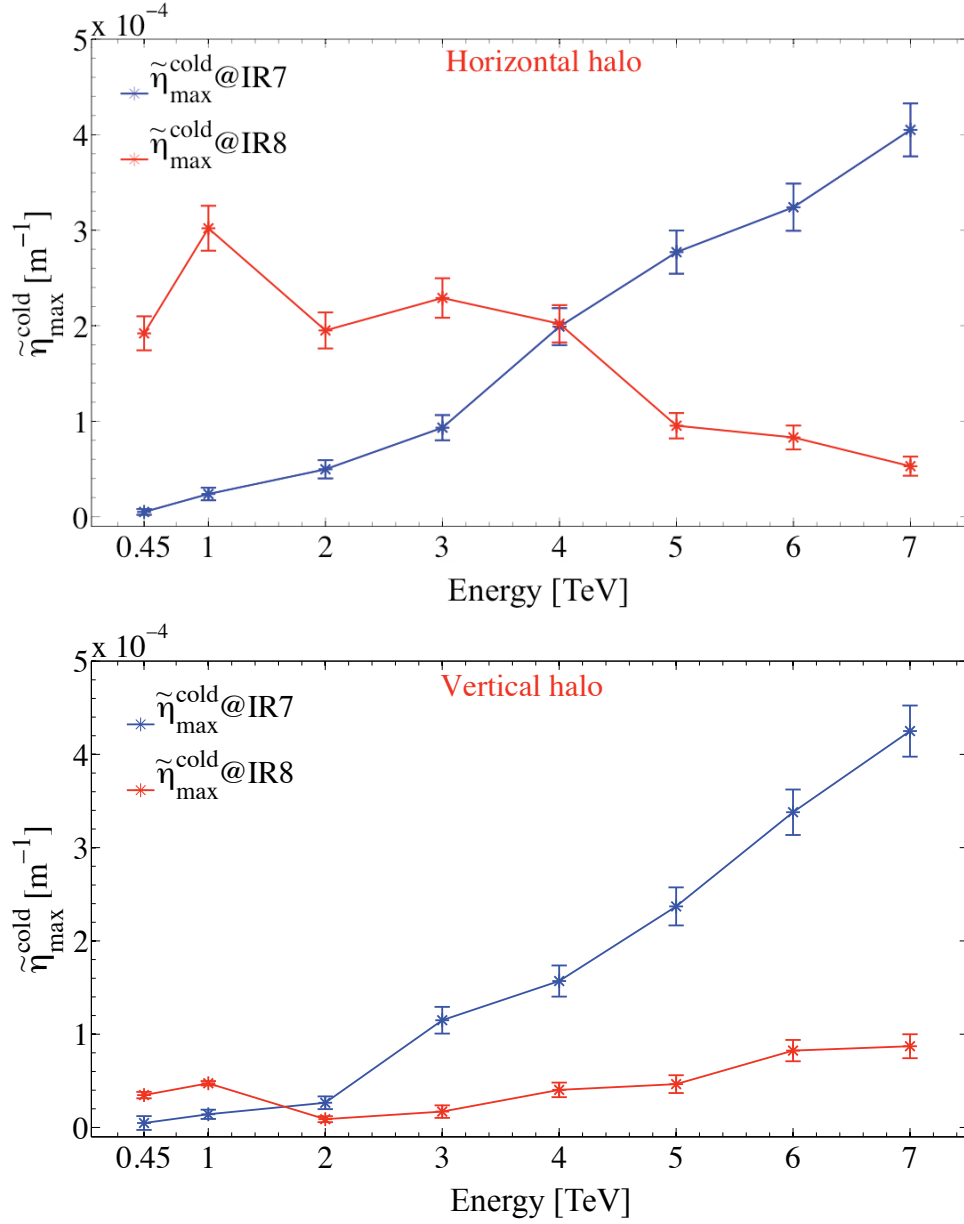
Figure 6.17: Comparison of $\tilde{\eta}_{max}^{cold}$ between IR7 (blue line) and IR8 (red line) for vertical (top) and horizontal (bottom) halo at different energies.

On the other hand the TCTH is installed in IR8 and it could be eventually used to intercept the particles which are lost in this region (7 degree phase advance from the tertiary) when they limit the beam intensity. The studies of cleaning performance during the energy ramp were concentrated on finding the collimator settings which minimize $\tilde{\eta}_{max}^{cold}$ at IR7. The vertical halo was therefore preferred since it shows the most important limitation at top energy.

Finally, the constant collimator settings can be used only for the commissioning of the acceleration ramp at low intensity ($<1\%$ of I_{nom}). For higher beam intensity the collimators must be closed before reaching the 7 TeV plateau.

6.1.6.2   Tolerance optimized settings during the ramp

In order to improve the cleaning efficiency while keeping relaxed tolerances, a different setup strategy was analyzed. This consists in moving the collimators already at the beginning of the energy ramp (450 GeV), by setting the primary collimators at $6\,\sigma$. The retraction between the TCPs and all the other collimators is kept unchanged (in mm) so that the tolerance budget is the same as in the constant setting case (see Table 6.9 and Fig. 6.18). This setting allows gaining a factor of 4 in cleaning efficiency at top energy. The intensity reach can be 8% of I_{nom} for the ideal machine.

Table 6.9: Collimator settings as a function of beam energy: the TCPs are set at $6\,\sigma$ from the beginning of the ramp. The retraction in mm between the primary and all the other collimators is kept unchanged as it is for the constant settings.

Tolerance optimized settings								
Energy [TeV]	Half gap [σ]							
	IR3			IR6		IR7		
	TCP	TCSG	TCLA	TCSG	TCDQA	TCP	TCSG	TCLA
0.45	8.3	9.6	10.3	7.3	8.3	6	7	10.3
1	9.5	11.4	12.5	8	9.5	6	7.5	12.5
2	10.6	13.2	14.6	8.6	10.6	6	8	14.6
3	12	15.4	17.2	9.4	12	6	8.6	17.2
4	13	16.8	19	10	13	6	9	19
5	13.6	18	20.2	10.3	13.6	6	9.3	20.2
6	14.4	19.2	21.7	10.8	14.4	6	9.7	21.7
7	15.2	20.4	23.2	11.1	15.2	6	10	23.2

6.1.6.3   Settings scaled with $\sqrt{\gamma}$ during the ramp

In order to reach the best possible performance, the half-gaps of the betatron cleaning collimators must follow the acceleration damping and be scaled with $\sqrt{\gamma}$ (relativistic γ factor) (see Table 6.10). The same is true for the protection elements in the dump region, while the momentum cleaning collimators can be closed following the steps foreseen for the tolerance optimized settings.

Fig. 6.18 shows the half-gaps of primary (n1) and secondary (n2) betatron collimators for the described settings. The n1 position does not change when shifting

Table 6.10: Optimal collimator settings as a function of the energy. The momentum cleaning collimators follow the same setup of the tolerance optimized settings.

Settings scaled with $\sqrt{\gamma}$								
Energy [TeV]	Half gap [σ]							
	IR3			IR6		IR7		
	TCP	TCSG	TCLA	TCSG	TCDQA	TCP	TCSG	TCLA
0.45	8.3	9.6	10.3	7.5	8	6	7	10
1	9.5	11.4	12.5	7.5	8	6	7	10
2	10.6	13.2	14.6	7.5	8	6	7	10
3	12	15.4	17.2	7.5	8	6	7	10
4	13	16.8	19	7.5	8	6	7	10
5	13.6	18	20.2	7.5	8	6	7	10
6	14.4	19.2	21.7	7.5	8	6	7	10
7	15.2	20.4	23.2	7.5	8	6	7	10
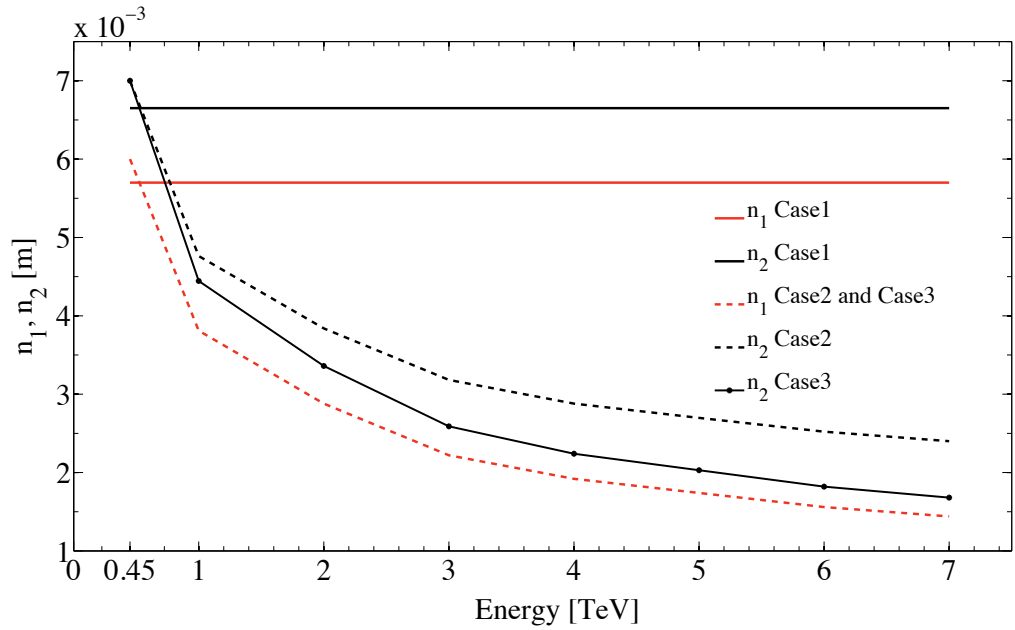
Figure 6.18: The half gaps of the IR7 TCPs (n1) and TCSGs (n2) are shown as a function of the beam energy for the proposed settings. Case 1 refers to the constant and case 2 to the tolerance optimized settings. In case 3 the collimator gaps are scaled with $\sqrt{\gamma}$.

from the tolerance optimized settings to the scaled with $\sqrt{\gamma}$ settings, while n2 becomes smaller at higher energies. As a consequence, T_b decreases as well as shown
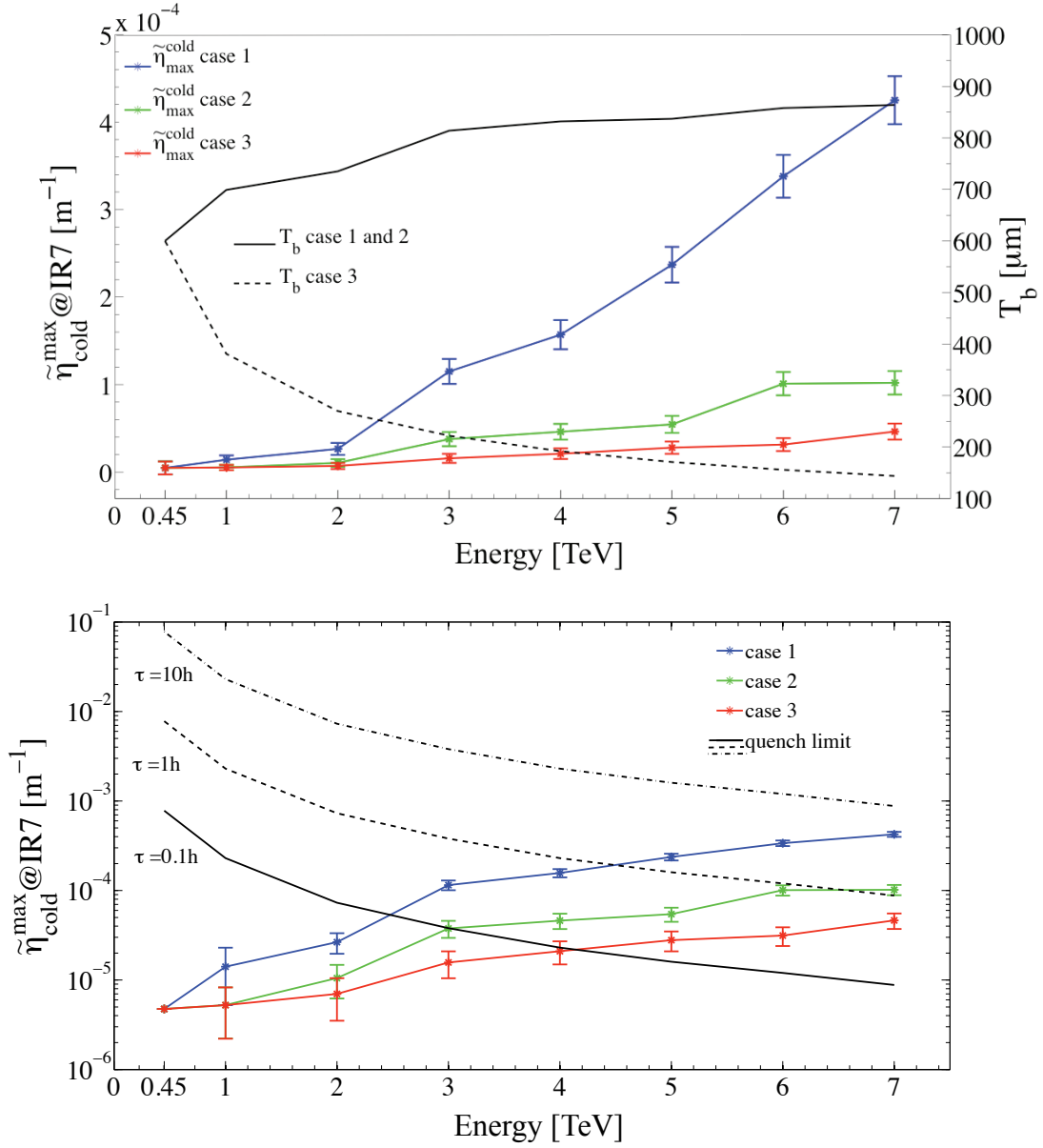
Figure 6.19: $\tilde{\eta}_{max}^{cold}$ for the various collimator settings is plotted as a function of the beam energy. The behavior of the tolerance budget (top) and of the equivalent quench limit, calculated for several beam life time values τ (bottom, semi-logarithmic scale), are also shown. Case 1 refers to the constant and case 2 to the tolerance optimized settings. In case 3 the collimator gaps are scaled with $\sqrt{\gamma}$.

in Fig. 6.19 (top). In the same figure $\tilde{\eta}_{max}^{cold}$ at IR7 is summarized as a function of the energy. The graph at the bottom of Fig. 6.19 compares $\tilde{\eta}_{max}^{cold}$ and $\tilde{\eta}_q$, calculated for several beam lifetimes. This permits to estimate at what energy each setting can

become critical. Scaling the collimator gaps with $\sqrt{\gamma}$ allows to accelerate the beam up to 4 TeV without significant intensity reduction if τ=0.1 hours.

6.2   Impact of imperfections

The results presented in the previous sections refer to an ideal machine without errors and perfect collimators. It is, however, well known that every accelerator is affected by unavoidable imperfections.

In order to give an evaluation of the realistic cleaning performance of the collimation system and its maximum intensity reach, several scenarios with combined imperfections were analyzed for the collision optics "lowb.coll_all" (see section 2.4.1) and are shown in the following sections. This is the first time that LHC cleaning efficiency and loss maps were simulated for multiple error scenarios. It is noted that these studies were very CPU intensive and could only be done for selected cases.

6.2.1   Jaw flatness errors

The LHC collimators are produced with stringent requirements on the flatness of the 1 m long jaws ($\sim$40 μm). Any large deformation of the jaws would create a reduction of the material traversed by the halo particles (active length) and could worsen the cleaning efficiency. However, the achievable flatness is technically limited and Fig. 6.20 summarizes the deformation measurements performed on different collimator families (TCP, TCSG, TCLA and TCT). A positive flatness means that jaws are deformed towards the beam while a negative flatness corresponds to outwards deformation.

The measurements show an average absolute flatness of 40.3±22.2 μm. The number of inward deformed jaws is approximately double with respect to the outward deformed ones.

Simulations were carried out for Beam 1 using both deformation types for primary, secondary, tertiary collimators and absorbers. The shape of the jaws in the code is defined starting from a parabolic function:

$$F(s) = \pm \frac{2 \cdot 10^{-3}}{5} \left(\frac{s^2}{l} - s \right) \tag{6.4}$$

where the collimator jaw length l and the longitudinal coordinate s (along the jaw) are expressed in m. The positive sign in front of eq. 6.4 gives a negative (outward) deformation whereas the negative sign defines a positive (inward) deformation. Each jaw is then described by a number n of segments that follow the parabola as shown in Fig. 6.21. Four segments were used for the presented simulations. The following non-flatness was applied to the jaws:

- $A_{def} = 100 \, \mu$m (in and outwards) for 1 m long jaws (TCSG, TCLA, TCT).
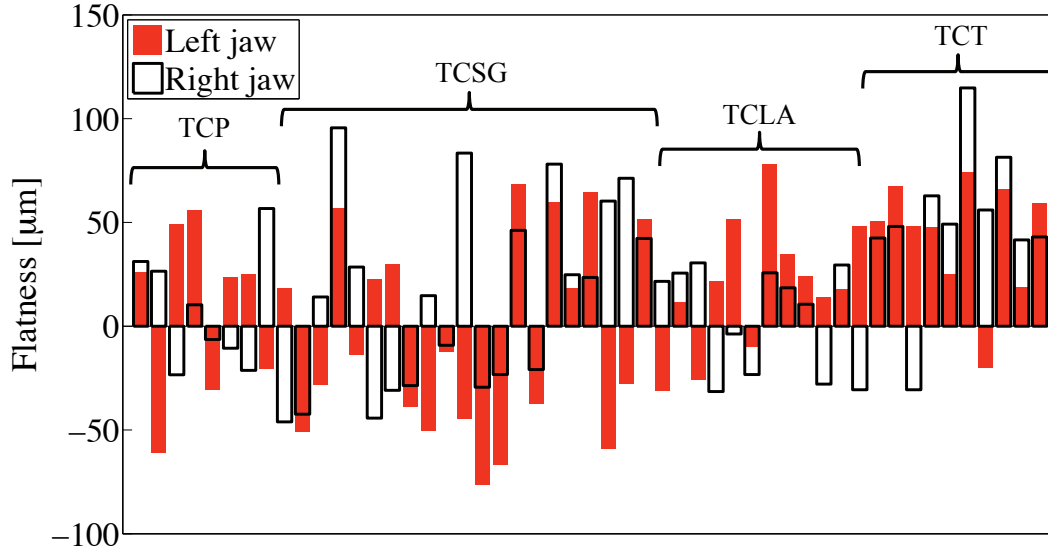
Figure 6.20: Flatness measurements for the different collimators separated by families (TCP, TCSG, TCLA, TCT).

- $A_{def} = 60\,\mu$m (in and outwards) for 0.6 m long jaws (TCP).

As a worst case study, the same systematic deformation was used for all jaws.

The half gap is always defined considering the point of the jaw which is the closest to the beam axis. The following results were found for the maximum local cleaning inefficiency around the ring:

1. Systematic outward deformation: a factor of 1.08 increase of inefficiency.

2. Systematic inward deformation: a factor of 1.11 increase of inefficiency.

A transient deformation, induced by the heating of the jaws during beam exposure, is expected to add to the initial deformation. The first secondary collimator of the betatron cleaning insertion (TCSG.A6L7.B1 for Beam 1) is particularly sensitive due to the high energy flux coming from the primary collimators. "Finite element model" (FEM) calculations predict a $30\,\mu$m outwards deformation during nominal operation with a 1 hour beam life time and $100\,\mu$m inwards bending for 0.2 hours beam life time [77]. The three betatron halos were tracked for Beam 1 in order to quantify the effect of this inward deformation of the first secondary collimator on the cleaning efficiency of the system. No additional reduction of the cleaning performance was found.
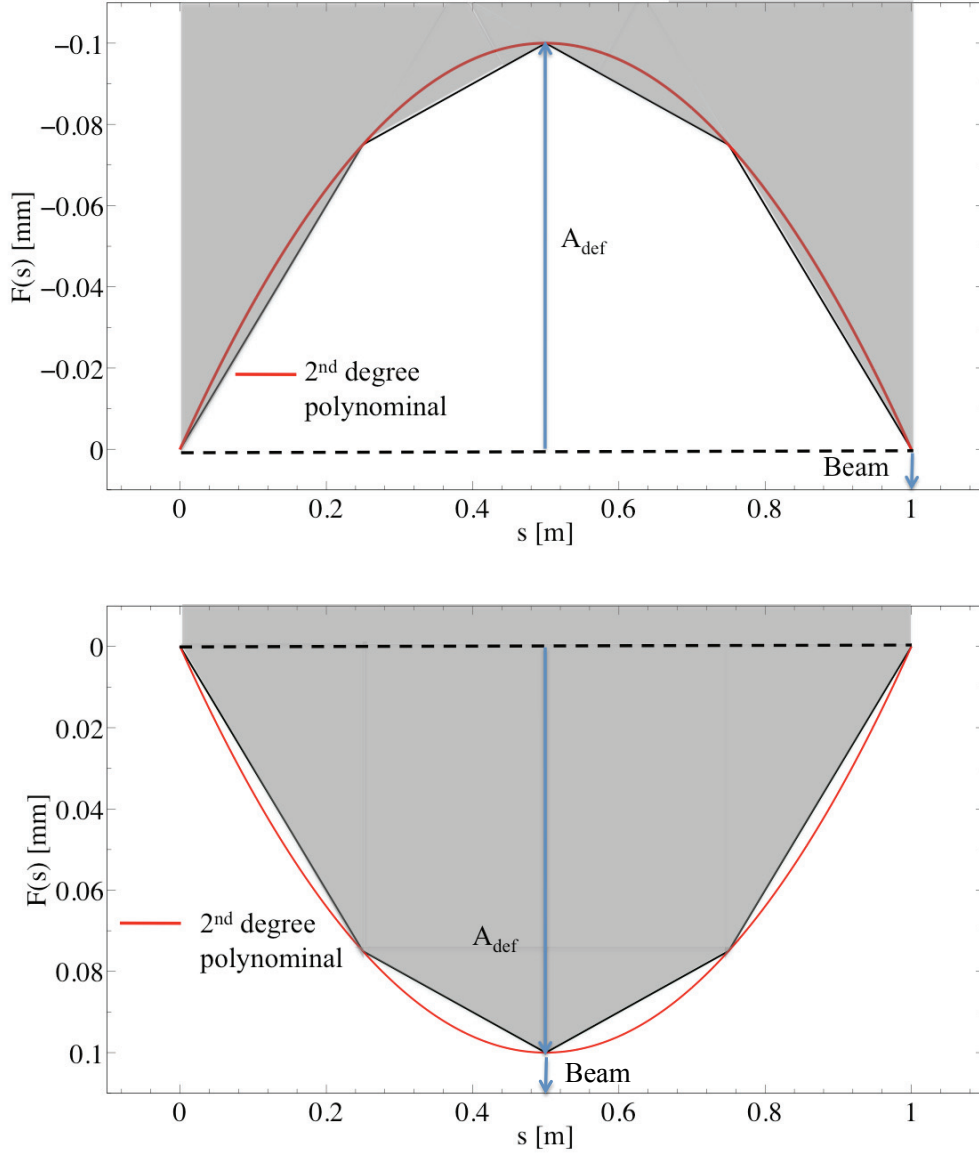
Figure 6.21: The approximation used to simulate 1 m long jaws with outwards (top) and inwards (bottom) deformation is shown. Here a case with 4 slices per jaw is presented. The number of slices is a simulation parameter.

6.2.2 Collimator setup errors

The beam based alignment for the setup of the collimators is affected by unavoidable errors in accuracy. In section 7.2.3 the beam based alignment method is described and the experimental results from beam tests are analyzed. These results served as input to the simulations. As described in section 5.2.2, the simulation input
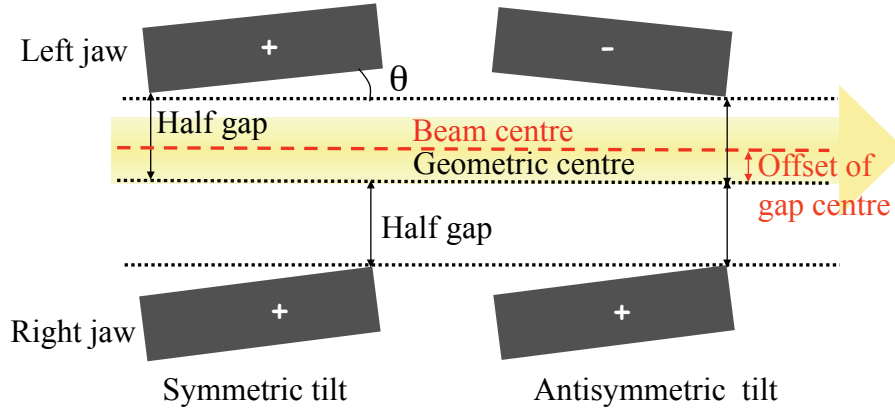
Figure 6.22: Illustration of various setup errors that were applied to the collimator jaws in simulations.

file "fort.3" allows to specify setup errors for the collimator jaws (see also Fig. 6.22); namely r.m.s and/or systematic jaw tilts (symmetric or antisymmetric), r.m.s and/or systematic offsets of the collimator gap with respect to the ideal position (beam centre) and r.m.s errors on the size of the collimator gap with respect to its ideal value (n times the beam size).

   For this work random errors were used with a Gaussian distribution cut at 3σ. Based on the experimental data the following imperfections were simulated:

   1. Jaw flatness errors as described in section 6.2.1 (inward).

   2. R.m.s error on gap centre: $50\,\mu$m.

   3. R.m.s error on gap size: 0.1σ.

   4. R.m.s. error on jaw angle to beam: $200\,\mu$rad.

   A factor of 2.1 loss in cleaning inefficiency was found with respect to the perfect scenario.

6.2.3   Machine alignment errors

The "BeamLossPattern" program in the collimation simulation package allows taking into account magnet and beam screen misalignments of the LHC elements (beam screens are first aperture limitation). Starting from the standard aperture model used to derive the loss maps, up to 20 seeds of misaligned apertures can be applied to a set of halo trajectories produced by "SixTrack". An r.m.s. offset in the horizontal ($\sigma_{\Delta x}$) and vertical ($\sigma_{\Delta y}$) planes has been defined for different families of elements on

Table 6.11: Horizontal and vertical r.m.s magnet misalignments at beam screen level for different families of machine elements. The numbers are based on design values and measurements performed on surface and in the LHC tunnel [78].

Element type	Description	Design		Measured	
		$\sigma_{\Delta x}$ [mm]	$\sigma_{\Delta y}$ [mm]	$\sigma_{\Delta x}$ [mm]	$\sigma_{\Delta y}$ [mm]
MB	main dipole	2.40	1.56	1.83	1.10
MQ	arc quadrupole	2.00	1.20	1.36	0.76
MQX	triplet quadrupole	1.00	1.00	1.53	1.53
MQWA	warm quadrupole	2.00	1.20	0.67	0.41
MQWB	warm quadrupole	2.00	1.20	0.67	0.41
MBW	warm dipole	1.50	1.50	1.96	1.49
BPM	beam position monitor	0.50	0.50	1.36	0.76
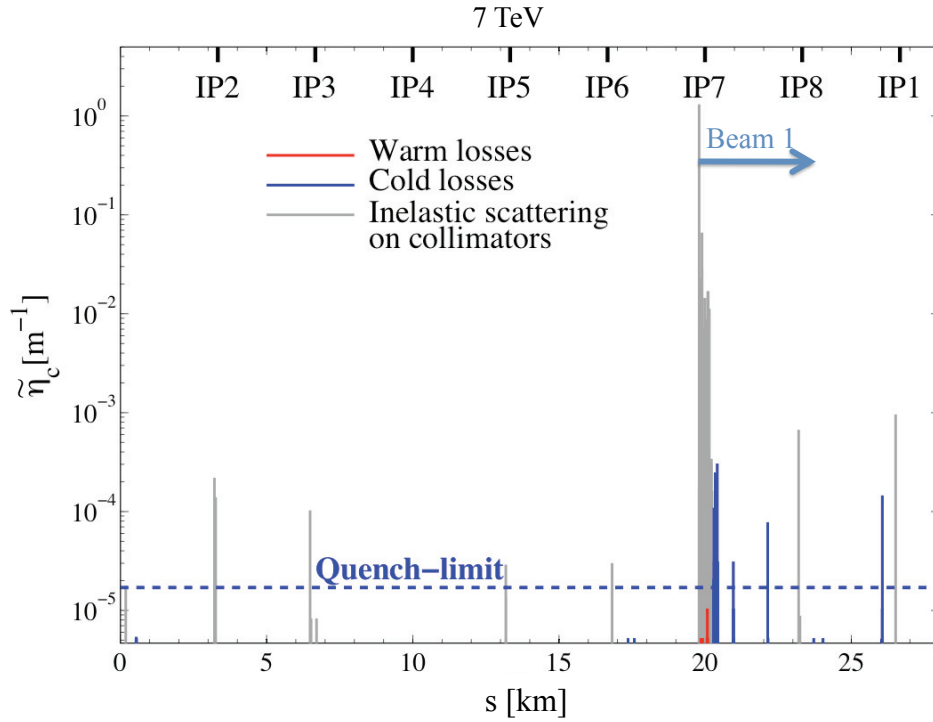
Figure 6.23: Loss map obtained for a horizontal halo of Beam 1 with one seed of jaw flatness errors, collimation setup errors and, most important, machine alignment errors (design values). This case refers to the collision optics "lowb.coll_all".

the basis of design values and measurements performed on surface and in the LHC

tunnel [78]. The applied imperfections are listed in Table 6.11.

The specified misalignment errors are used to generate Gaussian errors cut at 1.5σ to the geometric centre of each magnet in the LHC. This is only done at the level of the aperture model. Particle tracking is done with the ideal machine orbit and fields. The reduced aperture has different bottlenecks (one-sided) which lead to the appearance of loss peaks in unusual locations and an increase in the cleaning inefficiency. An example of a loss map is shown in Fig. 6.23 taking into account machine alignment errors (design), jaw flatness errors and collimation setup errors (1 seed example). Losses in the IR7 dispersion suppressor are a factor of 14.6 higher than for the ideal machine and the quench limit is exceeded in several points of arc 7-8 and 8-1.
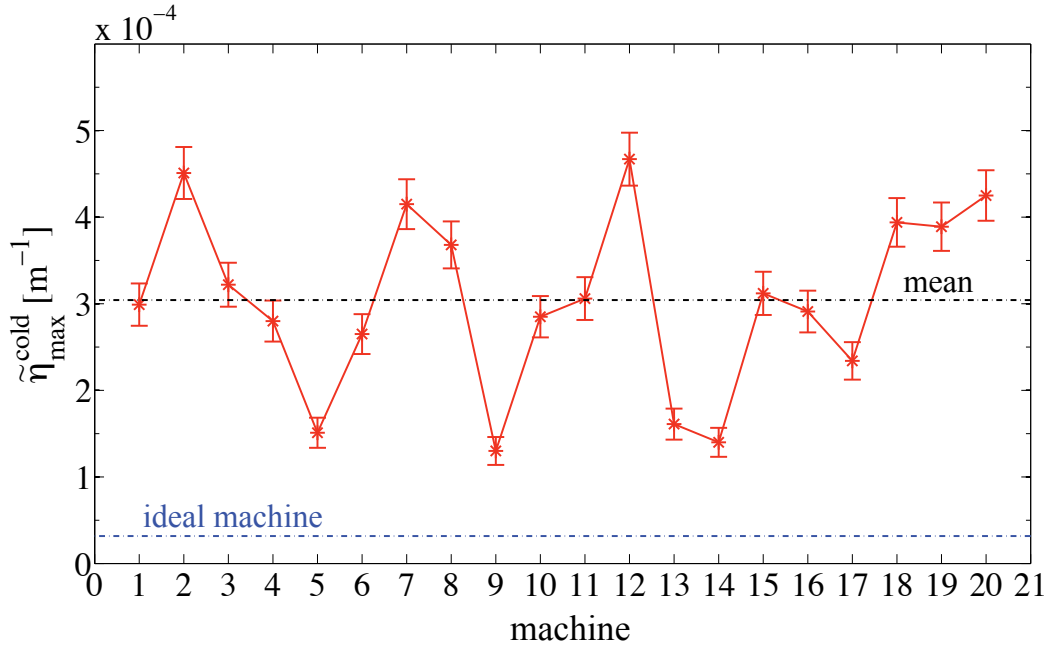
Figure 6.24: Cleaning inefficiency $\tilde{\eta}_{max}^{cold}$ for 20 different seeds of machine alignment errors (design values). The local cleaning inefficiency is increased on average by a factor of 9.5 with respect to the ideal machine. These results refer to a Beam 1 horizontal halo at top energy.

Fig. 6.24 summarizes the $\tilde{\eta}_{max}^{cold}$ values found for 20 different seeds of machine alignment errors (design values): the local cleaning inefficiency varies up to a factor of four for different seeds. The cleaning efficiency is degraded by about one order of magnitude.

The calculated maximum cleaning inefficiency averaged over the simulated seeds is:

1. $\overline{\eta_{max}^{cold}} = (3.0\pm0.2)\cdot10^{-4}\,\mathrm{m}^{-1}$ for machine alignment errors from design values.

2. $\overline{\eta_{max}^{cold}} = (2.7\pm0.2)\cdot10^{-4}\,\mathrm{m}^{-1}$ for machine alignment errors from measurements.

Results are in agreement within the simulation error. Both values are indicated in the summary plot shown in Fig. 6.26 (section 6.2.5, red point for design values, blue point for measured values). Studies reported in the following refer to the case of machine alignment errors due to design values.

6.2.4   Non ideal closed orbit

This section adds the effect of a non-ideal horizontal closed orbit for the study of collimation system performance.

Previous in-depth studies on orbit perturbations [14] defined a conservative scenario in compliance with the specified LHC orbit for the collision optics. On the basis of these results two kickers at 90 deg phase advance in arc 3-4 (MCBH.15L4.B1 and MCBH.13L4.B1) were used to generate a static horizontal closed orbit oscillation with maximum amplitude of $\pm4\,\mathrm{mm}$ in the arcs. The orbit was corrected to the specified $\pm3\,\mathrm{mm}$ maximum amplitude in the IRs (see Fig. 6.25).
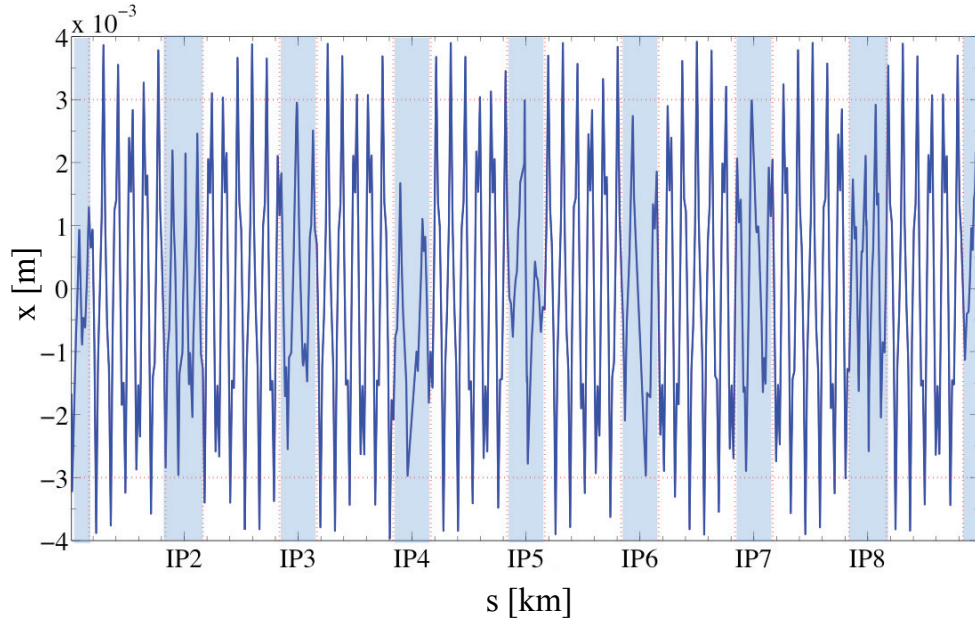
Figure 6.25: Horizontal closed orbit x at collision for Beam 1, as used for collimation studies. The orbit perturbation is corrected to $\pm3\,\mathrm{mm}$ in all insertion regions (highlighted) and adjusted to $\pm4\,\mathrm{mm}$ in the arcs, matching the LHC specification optics.

Simulations were carried out by using the standard initial halo distributions and the errors defined in the previous sections. The collimators were centered on the

non-ideal orbit and tracking was performed. This resulted in a further increase in
the local cleaning inefficiency by a factor of 1.16 (see Fig. 6.26).

6.2.5   Summary on imperfections

Fig. 6.26 shows the evolution of the collimation system performance when several
imperfections are applied. At this time scenario 5 is considered the most realistic,
which could limit the maximum intensity reach in collimation to $<5\%$ of I_{nom}.
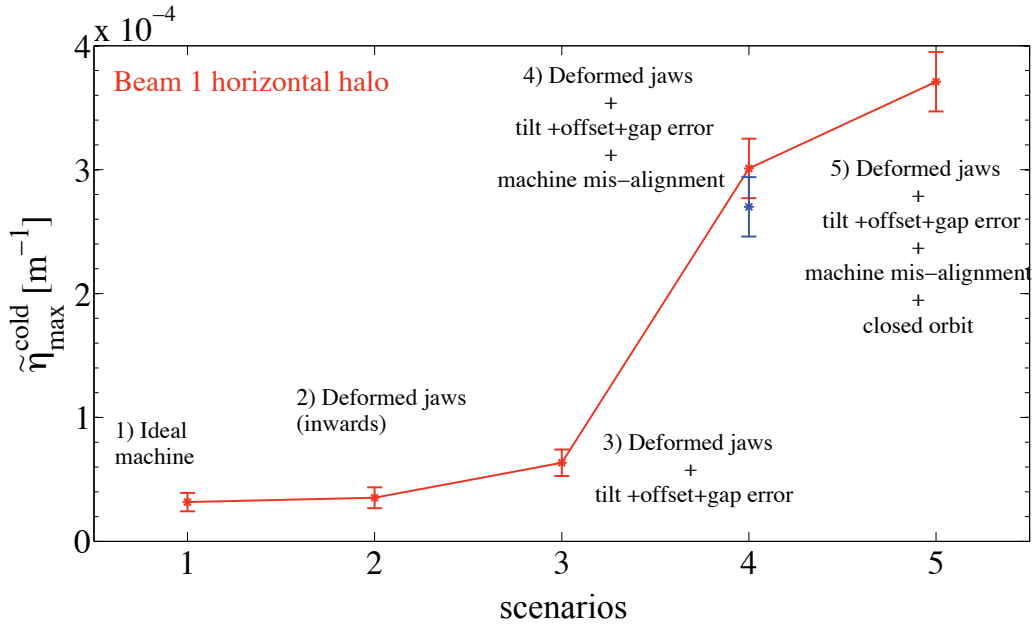
Figure 6.26: Local cleaning inefficiency for various error scenarios. The blue point
refers to machine alignment errors as defined by measurements.

This prediction is based on critical assumptions for the superconducting magnet
quench limit and a minimal beam life time of 0.2 h. Several imperfections are not
yet taken into account, namely effects from beta-beat, coupling and non-linearities
in the LHC. Also, no margin for threshold effects has been applied. For example, the
beam loss monitors will, by design, trigger a beam dump if losses reach 30% of the
quench limit, requiring in principle a factor of 3 margin in cleaning efficiency. On
the other side the 10 cm resolution used for claculating the loss maps implies that we
assume that each lost particle deposits its full energy within this bin length. If a 1 m
resolution was used, the losses would be more diluted with an average improvement
in local cleaning inefficiency by a factor of 5.

It is noted that the FLUKA predictions are a factor of 3.5 lower than the estimate
from the 10 cm bin size in the aperture (see section 6.1.2), for the same data set. This
is expected, as the shower will distribute the energy deposition in the longitudinal

direction of beam particles. It is concluded that these are strong hints at possible limitations of LHC intensity from cleaning of losses. The experience with first beams will provide further insight.

6.3 Impact of off-momentum beta-beat

Analytical studies were carried out to assess the consequences of off-momentum beta-beat on the effective collimator settings. The collimator jaws are ideally always centered around the closed orbit and intercept all particles which, at their phase location, have an oscillation amplitude A_z greater than the half gap z_{cut} (z refers to transfer coordinates x and y). A_z is determined by the sum of two contributions:

1. the betatron oscillation amplitude: $n \cdot \sqrt{\epsilon_z \beta_z(\delta)}$

2. the dispersion function: $D_z(\delta) \cdot \delta$

where $\delta = \Delta p/p$. The half gaps (in mm) of the nominal collimator settings are
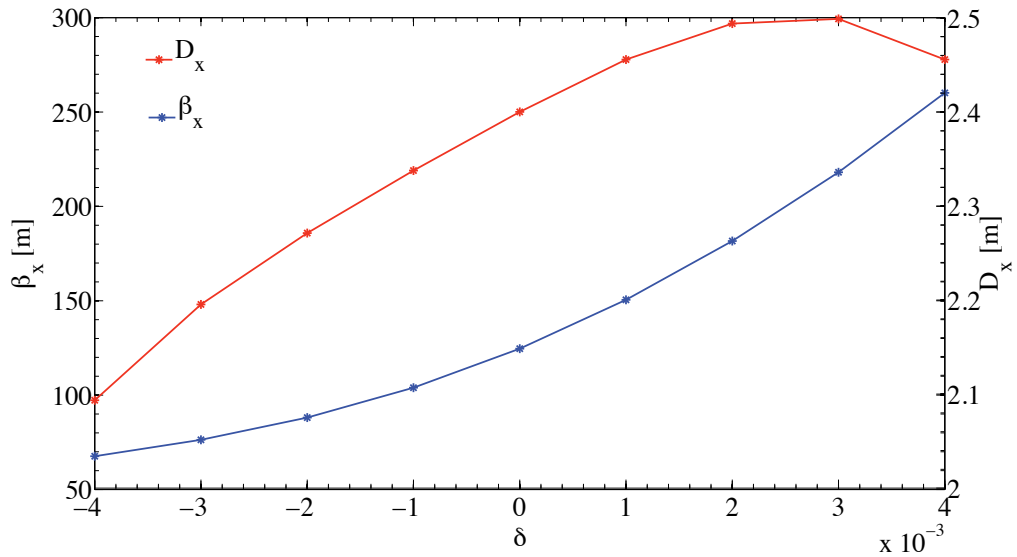
Figure 6.27: Variation of β_x and Δ_x as a function of particle momentum offset δ at the location of the horizontal primary collimator TCP.6L3.B1 (momentum cleaning insertion).

calculated considering a central on-momentum particle. If $\delta \neq 0$ for a given particle the effective betatron amplitude cut $n_{\beta_z cut}(i_{coll})$ at each collimator i_{coll} changes as a function of δ, β_z and D_z.

The cut in phase space produced by the nominal collimator settings can then be defined for each collimator as:

$$z_{cut}(i_{coll}) = n_{\beta_z cut}(i_{coll}, \delta) \cdot \sqrt{\epsilon_z \beta_z(i_{coll}, \delta)} + D_z(i_{coll}, \delta) \cdot \delta \tag{6.5}$$

from which, considering both collimator jaws and sufficient time for phase space mixing, it is possible to derive explicitly $n_{\beta_z cut}(i_{coll}, \delta)$ as:

$$n_{\beta_z cut}(i_{coll}, \delta) = \frac{\pm z_{cut}(i_{coll}) - D_z(i_{coll}, \delta) \cdot \delta}{\sqrt{\epsilon_z \beta_z(i_{coll}, \delta)}}. \tag{6.6}$$

Ideally the β-function is independent of beam energy, meaning that the off-momentum beta-beat is zero. However, in reality there is always some dependance of β_z on δ, which is minimized during the accelerator design. An example is shown for the location of the IR3 horizontal primary collimator TCP.6L3.B1 in Fig. 6.27. The effect of the off-momentum beta-beat on $n_{\beta_z cut}$ for this collimator is shown in Fig. 6.28 (red lines, 7 TeV settings). The blue lines show the phase space cut produced by the two jaws if the dispersion and the β-function are independent of δ.

Overlapping the δ-dependent phase cuts for all horizontal collimators and taking
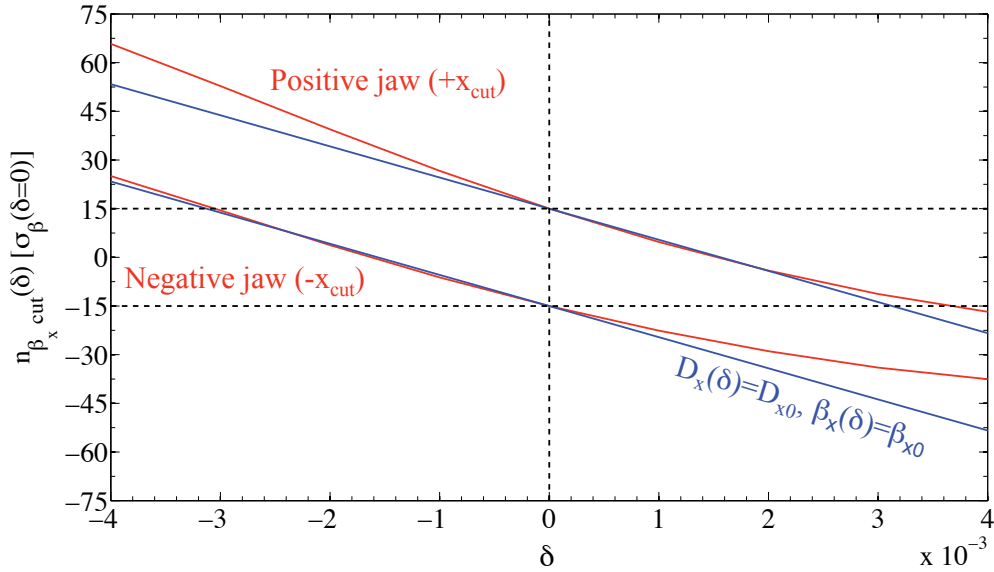
Figure 6.28: Phase space cut $n_{\beta_x cut}$ as a function of particle momentum offset δ for the IR3 horizontal primary collimator (red lines). The blue lines show $n_{\beta_x cut}$ in case of D_x and β_x being independent of δ, which is not the case for this location in the LHC.

into account the energy spread of the nominal LHC RF bucket (see section 3.1.2), the allowed phase space region for the circulating beam can be defined, as shown in
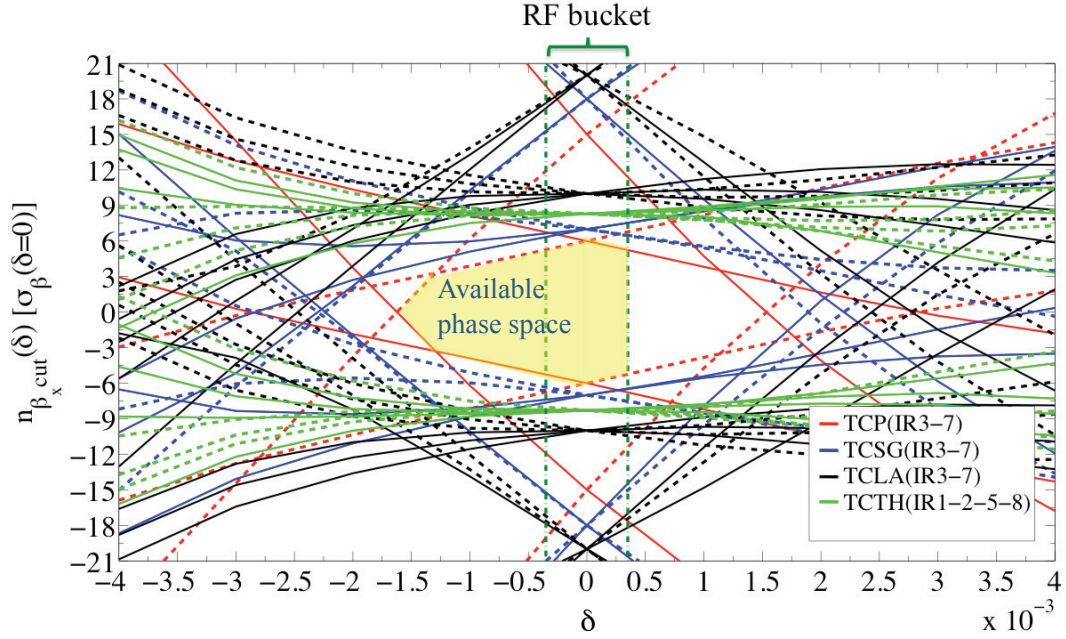
Figure 6.29: Phase space cut from all horizontal collimators in LHC, including both IR3 and IR7. The highlighted region indicates the space which can be populated by the beam halo. Note, that there is no mechanism to populate the phase space above the RF bucket while it can be populated below (synchrotron radiation).

Fig. 6.29. Due to the off-momentum beta-beat the IR7 primary collimators, though set at 6σ ($\delta = 0$), cut the betatron halo down at 3σ for $\delta = $ -0.13%. Primary collimator in IR3 intercepts all particles with $\delta \leq -0.16\%$. The dashed lines represents the reflections of the calculated curves with respect to the $n_{\beta_z cut} = 0$ axis. They define, for a fixed δ, the maximum possible betatron oscillation amplitude as imposed by phase space mixing. This is valid if the amplitude increase per turn is $\ll \sigma$ (stable beam) and if synchrotron oscillations are much slower than betatron oscillations. This is fully valid in the LHC (see Table 6.12 [13]).

Table 6.12: Synchrotron and betatron oscillation frequencies for LHC at injection and top energy.

	Synchrotron frequency [Hz]	Hor. betatron frequency [kHz]	Ver. betatron frequency [kHz]
450 GeV	61.8	722.2	666.4
7 TeV	21.4	722.6	666.5

Two different optics are possible in the LHC with the off-momentum beta-beat corrected either in the first (IP1→IP5) or in the second (IP5→IP1) half of the ring. The results presented refer to the second option. However, both optics were studied in this PhD thesis and the second option was shown to be the most favorable from the point of view of the collimation. It gives minimal reduction in terms of setting tolerances and was adopted as LHC standard optics. In both cases, for $\delta \leq -0.2\%$, the collimators keep their roles (i.e. TCPs act as a primary, TCSGs as a secondary collimators etc.). Still, the retraction of TCSGs with respect to TCPs in IR7 is reduced up to 30% if beta-beat takes place between IP1→IP5, whereas a 70% reduction is found for the other optics. The tolerance budget T_b at top energy is then reduced, in the best case to $0.7\,\sigma$. For example this would allow for orbit transients of $52.5\,\mu$m (30% of T_b). Off-momentum beta-beat will make operation more delicate.

Chapter 7

Test Results on Collimation Commissioning

Two prototypes of LHC horizontal secondary collimator were tested in 2006 during several SPS machine days (MDs). One collimator was installed in the long straight section at point 5 (LSS5) of the SPS ring and tested with circulating beam, while the other was installed in the TT40 transfer line for robustness tests with extracted beam. These experiments were devised, on the base of earlier 2004 experiments, to check the functionality of the final hardware and control systems and to develop the beam based collimator setting procedures. Results of these studies are presented in the following.

7.1 Collimator coordinate system

The operational naming conventions for the horizontal collimator jaws, as used in this chapter, are introduced in Fig. 7.1. For each jaw an upstream and a downstream corner are defined and are named respectively:

- LU: left jaw, upstream end

- LD: left jaw, downstream end

- RU: right jaw, upstream end

- RD: right jaw, downstream end.

The left jaw is on the positive side of the x axis while the right one is on the negative side. A positive tilt angle θ_x for the left jaw corresponds to having the LU corner closer to the beam axis. For the right jaw θ_x is positive if RU is further away from the beam axis (see Fig. 7.1).
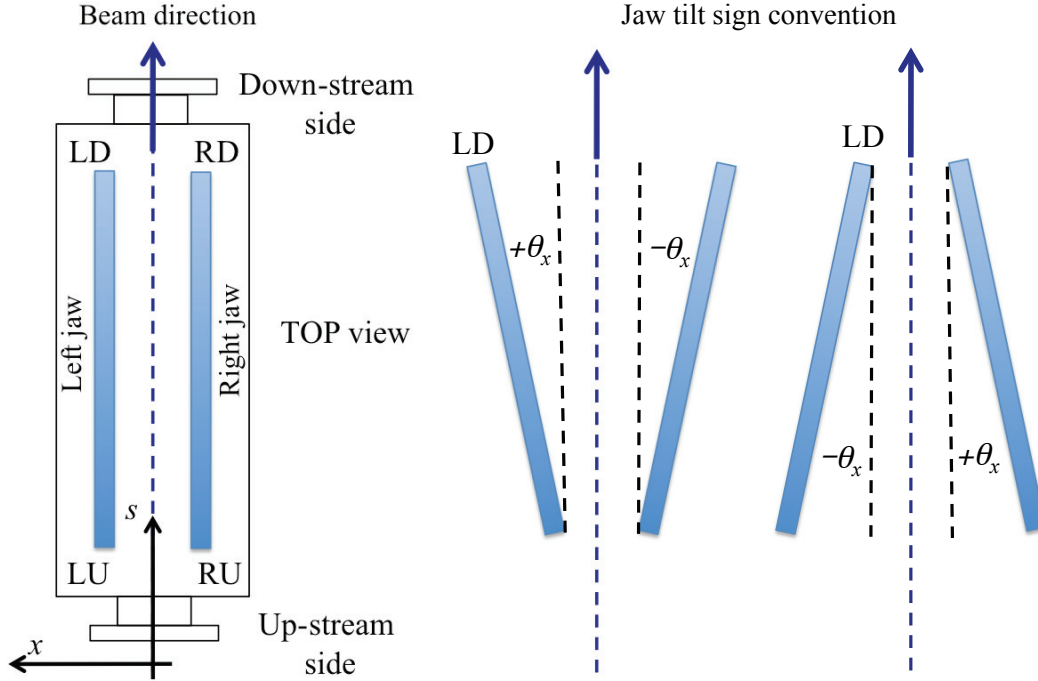
Figure 7.1: Operational naming conventions for the collimator jaws, the x position and the tilt angle θ_x. The top view is shown.

7.2   Tests with stored proton beam

The main objectives of the two 24 hours MDs were as follows [1]:

1. Check and calibration of the final collimator control system and of the communication architecture between the hardware and the control room.

2. Commissioning of the beam based alignment procedure and beam profile measurements, combined with beam loss and tail repopulation studies.

3. Impedance measurements for investigation of the "inductive bypass effect" [79].

The impedance measurements are out of the scope of this PhD work and will not be discussed here; more detailed information can be found in [60].

7.2.1   LHC collimator prototype in the SPS

An LHC prototype collimator was installed in the SPS ring in 2004 [18, 80]. This prototype was the base for series production of LHC collimators and has the same

---

[1]MD1 started on 31/10/2006 at 8:00 a.m. and finished on 01/11/2006 at 8:00 a.m.
MD2 started on 07/11/2006 at 8:00 a.m. and finished on 08/11/2006 at 8:00 a.m.

features as the final hardware. A precise system of motors and position sensors is implemented for the accurate setting of the collimator jaws:

1. Four stepping motors are used to move the corners of the two jaws.

2. Four resolvers are connected to the stepping motors and monitor the number of steps performed.

3. Six position sensors (four potentiometers and two linear variable differential transformers LVDT) are used to measure respectively the actual jaw positions and the upstream and downstream gaps.

4. Ten switches (one full-in and one full-out at each corner plus two anti-collision switches) are installed to trigger motor stops and to protect the collimator mechanical system.

It is noted that the 2004 prototype collimator did not have the final radiation-hard motors and sensors. However, its functionality is not affected by this for these tests. The described instrumentation is shown in Fig. 7.2 together with the temperature sensors of the collimator (4 "PT 100" sensors are installed).
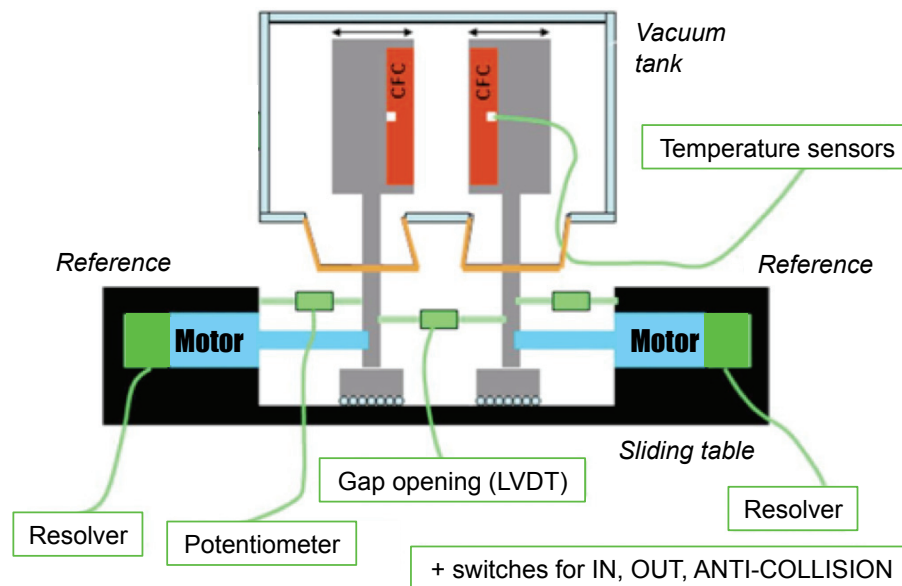
Figure 7.2: Schematic view of the movement control and instrumentation for the LHC prototype collimator used during the SPS tests.

The concept of the LHC collimator requires calibrating jaw positions precisely. During construction, inside gap and position of the jaws are accurately measured versus the outside gap. This calibration allows for precise monitoring and knowledge

of jaw positions with the position sensors outside of the vacuum (see Fig. 7.2). A minimal mechanical play is required. Metrology measurements in 2004 showed that the system has mechanical plays of the order of 30-40 μm which is a deterministic effect and can be taken into account for jaw movements. Jaws positions are monitored with about $\pm 20\mu$m accuracy, i.e. better than the collimator alignment in the tunnel.

The tested architecture of the collimator low-level control system and the communication between the different control levels worked as specified [81]. The graphical user interface for the steering of the LHC collimator jaws from the control room was successfully tested (see Fig. 7.3). Through this interface it is possible to input the
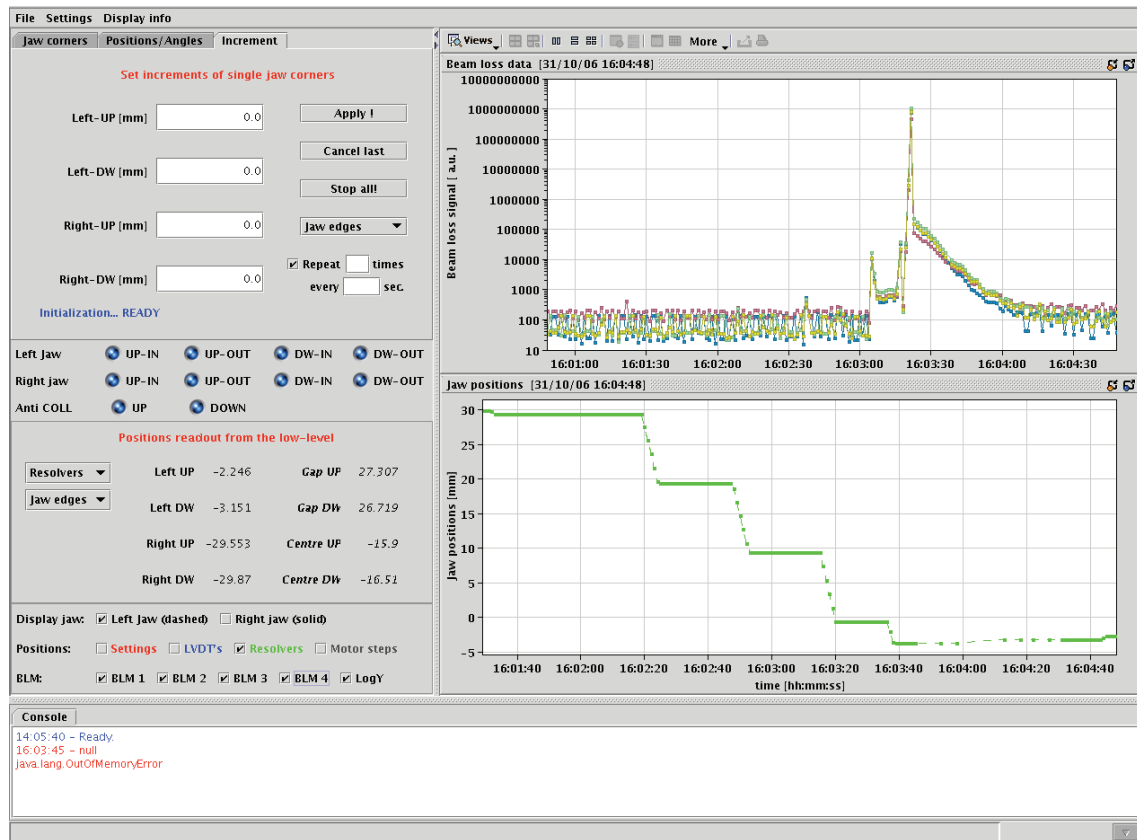
Figure 7.3: Main view of the graphical user interface for the steering of the LHC collimator jaws from the control room. The jaw position is displayed on the lower right display. Readings of Beam Loss Monitors during jaw movements are shown in the top right graph.

required movement and to either move the full jaws with a given angle (maximum allowed angle is 2 mrad) or to set each corner position independently. The status of the switches and the position readout from the sensors are displayed. Through selection flags it is possible to visualize the real time corner position measured by

the different sensors and the signals of the 4 BLM channels located downstream of the prototype (see section 7.2.3). Even if not displayed on this interface, further 216 SPS BLMs were located along the full ring and beam loss data were recorded with a frequency of 50 Hz. Beam profile and beam current measurements were also performed during the two MDs.

7.2.2 Beam conditions

Out of the 24 hours foreseen, approximately 10-11 hours per each MD were dedicated to collimation studies while the remaining time was used for beam setup and machine operation. The beam conditions and the optics parameters at the location of the collimator are summarized in Table 7.1. During MD1 low intensity tests were performed mainly with a single circulating bunch (last 8 hours), while MD2 was devoted to high intensity measurements: 288 bunches for the first 2 hours and 72 bunches for the last 9 hours.

Table 7.1: SPS beam condition and design optics parameters at the location of the horizontal collimator during the tests.

Beam parameter	Low intensity	High intensity
Bunch Population	$1.1 \cdot 10^{11}$ protons	
Number of bunches	1-4	72-288
Energy	270 GeV	
$\varepsilon_{n,x} = \varepsilon_{n,y}$	$1.5\,\mu$m	$3.5\,\mu$m
β_x	24.9 m	
β_y	87.9 m	
α_x	-0.7	
α_y	2.1	
D_x	-0.2 m	
D_y	0 m	
Q_x	26.1	
Q_y	26.2	
Q_s	0.0045	
$\sigma_{x'}$	$15\,\mu$rad	$22\,\mu$rad
σ_x	0.4 mm	0.6 mm

7.2.3 Collimator beam based alignment: centering jaws

The alignment and centering of a collimator with respect to the beam relies on beam loss measurements correlated with jaw movements. For this purpose two sets of beam

loss monitors were located at 8.9 m and at 12.3 m downstream of the collimator (see Fig. 7.4). They were used to measure the showers of particles produced by beam halo impact on the collimator jaws.
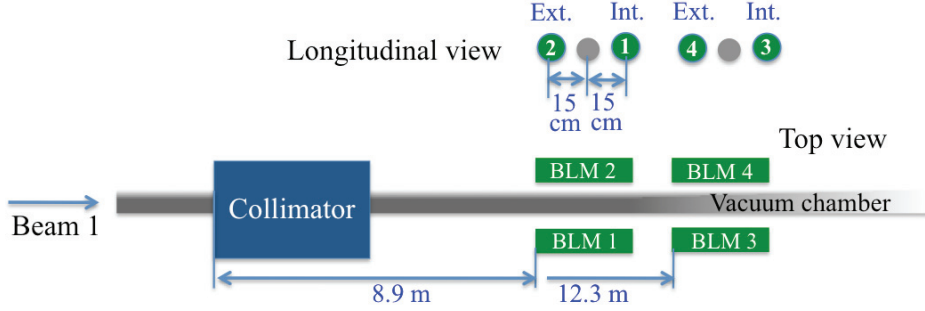
Figure 7.4: Setup of the Beam Loss Monitors installed downstream of the collimator.
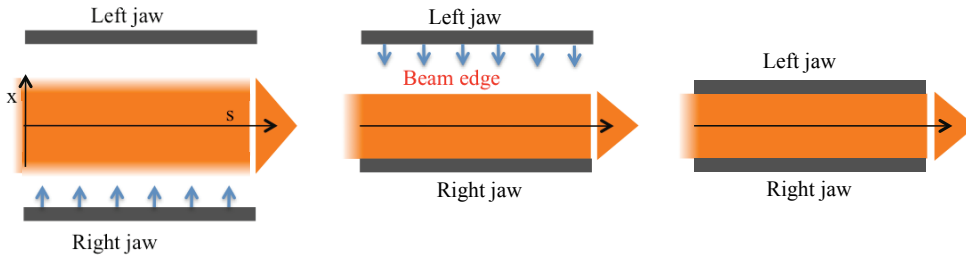
Figure 7.5: Beam based alignment technique: one jaw (right in this case) is moved in steps towards the beam until it touches it, defining a beam edge. The second jaw is then moved in as well until BLM signals indicate that it is touching the beam. Smaller consecutive steps allow a finer centering of the two jaws with respect to the beam.

The beam based alignment procedure works as follows:

1. One jaw is moved in steps towards the beam until significant losses are recorded by the BLMs.

2. Though the jaw is scraping only one side of the beam, after many turns an edge is produced on both sides of the beam due to betatron oscillations (see Fig. 7.5).

3. The second jaw is then moved in as well until BLM signals indicate that it has touched the beam halo. At this point the two jaws are centered with an accuracy equivalent to the size of the last step.

4. The fine alignment is obtained by consecutive movements of the two jaws as just described but with smaller steps.

The geometric centre of the collimator gap should then correspond to the beam centre within the defined accuracy.

Several collimator alignments were performed during the two MDs. One example is shown in Fig. 7.6 for MD1. The results for the two MDs are summarized in Table 7.2. The following observations are made:

- During MD1 an average beam based alignment accuracy of $30\,\mu$m was obtained with a stability of $\pm\,25\,\mu$m over more than 5 hours.

- For MD2 an average accuracy of $60\,\mu$m was used for a stability of $\pm\,75\,\mu$m over 5 hours.

Table 7.2: Summary of beam based alignment results for 2006. Position of the left and the right jaws are given after the end of the BLM-based centering procedure on the beam. From this the gap centre position is calculated (equal to beam centre). The accuracy in positioning of the collimator jaws is given by the size of the last step applied to the right and left jaws. The quadratic sum of these two values defines the accuracy in the beam centre determination.

MD1: October 31st - November 1st				
Time [hh:mm]		Left jaw	Right jaw	Gap center
Start	End	position [mm]	position [mm]	position [mm]
00:38	00:58	1.810 ± 0.010	-1.420 ± 0.010	0.195 ± 0.014
01:18	01:29	1.760 ± 0.010	-1.370 ± 0.010	0.195 ± 0.014
01:52	02:21	2.270 ± 0.010	-1.820 ± 0.010	0.225 ± 0.014
03:18	03:46	1.195 ± 0.050	-0.795 ± 0.050	0.200 ± 0.071
06:16	06:35	1.120 ± 0.020	-0.775 ± 0.020	0.175 ± 0.028
MD2: November 7th - November 8th				
Time [hh:mm]		Left jaw	Right jaw	Gap center
Start	End	position [mm]	position [mm]	position [mm]
23:54	00:13	5.600 ± 0.050	-5.125 ± 0.050	0.238 ± 0.071
00:53	01:15	3.735 ± 0.020	-3.450 ± 0.020	0.143 ± 0.028
05:00	05:33	1.490 ± 0.050	-1.310 ± 0.050	0.090 ± 0.071

It is noted that the evaluated beam centre was not corrected for real shifts of beam position. Measurements with beam position monitors were not available for the test periods. The reproducibility of the collimator centering is therefore better than the observed stability.
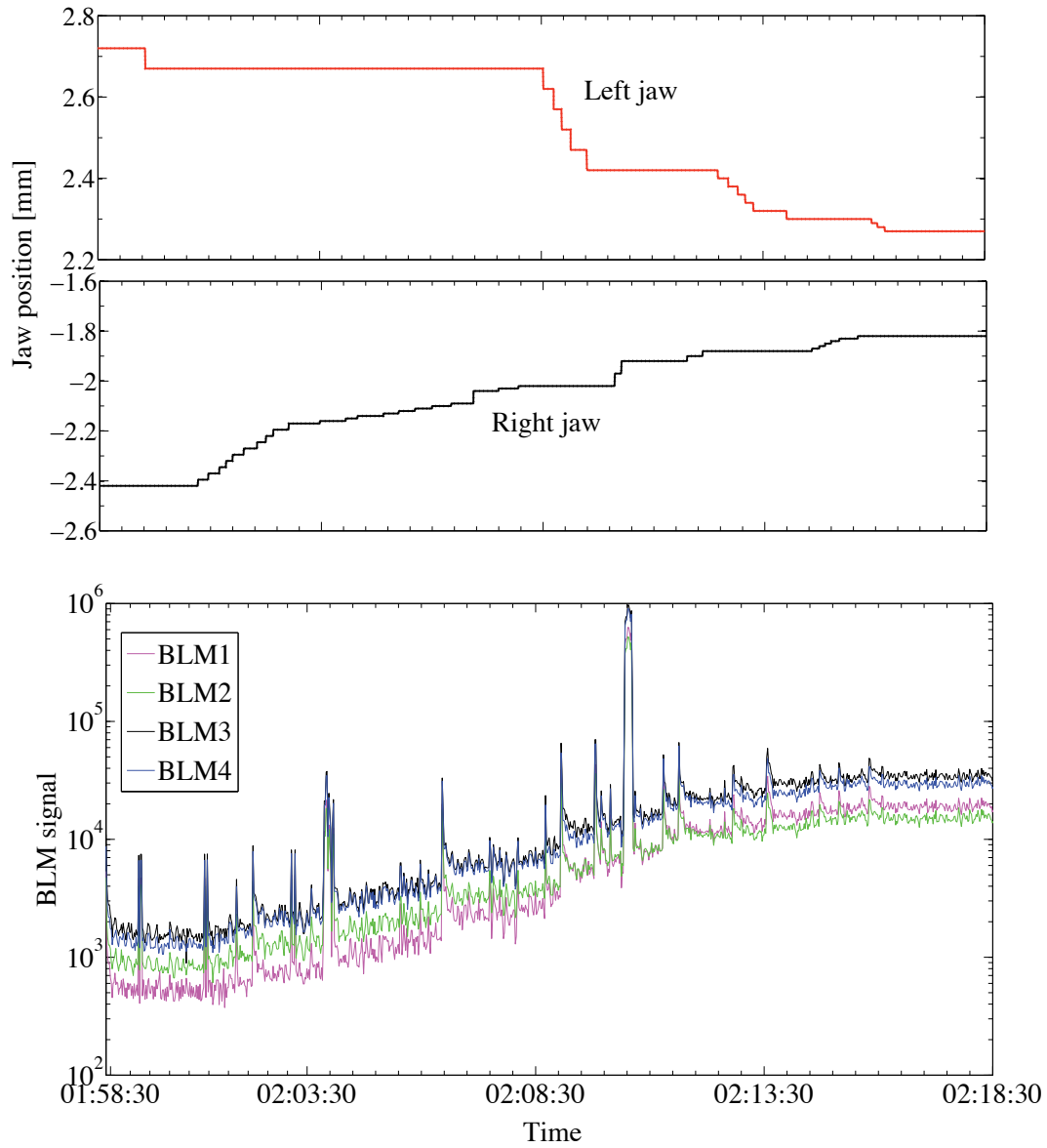
Figure 7.6: Example of beam based alignment during MD1 (November 1st 2006). The alignment is based on the readings of the 4 BLM channels just downstream of the collimator (bottom) when the two jaws are moved (top). The jaw angle was kept at zero for these measurements.

The manual beam based alignment of each collimator took on average around 20 minutes. From the collimator tests in the SPS the following conclusions are taken for setup of the LHC ring collimators:

• Setup time per collimator: 20 min

- Achievable alignment accuracy: $30\,\mu$m

- Setup time per LHC beam: 15 hours for 44 collimators (see section 4.3).

These results are used for performance simulations and commissioning plans in this PhD. The alignment procedure for many collimators in the LHC will be as follows [72]:

1. Set one collimator by using the described method in order to define a reference normalized position $n_{edge}\sigma$.

2. One edge of this collimator is then kept fixed to that position.

3. All the other collimator jaws in the considered plane are moved in, one by one, until touching the beam edge.

4. In this way all the collimators are calibrated to the same normalized beam position $n_{edge}\sigma$ for the reference beam orbit and local beta functions.

5. Afterwards, each collimator can be set by simple rescaling to its nominal position defined by the hierarchical order described in section 4.3.2.

This must be done for every plane: horizontal, vertical and skew.

An automatic setup procedure could reduce the evaluated time and will be prepared for the LHC in 2009. An initial manual setup will be still required, at least during the first phases of the machine commissioning.

7.2.4 Collimator beam based alignment: adjusting the jaw angle

Aligning the collimator ideally also involves adjusting the angles of the two jaws with respect to the beam envelope. The procedure for the angular scan is equivalent to the beam based alignment described above, except that it is based on consecutive movements of the two corners of each jaw. In Fig. 7.7 the concept of the angular alignment is depicted. It consists of the following steps:

1. The tilts of the retracted jaws are set to zero and a preliminary beam based alignment is performed, keeping the angle unchanged.

2. One single corner is then moved towards the beam until a peak of losses is registered by the BLMs, indicating that the corner is touching the beam. This introduces an angle on the jaw while producing an edge in the beam.

3. The second jaw corner is then moved in small steps, reducing progressively the tilt. No new loss should be registered by the BLM until the point where the second jaw end starts touching the beam.

4. At this stage the jaw should be parallel to the beam within an angle equal to the last step size divided by the jaw length l.
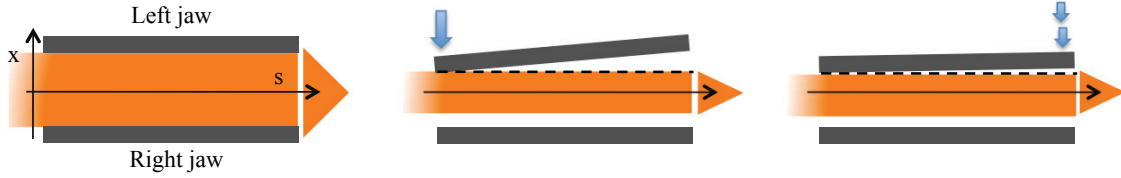
Figure 7.7: Angular adjustment procedure: one jaw corner is moved into the beam until it scrapes it. The second corner is moved as well but in smaller steps until new signals are recorded by the BLM. The jaw then should be aligned with an accuracy depending on the last step size and the collimator active length.

This did not work as expected in the performed tests. In Fig. 7.8 the stages of an angular scan as performed during MD1 are plotted. As a first approximation after the initial beam based alignment, the collimator jaws are considered parallel to the beam. Moving the upstream corner (LU: solid line) of the left jaw towards the beam with a 0.5 mm step resulted in a big spike of the BLM readout (Fig. 7.8, 1), consistent with an expected angle of $500\,\mu$rad (l = 1m) of the jaw. Based on this expectation, the following $50\,\mu$m movements of the down-stream corner (LD: dashed line) should not have provoked new losses. However small BLM signals appeared already at the first step (Fig. 7.8, 2).

This seemed to invalidate the starting hypothesis and to suggest that the jaw had an initial tilt. In order to verify this new assumption the LD corner was moved deeper into the beam by 0.5 mm (Fig. 7.8, 3). However, unexpected losses appeared with subsequent $50\,\mu$m movements of the LU corner (Fig. 7.8, 4) so that the second hypothesis was rejected. Two hypothesis were discussed:

1. This apparent inconsistent behavior could be ascribed to overall jaw vibrations induced by the motors when shifting one edge. Several metrology measurements showed nevertheless that this vibration is damped in one second while the corresponding BLM signals had longer decay times (see section 7.2.7).

2. Another explanation could be the change of the electromagnetic coupling field when varying the position of the resistive wall (the CFC collimator jaw) with respect to the proton beam. Quantitative estimates of such a possible effect and of its duration are beyond the scope of this thesis.

At the end, the angular scan had unclear conclusions and each beam based alignment was performed using as reference the zero angle (relying on collimator metrology during production). Then the precision of angular jaw alignment depends in practice on the accuracy of the collimator alignment in the tunnel.
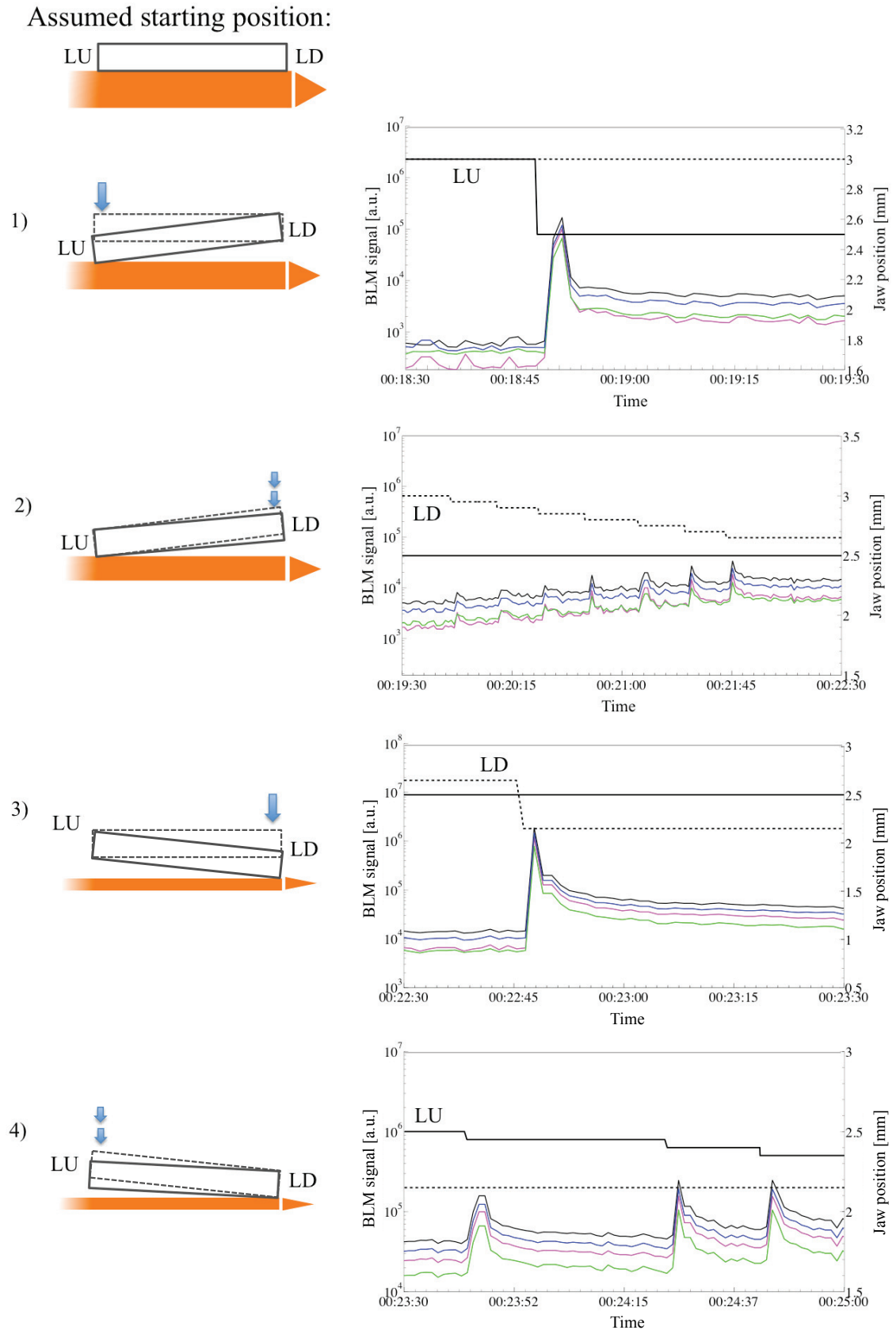
Figure 7.8: Illustration of jaw angle (left). Observed beam loss signals (right figure, left scale) and jaw position (right figure, right scale) during various adjustments. The same color code for the BLM readouts as in Fig. 7.6 applies.

This alignment is carried out by taking as reference two points on the collimator tank located at a distance $d = 640\,\text{mm}$ (see Fig. 7.9). Each point is aligned with a maximum error of $\delta x = 200\,\mu\text{m}$ to the beam line. The maximum tilt θ_{max} of a collimator in the tunnel is then given by:

$$\theta_{max} = \frac{\sqrt{2 \cdot \delta x^2}}{d} \tag{7.1}$$

which is equal to $442\,\mu\text{rad}$. It is noted that the internal collimator jaw alignment (jaw to tank to alignment points) is better than $50\,\mu\text{rad}$, much smaller than the above error.
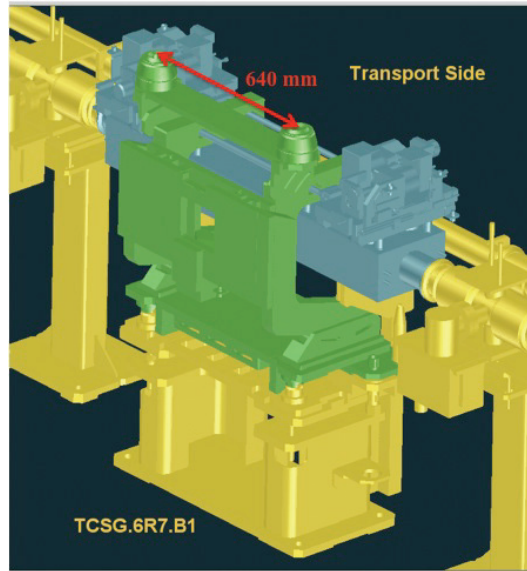
Figure 7.9: Sketch of a horizontal secondary collimator installed in the LHC tunnel. Two reference points located on the tank at a distance of 640 mm are used for the alignment of the collimator with respect the upstream and downstream elements of the machine.

7.2.5 Full beam scraping

An alternative method to find the beam centre position and to estimate the beam size at a collimator location is the full beam scraping. Moving one jaw into the beam distribution leads to scattering and absorption of the intercepted particles. Due to phase space mixing the jaw always limits on both sides of the beam distribution. The beam current circulating in the accelerator is reduced (Fig. 7.10).

The distribution of the beam particles in the normalized horizontal phase space $N(x, x')$ can be described by a Gaussian of the form:
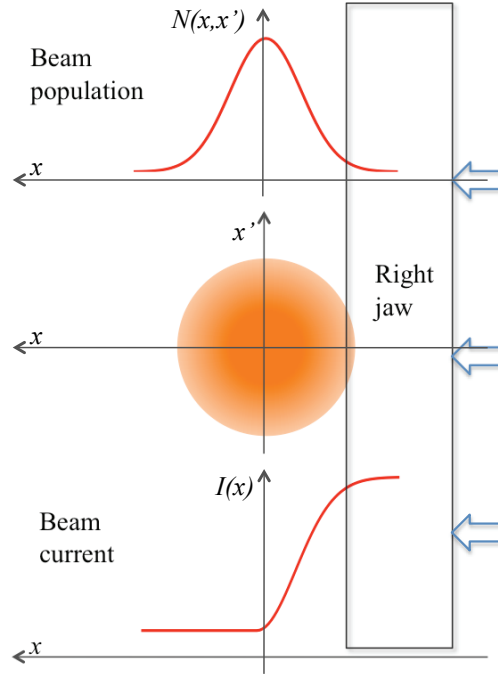
Figure 7.10: Beam scraping: one jaw is moved into the beam. The beam particle population in the normalized transverse phase space $N(x, x')$ (top) and the current intensity I (bottom) are shown as function of the position x of the jaw. The centre of the beam corresponds to the jaw position where the beam current goes to zero.

$$N(x, x') = \frac{1}{2\pi} exp \left(\frac{-x^2 - x'^2}{2\sigma^2} \right) \tag{7.2}$$

It can be shown that the drop of the beam current $I(x)$ as a function of the jaw position can be expressed as [82, 83]:

$$I(x) = I_0 \left[1 - exp(\frac{-(x - x_0)^2}{2\sigma_x^2}) \right]. \tag{7.3}$$

Here, I_0 is the beam current at the beginning of the scraping, x_0 is the beam centre (the point where $I(x)$ goes to zero) and σ_x is the beam size at the collimator.

In order to determine x_0 and to estimate the reproducibility of this method, a number of full beam scrapings were carried out. For each machine cycle the beam current was monitored (via Beam Current Transformers BCT) with a data acquisition time step of 10 ms. This acquisition was fully independent of the collimator control system and the synchronization between the two data sets was an important issue. The jaw position was recorded typically every 0.5 s. Several variations in the
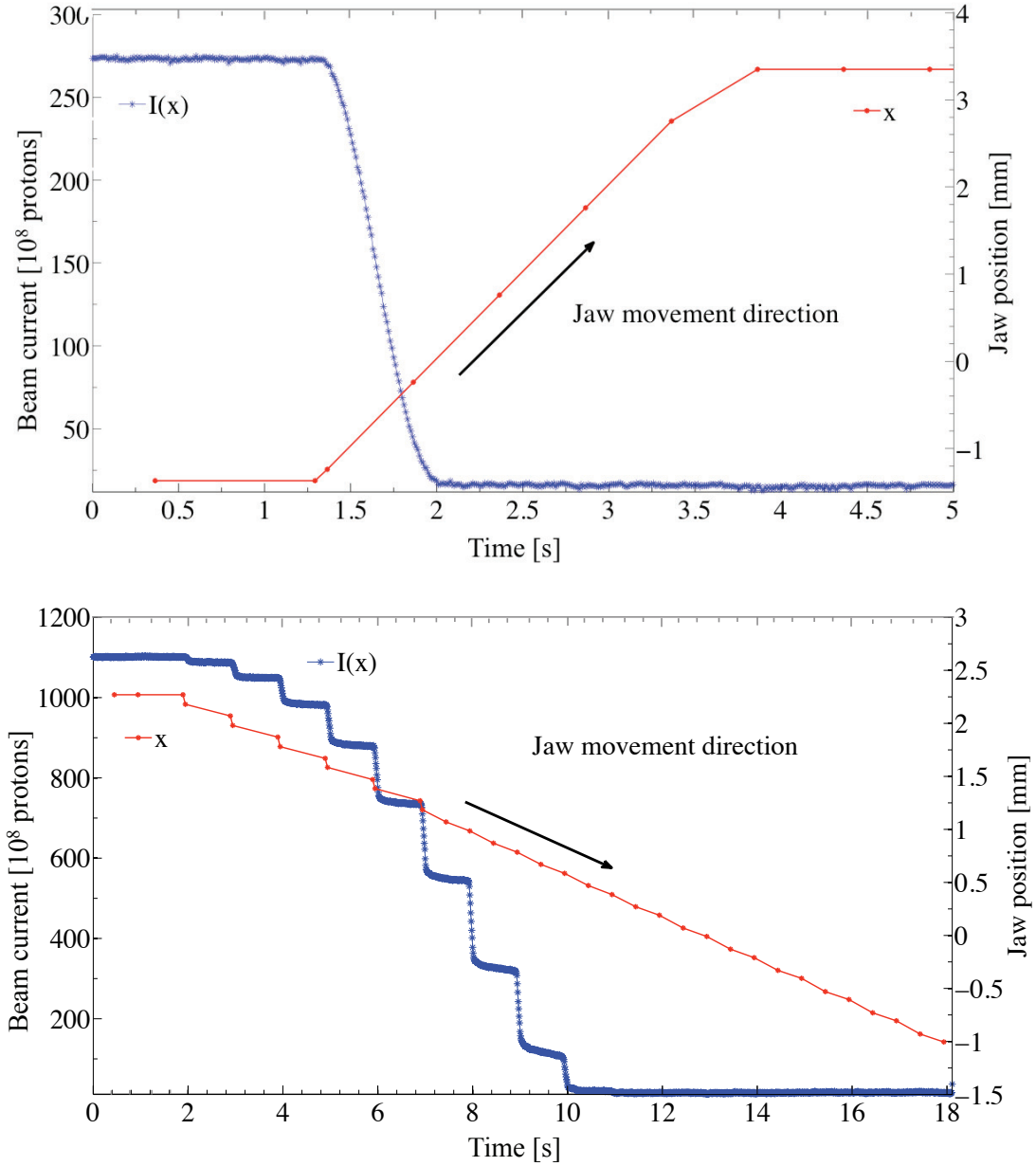
Figure 7.11: The beam current measured by the BCT and the jaw movements
are shown as a function of time for two independent tests. The jaw that scraped
the beam was either moved in one go from the initial to the ending position (top:
01:29:20 data in Table 7.3) or in steps (bottom: 02:21:52 data in Table 7.3).

acquisition time step of the jaw position (from 0.1 s up to 1 s) were observed. This
feature is still under investigation.

Once the temporal correlation between the BCT data and the jaw movement

data was defined (see Fig. 7.11), it was possible to express the beam current as a function of the jaw position (see Fig. 7.12), with a time deviation smaller than $10\,\mathrm{ms}$ (corresponding to $20\,\mu\mathrm{m}$ for the applied jaw speed of $2\,\mathrm{mm/s}$). In total 11 full beam
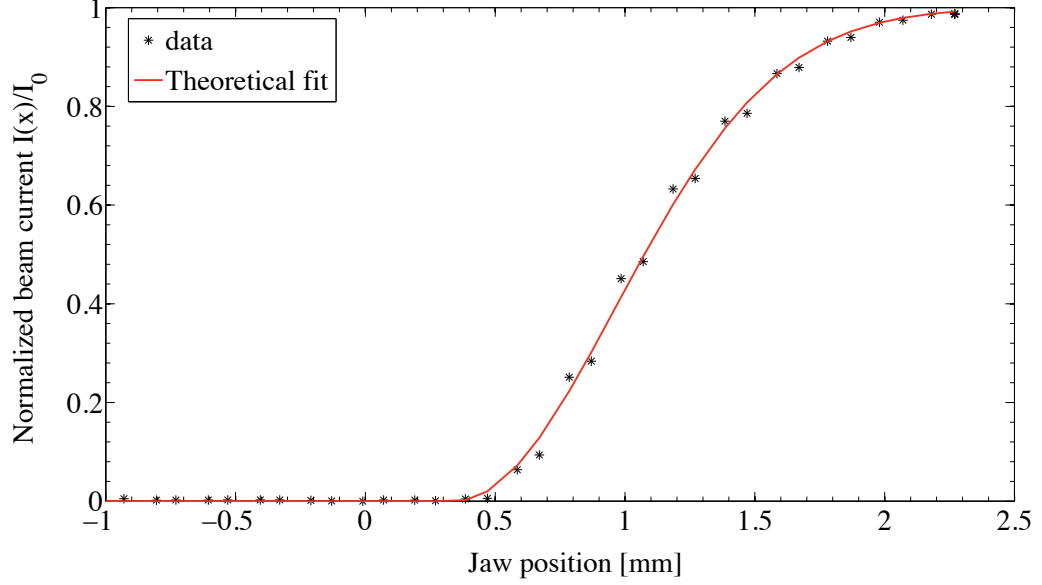
Figure 7.12: The beam current measured by the BCT is plotted as a function of the jaw position for the full beam scraping started at 02:21:52 of MD1. The fit given by equation 7.3 is also displayed (red line).

scrapings were performed. Several data sets were affected by problems of machine stability and data quality. These were not considered. The results for valid data sets are summarized in Table 7.3. The errors on the beam centre position quoted in the table are given by the sum of the fitting error plus $20\,\mu\mathrm{m}$ due to the synchronization error discussed above. From MD1 data the beam centre could be determined at an average position $\bar{x}_0 = 314\,\mu\mathrm{m}$ with a stability of $\pm 55\,\mu\mathrm{m}$ over 1 hour. For MD2 a large spread in the fitted beam centers was observed, corresponding to a stability of $\pm 235\,\mu\mathrm{m}$ over about 1.5 hours. The average centre position was $\bar{x}_0 = 31\,\mu\mathrm{m}$.

For the data at 02:21:52 and 02:33:37 the full beam scraping was performed by moving the jaw in steps into the beam. This was done to allow a longer acquisition time of the beam current for a defined position of the jaw. The 02:33:37 scraping started in between two consecutive SPS machine cycles, when a dead-time exists and the beam current is not recorded for $10\,\mathrm{s}$. This implied a loss of some data. In this case x_0 was evaluated by defining the best fit for the available data, whereas the beam size could not be calculated.

Several beam profile measurements by wire scanner were performed during the two MDs. Results of measurements preceding a beam scraping allowed to compare

Table 7.3: Summary of the results for beam centering with full beam scraping.

MD1: October 31st - November 1st				
Time [hh:mm:ss]		**Scraping**	**Beam centre**	$\boldsymbol{\sigma_x}$
Start	**End**	**jaw**	**position [mm]**	**[mm]**
01:29:20	01:29:37	right	+0.245±0.043	0.565±0.033
02:21:52	02:22:10	left	+0.345±0.064	0.619±0.031
02:33:37	02:33:54	left	+0.354±0.084	n.a.
MD2: November 7th - November 8th				
Time [hh:mm:ss]		**Scraping**	**Beam centre**	$\boldsymbol{\sigma_x}$
Start	**End**	**jaw**	**position [mm]**	**[mm]**
05:44:54	05:45:21	right	+0.096±0.033	0.560±0.047
06:20:52	06:21:19	left	−0.189±0.060	0.984±0.112
06:46:02	06:46:30	right	+0.282±0.033	0.908±0.024
07:24:53	07:25:20	left	−0.065±0.050	0.725±0.026

the calculated σ_x with the measured beam size (see Table 7.4). In two cases the results differ within the estimated error. On the other hand, a discrepancy by a factor of 1.8 is observed for the last measurement. No jaw movement that could justify this difference was performed between the profile scan and the scraping.

Table 7.4: Comparison between horizontal beam profile measurements by wire scanner and σ_x values calculated from beam scraping data (see Table 7.3).

	Beam profile measurements		**Full beam scraping**	
	Time	$\boldsymbol{\sigma_x}$	**Initial time**	$\boldsymbol{\sigma_x}$
	[hh:mm]	**[mm]**	**[hh:mm:ss]**	**[mm]**
MD1	01:19	0.582	01:29:20	0.565±0.033
MD2	05:42	0.591	05:44:54	0.560±0.047
	06:43	1.634	06:46:02	0.908±0.024

7.2.6   Comparison between beam based alignment and beam scraping results

The beam based alignment and the full beam scraping provide two completely independent ways for the determination of the beam centre position. The comparison of the results obtained with these two methods allows to have further information about the accuracy in centering the jaw positions with respect to the beam. In Table 7.5 the values of x_0 are summarized for measurements close in time. As data

close in time are selected, small changes in the beam conditions are expected (orbit, beam size etc.). In two cases the beam based alignment was immediately followed by a full scraping. Data differ on average by $58.7\,\mu$m, showing a good agreement between the two measurement methods. The maximum difference is 120μm.

Table 7.5: Comparison between beam centre positions determined through beam based alignment and beam scraping procedures for data sets close in time.

	Beam based alignment		Full beam scraping	
	final time [hh:mm]	Beam center [mm]	Initial time [hh:mm]	Beam center [mm]
MD1	01:29	0.195 ± 0.014	01:29:20	0.245 ± 0.043
	02:21	0.225 ± 0.014	02:21:52	0.345 ± 0.066
MD2	05:33	0.090 ± 0.071	05:44:54	0.096 ± 0.033

7.2.7 Beam loss response with stored beam

Moving the collimator jaw into the beam halo generates a shower of particles which is detected by the downstream BLMs and which is seen as a peak in the beam loss signal.

In the case of infinite aperture we would expect the following intensity loss ΔI_{jaw} for a movement of the collimator jaw by Δx from an initial position x_0 ($x_0 > \Delta x$):

$$\Delta I_{jaw}(x_0, \Delta x) = \int_{x_0}^{x_0 - \Delta x} I(x)dx. \tag{7.4}$$

This intensity loss occurs over a time T_{loss} given by the time of jaw movement T_{jaw} and the time T_p required for all particles of affected amplitude to reach the jaw:

$$T_{loss} = max(T_{jaw}, T_p). \tag{7.5}$$

For the results shown, T_{jaw} is between $10\,$ms and $1\,$s. The time T_p depends on the machine tunes and the coupling between the different planes [84].

In addition to the loss ΔI_{jaw} from jaw movement there is a loss contribution ΔI_τ from intensity lifetime τ. The total loss ΔI_{tot} over a given time is then:

$$\Delta I_{tot}(x) = \Delta I_{jaw}(x_0, \Delta x) + \Delta I_\tau. \tag{7.6}$$

with $x = x_0 - \Delta x$. The jaw may only intercept a fraction $F(x)$ of the intensity lifetime related loss ΔI_τ, the rest being lost in the machine aperture. The jaw will then intercept a total intensity:

$$\Delta I(x) = \Delta I_{jaw}(x_0, \Delta x) + F(x)\Delta I_\tau. \tag{7.7}$$

While the second term of eq. 7.7 constantly contributes to $\Delta I(x)$ the first term acts just over T_{loss}. The beam loss monitors record $\Delta I(x)/\Delta t$. The measured beam loss response is shown in Fig. 7.13. Another example is shown in Fig. 7.14.
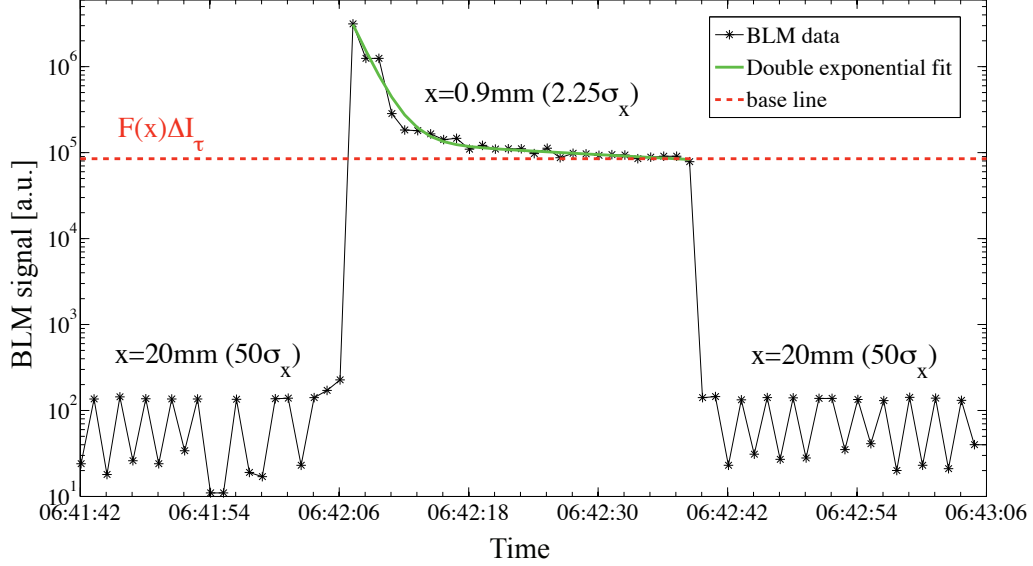
Figure 7.13: Measured beam loss response to a jaw movement from $50\sigma_x$ down to $2.3\sigma_x$ (averaged over the 4 BLM readings, MD 1 data). A part of the beam halo is scraped, leading to a loss peak with a double exponential tail. A new high loss plateau is approached, indicating that the jaw became an overall aperture bottleneck, intercepting protons lost due to intensity lifetime.

The loss response shows systematic long decays of the loss signals. This decay can be approximated by a double exponential function of the form:

$$I(t) = a \cdot e^{b \cdot t} + c \cdot e^{d \cdot t} \tag{7.8}$$

For the two shown examples we find the decay times in Table 7.6. An average time over all analyzed loss tails is also listed.

Specific tests proved that these tails were indeed beam-induced and not instrumental effects. The physics process related to this observation is still under investigation. Long decay times can affect the time required for beam based alignment of collimators in the LHC: waiting periods must be added before reliable BLM response can be obtained. This is already the case in the TEVATRON.

The beam loss signals in Fig. 7.13 and Fig. 7.14 indicate different loss rates $\Delta I(x)/\Delta t$ at the collimator jaw for different settings of jaw position. It is assumed that this is related to a different fraction of intensity losses being intercepted at the jaw (the rest goes into the aperture around the ring). Alternatively it has been
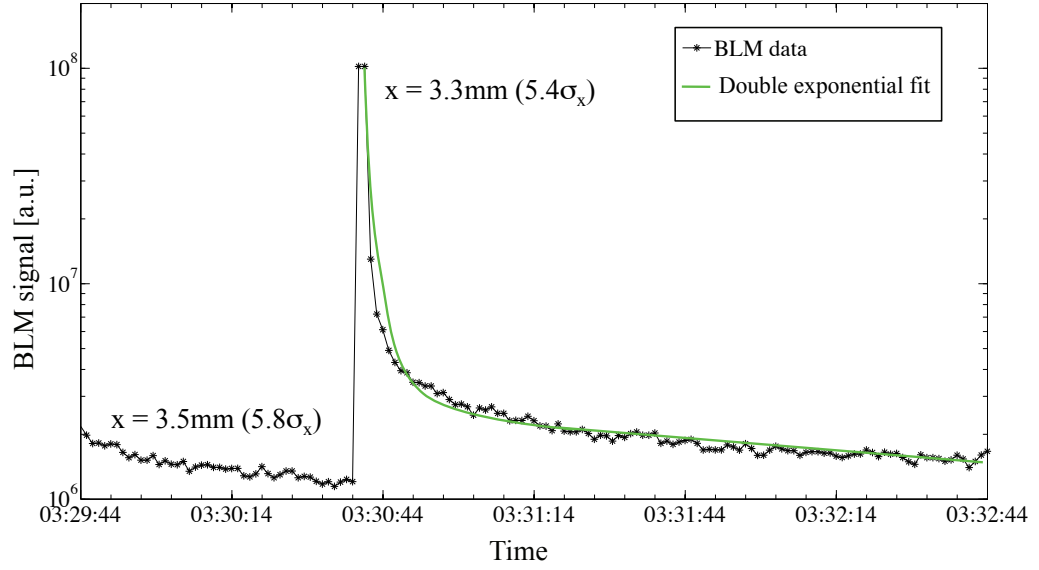
Figure 7.14: Measured beam loss response to a jaw movement from $5.8\sigma_x$ to $5.4\sigma_x$ (averaged over the 4 BLM readings, MD 2 data). A part of the beam halo is scraped, leading to a loss peak with a double exponential tail.

Table 7.6: Decay times for the two tail measurements shown in Fig. 7.13 and Fig. 7.14 and average values for all analyzed data sets. Average values include the standard deviation obtained from the data.

Loss reduction factor	Decay time [s]		
	Fig. 7.13	Fig. 7.14	average
10	1.2	2.4	2.0±0.9
100	11.7	15.2	10.6±3.9

suspected that the presence of the jaw can deplete the beam distribution close to the jaw surface, leading to higher loss rates close to the centre of the distribution. The beam lifetime would be a function of the jaw position. There exists, however, no conclusive theory for this. Also, the mechanism for generating losses that extend up to 20 s after completion of the jaw movement is not explained.

Other interesting observations were resulting from changes in beam tunes. During the tests the vertical tune Q_y was kept at 26.21 whereas the horizontal tune Q_x (nominally equal to 26.125) was changed in steps until the third integer resonance was reached (causing loss of the full beam). Red arrows in Fig. 7.15 indicate the changes of the rational part of Q_x. It is shown that the tune shifts ΔQ_x induced losses even without any jaw movement.
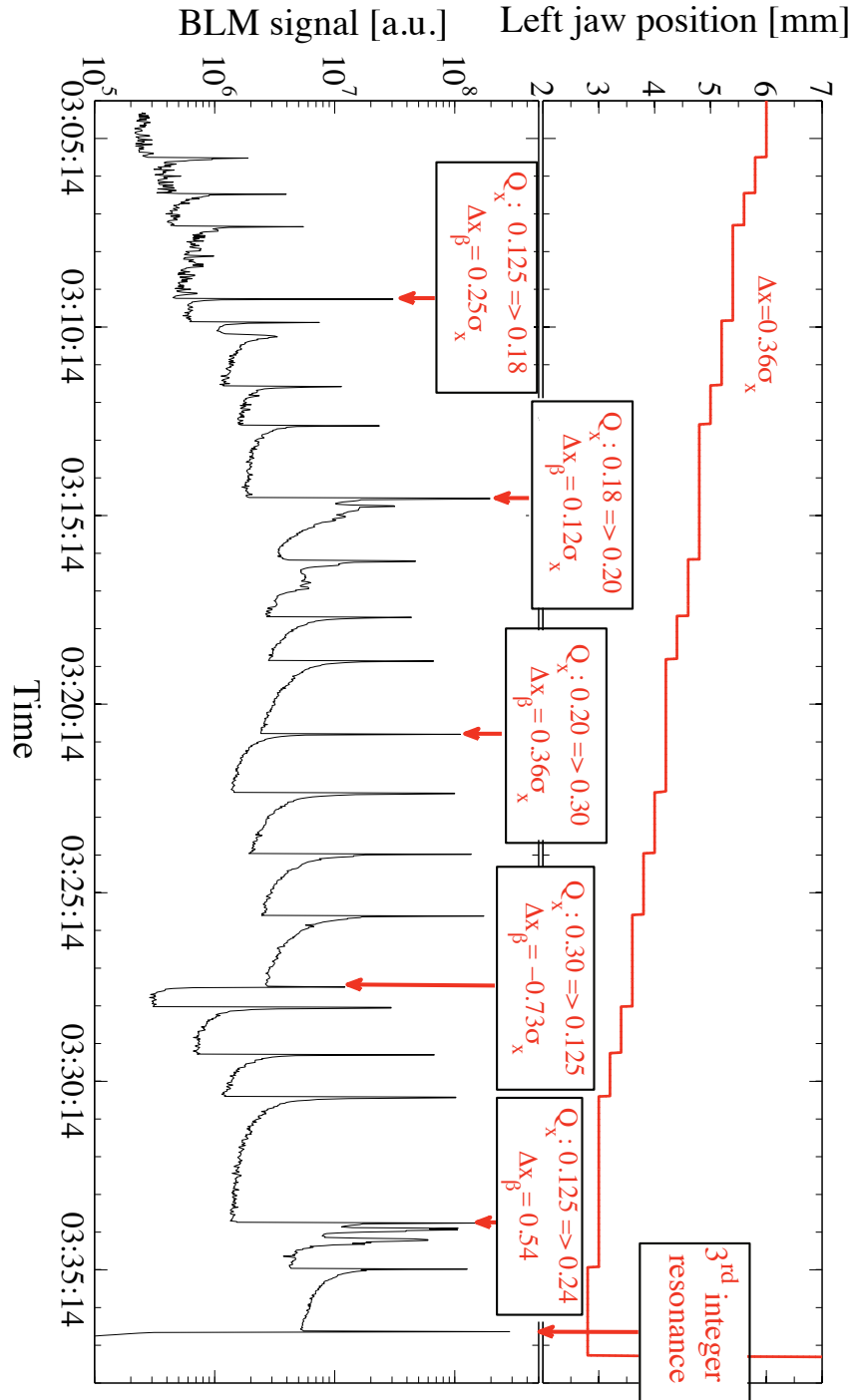
Figure 7.15: Jaw movements (top) and beam loss signals (bottom) versus time. The red arrows indicate changes in Q_x. Δx_β due to tune change is also indicated.

It is interesting to notice that the change of the horizontal tune caused a variation in the betatron orbit $\Delta x_\beta = x_{\beta,i+1} - x_{\beta,i}$ of up to $400\,\mu$m ($0.73\,\sigma_\beta$). The expected change is given by the relation:

$$\Delta x_\beta = \sqrt{\epsilon_x}\left[\sqrt{\beta_{x_{i+1}}}\cos(2\pi Q_{x_{i+1}}) - \sqrt{\beta_{x_i}}\cos(2\pi Q_{x_i})\right]. \qquad (7.9)$$

Measured orbit changes are listed in Table 7.7.

Table 7.7: Summary of BLM signals for different settings $x_0 - \Delta x$ of collimators and various tune changes ΔQ_x. Δx_β is the observed orbit change from tune changes. It is also indicated how many spurious "echo" signals were observed, if any.

MD2: November 7th - November 8th						
Time	**BLM**	x_0	Δx	ΔQ_x	$\Delta x_\beta\ [\sigma_x]$	**Echos**
[hh:mm:ss]	**[a.u.]**	$[\sigma_x]$	$[\sigma_x]$	$Q_{x,i+1} - Q_{x,i}$	$x_{\beta,i+1} - x_{\beta,i}$	#
03:09:28	$3.01\cdot10^7$	9.8	0.00	$+0.055$	$+0.25$	0
03:10:03	$6.83\cdot10^6$	9.8	0.36	0.000	0.00	1
03:14:45	$1.94\cdot10^8$	8.7	0.00	$+0.020$	$+0.12$	2
03:16:23	$4.28\cdot10^7$	8.7	0.36	0.000	0.00	3
03:21:02	$1.09\cdot10^8$	7.6	0.00	$+0.100$	$+0.36$	0
03:27:45	$9.40\cdot10^6$	6.5	0.00	-0.175	-0.73	0
03:34:02	$1.58\cdot10^8$	5.4	0.00	$+0.115$	$+0.54$	2
03:36:55	$2.81\cdot10^8$	5.1	0.00	$+0.09\bar{3}$	resonance	0

A change of horizontal orbit is equivalent to a change of the jaw position. It is therefore expected that tune changes induce beam losses through the change of orbit. The observed loss signals (see Fig. 7.15) are compatible with this explanation, plus some extra losses due to slightly reduced beam stability during the tune change.

The tune variation at 03:27:45 induced a negative orbit change, equivalent to a retraction of the jaw. Indeed, a sharp reduction in losses at the jaw is observed in Fig. 7.15. Also essentially no loss tail is observed, as one would expect.

During the measurements so called "echo" signals were recorded a few seconds after the initial spikes. These signals were generated by either jaw steps Δx or tune shifts ΔQ_x (see Fig. 7.8). All "echo" events from tune shifts or jaw movements are listed in Table 7.7. Table 7.8 contains information about the amplitude of the "echo" signals and their delay with respect to the first loss signal Δt. The observation could not be explained. Also "echoes" only appeared sporadically and might be related to machine stability problems.
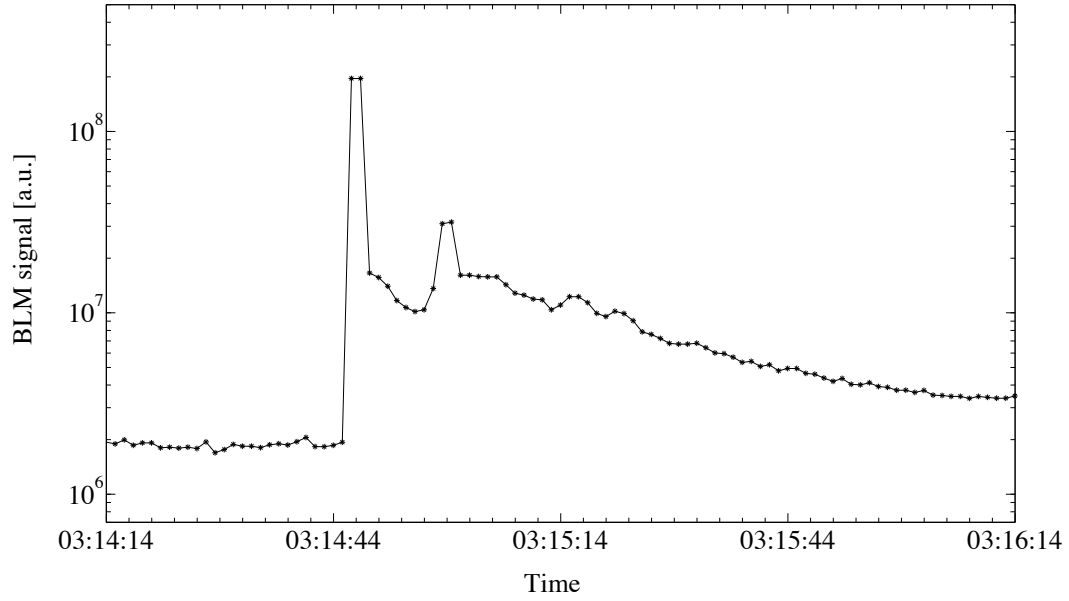
Figure 7.16: Zoom of the BLM signal versus time after a change in the horizontal tune at 3:14:45. An unexplained second loss peak appeared, also seen during other measurements.

Table 7.8: The BLM signal amplitude and the delay Δt with respect to the first peak are listed for the spurious "echo" signals appearing during MD2 (see Fig. 7.15).

MD2: November 7th - November 8th		
Time [hh:mm:ss]	BLM amplitude [a.u.]	Δt [sec]
03:10:03	$2.11 \cdot 10^6$	24
03:14:45	$1.06 \cdot 10^7$	12
	$2.27 \cdot 10^7$	17
03:16:23	$5.50 \cdot 10^6$	7
	$1.04 \cdot 10^6$	35
	$8.28 \cdot 10^5$	42
03:34:02	$9.52 \cdot 10^7$	8
	$5.36 \cdot 10^7$	26

7.3   Robustness tests

Robustness is one of the main features required for the phase 1 collimation system. A carbon-based collimator should be able to survive without damage not only during nominal operation but also in case of expected failures [44]. For this reason a

prototype of a secondary LHC collimator (TCSG) was installed in the TT40 beam extraction line and was exposed to robustness tests.

During first tests in 2004 a beam of $3.2 \cdot 10^{13}$ protons at 450 GeV was shot repeatedly against a secondary collimator jaw. The collimator survived well but showed about 300 μm permanent deformation of the jaw copper support (see section 4.3.1 for a jaw cross section). The copper was then replaced by alumina strengthened dispersion copper (GLIDCOP) with higher yield strength in order to keep the deformation of the jaw within the flatness requirements of 40 μm. A new collimator prototype was tested in 2006[2]. The priorities were:

1. Repetition of the 2004 high intensity robustness tests for the validation of the final jaw design with GLIDCOP supports.

2. Measurement of beam induced jaw vibrations and estimation of the maximum temporary transverse displacement during and after beam impact.

3. Investigation on usage of accelerometers and microphones for direct beam impact detection.

The beam parameters for the TT40 tests are summarized in Table 7.9. It is noted that a different bunch configuration was used but overall parameters were identical in 2004 and in 2006.

Table 7.9: Beam condition during high intensity TT40 tests.

Beam parameter	2004	2006
Bunch Population	$1.1 \cdot 10^{11}$ protons	
Number of bunches	4×72	6×48
Bunch spacing	25 nsec	
Bunch length	1 nsec	
Beam size (r.m.s) at collimator	1×1 mm^2	
Energy	450 GeV	

7.3.1   Experimental apparatus in 2006

A special collimator prototype was mounted in the TT40 extraction line for 2006: only the right jaw was installed. The collimator tank was equipped with four windows in order to perform vibration measurements using a Laser Doppler Vibrometer (LDV). Fig. 7.17 shows the prototype and the four points used for LDV measurements: three of them coincided with the implemented windows (1,3 and 4) while

---

[2] 09/11/2006 from 8:00 until 00:00

one fell on the jaw support table (2). Piezoelectric accelerometers, placed close to point 2, and one microphone were used for direct beam impact detection [85, 86]. Temperature sensors were installed upstream and downstream of the collimator jaw to check the influence of the beam intensity on the temperature rise.
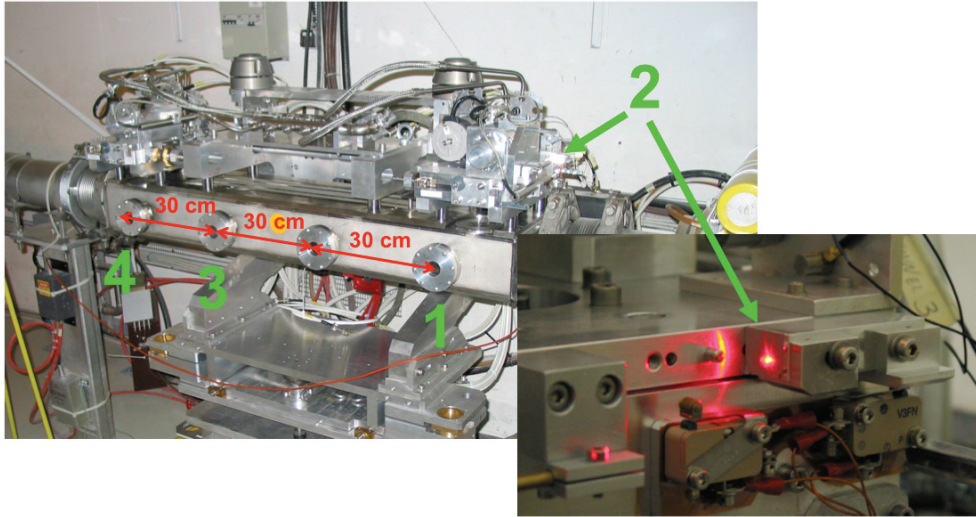
Figure 7.17: The tank of the prototype collimator was equipped with four windows for the measurements with the Laser Doppler Vibrometer. The 4 points used for the vibration measurements are shown: three points coincided with the windows while one fell on the jaw support table close to the accelerometers.
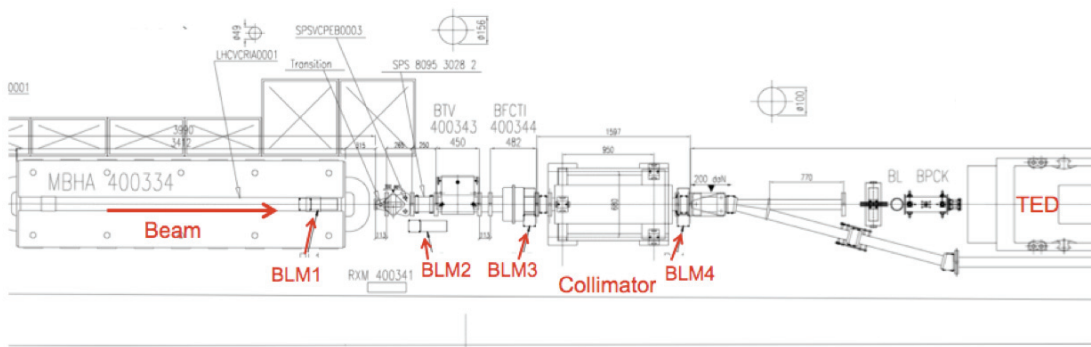
Figure 7.18: Scheme of the TT40 installation for robustness tests of a LHC prototype collimator. Three beam loss monitors (BLMs) are installed upstream of the collimator and one BLM is located between the prototype and the TED.

Four BLMs were used for measuring the showers of particles produced by the beam impacting on the collimator. One BLM was placed between the prototype and the downstream absorber (TED) while the remaining three were installed upstream of the collimator in order not to be saturated by showers of backscattered particles coming from the TED (see Fig. 7.18).

The collimator was remotely controlled through the LHC collimator control software. The jaw position was read through the same sensors as installed in the final LHC collimators: radiation hard LVDTs and resolvers with at least three times better accuracy than those mounted in the SPS prototype.

7.3.2   Beam based alignment with pulsed beam

A preliminary alignment of the collimator jaw with respect to the beam was required for the TT40 tests. The main reason for determining the beam centre was the need of controlling the impact parameter: a scan from 0 mm to 5 mm with steps of 1 mm (see Fig. 7.19) was foreseen for robustness tests.
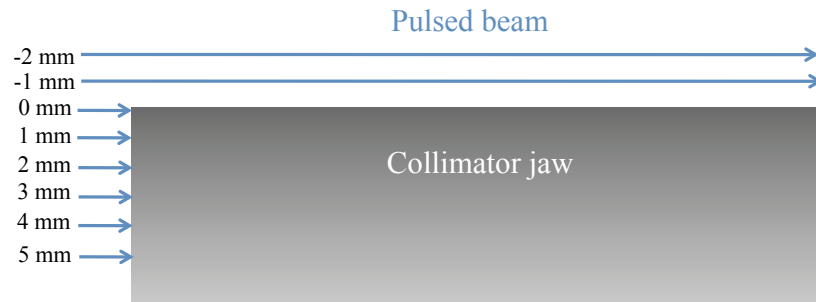
Figure 7.19: Scheme of impacts on the collimator jaw in TT40. The pulsed beam was shot against the collimator jaw with an impact parameter ranging from 0 mm to 5 mm with steps of 1 mm.

Since a pulsed, single-pass beam was used in TT40, the beam based alignment method differed from the one described in section 7.2.3. The collimator jaw was set at different positions and one batch was extracted form the SPS and shot towards the collimator. If the jaw was out from the beam trajectory the batch hit the TED and no losses were recorded by the BLMs, whereas BLM signals appeared as soon as the jaw intercepted the beam. The amplitude of the BLM readouts increased when setting the jaw deeper into the beam core and the maximum intensity was recorded when the full batch fell inside the jaw. In Fig. 7.20 the data for the first beam based alignment are shown. They can be fitted by a Gaussian. The beam centre corresponds to the half height of the Gaussian fit, about 3 mm in this case. The trajectory of the extracted beam was then moved in order to place the beam centre on the central position of the right jaw. A new beam based alignment was
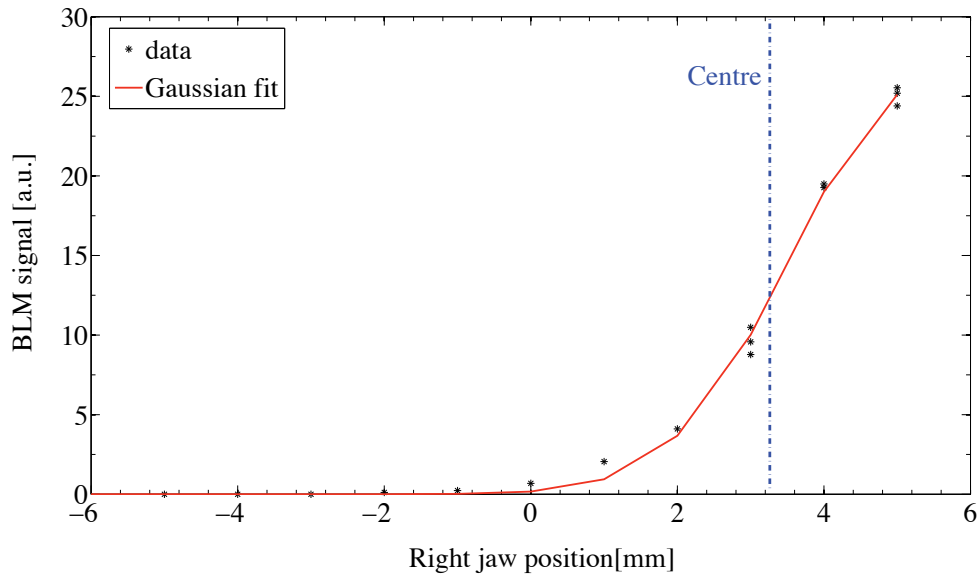
Figure 7.20: Measured beam loss versus jaw position for beam based alignment of the collimator jaw in TT40. The center of the beam corresponds to about the half height point of the Gaussian.
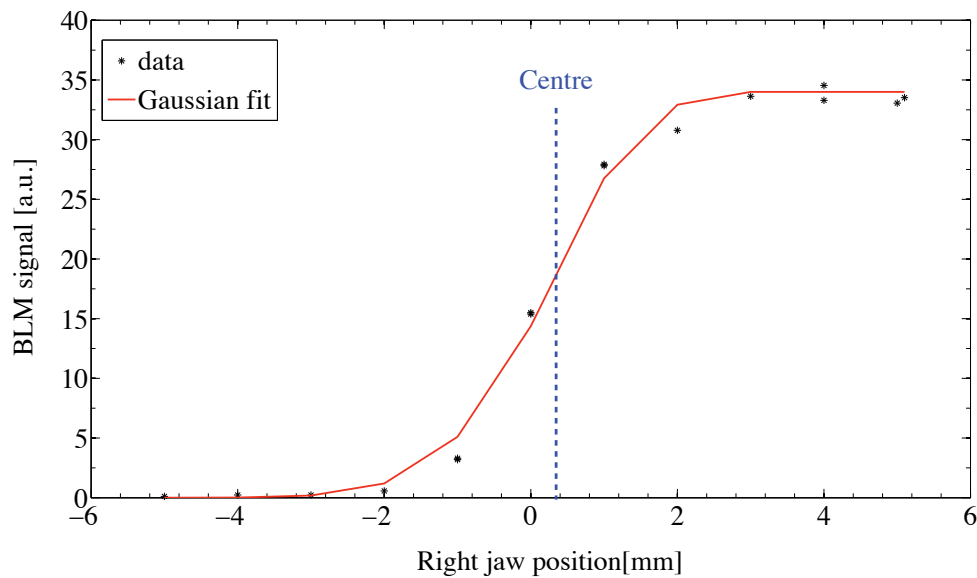
Figure 7.21: Measured beam loss versus jaw position for beam based alignment of the collimator jaw in TT40. The orbit was moved in order to have coincidence between the beam center and the centre of the jaw position.

performed. The results are shown in Fig. 7.21 and a good agreement with the expected new beam position is seen. The achievable accuracy was given by the 1 mm beam size.

Once the alignment was achieved, several extractions were performed with different intensities, impact parameters and LDV measurement points. They are summarized in Table 7.10. Some batches were shot directly against the TED to test the capability of the accelerometers and of the microphones to discriminate these impacts from direct hits on the collimator. The full intensity events ranged as foreseen from 5 mm to 0 mm and also down to negative impact parameters to re-check the beam centre position (see Fig. 7.19). The total number of extractions and the integrated intensity was limited by the maximum dose allowed by radiation protection: $2 \cdot 10^{15}$ protons for the full test run. It is noted that LDV results are reported in another PhD thesis [87].

7.3.3 Permanent jaw deformation

The examination of the collimator tested in 2004 showed that both jaws were bent outwards with respect to the beam. The maximum absolute deformation was 250 μm. The investigation of all the collimator components revealed that the CFC bar survived without surface damage nor deformation while the Cu contact plate, located just behind (see section 4.3.1), showed a deformation of about 300 μm. Finite
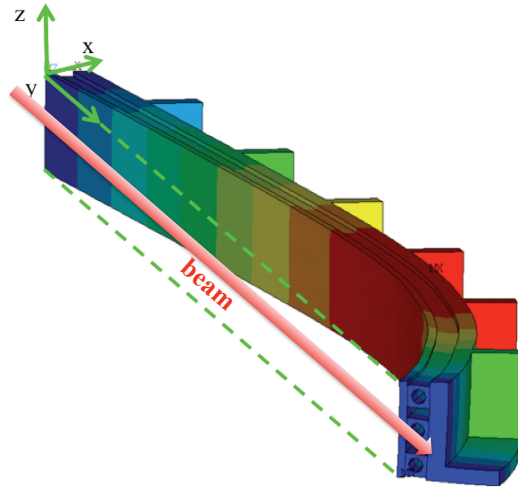
Figure 7.22: Cu plate model of the collimator prototype used during 2004 tests. FEM simulations reproduced the bend outwards with respect to the beam and showed a good agreement on the order of 50 μm with the measurements [69, 77].

element model (FEM) calculations allowed to reproduce the effects of the impacting beam on the Cu jaw support. A 350 μm deformation was predicted, in good agree-

Table 7.10: Extraction numbers, intensities, impact parameters and LDV measurement points used during the robustness tests.

extraction number	Intensity [10^{10} protons]	Impact parameter [mm]	Measurement point with LDV				time
			1	2	3	4	
1	480	TED					19:35
2	480	5			X		19:41
3	960	TED					19:53
4	960	5			X		19:58
5	1920	5			X		20:05
6	2880	TED					20:20
7	2880	5			X		20:24
8	2880	4			X		20:39
9	2880	3			X		20:54
10	2880	2			X		21:09
11	2880	1			X		21:14
12	2880	0			X		21:19
13	2880	−1			X		21:24
14	2880	−2			X		21:27
15	2880	−3			X		21:30
16	2880	TED					21:37
17	480	4			X		21:54
18	480	4			X		21:58
19	480	4			X		22:02
20	480	4			X		22:05
21	480	4				X	22:10
22	480	4				X	22:12
23	480	4				X	22:16
24	480	4				X	22:20
25	480	4	X				22:30
26	480	4	X				22:34
27	480	4	X				22:36
28	480	4	X				22:38
29	480	4		X			22:56
30	480	4		X			22:57
31	480	4		X			23:00
32	480	4		X			23:02
33	480	4		X			23:06
34	480	4		X			23:12

ment with the measurements. In Fig. 7.22 the simulation results for the deformed Cu plate are presented [69, 77].

The simulations also predicted that a GLIDCOP support exposed to identical beam conditions would have implied a much smaller permanent deformation ($16\,\mu$m). The collimator design was changed accordingly. The new collimator jaw was tested in 2006. In Fig. 7.23 the deformation of the jaws measured after the TT40 tests is compared with the straightness before beam exposure. For the old design the non-flatness was increased by $160\,\mu$m. For the new design no change was observed within the measurements accuracy of $20\,\mu$m.
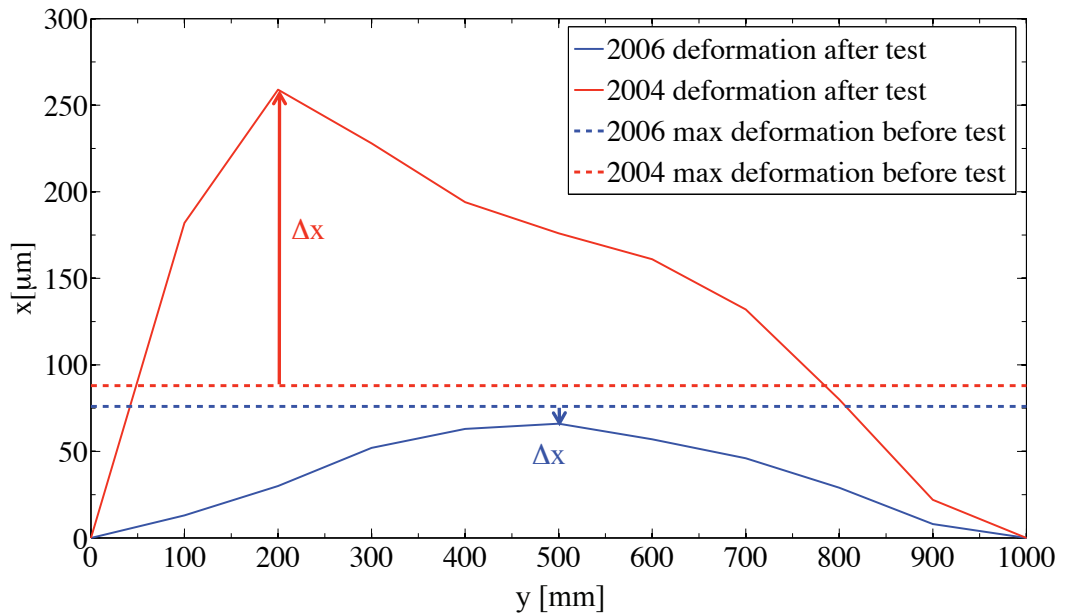
Figure 7.23: Comparison between the deformation of the jaws measured after the 2004 and 2006 robustness tests. The initially measured non-flatness before the beam exposure is also indicated [69, 77].

7.3.4   Jaw temperature

The temperatures of the collimator jaw (upstream and downstream) and of the cooling water (see section 4.3.1) were continuously monitored during the TT40 tests. The data corresponding to measurements with different beam intensity and impact parameters are shown in Fig. 7.24. The different beam impacts are indicated by numbers as defined in Table 7.10 ("extraction number"). The water temperature stayed more or less constant at 22-22.5 °C until full beam intensity was reached, then it increased linearly up to 33 °C ($\sim3 \cdot 10^{-3}$ °C s^{-1}). Afterwards it started decreasing

again for negative impact parameters. Similarly, the up-stream temperature of the collimator jaw increased smoothly from $24\,°C$ to $37\,°C$ and small temperature jumps appeared in coincidence with the beam impacts.

The downstream temperature sensor showed a high sensitivity to the beam hitting the collimator. Large spikes were observed. This is compatible with the fact that the peak temperature is expected to occur at the end of the collimator jaw. Simulations predicted an instantaneous peak temperature of about $350\,°C$ for hits with the maximum intensity ($2880\cdot10^{10}$ protons)[77]. The measured peak temperature of the downstream sensor is about $60\,°C$. This sensor was installed at the interface between the GLIDCOP plate and the CFC bar. An instantaneous peak temperature of about $100\,°C$ was calculated at this location[77] validating the hypothesis of a real heating of the overall jaw material.
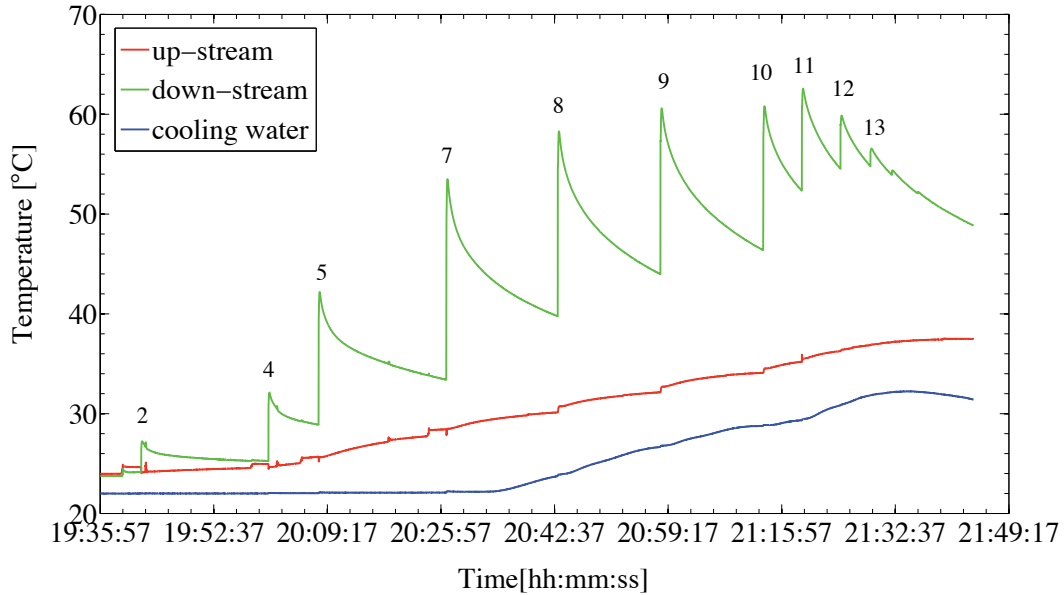
Figure 7.24: Measured temperature of collimator jaw (upstream red line, downstream green line) and cooling water (blue line) for beam hitting with different intensity and impact parameter. Numbers refer to extraction numbers as defined in Table 7.10.

The amplitude ΔT of the temperature spikes on downstream sensor varied as a function of the impact parameter and of the number of extracted batches. In Fig. 7.25 a quadratic increase of ΔT with the beam impact parameter is shown. A linear dependance between ΔT and the beam intensity (for a $5\,mm$ impact parameter) is shown in Fig. 7.26. Further analysis showed that the cooling time of the downstream sensor seems not to depend on the impact parameter: for extraction 7, 8 and 9 an half time (t_{half}) of $200\,s$ was calculated with good reproducibility.

It is noted that the downstream temperature sensors provide an excellent tool to detect beam shock impact. The signals can furthermore be used to estimate the amount of beam that hit the collimator jaw.
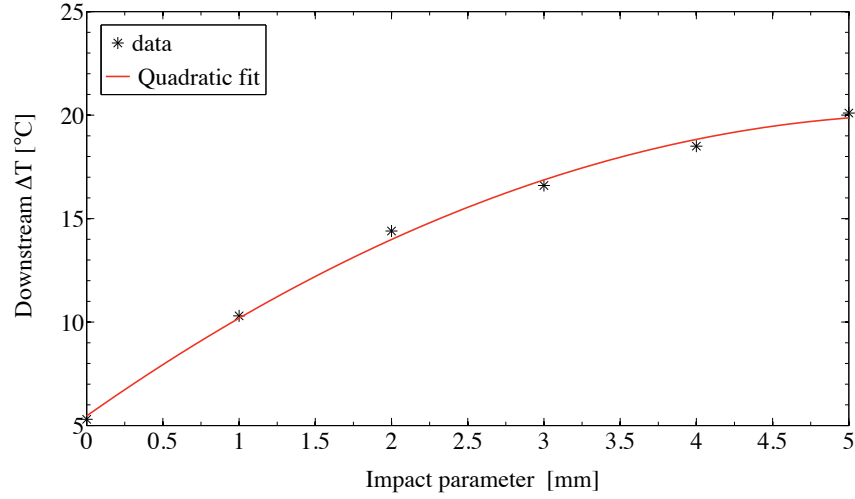
Figure 7.25: Temperature measured by the downstream temperature sensor as a function of the impact parameter. The data are fitted by a quadratic curve.
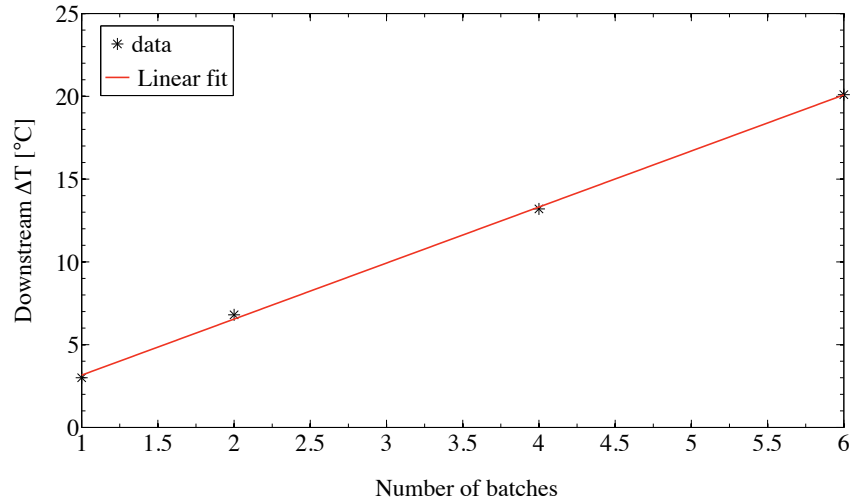
Figure 7.26: Temperature measured by the downstream temperature sensor as a function of the number of impacting batches (5 mm impact parameter). The data are linearly fitted.

Chapter 8

Optimized Strategy for LHC Collimation Commissioning

Intensity and luminosity reach of the LHC depend on the efficiency of the collimation system in providing beam cleaning and passive protection to the machine. This requires a specific setup of the full system for each operational scenario and the simultaneous control of more than 340 degrees of freedom with tight tolerances. In this chapter, expected intensity reach and collimator setting tolerances for different stages of the beam commissioning are derived, based on the studies presented in the pervious chapters. An optimized commissioning strategy for the LHC collimation system is described.

8.1   Goals of the commissioning strategy

The LHC collimation system is the most elaborate system of this kind built to date. The system has been described and analyzed in the previous chapters. Its many challenges have been presented:

- The high intensity LHC beams, circulating in sensitive superconducting magnets, require a highly efficient cleaning system. The needed collimation efficiency is orders of magnitudes beyond demands in previous accelerators.

- The required efficiency can only be reached by a four stage cleaning system (primary collimators → secondary collimators → active absorbers → tertiary collimators). A strict setting hierarchy must be respected (see section 4.3.2.1).

- The limited aperture and the small size of the LHC beams at $7\,\mathrm{TeV}$ ($\approx\!250\,\mu\mathrm{m}$ at collimators) implies collimation gaps as small as 2-3 mm. Consequently, setup and beam tolerances are more demanding than in previous colliders. Collimation tolerances in the LHC are around 20-100 μm [88].

143

- The full phase 1 collimation system includes 88 movable collimators (both beams). Every collimator jaw has 2 degrees of freedom. In total more than 340 stepping motors must be precisely calibrated and adjusted with respect to the beam around the 27 km long ring.

It would be unrealistic to assume that the LHC collimation system can provide its final performance from the first operation day. There will be an unavoidable learning period which will be used to optimize the system and its performance. This period should be as short as possible. It is therefore important to define an optimized commissioning strategy which is matched to the beam commissioning plan of the LHC and has the following overall goals:

- Maintain at all times the required passive machine protection.

- Minimize the number of collimators required for each step in beam commissioning, such reducing the work and beam time required for collimation.

- Maximize the performance for each commissioning step by defining the most efficient set of collimators to be used.

- Maximize the tolerance budget available for collimator setup errors or machine imperfections for each step of commissioning.

Such an optimized commissioning plan has been worked out based on the simulation and experimental results presented in the previous chapters. Various collimation scenarios have already been introduced for the simulation studies in chapter 6. The considered sets of collimators are partly related to using minimal systems of collimators and partly to the staged installation of collimators in the LHC. In the following the required sets of collimators and their settings are defined for various steps in beam commissioning. In addition, the tolerances for machine and collimator setup, which must be respected, are specified.

8.2   Performance assumptions

It has been shown in section 6.2 that the collimation cleaning efficiency and induced losses in superconducting magnets depend strongly on various imperfections. It was shown for selected simulation cases that local losses can be up to a factor of 11.3 higher when realistic imperfections are assumed. It has also been seen that FLUKA calculations predict energy deposition about a factor of 1.4 below the quench limit (see section 6.1.2) for the ideal machine and collimator setup. This amounts to a factor of 3.5 difference between performance estimates from proton tracking and full shower studies (more correct).

A commissioning plan should be conservative enough to ensure that it can be followed reasonably well with the real machine. The following assumptions are

therefore included in the described commissioning plan and the presented estimates of performance reach:

1. The performance reach with the realistic system is a factor of 11.3 lower than predicted by ideal simulations (as shown in section 6.2 for a few cases). Due to CPU time limitations only a restricted number of cases could be simulated with full imperfections. The other cases were scaled from the ideal performance predictions.

2. The factor of 3.5 lower predictions from FLUKA were not used to rescale the proton tracking results. Instead, this factor is kept for taking into account threshold effects. For example, the thresholds for beam-loss based aborts will be set nominally a factor of 3 below the quench threshold [89]. Collimation must then be even more efficient to avoid beam-loss triggered aborts. Other protection thresholds will further reduce the allowable beam loss. A factor of 3.5 for these effects might therefore not be too conservative.

3. Unavoidable uncertainties in the scattering cross-sections (proton tracking with collimators, FLUKA) and the accelerator models can be significant. Often at least a factor of 2 is quoted [67]. Here, no safety margin is included for this.

Beyond these assumptions, all performance estimates relate to the specified maximum beam loss rates and minimum intensity lifetimes of the LHC (see section 4.1.3.1). Also, the published quench limits are assumed for the superconducting magnets. Any surprise in beam stability or quench limits will change the performance reach of collimation.

8.3 One-stage collimation for pilot beam

A pilot beam will be used for initial commissioning of the LHC [64, 90]. This pilot beam consists of 1 bunch with 5×10^9 protons. Such a low intensity beam can be handled with a minimal set of collimators that implements a one-stage cleaning system and insures the required passive protection.

8.3.1 Required collimators

The following collimators and absorbers are used per beam:

- One primary collimator (TCP) in IR3, implementing a one-stage momentum cleaning.

- Three primary collimators (TCP) in IR7, implementing a one-stage betatron cleaning in horizontal, vertical and skew planes.

- Three collimators/absorbers (two TCDQs, one TCSG) in IR6 for beam dump protection.

- Two absorbers (one TCLI, one TDI) in IR2 or IR8 for injection protection.

- Six tertiary collimators (TCT) in IR1, IR2, IR5 and IR8 for triplet protection.

This setup consists of 15 collimators per beam. The required settings for the collimators, except the TCTs (see section 8.3.4), are summarized in Table 8.1 for three reference energies. The absorbers in IR2 and IR8 are set at $6.8\,\sigma$ during injection and are then retracted before starting the energy ramp.

   According to the estimates presented in section 7.2.3 the manual beam based setup of this system will take 5 hours ($\approx$20 min per collimator) per beam.

Table 8.1: Collimator settings for machine commissioning with pilot beam. Absorbers in IR2 and IR8 are set at $6.8\,\sigma$ during injection and are retracted before the energy ramp starts.

	Half-gaps[σ]		
	450 GeV	5 TeV	7 TeV
TCP-IR3	8.0	26.4	31.6
TCSG-IR6	7.0	23.0	27.6
TCDQ-IR6	8.0	26.4	31.6
TCP-IR7	5.7	18.8	22.5

8.3.2   Performance reach

The performance of this one-stage system is summarized in Fig. 8.1. The simulated performance is shown as a function of beam energy for three different ramp scenarios (see section 6.1.6), namely (1) constant gaps in mm, (2) gaps with constant tolerance budget "tolerance optimized setting" and (3) gaps scaled down with $\sqrt{\gamma}$ (constant gaps in terms of beam size). Lines referring to the beam intensities as foreseen for commissioning (pilot bunch, 43 bunches of 4×10^{10} protons and 156 bunches of 9×10^{10} protons [64]) and nominal operation are also shown.

   The one-stage system can support pilot beam up to 7 TeV beam energy with constant gaps (in mm). This facilitates the first energy ramps, as collimator settings do not need to be changed. The collimator settings listed in Table 8.1 refer to this case.

8.3.3   Tolerances

The resulting tolerances for the various energies are summarized in Fig. 8.2. The
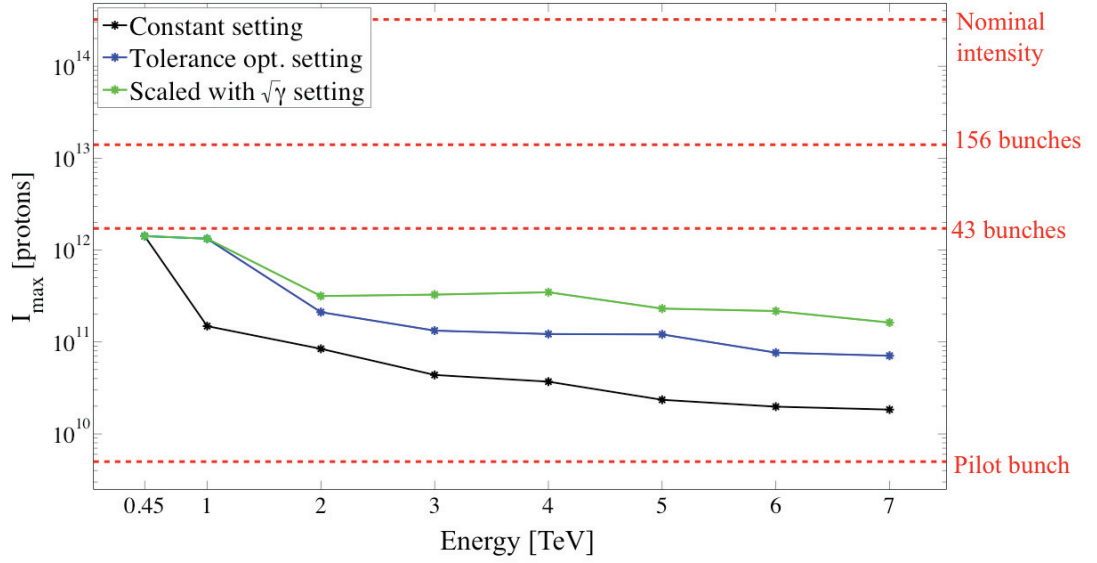
Figure 8.1: Maximum beam intensity reach for a minimal one-stage cleaning system.
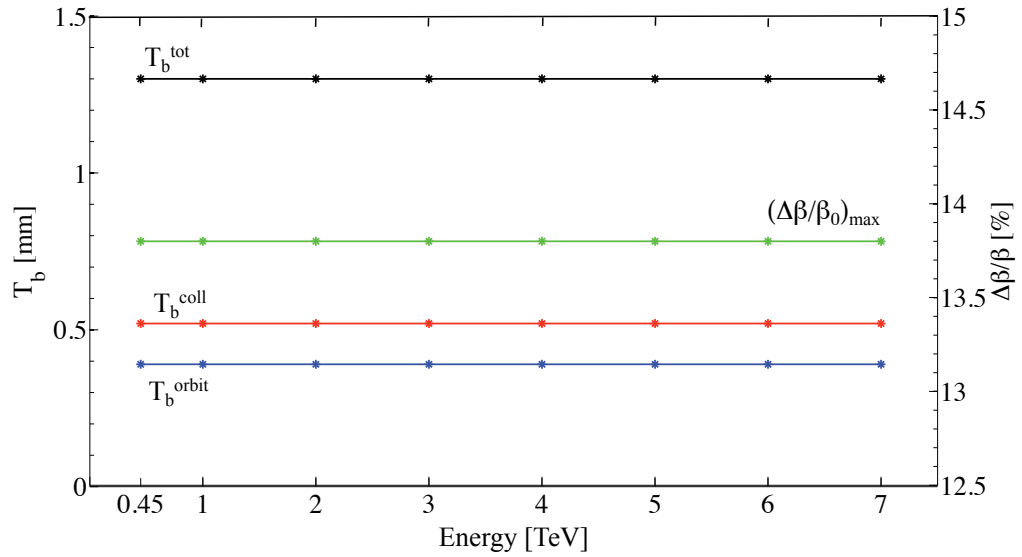
Figure 8.2: Tolerance budget T_b as a function of beam energy for a one-stage system in case of constant collimator setting (in mm) during the ramp. Allocation for transient orbit errors, transient beta-beat at the primary collimators and collimator-related errors are shown.

data assumes that collimators are not moved during the energy ramp. The total tolerance budget T_b^{tot} is defined as:

$$T_b^{tot} = n_2 - n_1; \tag{8.1}$$

where n_1 is the half-gap of the primary collimators and n_2 is the half-gap of the second closest element to the beam (for one-stage cleaning this is the TCSG in IR6). T_b^{tot} is attributed to these main contributions:

- Collimator setup and imperfections: $T_b^{coll} = 0.4 \times T_b^{tot}$.

- Transient orbit at collimator: $T_b^{orbit} = 0.3 \times T_b^{tot}$.

- Transient beta-beat at collimator: $T_b^{\beta} = 0.3 \times T_b^{tot}$.

The maximum allowed transient beta-beat at the primary collimators is given by:

$$\left(\frac{\Delta\beta}{\beta_0}\right)_{max} = 2\frac{\Delta A_{max}}{n_1} = \frac{2\,T_b^{\beta}}{n_1\,\sigma}. \tag{8.2}$$

Here, ΔA_{max} is the maximum allowed variation of normalized amplitude at the primary collimator due to transient beta-beat.

It is seen that tolerances are kept constant for the first energy ramps in the LHC.

8.3.4   Collimator settings in experimental insertions

This system is not compatible with a beta squeeze and a crossing angle in the experimental insertions. Tertiary collimators (TCT) will be set for protection of the triplet but should have no protection functionality: the triplet aperture should be in the shadow of the arc aperture (assuming nominal tolerances). The constant setting during the ramp is assumed and the half-gaps at the reference energies are listed in Table 8.2. It is noted that the required protection settings in the vertical and horizontal planes turn out to be identical.

Table 8.2: Tertiary collimator settings for operation with pilot beam. Crossing and separation schemes are set to zero (OFF see section 5.1).

	β_z^* [m]	TCTs half-gap[σ]		
		450 GeV	5 TeV	7 TeV
IR1	11	9.6	34.6	38.2
IR2	10	11.4	39.4	44.6
IR5	11	9.6	34.6	38.2
IR8	10	11.4	39.4	44.6

8.4   Minimal two-stage collimation for 43 bunches

The beam with 43 bunches of 4×10^{10} protons corresponds to about 0.5% of the nominal beam intensity but is already an unsafe beam. It can easily quench super-conducting magnets and can also induce damage on accelerator equipment. The stored energy of the beam at 7 TeV can reach the present state-of-the-art at the TEVATRON collider. In this case a two-stage collimation system is required.

8.4.1   Required collimators

The following collimators and absorbers are used per beam:

- One primary collimator (TCP) plus 4 absorbers (TCLA) in IR3, implementing a two-stage momentum cleaning.

- Three primary collimators (TCP) plus 5 absorbers (TCLA) in IR7, implementing a two-stage betatron cleaning.

- Three collimators/absorbers (two TCDQs, one TCSG) in IR6 for beam dump protection.

- Two absorbers (one TCLI, one TDI) in IR2 or IR8 for injection protection.

- Six tertiary collimators (TCT) in IR1, IR2, IR5 and IR8 for triplet protection.

This system consists of 24 collimators and absorbers per beam, corresponding to about 8 hours required for beam based alignment.

The collimator settings, except the TCTs (see section 8.4.4), are listed in Table 8.3. For the injection protection the same numbers as in section 8.3.1 are valid.

Table 8.3: Collimator settings for machine commissioning with a beam of 43 bunches. Absorbers in IR2 and IR8 are set at $6.8\,\sigma$ during injection and are retracted before the energy ramp starts.

	Half-gaps[σ]		
	450 GeV	5 TeV	7 TeV
TCP-IR3	8.3	13.6	15.2
TCLA-IR3	10.3	20.2	23.2
TCSG-IR6	7.5	7.5	7.5
TCDQ-IR6	8.0	8.0	8.0
TCP-IR7	6.0	6.0	6.0
TCLA-IR7	10.0	10.0	10.0

8.4.2   Performance Reach

The maximum intensity reach of this minimal two-stage system, for the different ramp settings defined above, is presented in Fig. 8.3. The system has its best performance if collimator gaps are reduced with $\sqrt{\gamma}$. Values in Table 8.3 refer to this case. Even then, the estimated performance reach is just below 7 TeV. In case that 7 TeV cannot be reached with this configuration, either intensity must be reduced or a third collimation family (e.g. secondary collimators) must be set up. In practice it would then be better to move to the next stage of settings described in section 8.5.
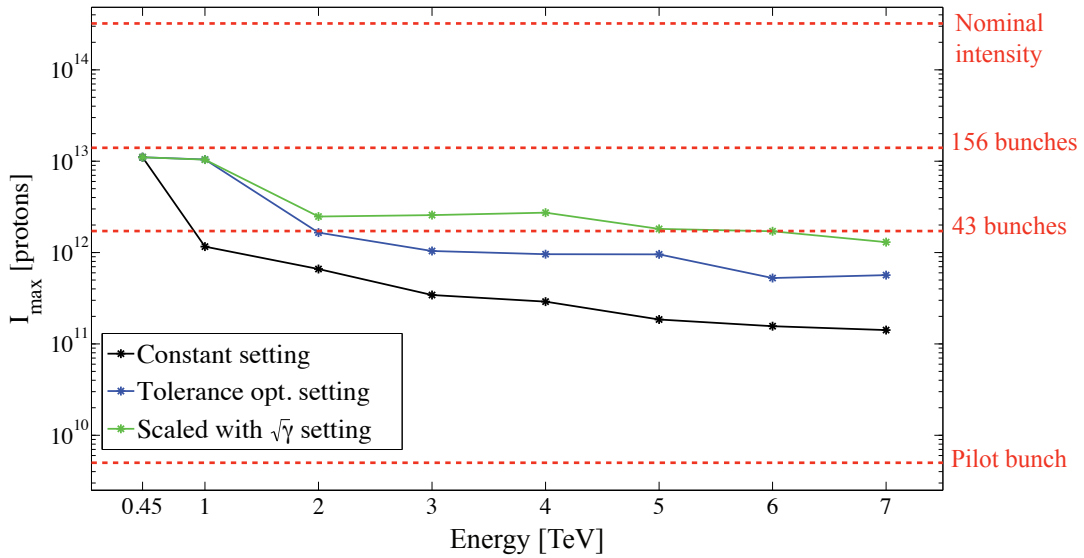
Figure 8.3: Maximum beam intensity reach for a minimal two-stage cleaning system.

8.4.3   Tolerances

From the performance estimates it is seen that collimation gaps should be decreased with $\sqrt{\gamma}$ during the energy ramp. Only then it can be imagined that 7 TeV could be reached with 43 bunches and the described collimator complement. In this case the gaps stay constant in terms of beam size (σ) during the ramp and the tolerance budget is reduced while increasing beam energy. The tolerances are shown in Figure 8.4. At 7 TeV we obtain a budget of 113 μm for transient orbit change and 15% transient beta-beat at the primary collimators. This assumption leaves 150 μm budget for collimator set up errors.
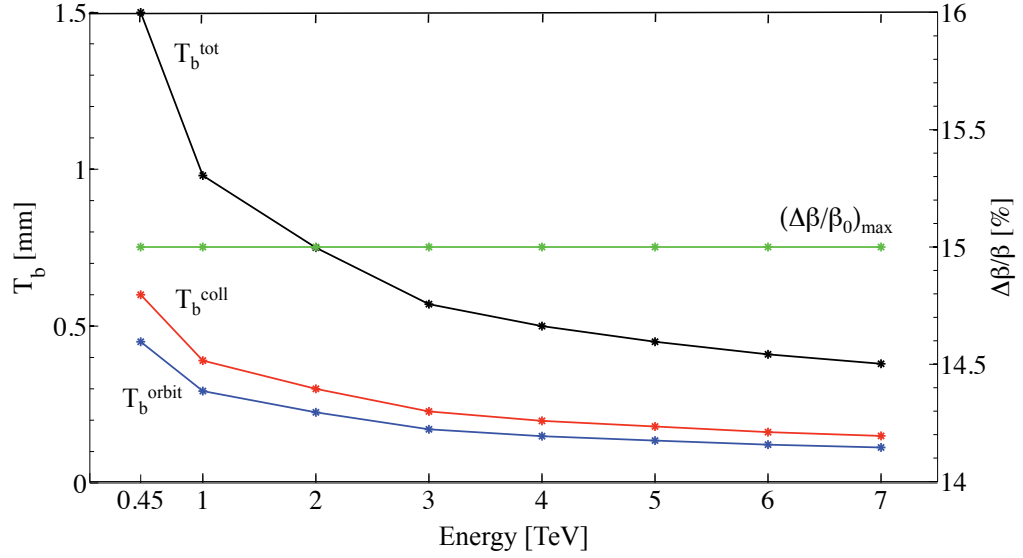
Figure 8.4: Tolerance budget T_b as a function of beam energy for a two-stage cleaning system when scaling the collimator settings with $\sqrt{\gamma}$ during the ramp.

8.4.4 Collimation Settings in Experimental Insertions

The basic two-stage cleaning system is compatible with a first squeeze of $\beta_z{}^*$ in the experimental insertions of IR1 and IR5 ($\beta_z{}^* = 2\,\mathrm{m}$). A run with collision at 5 TeV is planned at this intensity for the early stages of the beam commissioning as intermediate step before reaching the ultimate energy. For 43 bunches no crossing angle is required and foreseen. The correct setting of the tertiary collimators is important for reduced $\beta_z{}^*$ and has been studied in detail. The condition is that the triplet collimators must be shadowed by the tertiary collimators in order to avoid quenches and/or damage for the triplet quadrupoles.

Table 8.4: Tertiary collimator settings for collisions at 5 TeV. The crossing and separation schemes are OFF (see section 5.1).

	$\beta_z{}^*$ [m]	TCTs half-gap $[\sigma]$
IR1	2	17.4
IR2	10	38.4
IR5	2	17.4
IR8	10	38.4

8.5 Four-stage collimation with initial system for higher intensities

This collimator system uses all collimators that have been installed for the 2008 run of the LHC. All the most important collimators were included into the 2008 installation. It is therefore possible to set up a four stage cleaning and protection system, as it is required for intensities above 43 bunches.

8.5.1 Required collimators

The following collimators and absorbers were installed for the 2008 run:

- One primary (TCP) and four secondary (TCSG) collimators plus four absorbers (TCLA) in IR3, implementing a three-stage momentum cleaning.

- Three primary (TCP) and six secondary (TCSG) collimators plus five absorbers (TCLA) in IR7, implementing a three-stage betatron cleaning.

- Three collimators/absorbers (two TCDQs, one TCSG) in IR6 for beam dump protection.

- Two absorbers (one TCLI, one TDI) in IR2 or IR8 for injection protection.

- Six tertiary collimators (TCT) in IR1, IR2, IR5 and IR8 for triplet protection and a forth stage of cleaning.

In total, 34 collimators are considered and 11:20 hours are estimated for manual alignment of the system per beam.

Initially it is foreseen to operate the machine at a maximum energy of 5 TeV. Collimator settings, except the TCTs (see section 8.5.4), for this case and for injection energy are listed in Table 8.5.

8.5.2 Performance Reach

The performance reach improves with a four stage cleaning (see Fig. 8.5). In this case, the tolerance optimized setting allows machine operation with more than 43 bunches up to 5 TeV. Moreover, by scaling the collimator half-gaps with $\sqrt{\gamma}$, 156 bunches can be handled.

This system was optimized to guarantee the required machine protection during all the phases planned for the commissioning run.

Table 8.5: Collimator settings for the initial machine commissioning run with the 2008 system of collimators. Absorbers in IR2 and IR8 are set at $6.8\,\sigma$ during injection and are retracted before the energy ramp starts. Two different scenarios for collimator settings during the energy ramp are specified.

| | Half-gaps[σ] | | | |
| | 450 GeV | | 5 TeV | |
	Tolerance optimized	Scaled with$\sqrt{\gamma}$	Tolerance optimized	Scaled with$\sqrt{\gamma}$
TCP-IR3	8.3	8.3	13.6	13.6
TCSG-IR3	9.6	9.6	18.0	18.0
TCLA-IR3	10.3	10.3	20.2	20.2
TCSG-IR6	7.3	7.5	10.3	7.5
TCDQ-IR6	8.3	8.0	13.6	8.0
TCP-IR7	6.0	6.0	6.0	6.0
TCSG-IR7	7.0	7.0	9.3	7.0
TCLA-IR7	10.3	10.0	20.2	10.0
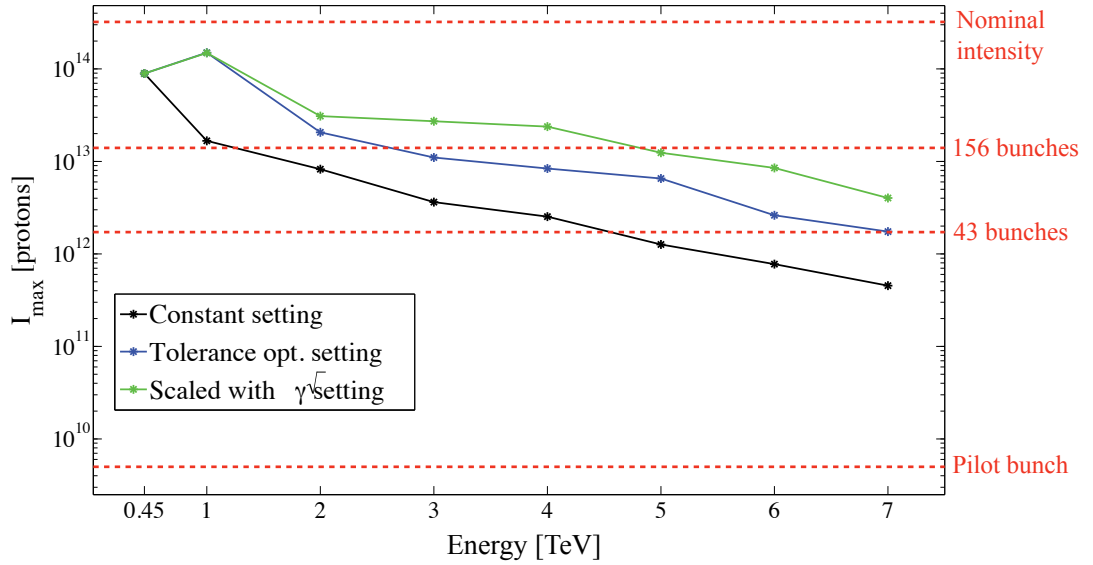
Figure 8.5: Maximum beam intensity reach for the collimation system as installed for the 2008 run. The initial maximum beam energy is 5 TeV.

8.5.3 Tolerances

Tolerances stay maximal during the full ramp if the tolerance optimized setting is applied to the considered system (see Fig. 8.6). The allowance for transient beta-beat
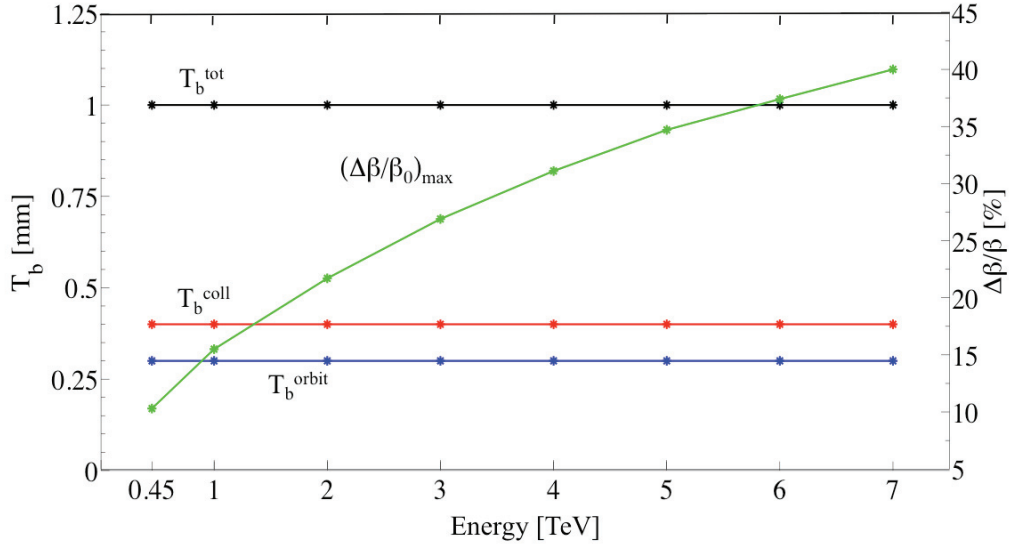
Figure 8.6: Tolerance budget T_b as a function of beam energy for the full phase 1 system and the 2008 collimation complement. Tolerance optimized setting is considered.
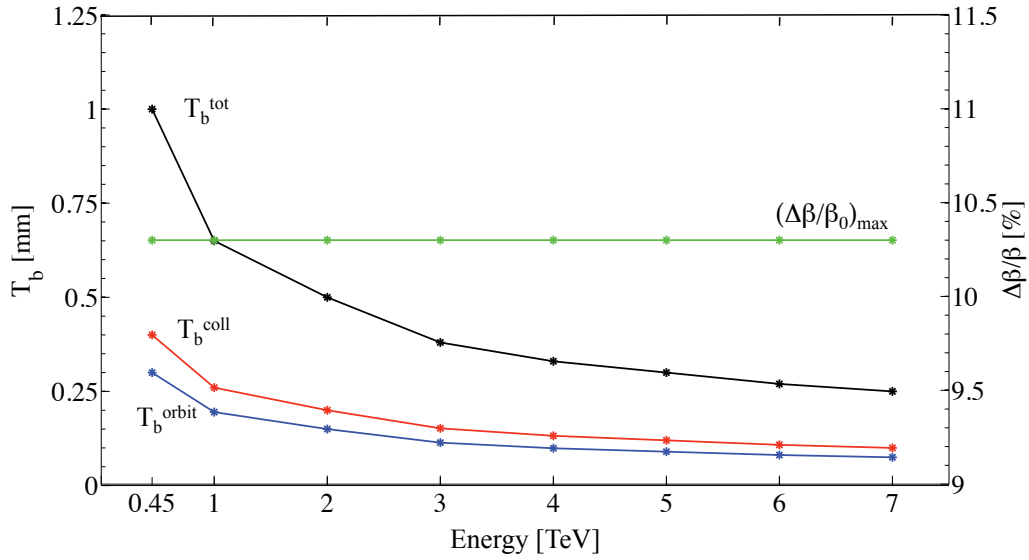
Figure 8.7: Tolerance budget T_b as a function of the energy for the full phase 1 system and the 2008 collimation complement. The collimator settings are scaled with $\sqrt{\gamma}$ during the energy ramp.

at the primary collimators increases to 40%.

The setting scaled with $\sqrt{\gamma}$ anyway has the best performance and must be adopted if the beam intensity is increased to 156 bunches. In this case, tolerances are significantly reduced with the energy. For example, at 5 TeV the tolerance budget is 120μm for collimator setup and 90μm for transient orbit with 10.3% transient beta-beat at the primary collimators. In case that these tight tolerances cannot be achieved, collimator gaps must be increase and the intensity should be reduced.

8.5.4 Collimation Settings in Experimental Insertions

This system is compatible with a $\beta_z{}^*$ of 2 m in IR1 and IR5 and a $\beta_z{}^*$ of 10 m in IR2 and IR8. A crossing angle is necessary for a beam with more than 43 bunches. The settings of tertiary collimators and the crossing angles are listed in Table 8.6.

Table 8.6: Tertiary collimator settings and crossing angles, for collisions at 5 TeV with more than 43 bunches and a four stage cleaning system as installed in 2008.

	Crossing angle [μm]	$\beta_z{}^*$ [m]	TCTs half-gap [σ]
IR1	± 92	2	17.3
IR2	± 170	10	37.3
IR5	± 92	2	14.8
IR8	± 170	10	33.8

The described collimator system refers to the 2008 installation and the vertical tertiary collimators in IR2 and IR8 are not yet installed. For maximum safety of the accelerator, this excludes the possibility of a $\beta_z{}^*$ squeeze to values smaller than 5 m in Alice and LHCb.

8.6 Four-stage collimation with the full phase 1 system for higher intensities

The full phase 1 collimation system will be installed for the 2009 run of the LHC. The full performance reach of the phase 1 system can be achieved in terms of cleaning efficiency, crossing angle and $\beta_z{}^*$.

8.6.1 Required collimators

The full phase 1 system consists of:

- One primary (TCP) and four secondary (TCSG) collimators plus four absorbers (TCLA) in IR3, implementing a three-stage momentum cleaning.

- Three primary (TCP) and eleven secondary (TCSG) collimators plus five absorbers (TCLA) in IR7, implementing a three-stage betatron cleaning.

- Three collimators/absorbers (two TCDQs, one TCSG) in IR6 for beam dump protection.

- Three absorbers (two TCLI, one TDI) in IR2 or IR8 for injection protection.

- Eight tertiary collimators (TCT) in IR1, IR2, IR5 and IR8 for triplet protection and a forth stage of cleaning.

- Two physics debris absorbers (TCLP) in IR1 and IR5.

An estimated time of 14:40 hours is needed for setting up the 44 collimators per beam installed along the ring.

Table 8.7: Collimator settings for machine operation with the full phase 1 system at higher intensities. Absorbers in IR2 and IR8 are set at $6.8\,\sigma$ during injection and are retracted before the energy ramp starts.

	Half-gaps[σ]		
	450 GeV	**5 TeV**	**7 TeV**
TCP-IR3	8.3	13.6	15.2
TCSG-IR3	9.6	18.0	20.2
TCLA-IR3	10.3	20.2	23.2
TCSG-IR6	7.5	7.5	7.5
TCDQ-IR6	8.0	8.0	8.0
TCP-IR7	6.0	6.0	6.0
TCSG-IR7	7.0	7.0	7.0
TCLA-IR7	10.0	10.0	10.0

At this stage the collimator openings must follow the adiabatic damping of beam size during the acceleration. Collimator settings are scaled with $\sqrt{\gamma}$ (see Table 8.7).

8.6.2   Performance Reach

The full phase 1 collimation system provides optimal performance which, however, is expected to be limited to below nominal intensity, as shown in Fig. 8.8. A factor of three improvement in cleaning efficiency would be required to arrive to 7 TeV top energy with 156 bunches. This relies on many assumptions, as outlined before. As experience is gained with the LHC it is expected that a better beam stability (longer lifetime τ) and reduced machine imperfections can be achieved. In this case the 7 TeV energy can be reached with a higher intensity. Finally, additional
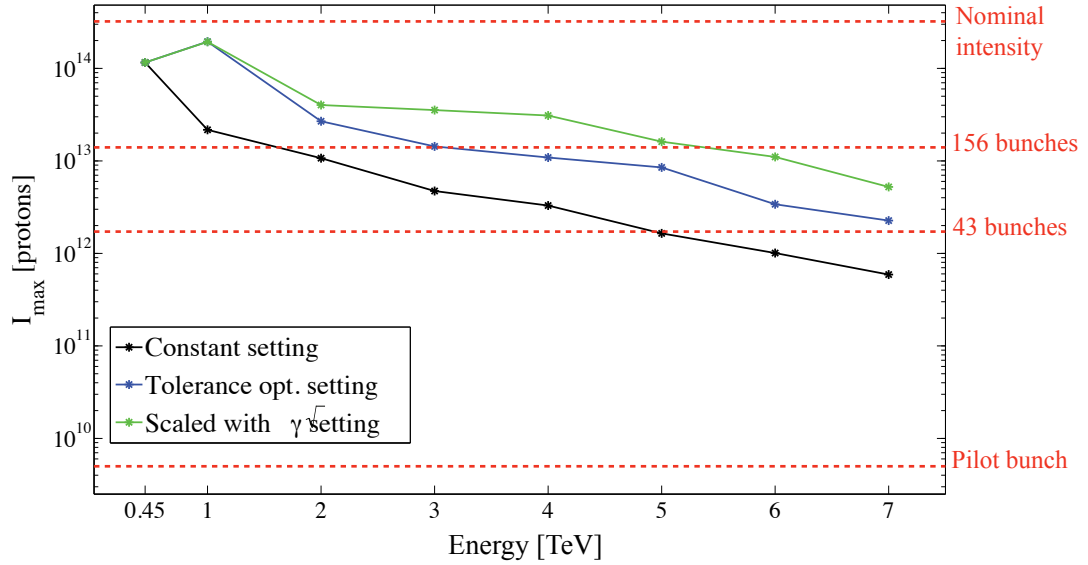
Figure 8.8: Maximum beam intensity reach for the full phase 1 system.

collimators from the phase 2 collimation project will further increase the intensity reach.

8.6.3   Tolerances

The best performance implies a strong reduction of the tolerances as a function of the energy. Tolerances vary with the beam energy as in the previous case (see Fig. 8.7). Optimal collimator operation becomes therefore more demanding when increasing the beam energy. The tolerance budget for collimator setup T_b^{coll} is reduced to around $100\,\mu$m at $7\,$TeV. Typically only $75\,\mu$m are left for transient orbit change and 10.3% transient beta-beat at the primary collimators.

8.6.4   Collimation Settings in Experimental Insertions

Half-gaps of the tertiary collimators at the four experimental insertions are given in Table 8.8. These settings refer to early ($\beta_z^* = 2$ m in IP1, IP5 and IP8) and nominal collision ($\beta_z^* = 0.55$ m in IP1 and IP5) optics. Any further squeeze of β_z^* in IP2 and/or IP8 requires to close the TCTs accordingly, in order to insure protection of the triplet magnets.

In all these cases, a crossing angle is needed and in Table 8.8 nominal values for optics version V6.503 are shown.

Table 8.8: Tertiary collimator settings for the optics foreseen for collisions at 7 TeV.

	Crossing angle [μm]	β_z* [m]	TCTs half-gap [σ]
IR1	± 92	2	20.3
IR2	± 240	10	36.5
IR5	± 92	2	17.4
IR8	± 140	2	18.6
IR1	± 143	0.55	8.3
IR2	± 124	10	45
IR5	± 143	0.55	8.3
IR8	± 170	10	30

8.7   Synthesis of Beam Commissioning Plan

This section summarizes the main features of the collimation commissioning plan presented before. In Fig. 8.9 the number of collimators per beam necessary for insuring adequate cleaning and passive machine protection is shown for the analyzed stages of beam commissioning. The corresponding cleaning inefficiency is shown in Fig. 8.10 for:
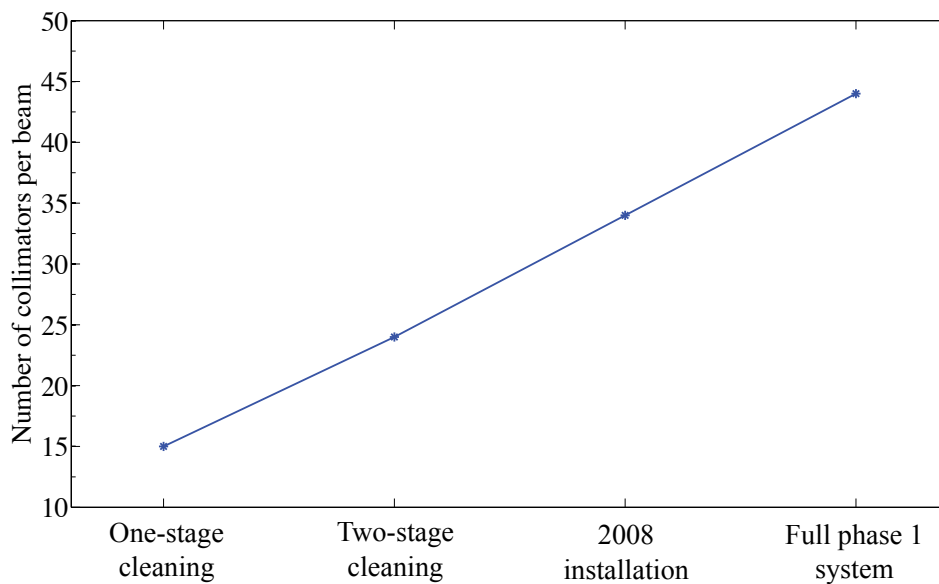
Figure 8.9: Number of needed collimators per beam as a function of the performance reaches foreseen by the machine commissioning plan.

- Constant settings for the one-stage cleaning system and collimator gaps scaled with $\sqrt{\gamma}$ (optimal performance) for the remaining scenarios (solid line).

- Tolerance optimized setting for multi-stage collimator complements (dashed line).

The efficiency gain factor with respect to the one-stage cleaning system is shown for the case of best performance.
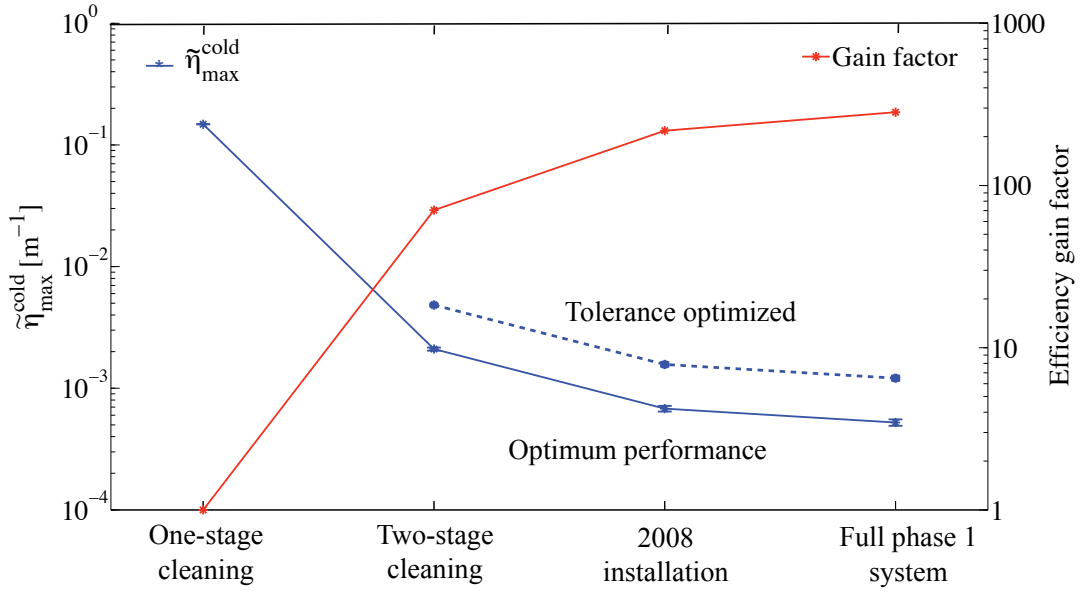
Figure 8.10: Maximum local cleaning inefficiency $\tilde{\eta}_{max}^{cold}$ at 7 TeV (blue lines) for the analyzed collimator complements. The solid blue line refers to a constant setting for the one-stage system and performance optimized collimator gaps for the remaining scenarios. The dashed blue line refers to tolerance optimized settings for multi-stage complements. The efficiency gain factor (red line) is shown for performance optimized collimator settings with respect to one-stage cleaning system.

Operation with the pilot beam is incompatible with any squeezed optics and crossing angle. Tertiary collimators are then in principle not needed because the triplet quadrupoles are shielded by the arc cold aperture. On the other hand, TCTs become essential when the beam intensity is increased and/or the triplet aperture becomes a machine bottleneck due to β_z^* squeeze.

The estimated time for the manual beam based setup of each complement depends on the number of collimators to be used and is shown in Fig. 8.11. Experimental tests showed that, on average, 20 minutes have to be taken into account for the alignment of each collimator (see section 7.2.3). A minimum time of 5 hours is then estimated for aligning the minimum one-stage system (pilot beam). A minimum of

about 15 hours is necessary per beam for setting up the full phase 1 system. An automized calibration procedure will be implemented to reduce setup time.

In the LHC, a new beam based alignment of the full system will have to be performed after any substantial change in the beam parameters. If the machine is stable, collimators will be put to reference positions from the last beam based alignment. High reproducibility of the accelerator and beam parameters are fundamental for avoiding frequent collimator setup and for obtaining high efficiency of the accelerator for physics.
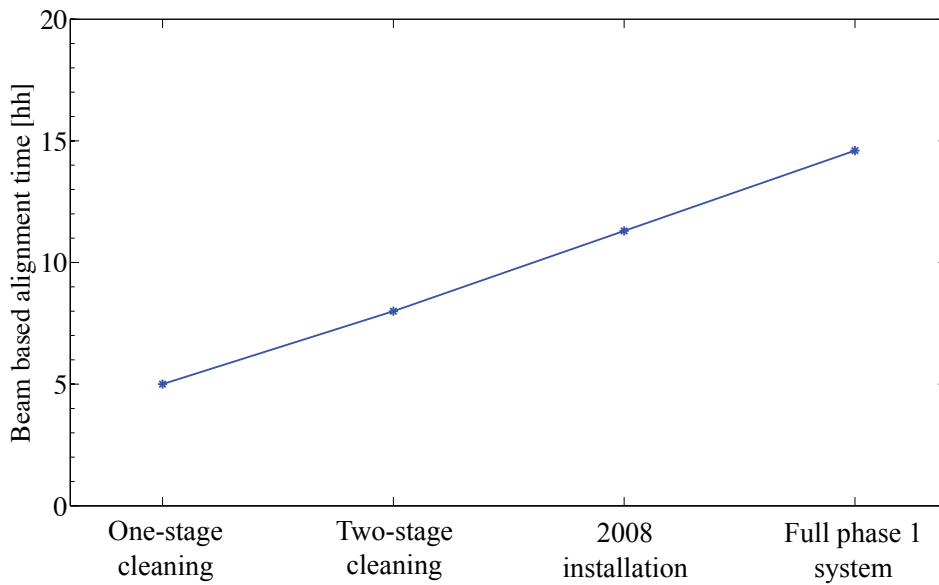
Figure 8.11: Estimate of beam time required for manual beam based alignment of the analyzed collimator complements per beam.

Tolerance budget requirements for optimized performance reach become more demanding when increasing the intensity and the number of collimators (see Fig. 8.12, 8.13 and 8.14). The minimum tolerance budget T_b^{coll} for collimator-related imperfections is $100\,\mu$m. The corresponding allowance for the machine are 10.3% transient beta-beat and $75\,\mu$m transient orbit change at the primary collimators.

Initially less stringent tolerances might be preferred. The tolerance optimized setting allows operation of the full phase 1 system with maximal tolerances. T_b^{coll} of $390\,\mu$m, transient orbit change of $300\,\mu$m and 40% transient beta-beat at the primary collimators are then allowed at top energy (see Fig. 8.14). In this case the performance reach is reduced by about a factor of 2 (see Fig. 8.10).

If difficulties are encountered in achieving the required tolerances for optimized performance, the collimators can be set to larger openings. This could imply a reduction in the maximum allowed beam intensity.
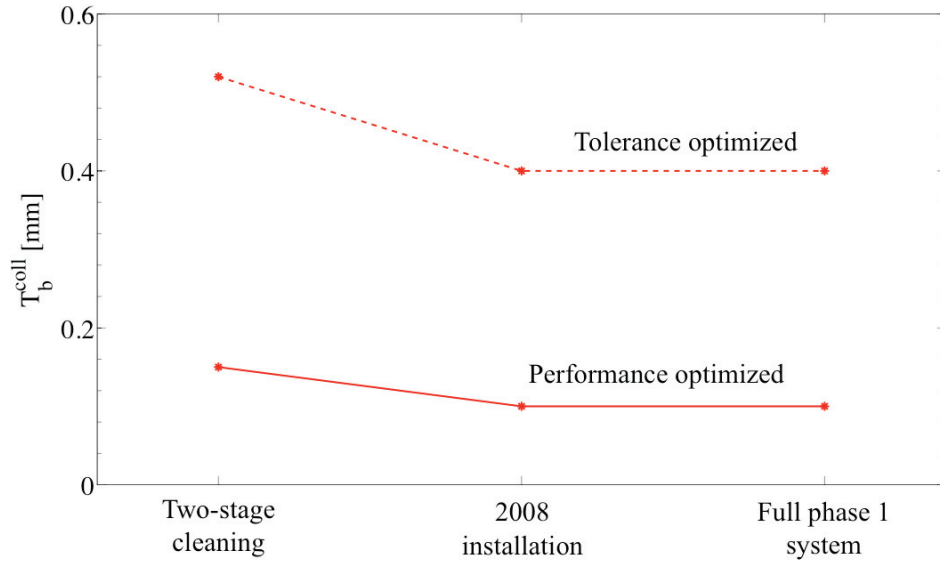
Figure 8.12: The available tolerance budget for collimator setup at top energy is shown for performance and tolerance optimized settings of multi-stage cleaning.
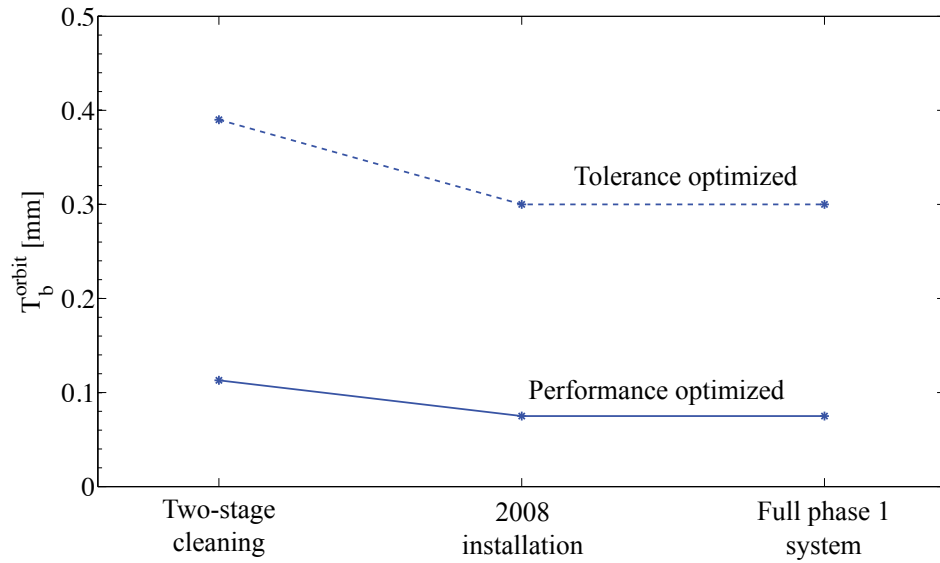
Figure 8.13: The available tolerance budget for transient orbit change at top energy is shown for performance and tolerance optimized settings of multi-stage cleaning.

8.8   Collimation master table

The expected steps in beam commissioning of the LHC and the collimation system were described above. However, it can be envisaged that the beam commissioning
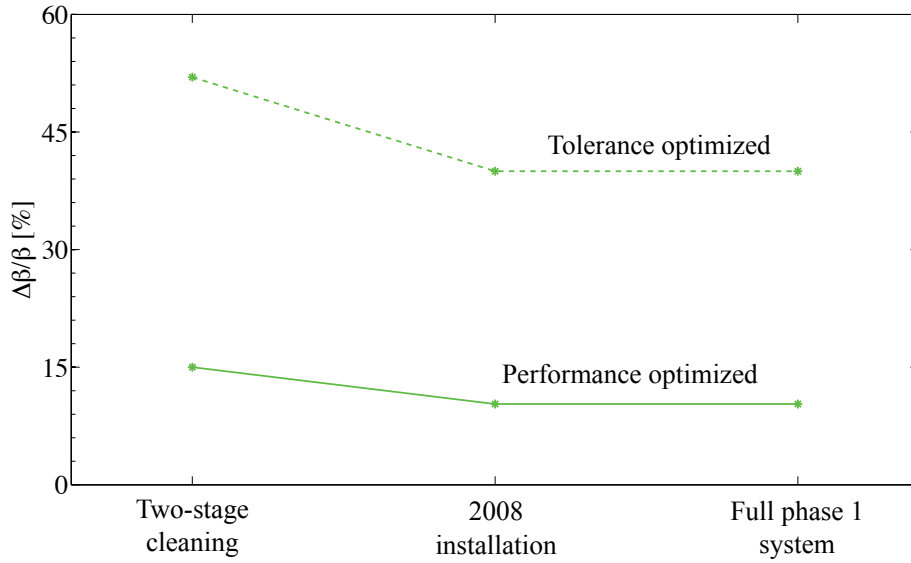
Figure 8.14: The available tolerance budget for transient beta-beat at the primary collimators at top energy is shown for performance and tolerance optimized settings of multi-stage cleaning.

might deviate from the foreseen procedure for various possible reasons. In this case, the appropriate collimator settings must be redefined in a short time.

The collimation system is an elaborate scheme with various families and strict hierarchical settings for adequate cleaning and passive machine protection. Any proposed setup must be carefully checked for full consistency with the setting rules.

In order to allow for fast reaction time without compromising safety aspects, a master table for collimation has been defined as a part of this PhD work. It contains a large variety of collimator settings, according to the results of all the collimation studies performed for the LHC. The consistency and safety of the proposed settings are carefully checked for this table.

The collimation master table is too complicated and too involved to be placed into this report. The cases described above were estimated from this table. The master table will be used as the reference for collimation setup and will be updated from the accelerator physics side as the knowledge and experience of LHC collimation will expand. A released version will be made available for accelerator operation after initial beam commissioning.

Chapter 9

Conclusions

The high intensity beams of the Large Hadron Collider advance the state-of-the-art in stored beam energy by two-three orders of magnitude. For nominal parameters up to $360\,\mathrm{MJ}$ of stored energy will circulate at $11\,\mathrm{kHz}$ through the LHC super-conducting magnets with quench limits of around $5\,\mathrm{mJ\,s^{-1}\,cm^{-3}}$. A sophisticated four-stage collimation system in the LHC will intercept and absorb unavoidable fractional beam losses of up to 0.1% of stored energy per second (corresponding to $500\,\mathrm{kW}$). For this purpose 88 collimators are installed in a first phase around the $27\,\mathrm{km}$ long ring, mainly concentrated in the two cleaning insertions. LHC collimators have excellent robustness and survive beam shock impact of up to 2 MJ, as shown in this thesis. It is described how temperature sensors can be used for detection of beam impact, providing a measure of the intensity that hit the collimator.

The LHC collimation system shall provide a cleaning efficiency (absorption of losses) of better than 99.99% for the $7\,\mathrm{TeV}$ LHC beams. This PhD thesis has extended earlier studies on the achievable cleaning efficiency, taking into account for the first time realistic static imperfections. The extended simulations include, in particular, manufacturing errors on flatness of collimators, collimator setup errors, design orbit errors and magnet alignment and manufacturing errors. The imperfections for magnet manufacturing and alignment were studied both for design limits and measured values. A model of collimator jaw flatness was based on measurements during the production and assembly of collimators.

The achievable collimator setup accuracy was assessed with beam for an LHC prototype collimator installed in the SPS accelerator. In the collimation gap an accuracy of $50\,\mu\mathrm{m}$ for its centering on the beam and 0.1σ for its width was achieved. Tests with SPS beam on angular alignment of the jaws with respect to the beam envelope were not successful. Therefore the angular setup error is given by the $200\,\mu\mathrm{rad}$ alignment accuracy of the collimator. Various interesting observations in beam loss signals (beam loss tails and echoes) were found during the setup tests of the LHC collimator when it touched particles in the SPS beam halo. They can have an impact on collimator setup, if similar features appear in the LHC.

The simulations show that the combined static imperfections, described above, have a strong effect on the achievable cleaning efficiency, reducing it by a factor of 11

if compared to the ideal performance. The intensity reach of the phase 1 collimation system is then predicted to be below 5% of nominal intensity. Higher beam intensities would require lower than specified peak losses (better beam stability), better collimator setup, reduced machine imperfections or a collimation upgrade (phase 2). Collimator-induced impedance can introduce another independent intensity limit from collimation. It is shown that an important trade-off between impedance and cleaning efficiency exists. The LHC impedance is reduced when opening collimator gaps, while the predicted efficiency is degraded significantly.

The foreseen steps in beam commissioning of the LHC are analyzed, taking into account the achievable collimation efficiency. A large variety of cases is considered, covering the expected evolution in beam intensity (from pilot to nominal beam), in β_z^*, in maximum beam energy (from $450\,\mathrm{GeV}$ over $5\,\mathrm{TeV}$ to $7\,\mathrm{TeV}$) and in bunch pattern. Appropriate collimator complements and the required collimation gaps are defined for each step. The defined collimation gaps cover the full energy range from injection through the energy ramp to top energy. Various possibilities for collimator settings during the energy ramp are analyzed.

An optimized strategy for the commissioning of the collimation system is defined on the basis of the simulations. The proposed scenario guarantees the required beam cleaning and machine protection. At the same time the number of required collimators is minimized and the available tolerances for collimator setup, transient beta-beat and transient orbit changes are maximized ("tolerance budget"). An analysis of consequences from off-momentum beta-beat for LHC collimation was performed in this PhD and guided the choice for the standard LHC optics. Still, the collimation-related tolerance budget can be decreased by 30% due to off-momentum beta-beat.

The proposed collimation commissioning starts with 30 collimators and a tolerance budget that is relaxed by a factor of 4 for a given beam energy. The cleaning efficiency is then improved in steps until a factor of 300 is gained with 88 collimators and achievement of tightest tolerances. The plan is summarized in a collimation master table which summarizes a large number of consistent collimator settings. It will be updated and completed during collimator commissioning and will then be made available for machine operation.

Based on the experience from LHC collimator tests in the SPS it is predicted that the collimation setup time varies from initially 5 hours to finally about 15 hours for each calibration and each beam. It is shown that less than 0.1% of nominal intensity (1-5 nominal bunches) can be used at maximum for collimator beam based alignment in the LHC. It is therefore excluded to calibrate collimator positions for each fill, as it is done in the Tevatron. Reproducibility of the LHC accelerator is therefore crucial in order to maximize the validity of a given collimator setup.

A firm foundation for the setup of the LHC collimation system has been established and will support the endeavor to bring the biggest machine that mankind built into operation.

Appendix A

Phase 1 collimator database

A.1 Beam 1

Table A.1: List of phase 1 collimators. Name, length, azimuthal angle, material and nominal simulated settings at injection and collision energy are indicated.

Name	Length [m]	Angle [deg]	Material	Half-gap[σ_z]	
				injection	collision
TCL.5R1.B1	1.0	0.0	Cu	out	10.0
TCTH.4L2.B1	1.0	0.0	Cu-W	out	8.3
TDI.4L2	4.0	90.0	C-C	6.8	out
TCTVB.4L2	1.0	90.0	Cu-W	out	8.3
TCLIA.4R2	1.0	90.0	CFC	6.8	out
TCLIB.6R2.B1	1.0	90.0	CFC	6.8	out
TCP.6L3.B1	0.6	0.0	CFC	8.0	15.0
TCSG.5L3.B1	1.0	0.0	CFC	9.3	18.0
TCSG.4R3.B1	1.0	0.0	CFC	9.3	18.0
TCSG.A5R3.B1	1.0	170.7	CFC	9.3	18.0
TCSG.B5R3.B1	1.0	10.8	CFC	9.3	18.0
TCLA.A5R3.B1	1.0	90.0	Cu-W	10.0	20.0
TCLA.B5R3.B1	1.0	0.0	Cu-W	10.0	20.0
TCLA.6R3.B1	1.0	0.0	Cu-W	10.0	20.0
TCLA.7R3.B1	1.0	0.0	Cu-W	10.0	20.0
TCTH.4L5.B1	1.0	0.0	Cu-W	out	8.3
TCTVA.4L5.B1	1.0	90.0	Cu-W	out	8.3
TCL.5R5.B1	1.0	0.0	Cu	out	10.0

Name	Length [m]	Angle [deg]	Material	Half-gap[σ_z]	
				injection	collision
TCDQA.A4R6.B1	3.0	0.0	CFC	8.0	8.0
TCDQA.B4R6.B1	3.0	0.0	CFC	8.0	8.0
TCSG.4R6.B1	1.0	0.0	CFC	7	7.5
TCP.D6L7.B1	0.6	90.0	CFC	5.7	6
TCP.C6L7.B1	0.6	0.0	CFC	5.7	6
TCP.B6L7.B1	0.6	127.5	CFC	5.7	6
TCSG.A6L7.B1	1.0	141.1	CFC	6.7	7
TCSG.B5L7.B1	1.0	143.5	CFC	6.7	7
TCSG.A5L7.B1	1.0	40.7	CFC	6.7	7
TCSG.D4L7.B1	1.0	90.0	CFC	6.7	7
TCSG.B4L7.B1	1.0	0.0	CFC	6.7	7
TCSG.A4L7.B1	1.0	134.6	CFC	6.7	7
TCSG.A4R7.B1	1.0	46.3	CFC	6.7	7
TCSG.B5R7.B1	1.0	141.5	CFC	6.7	7
TCSG.D5R7.B1	1.0	51.4	CFC	6.7	7
TCSG.E5R7.B1	1.0	130.5	CFC	6.7	7
TCSG.6R7.B1	1.0	0.5	CFC	6.7	7
TCLA.A6R7.B1	1.0	90.0	Cu-W	10	10
TCLA.B6R7.B1	1.0	0.0	Cu-W	10	10
TCLA.C6R7.B1	1.0	90.0	Cu-W	10	10
TCLA.D6R7.B1	1.0	0.0	Cu-W	10	10
TCLA.A7R7.B1	1.0	0.0	Cu-W	10	10
TCTH.4L8.B1	1.0	0.0	Cu-W	out	8.3
TCTVB.4L8	1.0	90.0	Cu-W	out	8.3
TCTH.4L1.B1	1.0	0.0	Cu-W	out	8.3
TCTVA.4L1.B1	1.0	90.0	Cu-W	out	8.3

A.2   Beam 2

Table A.2: List of phase 1 collimators. Name, length, azimuthal angle, material and nominal simulated settings at injection and collision energy are indicated.

Name	Length [m]	Angle [deg]	Material	Half-gap[σ_z]	
				injection	collision
TCTH.4R8.B2	1.0	0.0	Cu-W	out	8.3
TDI.4R8	4.0	90.0	C-C	6.8	out
TCTVB.4R8	1.0	90.0	Cu-W	out	8.3
TCLIA.4L8	1.0	90.0	CFC	6.8	out
TCLIB.6L8.B2	1.0	90.0	CFC	6.8	out
TCP.D6R7.B2	0.6	90.0	CFC	5.7	6
TCP.C6R7.B2	0.6	0.0	CFC	5.7	6
TCP.B6R7.B2	0.6	127.5	CFC	5.7	6
TCSG.A6R7.B2	1.0	141.1	CFC	6.7	7
TCSG.B5R7.B2	1.0	143.5	CFC	6.7	7
TCSG.A5R7.B2	1.0	40.7	CFC	6.7	7
TCSG.D4R7.B2	1.0	90.0	CFC	6.7	7
TCSG.B4R7.B2	1.0	0.0	CFC	6.7	7
TCSG.A4R7.B2	1.0	134.6	CFC	6.7	7
TCSG.A4L7.B2	1.0	46.3	CFC	6.7	7
TCSG.B5L7.B2	1.0	141.5	CFC	6.7	7
TCSG.D5L7.B2	1.0	51.4	CFC	6.7	7
TCSG.E5L7.B2	1.0	130.5	CFC	6.7	7
TCSG.6L7.B2	1.0	0.5	CFC	6.7	7
TCLA.A6L7.B2	1.0	90.0	Cu-W	10	10
TCLA.B6L7.B2	1.0	0.0	Cu-W	10	10
TCLA.C6L7.B2	1.0	90.0	Cu-W	10	10
TCLA.D6L7.B2	1.0	0.0	Cu-W	10	10
TCLA.A7L7.B2	1.0	0.0	Cu-W	10	10
TCDQA.A4L6.B2	3.0	0.0	CFC	8.0	8.0
TCDQA.B4L6.B2	3.0	0.0	CFC	8.0	8.0
TCSG.4L6.B2	1.0	0.0	CFC	7	7.5
TCTH.4R5.B2	1.0	0.0	Cu-W	out	8.3
TCTVA.4R5.B2	1.0	90.0	Cu-W	out	8.3
TCL.5L5.B2	1.0	0.0	Cu	out	10.0

Name	Length [m]	Angle [deg]	Material	Half-gap[σ_z]	
				injection	collision
TCP.6R3.B2	0.6	0.0	CFC	8.0	15.0
TCSG.5R3.B2	1.0	0.0	CFC	9.3	18.0
TCSG.4L3.B2	1.0	0.0	CFC	9.3	18.0
TCSG.A5L3.B2	1.0	170.7	CFC	9.3	18.0
TCSG.B5L3.B2	1.0	10.8	CFC	9.3	18.0
TCLA.A5L3.B2	1.0	90.0	Cu-W	10.0	20.0
TCLA.B5L3.B2	1.0	0.0	Cu-W	10.0	20.0
TCLA.6L3.B2	1.0	0.0	Cu-W	10.0	20.0
TCLA.7L3.B2	1.0	0.0	Cu-W	10.0	20.0
TCTH.4R2.B2	1.0	0.0	Cu-W	out	8.3
TCTVB.4R2	1.0	90.0	Cu-W	out	8.3
TCTH.4R1.B2	1.0	0.0	Cu-W	out	8.3
TCTVA.4R1.B2	1.0	90.0	Cu-W	out	8.3
TCL.5L1.B2	1.0	0.0	Cu	out	10.0

Appendix B

Beam loss maps during collimator beam based alignment

Loss maps for various collimator types during beam based setup as presented in section 6.1.3.

Figure B.1: Loss map for the $17\,\mathrm{m}\ \beta_z{}^*$ injection optics and the Beam 1 horizontal halo. The TCP.C6L7.B1 collimator is set at $6\,\sigma$ while the last secondary collimator (TCSG.6R7.B1) has an half gap of $5.7\,\sigma$. The rest of the collimation system is set at the nominal openings.

Figure B.2: Loss map for the $17\,\mathrm{m}$ $\beta_z{}^*$ injection optics and the Beam 1 horizontal halo. The TCP.C6L7.B1 collimator is set at $6\,\sigma$ while the last absorber collimator (TCLA.A7R7.B1) has an half gap of $5.7\,\sigma$. The rest of the collimation system is set at the nominal openings.
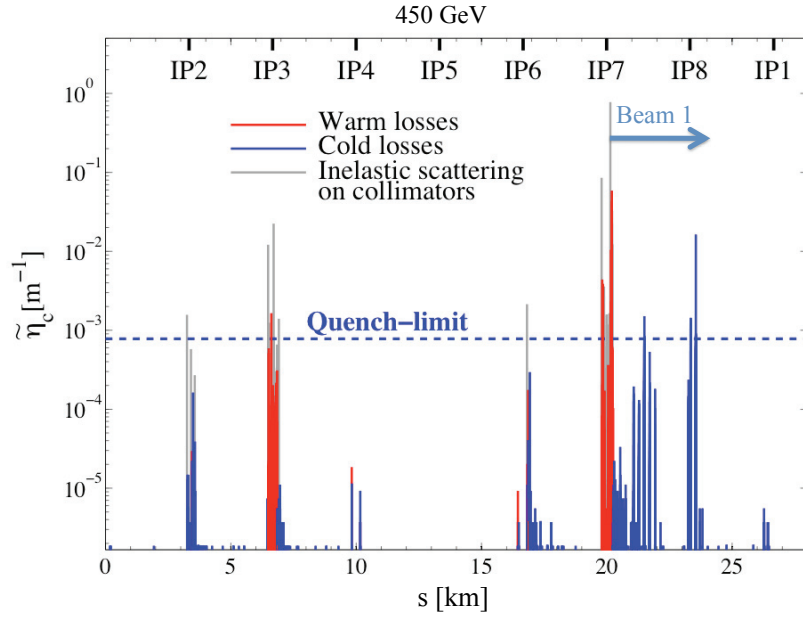

Figure B.3: Loss map for the low-beta optics and the Beam 1 horizontal halo. The TCP.C6L7.B1 collimator is set at $6.3\,\sigma$ while the last secondary collimator (TCSG.6R7.B1) has an half gap of $6\,\sigma$. The rest of the collimation system is set at the nominal openings.
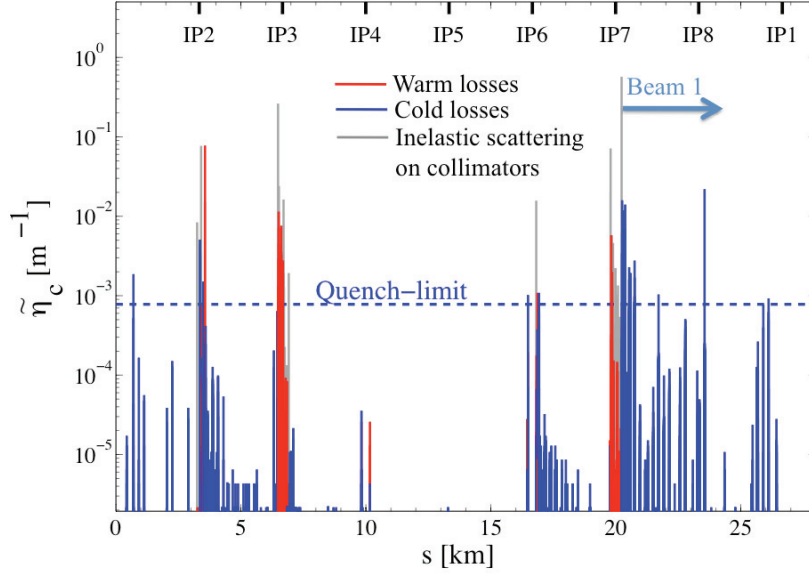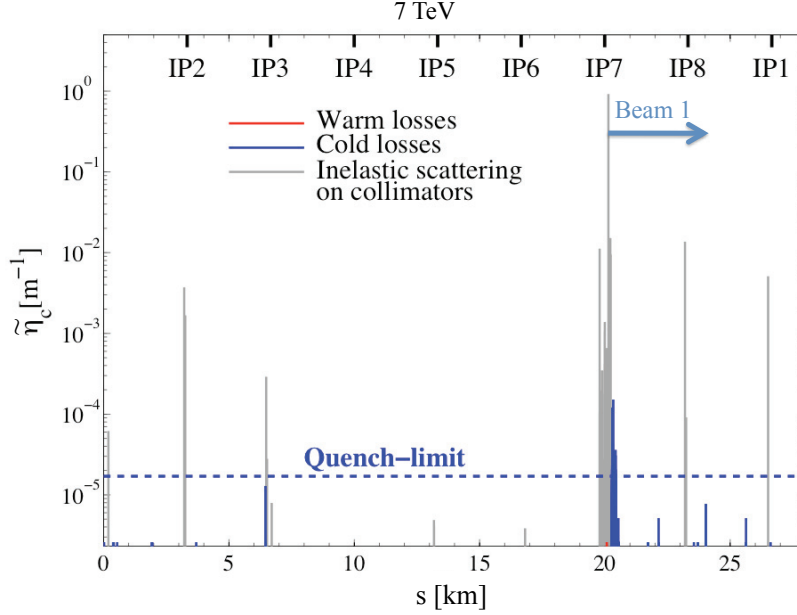
Figure B.4: Loss map for the low-beta optics and the Beam 1 horizontal halo. The TCP.C6L7.B1 collimator is set at $6.3\,\sigma$ while the last secondary absorber (TCLA.A7R7.B1) has an half gap of $6\,\sigma$. The rest of the collimation system is set at the nominal openings.

Figure B.5: Loss map for the low-beta optics and the Beam 1 horizontal halo. The TCP.C6L7.B1 collimator is set at $6.3\,\sigma$ while the horizontal tertiary collimator in IR2 (TCTH.4R2.B1) has an half gap of $6\,\sigma$. The rest of the collimation system is set at the nominal openings.

Figure B.6: Loss map for the low-beta optics and the Beam 1 horizontal halo. The TCP.C6L7.B1 collimator is set at $6.3\,\sigma$ while the vertical tertiary collimator in IR2 (TCTVB.4R2.B1) has an half gap of $6\,\sigma$. The rest of the collimation system is set at the nominal openings.
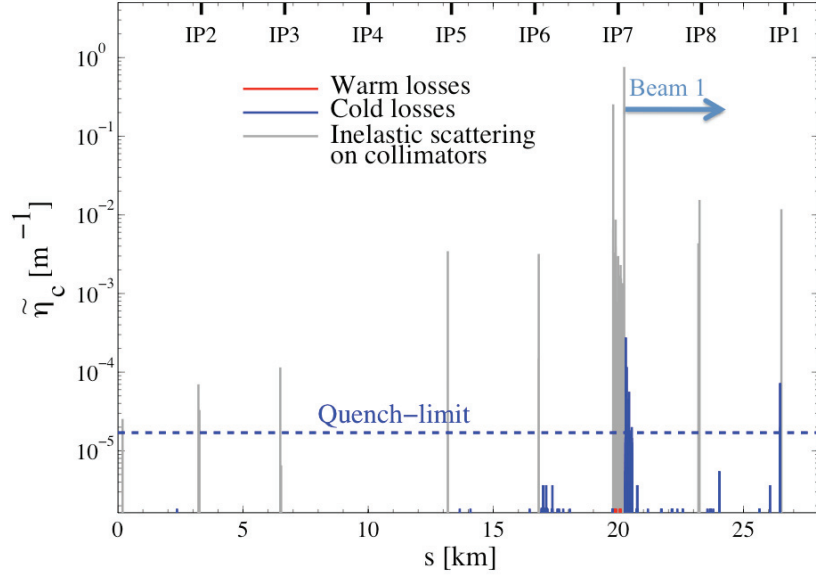

Figure B.7: Loss map for the low-beta optics and the Beam 1 horizontal halo. The TCP.C6L7.B1 collimator is set at $6.3\,\sigma$ while the horizontal tertiary collimator in IR5 (TCTH.4R5.B1) has an half gap of $6\,\sigma$. The rest of the collimation system is set at the nominal openings.
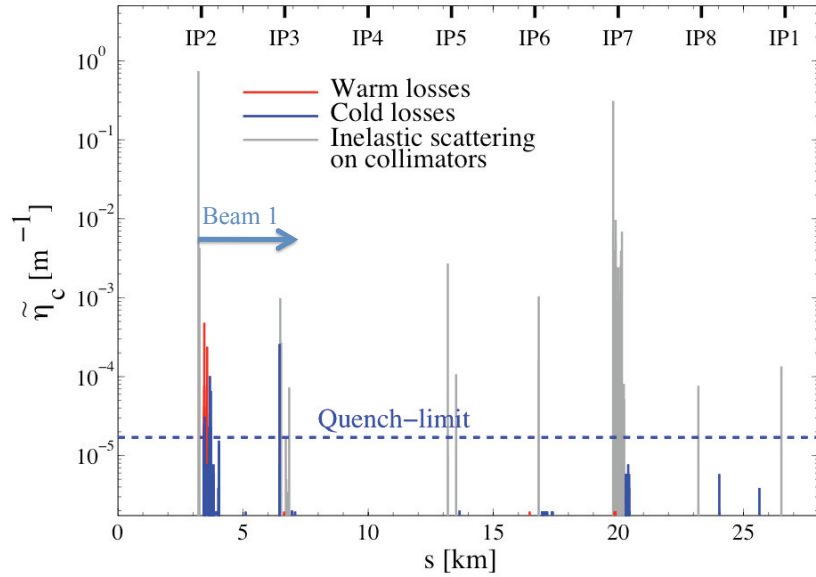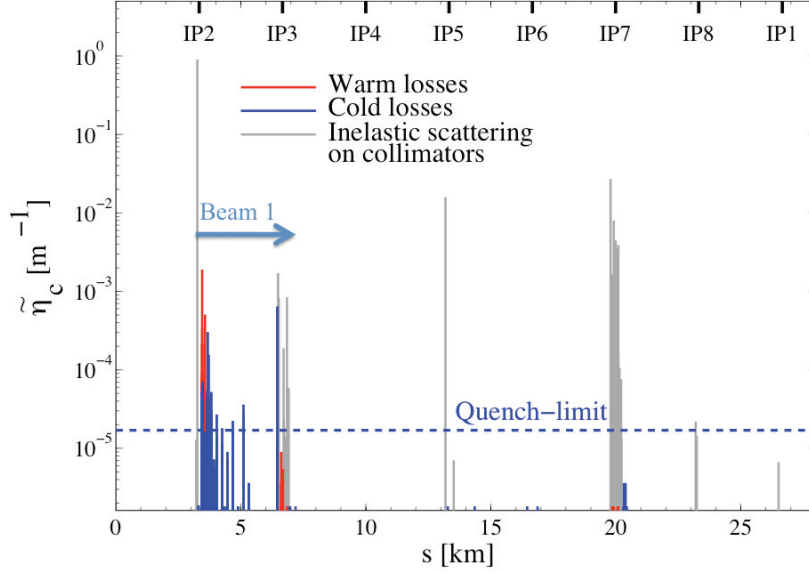
Figure B.8: Loss map for the low-beta optics and the Beam 1 horizontal halo. The TCP.C6L7.B1 collimator is set at $6.3\,\sigma$ while the vertical tertiary collimator in IR5 (TCTVA.4R5.B1) has an half gap of $6\,\sigma$. The rest of the collimation system is set at the nominal openings.
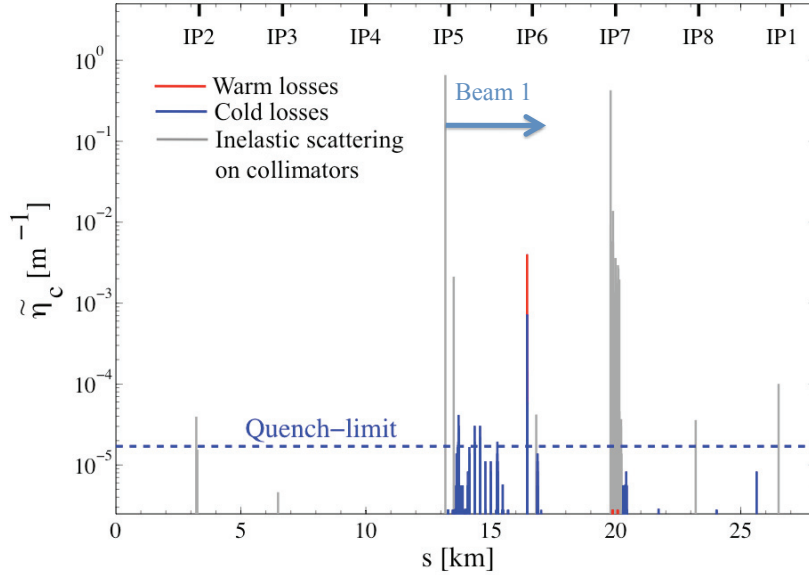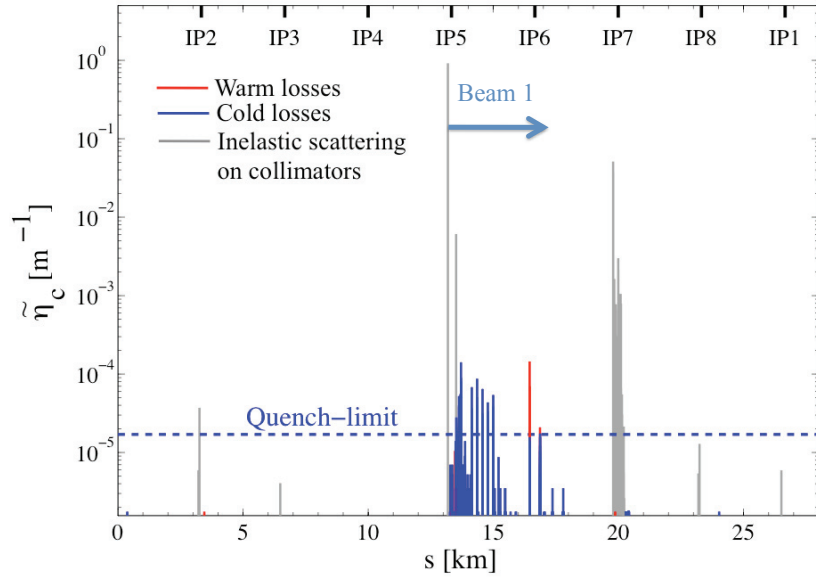
Bibliography

[1] *"LHC Design Report, Volume I: The LHC Main Ring"*, CERN Editorial Board, CERN-2004-003, 2004.

[2] J. Rossbach, P. Schmüser, *"Basic course on accelerator optics"*, CAS‑CERN Accelerator School: 5th general accelerator Physics course, CERN 94-01 vol. 1, 1994.

[3] K. Potter, *"Luminosity measurements and calculations"*, CAS‑CERN Accelerator School: 5th general accelerator Physics course, CERN 94-01 vol. 1, 1994.

[4] http://atlas.ch, ATLAS collaboration.

[5] http://cms-project-cmsinfo.web.cern.ch/cms-project-cmsinfo/index.html, CMS collaboration.

[6] http://lhcb-public.web.cern.ch/lhcb-public, LHCb collaboration.

[7] http://totem.web.cern.ch/Totem, TOTEM collaboration.

[8] http://press.web.cern.ch/Public/en/LHC/LHCf-en.html, LHCf collaboration.

[9] http://aliceinfo.cern.ch/Public/Welcome.html, ALICE collaboration.

[10] J.B. Jeanneret, D. Leroy, L. Oberli and T. Trenckler, *"Quench levels and transient beam losses in the LHC magnets"*, LHC Project Report 44, 1996.

[11] R. Assmann et al., *"Requirements for the LHC collimation system"*, proceedings of the European Particle Accelerator Conference EPAC02, Paris, France, 2002.

[12] D.A. Edwards, M.J. Syphers, *"An introduction to the Physics of high energy accelerators"*, Wiley-Interscience Publication, 1993.

[13] E. Shaposhnikova, *"Time scales for the motion of uncaptured particles with RF off and RF on in LHC"*, LHC Project Note 281, 2002.

[14] G. Robert-Demolaize, *"Design and performance optimization of the LHC collimation system"*, LHC Project Report 981, 2006.

[15] R. Assmann, F. Schmidt and F. Zimmermann, *"Equilibrium beam distribution and halo in the LHC"*, proceedings of the European Particle Accelerator Conference EPAC02, Paris, France, 2002.

[16] J.P. Koutchouk, *"The LHC dynamic aperture"*, LHC Project Report 296, 1999.

[17] J.B. Jeanneret, R. Ostojic, *"Geometrical acceptance in LHC version 5.0"*, LHC Project Note 111, 1997.

[18] S. Redaelli, R. Assmann and G. Robert-Deomlaize, *"LHC aperture and commissioning of the collimation system"*, proceedings of the LHC Project Workshop "Chamonix XIV", 2005.

[19] A. Wrulich, *"Single-beam lifetime"*, CAS - CERN Accelerator School: 5th general accelerator Physics course, CERN 94-01 vol. 1, 1994.

[20] http://mad.home.cern.ch/mad, AB/ABP accelerator Physics group.

[21] K.L.F. Bane, *"A simplified model of intrabeam scattering"*, proceedings of the European Particle Accelerator Conference EPAC02, Paris, France, 2002.

[22] F. Zimmermann, M.P. Zorzano, *"Touschek scattering in HERA and LHC"*, LHC Project Note 244, 2000.

[23] M. Lamont, *Estimates of annual proton doses in the LHC*, LHC Project Note 375, 2005.

[24] R.P. Walker, *"Synchrotron radiation"*, CAS - CERN Accelerator School: 5th general accelerator Physics course, CERN 94-01 vol. 1, 1994.

[25] E. Keil, *"Synchrotron radiation dominated hadron colliders"*, proceedings of the 17th Particle Accelerator Conference PAC97, Vancouver, Canada, 1997.

[26] R.P. Walker, *"Radiation damping"*, CAS - CERN Accelerator School: 5th general accelerator Physics course, CERN 94-01 vol. 1, 1994.

[27] R. Schmidt et al., *"LHC machine protection"*, LHC Project Report 1053, 2007.

[28] R. Steinhagen, *"LHC beam stability and feedback control - orbit and energy"*, CERN Thesis, RWTH Aachen Univ., 2007.

[29] B. Goddard et al., *"Protection of the LHC against unsynchronised beam aborts"*, LHC Project Report 916, 2006.

[30] V. Kain, *"Machine protection and beam quality during the LHC injection process"*, CERN-THESIS-2005-047, 2005.

[31] E.B. Holzer et al., *"Design of the beam loss monitoring system for the LHC ring"*, proceedings of the European Particle Accelerator Conference PAC04, Lucerne, Switzerland, 2004.

[32] H. Bichsel, D.E. Groom and S.R. Klein, *"Passage of particles through matter"*, The Review of Particle Physics web page, Reviews Tables and Plots.

[33] N. Catalan-Lasheras, *"Transverse and longitudinal beam collimation in a high-energy proton collider (LHC)"*, CERN-THSIS-2000-019.

[34] H.A. Bethe, *"Moliere's theory of multiple scattering"*, Physical Review 89, pp.1256-1266, 1953.

[35] R.M. Barnett et al., *"Cross-section formulae for specific processes"*, Physical Review D, vol. 54, Issue 1, pp.179-198, 1996.

[36] K. Goulianos, *"Diffractive interactions of hadrons at high energies"*, Physics Reports vol. 101, pp.171-219, 1983.

[37] R.M. Barnett et al., *"Atomic and nuclear properties of materials"*, Physical Review D, vol. 54, Issue 1, pp.72-73, 1996.

[38] G. Bellettini et al., *"Proton-nuclei cross-section at 20 GeV"*, Nuclear Physics vol. 79, pp. 609-624, 1966.

[39] T. Trenkler and J.B. Jeanneret, *"The principles of two stage betatron and momentum collimation in circular accelerators"*, LHC note 312, 1995.

[40] J.B. Jeanneret, *"Optics of a two-stage collimation system"*, Physical Review Special Topics: Accelerators and Beams, 1998.

[41] R. Assmann et al., *"Designing and building a collimation system for the high intensity LHC beam"*, LHC Project Report 640.

[42] R. Assmann et al., *"The final LHC collimation system"*, LHC Project Report 919, 2006.

[43] http://ab-div-bdi-bl-blm.web.cern.ch/ab-div-bdi-bl-blm/Quench levels

[44] R. Assmann et al., *"Preliminary beam-based specifications for the LHC collimators"*, LHC Project Note 277.

[45] G. Robert-Demolaize et al., *"A new version of SixTrack with collimation and aperture interface"*, proceedings of the 21st Particle Accelerator Conference PAC05, Knoxville, TN, USA, 2005.

[46] R. Assmann, *"Collimators and cleaning: could that limit the LHC performance?"*, proceedings of the Chamonix XII Workshop, 2003.

[47] R. Assmann, B. Goddard, E. Vossenberg and E. Weisse, *"The consequences of abnormal beam dump actions on the LHC collimation system"* , LHC Project Note 293, 2002.

[48] D. Bocian, B. Dehning and A. Siemko, *"Modeling of Quench Limit for Steady State Heat Deposits in LHC Magnets"*, IEEE Transactions on Applied Superconductivity, Volume 18, Issue 2, pp. 112 - 115, June 2008,.

[49] F. Zimmermann et al., *"Tune shift induced by nonlinear resistive wall wake field of flat collimator"*, proceedings of the European Particle Accelerator Conference EPAC06, Edinburgh, UK, 2006.

[50] G. Kotzian, W. Höfle, E. Vogel, *"LHC transverse feedback damping efficiency"*, LHC Project Report 1156, 2008.

[51] E. Metral, *"Overview of Impedance and Single-Beam Instability Mechanisms"*, proceedings of the 21st Particle Accelerator Conference PAC05, Knoxville, TN, USA, 2005.

[52] R. Assmann et al., *"An improved collimation system for the LHC"*, LHC Project Report 773, 2004.

[53] J. Smith, *"LARP phase 2 collimator progress and plans"*, talk presented at the 7th Phase 2 Specification and Implementation meeting, CERN, June 13th, 2008.

[54] A. Bertarelli et al., *"The mechanical design for the LHC collimators"*, LHC Project Report 786, 2004.

[55] T. Weiler et al., *"LHC collimation system hardware commissioning"*, proceedings of the 22nd Particle Accelerator Conference PAC07, Albuquerque, NM, USA, 2007.

[56] O. Aberle et al., *"Collimator integration and installation example of one object to be installed in the LHC"*, proceedings of the European Particle Accelerator Conference EPAC08, Genoa, Italy, 2008.

[57] M.K. Craddock et al.,*"Optics solutions for the collimation insertion of LHC"*, LHC Project Report 305, 1999.

[58] S. Redaelli, *"Cleaning efficiency and beam losses with 0.6m long TCPs at IR7"*, talk presented at the 59th Collimation Working Group, CERN, June 13th, 2005.

[59] T. Weiler, private communication.

[60] E. Metral et al., *"Transverse impedance of LHC collimators"*, LHC Project Report 1015, 2007.

[61] T. Weiler et al., *"Beam cleaning and beam loss control"*, proceedings of Advanced Beam Dynamic Workshop on High-Intensity, High-Brightness Hadron Beams, Nashville, TN, US, 2008.

[62] V. Shiltsev et al., *"LHC particle collimation by hollow electron beams"*, proceedings of the European Particle Accelerator Conference EPAC08, Genoa, Italy, 2008.

[63] W. Scandale, *"Crystal collimation as an option for the LHC"*, Proceedings of International Conference on Charged and Neutral Particles Channeling Phenomena, Frascati, Italy, 2006.

[64] R.Bailey, *"Summary Of Overall Commissioning Strategy For Protons"*, proceedings of the Chamonix XV Workshop, 2006, Divonne, France.

[65] F. Schmidt, *"SixTrack, user reference manual"*, CERN SL/94-56, 1994.

[66] Collimation Project web page: http://lhc-collimation-project.web.cern.ch/lhc-collimation-project/code-tracking.htm.

[67] R. Assmann et al., *"Tools for predicting cleaning efficiency in the LHC"*, proceedings of the 20th Particle Accelerator Conference PAC03, Portland, OR, USA, 2003.

[68] T. Trenkler, J.B. Jeanneret, *"K2, a software package evaluating collimation systems in circular colliders (manual)"*, CERN SL/94105 (AP), 1994.

[69] A. Bertarelli et al., *"Permanent deformation of the LHC collimator jaws induced by shock beam Impact : an analytical and numerical interpretation"*, proceedings of the European Particle Accelerator Conference EPAC06, Edinburgh, UK, 2006.

[70] M. Santana-Leitner et al., *"Optimization of the active absorber scheme for the protection of the Dispersion Suppressor"*, LHC-Project-note, to be published.

[71] B. Goddard et al., *"Results of the studies on energy deposition in IR6 superconducting magnets from continuous beam loss on the TCDQ system"*, LHC-Project-Report-1052, 2007.

[72] R. Assmann, *"Beam commissioning of the collimation system"*, proceedings of the Chamonix XV Workshop, 2006, Divonne, France.

[73] C. Bracco et al., *"Collimation efficiency during commissioning"*, LHC-Project-Report-920, proceedings of the European Particle Accelerator Conference EPAC06, Edinburgh, UK, 2006.

[74] J.P. Koutchouk, L. Rossi and E. Todesco, *"A solution for phase 1 upgrade of the LHC low-beta quadrupoles based on Nb-Ti"*, LHC-Project-Report-1000.

[75] O. Brüning et al., *"The nominal operational cycle of the LHC beam (version 1)"*, LHC-Project-Note-313.

[76] C. Bracco et al., *"Scenarios for beam commissioning of the LHC collimation system"*, proceedings of the 22nd Particle Accelerator Conference PAC07, Albuquerque, NM, USA, 2007.

[77] A. Dallocchio,*"Study of thermo-mechanical effects induced in solids by high energy particle beams: analytical and numerical methods"* CERN-THESIS, to be published.

[78] J.B. Jeanneret, *"Geometrical tolerances for the qualification of LHC magnets"*, LHC-Project-Report-1007, 2006.

[79] A. Koschik et al., *"Transverse resistive wall impedance and wake function with "Inductive Bypass""* , proceedings of the European Particle Accelerator Conference PAC04, Lucerne, Switzerland, 2004.

[80] R. Assmann et al., *"LHC collimation : design and results from prototyping and beam tests"*, proceedings of the 21st Particle Accelerator Conference PAC05, Knoxville, TN, USA, 2005.

[81] S. Redaelli et al., *"The LHC collimator controls architecture-design and beam tests"*, proceedings of the 22nd Particle Accelerator Conference PAC07, Albuquerque, NM, USA, 2007.

[82] A. Jansson et al., *"Collimator scans to measure Tevatron emittance"*, Tevatron Beam Study Report, January 21st, 2003.

[83] H. Burkhardt and R. Schmidt, *"Intensity and luminosity after beam scraping"*, CERN Internal Note, CERN-AB-2004-032-ABP, 2004.

[84] M. Seidel, *"The proton collimation system of HERA"*, PhD thesis, Universität Hamburg, 1994.

[85] S. Redaelli et al., *"Detecting impacts of proton beams on the LHC collimators with vibration and sound measurements"*, proceedings of the 21st Particle Accelerator Conference PAC05, Knoxville, TN, USA, 2005.

[86] S. Redaelli, *"Accelerometer and microphone measurements of the LHC collimator"*, talk presented at the Workshop on Materials for Collimators and Beam Absorbers, CERN, Geneva, 2007.

[87] H. Richter, R. Wilfinger et al., *"LHC collimator jaw vibration measurements during TT40 high intensity collimator test 2006"*, CERN technical note, to be published.

[88] R. Assmann and J.B. Jeanneret, *"Efficiency for the imperfect collimation system"*, LHC-Project-Report-598, 2002.

[89] E.B. Holzer et al., *"Generation of 1.5 million beam loss threshold values"*, proceedings of the European Particle Accelerator Conference EPAC08, Genoa, Italy, 2008.

[90] M. Lamont et al., *"A staged approach to LHC commissioning"*, LHC Project Report 949, 2006.

Curriculum Vitae

Chiara Bracco

PERSONAL DATA

name	Chiara Bracco
DOB	July 31st 1977, Biella- Italy
e-mail	chiara.bracco@cern.ch

EDUCATION AND QUALIFICATION

June 2005	I started the PhD at the École Polytechnique Fédérale de Lausanne (EPFL).
thesis' title	"Commissioning scenarios and tests for the LHC collimation system"
July 2004	Italian "Laurea" in Physics at "Universitá degli studi di Milano"
subject	Applied Physics
score	110/110 cum laude
thesis' title	"Setup of a cryogenic apparatus for measurements at controlled temperature and application to characterization of electric transport properties of superconducting tapes in MgB_2/Ni"
July 1996	Scientific secondary school "Liceo A. Avogadro", Biella.
score	56/60

RESEARCH EXPERIENCES

From June 2007   I am working at CERN as a PhD student in the accelerator beam group (AB/ABP) supervised by Dr. Ralph Assmann (leader of the LHC collimation project).

February 2003   During the master thesis period I've been working at the
July 2004   INFN LASA laboratories (Segrate, Milano) supervised by Dr. Giovanni Volpini and Prof. Giovanni Bellomo.

PUBLICATIONS

As main author:

C. Bracco, *"Messa a punto di un apparato criogenico per misure a temperatura controllata e applicazione alla caratterizzazione delle proprietá di trasporto elettrico di nastri superconduttori di MgB_2/Ni"*, Master Thesis, Milan, Italy, July 2007.

C. Bracco et al., *"LHC collimation efficiency during commissioning"*, LHC-Project-Report-920, proceedings of the European Particle Accelerator Conference EPAC06, Edinburgh, UK, 2006.

C. Bracco et al., *"Scenarios for beam commissioning of the LHC collimation system"*, proceedings of 22nd Particle Accelerator Conference PAC07, Albuquerque, NM, USA, 2007.

As coauthor:

R. Assmann et al., *"The final collimation system for the LHC"*, LHC-Project-Report-919, proceedings of the European Particle Accelerator Conference EPAC06, Edinburgh, UK, 2006.

G. Robert-Demolaize et al., *"Critical beam losses during commissioning and initial operation of the LHC"*, proceedings of the Chamonix XV Workshop, 2006, Divonne, France.

G. Robert-Demolaize et al., *"Critical halo loss locations in the LHC"*, LHC-Project-Report-940, proceedings of the European Particle Accelerator Conference EPAC06, Edinburgh, UK, 2006.

R. Bruce et al., *"Ion and proton loss patterns at the SPS and LHC"*, proceedings of the CARE-HHH-APD Workshop on Finalizing the Roadmap for the Upgrade of the CERN and GSI Accelerator Complex, CERN, Geneva, 2007.

B. Goddard et al., *"Results of the studies on energy deposition in IR6 superconducting magnets from continuous beam losses on the TCDQ system"*, LHC-Project-Report-1052, 2007.

E. Metral et al., *"Transverse impedance of LHC collimators"*, proceedings of the 22nd Particle Accelerator Conference PAC07, Albuquerque, NM, USA, 2007.

G. Robert-Demolaize et al., *"Performance reach of the LHC"*, proceedings of the 22nd Particle Accelerator Conference PAC07, Albuquerque, NM, USA, 2007.

T. Weiler et al., *"Beam loss response measurements with an LHC prototype collimator in the SPS"*, proceedings of the 22nd Particle Accelerator Conference PAC07, Albuquerque, NM, USA, 2007.

R. Bruce et al., *"Measurements of heavy ions beam losses from collimation*, LHC-Project-Report-1109, proceedings of the European Particle Accelerator Conference EPAC08, Genoa, Italy, 2008.

L. Lari et al., *"Evaluation of beam losses and energy deposition for a possible phase II design for LHC collimation"*, LHC-Project-Report-1115, proceedings of the European Particle Accelerator Conference EPAC08, Genoa, Italy, 2008.

L. Lari et al., *"Preliminary exploratory study of different phase II collimators"*, LHC-Project-Report-1114, proceedings of the European Particle Accelerator Conference EPAC08, Genoa, Italy, 2008.

T. Weiler et al., *"Beam cleaning and beam loss control"*, proceedings of Advanced Beam Dynamic Workshop on High-Intensity, High-Brightness Hadron Beams, Nashville, TN, US, 2008.

M. Santana-Leitner et al., *"Optimization of the active absorber scheme for the protection of the Dispersion Suppressor"*, LHC-Project-note, to be published.

Acknowledgments

I am leaving the status of student at last! This is the best time to thank all the people who have been sustaining (and also standing) me during this long time, almost my full life, and especially during this PhD.

First of all I would like to thank my supervisors: Ralph Assmann and Leonid Rivkin for guiding me along this demanding but rewarding period. Special thanks also to Aurelio Bay and Albin Wrulich who welcomed and took care of me during my first year at the EPFL.

Thanks to Lucio Rossi who encouraged me to apply for a PhD at CERN giving me, in this way, the opportunity to discover this crazily interesting world. Many thanks to Steve Peggs for agreeing to be a member of my PhD jury and to Giulia Bellodi who accepted to read my thesis trying to improve my english. Thanks to Jean Bernard Jeanneret for teaching me all the secrets about collimation theory and to Elias Metral who made "impedance" much less mysterious to my hears.

A huge "thank you!!" to the collimation team: Valentina Previtali, Stefano Redaelli, Guillaume Robert-Demolaize and Thomas Weiler who made tracking pleasant and also funny. Thanks to all CERN people with whom I have been working and in particular to the members of the AB/ABP group that hosted me during the last years. This work would not have been possible without your help and collaboration.

Many thanks also to the colleagues from other laboratories: SLAC, FNAL, BNL and Kurchatov institute for helping us in further improving the LHC collimators.

This is then especially the time to thank all my family (in italian): "grazie per aver ancora una volta condiviso con me momenti difficili e soddisfazioni.......almeno stavolta non avete dovuto anche pagare!".

Special thanks obviously to Marco and my cat Tommaso (he can obviously read english) who were also physically close to me and took the best and the worst part of my emotional exuberance.

Thanks to my old and new friends: Ingrid, Lucia, Marco, Laura, etc. etc........you are too many to fit in here but all of you fit in my heart! Please stop crying guys!!! Last but not least, thanks to my biggest and youngest fan Stefano: don't forget your italian-french-swiss aunt now that you go back to Italy!

Thanks again sincerely to all of you but now, please, let me stop writing!!!!

Chiara